

Double actuator cylinder (AC) model of a tandem vertical-axis wind turbine (VAWT) counter-rotating rotor concept operating in different wind conditions

Department of Wind Energy Master Report

Ang Li

DTU Wind Energy-M-0172

July 2017

DTU Wind Energy
Department of Wind Energy



Authors: Ang Li

Title: Double actuator cylinder (AC) model of a tandem vertical-axis wind turbine (VAWT) counter-rotating rotor concept operating in different wind conditions

DTU Wind Energy-M-0172
July 2017

Project Period:
October 2016 – July 2017

ECTS: 45

Education: Master of Science

Supervisors:

Uwe Schmidt Paulsen
Helge Aagaard Madsen

DTU Wind Energy

Carlos Simão Ferreira
Delphine De Tavernier

TU Delft

Remarks:

This report is submitted as partial fulfillment of the requirements for graduation in the above education at the Technical University of Denmark.

As the student is an EWEM-student the education is carried out on both DTU and TUDelft, The Netherlands

DTU Wind Energy is a department of the Technical University of Denmark with a unique integration of research, education, innovation and public/private sector consulting in the field of wind energy. Our activities develop new opportunities and technology for the global and Danish exploitation of wind energy. Research focuses on key technical-scientific fields, which are central for the development, innovation and use of wind energy and provides the basis for advanced education at the education.

We have more than 240 staff members of which approximately 60 are PhD students. Research is conducted within nine research programmes organized into three main topics: Wind energy systems, Wind turbine technology and Basics for wind energy.

Technical University of Denmark

Department of Wind Energy
Frederiksborgvej 399
4000 Roskilde
Denmark

www.vindenergi.dtu.dk

Double actuator cylinder (AC) model of a tandem vertical axis wind turbine (VAWT) counter-rotating rotor concept operating in different wind conditions

Master of Science Thesis

For obtaining the degree of Master of Science in Aerospace Engineering
at Delft University of Technology and in Engineering Wind Energy at
Technical University of Denmark.

Ang Li

July 31, 2017

European Wind Energy Master
DUWIND - Delft University of Technology
DTU Wind Energy - Technical University of Denmark



Technical University
of Denmark



Abstract

Due to the potential to reduce the cost of energy (CoE) by decreasing the distance between Vertical Axis Wind Turbines (VAWTs) and applying the counter-rotating layouts of the rotors in the VAWT wind farm [38], the aerodynamics of the double-rotor setup should be correctly modelled. The aim of this thesis is to evaluate the influence between the VAWT rotors with the Double Actuator Cylinder (DAC) model [36] which will be validated against the panel code [14]. The DAC model is developed from the original Actuator Cylinder (AC) model [32] which includes the Modified-Linear (Mod-Lin) correction [25]. The original AC model for modelling single rotor is investigated, modified and validated against the panel code to be sufficient which is the premise for a sufficient DAC model. The original AC model is modified step by step to become a dynamic AC model including Cheng's modification [8], flow curvature effect and unsteady aerodynamics. The unsteady aerodynamics is included by coupling the modified Risø dynamic stall model [18] with the AC model. An investigation with Migliore's conformal mapping method [33] as well as panel code revealed that the modified Risø dynamic stall model [18] implicitly take into account the flow curvature effects. The derived dynamic AC model is validated to show good agreements with the panel code. It is also revealed that further improvements could be made to the Mod-Lin correction method. The DAC model is finally derived, and the implementation is validated with the *mirror effect*. The performance of the DAC model on predicting the influence between the two rotors is then investigated.

In a first comparison of the thrust and power coefficient from the DAC model and panel code, the values are not well predicted with the DAC model for high loading cases for different rotational direction setups, with the maximum relative error to be 11%. Secondly, for the condition of placing the two rotors very close together, there will be around 2% increase of aerodynamic power according to results from panel code, but the increment is underestimated by the DAC model. Thirdly, it is validated that the variations of the thrust and power coefficient with the distance between the two rotors are also underestimated by the DAC model. Fourthly, the influence due to the phase difference is investigated with the panel code and shown it could be neglected because the mean values of thrust and power of the two rotors only have small variation with it. Finally, according to the results from panel code, the influence between the two rotors will result in a lead or lag of the phase of the azimuthal variation of loadings, angle of attack and local thrust coefficient, depending on the rotational direction layout of the two rotors. The influence will also

result in transfer of the value of aforementioned variables between windward and leeward part of the rotor. The former effect is well modelled with the DAC model while there will be minor issues on modelling the latter effect.

Preface

This thesis was prepared at Department of Wind Energy at Technical University of Denmark in fulfilment of the requirements for obtaining the degree of Master of Science in Engineering Wind Energy at Technical University of Denmark and in Aerospace Engineering at Delft University of Technology.

Acknowledgements

This master thesis is the final work for obtaining the degree of Master of Science in Engineering Wind Energy at Technical University of Denmark and in Aerospace Engineering at Delft University of Technology. I would like to express my sincere gratitude to everyone who supported me throughout this thesis work. This project is not going to be possible without your help and guidance.

Firstly I would like to thank my supervisors Uwe Schmidt Paulsen and Helge Aagaard Madsen from DTU. I would like to thank Uwe for his help in explaining the Double Actuator Cylinder model, introducing the mirror effect and the setting up of the HAWC2 code for VAWT. His enthusiasm, positiveness, patience and friendliness have been extremely helpful. I would like to thank Helge for his help in grasping the concept the Actuator Cylinder model, Mod-Lin correction, dynamic stall model and conformal mapping method. His supervision and critical judgements help me to find out present shortcomings and provide guidance for improvements. Secondly, I would like to thank my supervisors Carlos Simão Ferreira and Delphine De Tavernier from TU Delft. I would like to thank Carlos for his help in many important aspects of VAWT modelling especially the direction of the lift force in dynamic stall modelling. He also provides the panel code of U2DiVA which is a very useful tool and has been used in different ways in this reports. I would like to thank Delphine for verifying the implementation of the Actuator Cylinder model and guiding me with the using of the panel code of U2DiVA. I was very impressed with the manual you made and also the feedback you gave. I would like to thank all my supervisors for the supervisory meeting every two weeks, the meetings provide me guidelines of the further researches.

I would like to thank Georg Pirrung for explaining the extended Risø dynamic stall model. I also want to thank my friend Gary Kwan Yuan for suggestions on English grammar. I would like to thank Naja Møller for arranging the working place in DTU Risø. I would also like to thank all my teachers in DTU and TU Delft for providing me with the knowledge in wind energy.

Special appreciations to my family and girlfriend for the supports and encouragements even though we are thousands of miles away. To my mother, I am very grateful for

the opportunities you offered me. Your unconditional love and care helped through the challenges in my life. To my girlfriend, I would like to thank you for accompanying me and encouraging me through the study.

Roskilde, Denmark

July 31, 2017

Ang Li

Contents

Abstract	i
Preface	iii
Acknowledgements	v
Contents	x
List of Figures	xv
List of Tables	xvii
Nomenclature	xxii
1 Introduction	1
1.1 Research Objectives and Questions	2
1.2 Methodology	4
2 Literature Review	7
2.1 Working principles of the VAWT	7
2.1.1 Types and layout of VAWT	7
2.1.2 Energy conversion	8
2.2 Aerodynamic models for VAWTs	8
2.2.1 Streamtube models	9
2.2.2 Actuator Cylinder model	11
2.2.3 Vortex and Panel models	13
2.2.4 Computational Fluid Dynamics models	15
2.2.5 Ability of modelling double-rotor layouts	15
2.3 Unsteady flow effects	16
2.3.1 Dynamic stall effect	16
2.3.2 Dynamic stall modelling	19
2.3.3 Flow curvature effect	21
2.3.4 Blade wake interaction	21

3	Actuator Cylinder Model	23
3.1	Implementation procedure	23
3.1.1	Discretization method	26
3.1.2	The influence coefficients	28
3.1.3	Calculate loadings at the control points.	28
3.1.4	Mod-Lin correction method	32
3.1.5	Iteration method for converged solutions	33
3.1.6	Calculate the velocity at arbitrary points	35
3.2	Validation against HAWC2 code	37
3.3	Some aspects for the Actuator Cylinder model	39
3.3.1	Matrix formulations	39
3.3.2	Clockwise rotation and mirror effect	43
3.3.3	Cheng's modified Actuator Cylinder model	46
3.3.4	The explicit form of the wake terms	49
3.3.5	The continuity of velocity	52
3.3.6	The mounting point	59
3.4	Validation against the panel code	66
3.4.1	The choice of airfoil and airfoil polar	66
3.4.2	Power coefficient and thrust coefficient	67
3.4.3	Detailed validation against panel code	70
3.4.4	Reasons of loading deviations	72
3.4.5	Possible improvements	73
3.5	Conclusions of the chapter	73
4	Simplifications and analytical Solutions	75
4.1	Analytical solutions of influence coefficients	75
4.1.1	Transformation to polar coordinate system	75
4.1.2	Analytical solution of I_1	76
4.1.3	Analytical solution of I_2	77
4.1.4	Analytical solution of I_1 for control points	78
4.2	Analytical solutions of w_x^n	79
4.2.1	Derivation of the analytical solution	79
4.2.2	Validation of the analytical solutions	81
4.2.3	Analytical validation of the continuity of w_x^n	83
4.2.4	Continuous analytical solution of w_x^n	84
4.3	Properties of the influence coefficients	85
4.3.1	Influence coefficient I_1	85
4.3.2	Influence coefficient I_2	86
4.4	Issues of numerical integration method	87
4.5	Conclusions of the chapter	89
5	Flow curvature effect	91
5.1	Conformal mapping method	91
5.1.1	Migliore's method	91
5.1.2	Virtual camber and virtual incidence	94
5.1.3	Investigate virtual camber with panel code	96
5.1.4	Local angle of attack at three-quarter chord point	98
5.2	Evaluate at three-quarter chord point	100

5.2.1	The evaluation point and aerodynamic centre	100
5.2.2	Implementation of the method in AC model	100
5.3	Validation against panel code	105
5.3.1	Validate normal and tangential loadings	105
5.3.2	Validate lift and drag coefficient	106
5.4	Four different AC models	109
5.5	Conclusions of the chapter	110
6	Unsteady Aerodynamics	111
6.1	Risø dynamic stall model	111
6.1.1	Steady lift decomposition	111
6.1.2	Dynamics of attached flow and trailing edge separation	113
6.1.3	Indicial formulation	114
6.1.4	Application in different flow conditions	116
6.2	Pirrung's extended Risø model	116
6.2.1	Pirrung's simplification	116
6.2.2	Pirrung's modification	117
6.3	Validation of the inviscid part of Risø model	119
6.3.1	Investigation with step response	119
6.3.2	Validation with harmonic pitching	120
6.4	Coupling dynamic stall model with AC model	123
6.4.1	The flow chart of implementation	123
6.4.2	Transform between discretization methods	124
6.4.3	Two different dynamic AC models	126
6.5	Direction of applying the lift force	126
6.5.1	Definition of two types of angle of attack	126
6.5.2	Different possible type-one angle of attacks	127
6.5.3	Reasoning with the bound vortex	129
6.6	Validation of the direction of lift force	130
6.6.1	Validation of drag coefficient from panel code	130
6.6.2	Validation of loadings from the AC model	131
6.7	Performance of dynamic AC model	133
6.7.1	Comparison of two dynamic AC models	134
6.7.2	Validation of the induced velocities	135
6.7.3	Effective angle of attack and relative wind speed	140
6.7.4	Normal and tangential loadings	140
6.7.5	Thrust and power coefficient	141
6.7.6	The influence of Mod-Lin method	142
6.8	Relationship with Pirrung's extended model	145
6.8.1	Investigation of Pirrung's extended model	145
6.8.2	Comparison of the two methods	147
6.8.3	VAWT at zero wind speed	148
6.9	Conclusions of the chapter	149
7	Double Actuator Cylinder Model	153
7.1	Theoretical background and derivation	153
7.1.1	Definition of non-dimensioned coordinate systems	153
7.1.2	Derivation with linear solution properties	155

7.1.3	Multiple Actuator Cylinder model	157
7.2	Implementation of the DAC model	157
7.2.1	Four different types of the DAC models	157
7.2.2	DAC model based on original AC model	158
7.2.3	DAC model based on Cheng's AC model	159
7.2.4	Matrix formulations	160
7.3	Layouts of the two rotors	163
7.3.1	Different cases of rotational direction layouts	165
7.3.2	Validation with mirror effect	165
7.3.3	Validation with infinite distance between rotors	170
7.3.4	Power and thrust coefficients	171
7.4	Influence between rotors for different layouts	175
7.4.1	investigation of the influence with panel code	175
7.4.2	Influence between rotors from DAC models	180
7.5	Variation of the influence with distance	189
7.5.1	<i>Counter-Rotating</i> layout	189
7.5.2	<i>Co-Rotating</i> layout	192
7.5.3	Predicting relative relationship of thrust and power coefficient	194
7.6	Influence due to phase difference	194
7.6.1	<i>Counter-Up</i> layout	195
7.6.2	<i>Counter-Down</i> layout	196
7.6.3	<i>Co-Rotating</i> layout	196
7.7	Conclusion	197
8	Final Remarks	199
8.1	Conclusions	199
8.2	Recommendations	201
A	Derivation of equations	203
A.1	Derivation of the thrust coefficient and power coefficient	203
A.1.1	Derivation of the thrust coefficient	203
A.1.2	Derivation of the power coefficient	204
A.2	Transform from Cartesian to polar coordinate	205
A.3	Calculate analytical solution with Cauchy principal value	207
A.4	Derivation of Pirrung's simplification	208
A.5	Derivation of Pirrung's extended model	210
B	Results from steady AC models	213
	Bibliography	223

List of Figures

2.1	Comparison of the forces in x - and y -direction from vortex model and two DMST models [14].	11
2.2	Lifting line model with horseshoe vortices [23].	14
2.3	Approximation of the body surface by panel elements [23].	14
2.4	The onset of leading edge separation of the dynamic stall process with NACA0015 airfoil [11].	17
3.1	The distributed normal and tangential loadings in the non-dimensioned coordinate system of the Actuator Cylinder model.	24
3.2	The regions and the integration path of the Actuator Cylinder model. . . .	25
3.3	The velocity components and the angle of attack in the AC model for counter-clockwise rotating rotor.	30
3.4	The components of the aerodynamic forces in the AC model for counter-clockwise rotating rotor.	31
3.5	Flow chart of the iteration process for the Actuator Cylinder model.	34
3.6	Interpolation of the variables on the Actuator Cylinder.	35
3.7	Validation of the induced velocities in x - and y -direction and angle of attack with HAWC2 code, with $\sigma = 0.1$, $B = 2$	38
3.8	The components of velocities and aerodynamic forces for the clockwise rotating rotor.	44
3.9	The mirror effect between two rotors with different rotational directions. . .	44
3.10	Validation of the mirror effect with induced velocities and distributed loadings, with $\sigma = 0.1$, $B = 2$	45
3.11	Validation of the continuity of the induced velocities from the original AC model, with $\sigma = 0.1$, $B = 2$	53
3.12	Validation of the continuity of the induced velocities from the Cheng's modified AC model, with $\sigma = 0.1$, $B = 2$	54
3.13	The components of the induced velocity due to normal and tangential loadings, with $\sigma = 0.1$, $B = 2$	55
3.14	The definition of the normal and tangential induced velocities.	56
3.15	Validation of the continuity of the normal and tangential induced velocities, with $\sigma = 0.1$, $B = 2$	57
3.16	Components of normal induced velocity $w_n[-]$, with $\sigma = 0.1$, $B = 2$	58
3.17	Components of tangential induced velocity $w_t[-]$, with $\sigma = 0.1$, $B = 2$	59

3.18	The mounting point and the evaluation point of the VAWT blade.	60
3.19	Validation of the implementation with the angle of attack against the HAWC2 code for different mounting points, with $\lambda = 4$, $\sigma = 0.1$, $B=2$	64
3.20	Relate the mounting location to a constant pitch angle.	65
3.21	Verification of the NACA0015 airfoil polar for the inviscid flow with panel code.	68
3.22	Validation of thrust coefficient and power coefficient for different tip speed ratio and solidity.	68
3.23	Validation of the AC model with the panel code, with $\lambda = 4$, $\sigma = 0.07$, $B = 2$, $\theta_p = 0$, mounted at $1/4c$	71
3.24	Validate the inviscid lift and drag coefficient used in the AC model against that calculated from the panel code.	72
4.1	Relative error of the influence coefficient from numerical integration method with $\delta=0.01$ versus number of sub-sections N_s	88
4.2	Relative error of the influence coefficient from numerical integration method with $\delta=0.0001$ versus number of sub-sections N_s	89
5.1	Coordinate systems for the conformal mapping method [33].	92
5.2	The original NACA0015 airfoil and its virtual airfoil, with $\lambda = 3$, $c/R=0.1$, $\theta = 90^\circ$, $\theta_p = 0^\circ$, mounted at $1/4 c$	94
5.3	The incidence angle α_i and the camber y_c/c for NACA0015 airfoil, with $c/R=0.26$, $\lambda = 5.5$, $\theta_p = 0^\circ$ mounted at $1/4 c$	95
5.4	Comparison of the lift coefficient for the virtual and original airfoil, with $c/R=0.1$, $\lambda = 3$, $\theta_p = 90^\circ$ mounted at $1/4 c$	97
5.5	Validation of the method of shifting the lift coefficient curve, with $c/R=0.1$, $\lambda = 3$, $\theta_p = 90^\circ$ mounted at $1/4 c$	97
5.6	The error of the lift coefficient for the two methods of shifting the lift curve, with $c/R=0.1$, $\lambda = 4$, $\theta_p = 0^\circ$ mounted at $1/4 c$	98
5.7	The relationship of the camber and local angle of attack at the three-quarter chord point, with $c/R=0.1$, $\lambda = 4$, $\theta_p = 0^\circ$ mounted at $1/4 c$	99
5.8	The mounting point M , evaluation point E and the aerodynamic centre A on the airfoil.	101
5.9	Comparison of the difference of relative wind speed at $1/4 c$ point and $3/4 c$ point.	103
5.10	The direction of the aerodynamic forces.	104
5.11	Validation of the normal and tangential loading, with $\sigma = 0.1$, $B=2$, mounted at $1/4 c$	106
5.12	The decomposition of lift force in $\alpha_{1/4}$ direction to lift and drag in $\alpha_{3/4}$ direction.	107
5.13	Validation of the lift coefficient C_L versus angle of attack at $1/4 c$ and $3/4 c$	108
5.14	Validation of the drag coefficient C_L versus angle of attack at $1/4 c$ and $3/4 c$	109
6.1	The step response of the NACA0015 airfoil and the flat plate.	120
6.2	The additional angle of attack due to pitching motion.	121
6.3	Validation of the inviscid part of Risø dynamic stall model with the azimuthal variation of angle of attack.	123

6.4	Validation of the inviscid part of Risø dynamic stall model with the lift coefficient versus angle of attack.	124
6.5	Flowchart of the iteration process for the coupled dynamic Actuator Cylinder model.	125
6.6	Decomposition of the total lift for the type-one angle of attack to lift and drag for the type-two angle of attack.	127
6.7	The decomposition of the lift and drag coefficient in Risø dynamic stall model [18].	128
6.8	Validation of the normal and tangential loading for the M_1 and M_2 method with original Mod-Lin correction, with $\lambda = 4$, $\sigma = 0.07$, $B = 2$	132
6.9	Validation of the normal and tangential loading for the M_1 and M_2 method with Cheng's Mod-Lin correction, with $\lambda = 4$, $\sigma = 0.07$, $B = 2$	133
6.10	Comparison of the normal and tangential loading from two dynamic AC models, with $\sigma = 0.1$, $B = 2$	134
6.11	Validation of the steady induced velocity in x - and y -directions, with $\sigma = 0.1$, $B = 2$	136
6.12	Validation of the dynamic induced velocity in x - and y -direction, with $\sigma = 0.1$, $B = 2$	138
6.13	Validation of the dynamic normal and tangential induced velocity, with $\sigma = 0.1$, $B = 2$	139
6.14	Validation of the angle of attack and relative wind speed, with $\sigma = 0.1$, $B = 2$	141
6.15	Validation of the thrust and power coefficient from the dynamic AC model.	142
6.16	Demonstration of further improvements to the Mod-Lin correction method with the normal and tangential loadings, with $\sigma = 0.1$, $B = 2$	144
6.17	Comparison of the unsteady lift coefficient of the attached flow from Pirrung's extended model and Risø dynamic stall model, with $\sigma = 0.1$, $B = 2$	146
6.18	Comparison of the unsteady drag coefficient of the attached flow from Pirrung's extended model and Risø dynamic stall model, with $\sigma = 0.1$, $B = 2$	148
6.19	Demonstration of the direction of the lift force in the condition of zero wind speed	149
7.1	The coordinate systems for the Double Actuator Cylinder model	154
7.2	The four different rotational direction layouts of a double-VAWT layout.	164
7.3	Validation of the mirror effect for the Counter-Up and Counter-Down layout from the DAC2 model with induced velocities and loadings, with $\lambda = 4$, $\sigma = 0.07$, $B = 2$, $d = 0.1$	166
7.4	Validation of the mirror effect for the Counter-Up and Counter-Down layout from the DAC4 model with induced velocities and loadings, with $\lambda = 4$, $\sigma = 0.07$, $B = 2$, $d = 0.1$	167
7.5	Validation of the mirror effect for the Co-Rotating layout from the DAC2 model with induced velocities and loadings, with $\lambda = 4$, $\sigma = 0.07$, $B = 2$, $d = 0.1$	168
7.6	Validation of the mirror effect for the Co-Rotating layout from the DAC4 model with induced velocities and loadings, with $\lambda = 4$, $\sigma = 0.07$, $B = 2$, $d = 0.1$	169
7.7	Validation when the distance between the two rotors is infinitely large with the induced velocities and loadings from the DAC2 and DAC4 model, with $\lambda = 4$, $\sigma = 0.07$, $B = 2$	170

7.8	Thrust and power coefficient for different tip speed ratio and solidity with the Counter-Up layout from four DAC models, with $B = 2$, $d = 0.2$	172
7.9	Thrust and power coefficient for different tip speed ratio and solidity with the Counter-Down layout from four DAC models, with $B = 2$, $d = 0.2$	173
7.10	Thrust and power coefficient for different tip speed ratio and solidity with the Co-Rotating layout from four DAC models, with $B = 2$, $d = 0.2$	174
7.11	Comparison of the local power coefficient calculated from two methods, with $\sigma = 0.1$, $B = 2$	177
7.12	Comparison of the variables for the Counter-Up layout and Counter-Down layout against the single rotor layout from the panel code, with $\lambda = 4$, $\sigma = 0.1$, $B = 2$, $d = 0.1$	178
7.13	Comparison of the variables for the Co-Rotating layout against the single rotor layout from the panel code, with $\lambda = 4$, $\sigma = 0.1$, $B = 2$, $d = 0.1$	179
7.14	Comparison of the variables for the Counter-Up layout and Counter-Down layout against the single rotor layout from DAC2 model, with $\lambda = 4$, $\sigma = 0.1$, $B = 2$, $d = 0.1$	181
7.15	Comparison of the variables for the Co-Rotating layout against the single rotor layout from DAC2 model, with $\lambda = 4$, $\sigma = 0.1$, $B = 2$, $d = 0.1$	184
7.16	Comparison of the variables for the Counter-Up layout and Counter-Down layout against the single rotor layout from DAC4 model, with $\lambda = 4$, $\sigma = 0.1$, $B = 2$, $d = 0.1$	186
7.17	Comparison of the variables for the Co-Rotating layout against the single rotor layout from DAC4 model, with $\lambda = 4$, $\sigma = 0.1$, $B = 2$, $d = 0.1$	188
7.18	Influence of the distance on the thrust coefficient and power coefficient for the Counter-Up layout, with $\lambda = 4$, $\sigma = 0.07$, $B = 2$	190
7.19	Influence of the distance on the thrust coefficient and power coefficient for the Counter-Down layout, with $\lambda = 4$, $\sigma = 0.07$, $B = 2$	191
7.20	Influence of the distance on the thrust coefficient and power coefficient for the Co-Rotating layout, with $\lambda = 4$, $\sigma = 0.07$, $B = 2$	192
7.21	Influence of the distance on the mean value of the thrust coefficient and power coefficient for the two rotors of the Co-Rotating layout, with $\lambda = 4$, $\sigma = 0.07$, $B = 2$	193
7.22	Influence of the phase difference on the thrust coefficient and power coefficient for the Counter-Up layout, with $\lambda = 4$, $\sigma = 0.1$, $B = 2$, $d = 0.1$	195
7.23	Influence of the phase difference on the thrust coefficient and power coefficient for the Counter-Down layout, with $\lambda = 4$, $\sigma = 0.1$, $B = 2$, $d = 0.1$. . .	196
7.24	Influence of the phase difference on the thrust coefficient and power coefficient for the Counter-Down layout, with $\lambda = 4$, $\sigma = 0.1$, $B = 2$, $d = 0.1$. . .	197
B.1	Validate the AC1 and AC3 model against panel code, with $\lambda = 3$, $\sigma = 0.1$, $B = 2$	214
B.2	Validate the AC1 and AC3 model against panel code, with $\lambda = 4$, $\sigma = 0.1$, $B = 2$	215
B.3	Validate the AC2 and AC4 model against panel code, with $\lambda = 3$, $\sigma = 0.1$, $B = 2$	216
B.4	Validate the AC2 and AC4 model against panel code, with $\lambda = 4$, $\sigma = 0.1$, $B = 2$	217

B.5	Validate the AC2 and AC4 model against panel code, with $\lambda = 4$, $\sigma = 0.12$, $B = 2$	218
B.6	Validate the AC2 and AC4 model against panel code, with $\lambda = 5$, $\sigma = 0.07$, $B = 2$	219
B.7	Validation of the normal and tangential loadings from the AC_2^{dyn} and AC_4^{dyn} model against the panel code, with $B = 2$	220
B.8	Validation of the DAC models on predicting the relationship of the thrust coefficient for different rotational direction layouts.	221
B.9	Validation of the DAC models on predicting the relationship of the power coefficient for different rotational direction layouts.	222

List of Tables

3.1	Four different cases of moving all the control points on the Actuator Cylinder.	50
3.2	Four different cases of moving one control point on the Actuator Cylinder.	50
5.1	Four different Actuator Cylinder Models.	109
6.1	Approximated coefficients for the inviscid step response.	119
7.1	Four different Double Actuator Cylinder Models.	157
7.2	Decrements of normalised thrust and power coefficient with distance d increase from 0.02 to 2.0 for the Counter-Up layout.	190
7.3	Decrements of normalised thrust and power coefficient with distance d increase from 0.02 to 2.0 for the Counter-Down layout.	192
7.4	Decrements of averaged value of normalised thrust and power coefficient with distance d increase from 0.02 to 2.0 for the two rotors of <i>Co-Rotating</i> layout.	193

Nomenclature

Latin symbols

Δt	Time step
a	Induction factor
A_i, b_i	Airfoil geometry dependent coefficients
B	Number of blades
c	Chord length
C_d	Drag coefficient
C_d^{dyn}	Dynamic drag coefficient
C_L	Lift coefficient
C_L^p	Lift coefficient for unsteady attached flow
C_L^{dyn}	Dynamic lift coefficient
C_L^{st}	Steady lift coefficient
C_p	Power coefficient
C_T	Thrust coefficient
$C_{d,ind}$	Induced drag coefficient
$C_{d,tor}$	Drag coefficient due to torsion rate
$C_{L,\alpha}$	Slope of lift polar
$C_{L,circ}$	Circulatory part of the lift coefficient
$C_{L,tor}$	Lift coefficient due to the torsion rate
$C_{p,l}$	Local power coefficient
$C_{T,l}$	Local thrust coefficient

D	Aerodynamic drag force
d	Non-dimensioned distance between two rotors
f	Scaling factor for the control point coordinate
F_n	Normal blade force
F_t	Tangential blade force
I_1, I_2	Influence coefficients
k	Reduced frequency
k_a	Correction factor of the Mod-Lin correction
L	Aerodynamic lift force
N	Number of sections
N_s	Number of subsections
Q_n	Non-dimensioned normal loading
Q_t	Non-dimensioned tangential loading
R	Radius of the rotor
r	Non-dimensioned distance to Actuator Cylinder centre
t	Time
T_f	Time constant for the lag in boundary layer
T_p	Time constant for the pressure
T_u	Time constant for the velocity
U	Velocity
V_∞	Free-stream velocity
V_n	Normal velocity
V_t	Tangential velocity
V_{rel}	Relative velocity
w_n	Non-dimensioned normal induced velocity
w_t	Non-dimensioned tangential induced velocity
w_x	Non-dimensioned induced velocity in x -direction
w_y	Non-dimensioned induced velocity in y -direction
x_i, y_i, g_i	The i -th aerodynamic state variable

Greek symbols

α	Angle of attack
α_0	Zero-lift angle of attack
α_E	Effective angle of attack
α_g	Geometric angle of attack
α_i	Incidence angle
α_v	Virtual angle of attack
λ	Tip-speed ratio
ω	Rotational velocity
ω_p	Angular frequency of the harmonic pitching motion
ϕ	Indicial response function
σ	Rotor solidity
θ	Azimuthal angle
θ_p	Pitch angle

Abbreviations

1/4 c	Quarter chord point
3/4 c	Three-quarter chord point
AC	Actuator Cylinder
AoA	Angle of attack
B-L	Beddoes-Leishman
CFD	Computational Fluid Dynamics
DMST	Double Multiple streamtube
HAWT	Horizontal Axis Wind Turbine
L-N-K	Larsen-Nielsen-Krenk
LE	Leading edge
Mod-Lin	Modified-linear
MST	Multiple streamtube
N-S	Navier-Stokes
RHS	Right-hand side

SST	Single streamtube
TE	Trailing edge
U2DiVA	Unsteady Two-Dimensional Vorticity Aerodynamics model
VAWT	Vertical Axis Wind Turbine
VT	Vorticity Transport

Subscript

A	Aerodynamic centre
b	The properties of one blade
E	Evaluation point
h	The number of the rotor inducing velocities
j	The number of the control point inducing velocities
j	The number of the control point to be evaluated
k	The number of the rotor to be evaluated
M	Mounting point
n	In normal direction
t	In tangential direction
x	In x -direction
y	In y -direction

Superscript

n	Due to normal loading
t	Due to tangential loading
1/4	At quarter chord point
3/4	At three-quarter chord point
dyn	Dynamic properties

Introduction

In recent years, the Vertical Axis Wind Turbines (VAWTs) have been gaining more interest in wind energy research due to the potential to decrease the cost of energy (CoE) compared to Horizontal Axis Wind Turbines (HAWTs) for large-scale offshore wind turbines and small turbines for urban applications [14]. One of the reasons is the possibility to decrease the distance between the rotors without losing much efficiency compared to the HAWTs [9] [37]. Because of this, there is much interest in assessing the performance of VAWTs placed close together. The potential of increasing the efficiency of the VAWT farms with the counter-rotating layout is introduced and investigated with experimental data by Dabiri[9], and also investigated numerically with Computational Fluid Dynamics (CFD) modelling in the European project of INFLOW [38]. The concept TWINFLOAT® proposed by Nénuphar is to benefit from this phenomenon with two counter-rotating rotors placed together on one single floater.

In order to assess the performance of the double VAWTs layouts for different layouts, such as rotational directions, the distance between rotors and phase difference as well as operational conditions, it is necessary to model the aerodynamics of double VAWTs layouts correctly. The Actuator Cylinder (AC) model is a method with low computational effort based on the steady-state Euler equations to model the aerodynamics of VAWT[32] and has been shown to have a good agreement with more computational *expensive* vortex based codes by Ferreira [13]. The model has been widely used [25][14][36] and has also been implemented in the aeroelastic code of HAWC2 [31] which is widely used for HAWT applications in the academic and industry. The original AC model was initially derived and intended for the calculation of a single VAWT rotor. The AC model is extended by Ning [36] to become a multiple AC model with matrix formulations. However, some important aspects such as dynamic stall effect, flow curvature effect are needed to be correctly modelled in the model and verification are also strongly needed.

In this master thesis work, the details of the implementations of the original AC model by

Madsen [32] and Cheng's modified AC model [8] are firstly introduced and some important aspects are also discussed in Chapter 3. In this chapter, the implementation is validated with the HAWC2 code, and the performance of the model is evaluated with the panel code. Simplifications and analytical solutions are introduced and discussed in Chapter 4. In Chapter 5, the flow curvature effect is investigated with conformal mapping method as well as panel code, and the method of modelling the flow curvature effect in the AC model is introduced and also validated. In Chapter 6, the Risø dynamic stall model and the modifications are introduced and coupled with the AC model, and the performance of the coupled dynamic AC model is validated with the panel code. The Double Actuator Cylinder (DAC) model is developed and implemented in Chapter 7, the influences between the two rotors in the double rotor setup will be investigated with the panel code, and the performance of the DAC model on predicting the influences will be validated.

This thesis work firstly provides a reliable extended AC model for one single VAWT rotor, with flow curvature effect and unsteady aerodynamics modelled, which is validated with the panel code. In the end, an extended DAC model for modelling the aerodynamics of double VAWTs will be developed, which will provide guidelines for the VAWT farm design.

1.1 Research Objectives and Questions

Research Objectives

The main goal of this project is to model the aerodynamics of double VAWTs by developing the Double Actuator Cylinder model from the original Actuator Cylinder model which is for single VAWT rotor.

- Sub-objective 1: Update the original AC model with modifications and validate against both HAWC2 code and panel code. Investigate the impact of the flow curvature effect and unsteady aerodynamics on the solutions from the AC model.
- Sub-objective 2: Include the flow curvature effect and unsteady aerodynamics in the AC model, and validate the coupled dynamic AC model with the panel code.
- Sub-objective 3: Extend the original AC model to DAC model and validate the performance of the extended model on predicting the influences between the two rotors for different layouts and operational conditions.

Research Questions:

1. What models are appropriate for the calculation of the aerodynamics of multiple VAWTs?

- (a) What are the assumptions and theories behind the aerodynamic models?

- (b) Which models can model the multiple VAWTs layouts sufficiently?
 - (c) What are the fidelity and computational efforts of different aerodynamic models?
2. How to include the flow curvature effect and the dynamic stall effect in the AC model?
- (a) How could the flow curvature effect be modelled in the AC model?
 - (b) What dynamic stall model should be coupled with the AC model?
 - (c) How to obtain the parameters needed for the dynamic stall model?
 - (d) What is the relationship between the dynamic stall model and the flow curvature model?
 - (e) How should the flow curvature effect be included correctly in order to avoid double consideration of this effect?
3. How reliable is the coupled dynamic single AC model to model the aerodynamics of the single VAWT rotor?
- (a) What model is proper to be used as a reference for the validation?
 - (b) What parameters are dominant for the results and have to be evaluated?
 - (c) What improvements have been made with the flow curvature model and dynamic stall model implemented?
 - (d) What further improvements could be done to the Mod-Lin correction method of the linear model?
4. How to develop the Double Actuator Cylinder model from the single Actuator Cylinder model?
- (a) How to derive the equations of the induced velocities for the DAC model?
 - (b) How should the non-dimensioned coordinate system be defined, let the influence coefficients for the DAC model to be in the similar form as that of the single AC model?
 - (c) How to model the skewed flow especially when one rotor is in the wake of another?
5. How reliable is the DAC model to predict the influence between the two rotors?
- (a) How well is the influence between the two rotors modelled for different rotational direction layouts of the two rotors?
 - (c) How well is the model to predict the thrust and power coefficient for different layouts and operational conditions?

- (d) How well is the model for predicting the influence due to the distance between the two rotors?
- (e) What is the influence between the two rotors due to the phase difference?

1.2 Methodology

In this section, there will be an overview of the methodologies introduced and applied in this thesis. This will serve as a brief overview, and for detailed elaboration, please refer to the corresponding chapter.

- CHAPTER 2: Review of the relevant literature to obtain knowledge of relevant background theories as well as knowing the state-of-art in order to make decisions of the work to be carried out.
- CHAPTER 3: Implement and validate the Actuator Cylinder model with discussions on some aspects of the model which ensure a sufficient tool for further DAC model development.
 - Implement the Actuator Cylinder model with modified-linear (Mod-Lin) correction in the MATLAB and then validate against HAWC2.
 - Introducing Cheng's modified AC model as well matrix formulation of the equations of induced velocity.
 - Implement both counter-clockwise and clockwise rotational direction setup for the AC model and introduce the *Mirror effect*.
 - Derive the explicit form of the wake terms for different conditions and then investigate the continuity of the induced velocities.
 - Validate the results from the AC model with that from the panel code of U2DiVA and propose possible improvements to the AC model.
- CHAPTER 4: Simplify the calculation of the induced velocities by deriving the analytical solutions of the influence coefficients as well as the induced velocity of w_x^n , which is in x -direction due to normal loadings, on the Actuator Cylinder.
 - Derive the analytical solutions of the influence coefficients with analytical integration method in the polar coordinate system. The singularity problem is dealt with Cauchy principal value.
 - Derive the analytical solution of the induced velocity of w_x^n for the special condition that evaluating on the control points, and validate against Madsen's analytical solutions.
 - Validate the continuity of velocity of w_x^n with the analytical solution of it.
 - Investigate the properties of the influence coefficient as well as issues of the numerical integration method.

- CHAPTER 5: Investigate the flow curvature effect with conformal mapping method as well as panel code, and validate the method of evaluating at the three-quarter chord point of the airfoil.
 - Implement the Migliore's conformal mapping method and investigate the property of the resulting virtual airfoil with the panel code.
 - Investigate the method of evaluating at the three-quarter chord point and implement this method in the Actuator Cylinder model.
 - Validate the modified AC model with the panel code by comparing the distributed loadings as well as lift and drag coefficients.
 - Summarise different possible AC models with their specifications.
- CHAPTER 6: Couple the Risø dynamic stall model with the Actuator Cylinder model to become the coupled dynamic AC model, and the inviscid part is validate against the panel code.
 - Introduce the Risø dynamic stall model as well as Pirrung's simplification and modification.
 - Validate the inviscid part of the dynamic stall model with panel code for the harmonic pitching motion.
 - Implement the dynamic stall model in the AC model and investigate the direction to apply the lift and forces.
 - Validate the results of induced velocity, distributed loadings, angle of attack and relative wind speed from the coupled dynamic AC model with the panel code.
- CHAPTER 7: Derive the Double Actuator Cylinder model and evaluate the model for modelling the influence between the two rotors for different layouts with panel code.
 - Derive the DAC model from the linear solutions of the original AC model with certain non-dimensioned coordinate systems, so that the induced velocities are in the form of the additive summation of that from the original AC model.
 - Implement the DAC model in the MATLAB code with validation of the mirror effect as well as for the condition of the infinite distance between the two rotors.
 - Validate the model on predicting the thrust and power coefficient for different operational conditions and rotational direction layouts, and also validate the variation of the thrust and power coefficient with the increasing of the distance between the two rotors.
 - Validate the DAC model on predicting the influence between the two rotors for different rotational direction layouts with the panel code.
 - Investigate the influence due to the phase difference between the two rotors and determine whether the influence is signification or could be neglected.

Literature Review

This chapter will present an overview of the relevant theories and models for the modelling of the aerodynamics of the VAWTs. The first part will be the working principles of the VAWT focusing on the types and layout as well as the energy conversion. Secondly, there will be introductions about various aerodynamic models for the VAWT. The third part will be introduction and modelling of unsteady aerodynamic effects. Finally, the flow curvature effect and the blade wake interaction will also be introduced.

2.1 Working principles of the VAWT

In this section, different types and layouts of VAWT will be firstly introduced with their working principle and performances. The energy conversion process of Darrieus-type VAWT will then be explained.

2.1.1 Types and layout of VAWT

For modern days, there are mainly two types of VAWTs which are the Darrieus-type and Savonius-type turbines.

The Darrieus-type turbine is a lift-driven machine with two or more straight or curved blades that the cross-sections are airfoil shaped. The blades are attached with beams to the central shaft and rotate together with the same angular velocity. The power coefficient is higher than that of the drag-driven machines because the aerodynamic lift to drag ratio is high for the airfoil, which then let the Darrieus-type turbine more favourable for the power production proposes.

The Savonius-type turbine is the otherwise a drag-driven machine with two or more scoops. When looking down the rotor from above, the two-scoop setup will look like an 'S' shape. The difference between the drag forces on the two sides of the scoop will result in a net torque which directly corresponds to the extraction of aerodynamic power from the flow. However, this type of turbines will have lower power coefficient and are mainly used as wind speed anemometers [21].

2.1.2 Energy conversion

The aerodynamic power is resulting from the torque on the shaft which is directly from the combined effect of the aerodynamic lift and drag forces for both HAWT and VAWT. However, the energy conversion of the VAWT is different from that of the HAWT.

For simplicity, it could be considered that the energy conversion occurs in the swept area of the blades. For the straight bladed Darrieus-type VAWT, the swept area will be the side area of a cylinder which is parallel to the rotational axis, and the rotational axis is perpendicular to the incoming wind velocity if neglecting the vertical components. For the HAWT, the swept area will be a disk instead which is normal to the rotational axis. If the zero-yaw angle condition is assumed and neglecting the vertical velocity component, the incoming wind velocity is parallel to the rotational axis.

The continuous shedding of vortices due to the continuous variation of bound circulation is an inherent feature for the VAWT. The rate of the shed vorticity, which corresponding to the rate of azimuthal change in the bound circulation is strongly related to the generation of the wake and which is then strongly related to the energy conversion. Ferreira [14] concluded that the energy conversion is based on the azimuthal variation of the blade's bound circulation for the VAWT. However, the energy conservation of the HAWT is not dependent on the variation of the bound circulation. It could be demonstrated by the HAWT operating in a uniform inflow which does not have the azimuthal variation of the bound circulation of the blade.

Another inherent feature of the VAWT is the instantaneous 2D blade loadings are decoupled from the aerodynamic power in the inviscid flow which has been shown by Ferreira [12], this effect is also shown by Madsen [32]. It means a change in the bound circulation will cause the transfer of the loadings between the upwind and downwind part of the rotor with the integral value which is the total torque remains unchanged. As a result, a constant pitch angle or a camber will not change the total power. However, when the viscosity is considered, there might be slight differences due to the viscous effect.

2.2 Aerodynamic models for VAWTs

In this section, a variety of aerodynamic models for the VAWTs will be introduced. These methods are categorised in the order of increasing fidelity which are the Streamtube (ST)

models, Actuator Cylinder (AC) models, Vortex based models and Computational Fluid Dynamics (CFD) models.

2.2.1 Streamtube models

The streamtube (ST) models are inherited from the Blade Element Momentum (BEM) model for the application of HAWTs [19]. The BEM model is a combination of blade element theory and momentum theory, the former is to discretize the blade into elements, and the local aerodynamic forces for each element are calculated, and latter is to model the rotor with a permeable actuator disc with body forces distributed on it.

The foundation of the ST model is the conservation of mass and the momentum theorem. When the flow passes the actuator disk, the inflow mass is equal to that of the outflow, and energy is extracted from the flow by reducing the flow speed. The converged solution of induction is obtained by coupling the two models with an iterative calculation process that the total thrust force resulting from the blades are balanced with the rate of the momentum change between the flow and the rotor.

The ST models for VAWT borrow the blade element theory but apply for different azimuthal locations of the blade to calculate the azimuthal distribution of the lift and drag forces from the flow properties, and the momentum theory is applied for every streamtube to calculate the corresponding inductions. Different streamtube models have been developed and could be further categorised in the order of increasing complexity into single streamtube model (SST), multiple-streamtube model (MST) and double multiple-streamtube model (DMST). The three models will then be introduced respectively as below.

Single streamtube model

The first streamtube model developed for the calculation of the VAWT aerodynamics is the Single Streamtube (SST) model derived in 1974 by Templin [43]. In the model, the entire rotor is modelled by a single actuator disk placed at the centre line of the rotor which is perpendicular to the flow and enclosed in a single streamtube. As a result, the induced velocity of the flow will be uniform inside the streamtube which result the whole rotor will have the same induction factor. For the VAWT, the induction usually varies with the azimuthal location of the rotor, which corresponds to a variation of induction in the width direction of the rotor, as a result the SST model is very limited for modelling VAWT. The maximum value of the power coefficient follows the Betz limit of $16/27$ which corresponds to the actuator disk theory.

Multiple streamtube model

The Multiple Streamtube (MST) model is an improvement to the SST model by Strickland [41] with the flow through the rotor divided into multiple streamtubes that are parallel to the flow direction instead of a single streamtube. The properties in different streamtubes are independent with each other according to the streamtube theory. For every streamtube, an actuator disk is placed at the centreline of the rotor inside the streamtube perpendicular to the flow. The conservation of mass and the momentum theorem are applied for each streamtube and will result in the non-uniform axial induction in the width direction of the rotor which solves the problem of the uniform axial induction from the SST model. In addition, the MST model can model the variation in the width direction of the inflow speed of the VAWT, which is another improvement to the SST model. However, there will only be one axial induction factor for each of the streamtube which results in the axial induction factor for the upwind and downwind part of a streamtube is identical. The MST model is having good performance for the low loading cases which correspond to low Tip speed ratio λ and solidity σ . The maximum power efficiency also satisfies the Betz limit of 16/27.

Double multiple streamtube model

The Double Multiple Streamtube (DMST) model developed by Paraschivoiu [37] is the most commonly used and state-of-the-art streamtube model for the VAWT which is more complex than the previous models. The DMST model further improves the MST model by applying a pair of tandem actuator disks for each streamtube which represents the upwind and downwind part of the rotor inside this streamtube respectively. This enables the modelling the difference of axial induction factor for the upwind and downwind part which is an improvement to the MST model.

However, the distance between the upwind and downwind parts of the rotor in the streamtube is not taken into account in the model. Moreover, the axial induction of the downwind part is directly influenced by the upwind part, but the upwind part is not directly influenced by the downwind part. The wake of the upwind flow is assumed to be fully expended inside the VAWT $V_{w,u} = V_\infty(1 - 2a_u)$. This result the downwind part of the rotor experience a reduced equivalent inflow free-wind speed of $V_{\infty,d} = V_{w,u}$.

For the DMST model, the Betz limit is no longer valid for the tandem actuator disk pair anymore, and the maximum power coefficient is derived to be 16/25 by Newman [35]. According to Ferreira [14], only the inductions in the flow direction is calculated for the DMST model and neglecting the inductions in the perpendicular direction of the flow will result in insufficient estimation of the tangential forces. The lateral induction factor was introduced to improve the performance of the DMST model. The results of the non-dimensioned forces in the x -direction and y -direction from the original and modified DMST model are compared with that from the panel code in Figure 2.1a and Figure 2.1b. From the figures, it could be concluded that there are notable improvements in the upwind part of the rotor, but there is still offset for the downwind part of the rotor.

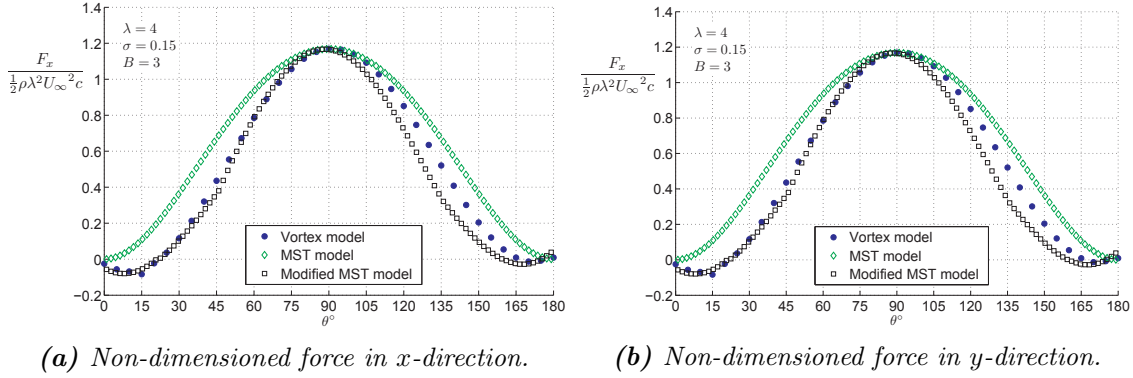


Figure 2.1: Comparison of the forces in x- and y-direction from vortex model and two DMST models [14].

Comment on the streamtube models

It should be noted that the streamtube model for the calculation of the VAWT is a forced application of the actuator disk concept, which is inherited from the application of HAWTs, on the calculation of VAWTs [14]. This is because the SST and MST model apply the actuator at the centre of the rotor which could not represent the swept area of the rotor [32] where the loadings are located. Moreover, for the MST and DMST model, the streamtube theory results in the assumption that the flow in a certain streamtube is only dependent on the loadings on upwind and downwind part of the rotor in this streamtube. As a result, the loadings on other parts of the rotor will not directly influence the flow in that streamtube which is not physical. For the DMST model, the downwind actuator disk property was assumed to be only dependent on the upwind one in the same streamtube with the fully expanded wake. This will result in the DMST model not able to model the influence of the downwind part of the rotor on the upwind part [14]. The MST and DMST models validated by Ferreira [13], the conclusion is that results from the MST model deviate significantly from the high fidelity methods because of the simple induction model. However, the DMST model is fundamentally incorrect when modelling the effect of changing the constant pitch angle which should be discontinued.

2.2.2 Actuator Cylinder model

The Actuator Cylinder (AC) model is a quasi-steady Eulerian model developed by Madsen in his PhD study [32]. The model defines a 2D Actuator Cylinder surface coincide with the swept area of the 2D VAWT rotor. The time-averaged distributed loadings are represented by volume forces on the AC which will balance the pressure jump $\Delta p(\theta)$ when passing the AC. By introducing the induced velocities of w_x , w_y and combine the Euler equation with the equation of continuity, will get a Poisson-type equation as Equation 2.3. The induced velocities are then the function of the normal loadings on the AC as well as geometric

properties. This model will be called the original AC model in the following of this report.

$$\frac{\partial w_x}{\partial x} = -\frac{\partial p}{\partial x} + f_x + g_x \quad (2.1)$$

$$\frac{\partial w_y}{\partial y} = -\frac{\partial p}{\partial y} + f_y + g_y \quad (2.2)$$

$$\frac{\partial^2 p}{\partial x^2} + \frac{\partial^2 p}{\partial y^2} = \left(\frac{\partial f_x}{\partial x} + \frac{\partial f_y}{\partial y} \right) + \left(\frac{\partial g_x}{\partial x} + \frac{\partial g_y}{\partial y} \right) \quad (2.3)$$

Modified linear solution

The linear solution of the AC model with a simple modification is shown to have good agreements with the full AC model [31], this modification method is named *Mod-Lin* and has been implemented in the HAWC2 code [32]. The modification is by multiply the induced velocities with a correction factor which is calculated with the average induction in the flow direction. The average induction is calculated from the thrust coefficient with a polynomial equation [25]. The 2D model was shown to have good agreements with more computationally intensive methods [13]. Moreover, a more general 3D model was also introduced by Madsen [32].

Actuator Cylinder model in HAWC2

The AC model with the Mod-Lin correction is also implemented in the aeroelastic code of HAWC2 with the details explained in [31]. The Beddoes-Leishman type dynamic stall model in the HAWC2 code serves as an extension and could be coupled with the AC model [25]. However, details of the implementation are not explicitly shown, and the flow curvature effect might not be well modelled, in the currently latest version of 12.4, with the aerodynamic centre located at the half chord point. The detailed validation of the converged solutions such as the distributed loadings, induced velocities and angle of attack with the results from higher fidelity methods such as vortex based codes or CFD code is lacking. As a result, further verification, as well as improvements of the AC model, are beneficial.

Cheng's modification

There is another modification to the AC model developed by Cheng [8] that the induced velocities in x - and y -direction are calculated with the contribution from both normal and tangential loadings, instead of only the contribution due to the normal loadings as in the original AC model. Even though this modification will not have a significant difference with the original model according to Cheng [8], detailed investigations are favourable. This modification will be called Cheng's modification in the following of this report.

Double Actuator Cylinder model

The AC model is initially limited to model the single VAWT. However the model has been further extended for the application of multiple rotors by Ning [36]. A method of calculating the linear solution of the induced velocity with matrix operation is also introduced, which requires the assembly of influence coefficient matrix. The correction factors for the Mod-Lin correction method are calculated from the thrust coefficients of each rotor and then applied on the rotors respectively. However, in Ning's paper, there is lacking consideration of the dynamic stall effect and the flow curvature effect. Besides, only some results of power coefficients are shown instead of detailed parameter studies. Moreover, there is also lack of detailed comparison of the results from the vortex based code or CFD code for the variables such as the azimuthal distribution of loadings and angle of attack in rotor scale to verify the model.

2.2.3 Vortex and Panel models

The vortex and panel models are widely used for the field of wind energy and aerospace in both industry and research. The models are between the streamtube models as well as the Actuator Cylinder model and the Navier-Stokes solvers such as CFD method in term of the fidelity. The vortex based models are kinematic models and use the Lagrangian approach which models the vortex shedding and the evolution of the wake [23]. This allows the wake could be modelled and then the unsteady effects could also be modelled. The models are very general and not only limited to one HAWT or VAWT applications, which means it could be as simple as a single oscillatory airfoil or could be as complex as a wind farm.

Vortex models

The vortex models are based on the vorticity equations [23] which are derived from the Navier-Stokes equations. For the vortex model, the airfoil is modelled with a 2D lifting line which is located at quarter chord point of the airfoil where is also the aerodynamic centre, and the boundary condition of impermeability is applied at the collocation point which is the three-quarter chord point [23]. According to the Helmholtz's second theorem that a vortex filament is not able to begin or end in a fluid which results in a closed vortex system called horseshoe vortex consisting of the bound vortex, trailing vortex and shed vortex [23] and is demonstrated in Figure 2.2. According to Kelvin's theorem, the circulation around a closed curve in the same fluid elements will remain the same in time for the barotropic ideal fluid. Thus, the shed vorticity could be determined from the variation of the bound vorticity. The induced velocity in the flow field could be obtained from the Biot-Savart law, and the lift force could be determined from the Kutta-Joukowski theorem.

Strickland [42] is one of the first to develop the 3D vortex model of the VAWT and the model is further developed and improved by different authors. The results from that vortex model are compared with the measurement data of the Sandia 17m VAWT and shown to have good agreements between each other.

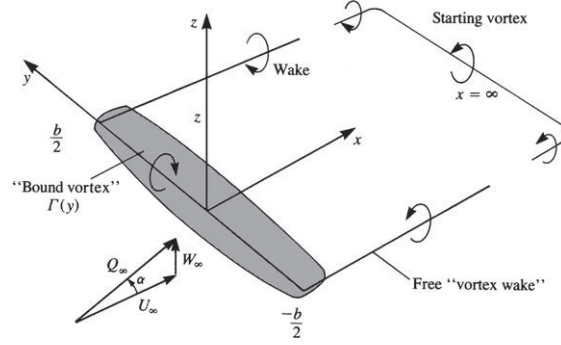


Figure 2.2: Lifting line model with horseshoe vortices [23].

Panel models

The panel model is an extension of the lifting line approach with the aerodynamic surface modelled with multiple panels, which is the 2D airfoil in our application. It should be noted that the panel model could also model 3D surfaces, which is demonstrated in Figure 2.3. Every panel satisfies the non-perturbation condition with its own value of circulation. As a result, the panel model could model the shape of the airfoil including the thickness of the airfoil. With the assumption of the potential flow, the numerical solution could then be simplified.

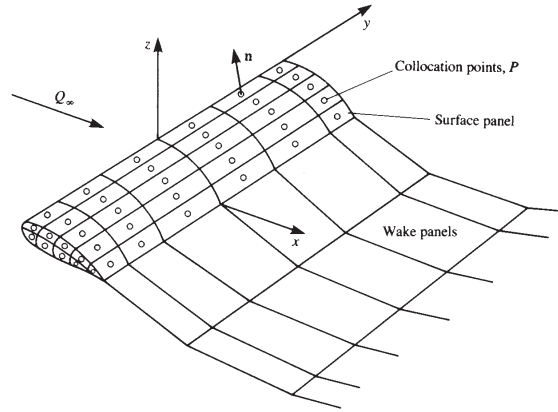


Figure 2.3: Approximation of the body surface by panel elements [23].

With the definition of the velocity potential, the velocity could be obtained with the calculation of gradient of the potential. With the panels attached to the airfoil even the airfoil experience oscillatory movements. As a result, the trailing edge separation could not be modelled by the basic panel model. The double-wake panel method is a modified 2D panel model developed Zanon et al. [49] to model the trailing edge separation. With an additional vortex shedding at the location of the trailing edge separation point, the trailing edge separation point could then be modelled. The semi-empirical boundary layer equations could also be coupled with the inviscid solution, and the famous solver of XFOIL is an example of it [10].

2.2.4 Computational Fluid Dynamics models

The Computational Fluid Dynamics (CFD) models are high-fidelity models but also correspond to high computational efforts. The basis is to solve the Navier-Stokes (N-S) equations at every element of the mesh. For the calculation, a mesh should be generated for the flow field by discretizing into finite volumes which are permeable with conservation of mass. The boundary condition should be defined with either the values at the boundary which correspond to the Dirichlet boundary condition or with the flux which correspond to the Neumann boundary condition. For the VAWT application, there should be a high fidelity grid near the blades in order to be sufficient. As a result, an unstructured mesh whose size element size is increasing when the location is further away from the airfoil could be applied in order to save the computational efforts.

The CFD method could be further categorised by the method of calculating the viscous part of the flow which correspond to the turbulence. The methods are introduced in the order of decreasing of fidelity. The most accurate is the Direct Numerical Simulation (DNS) method which solves the full N-S equation down to the size of the Kolmogorov scale which is the smallest scale of the turbulence. However, for a mesh of such small size will cause the computational effort to be incredible large and not very applicable. The Large Eddy Simulation (LES) is a space-filtered method which only solves large scale of turbulence. The Reynolds-Averaged Navier-Stokes (RANS) model is based on the time-averaged N-S equations which is having lower fidelity as well as computational efforts. The closure of the equation could be modelled by turbulence modellings of $k - \omega$ or $k - \epsilon$. There is also hybrid models such as the Detached-Eddy Simulations (DES) is a combination of the RANS model for the flow near the solid boundary and the LES model is applied for the outer flow region.

In addition, there is a model called Vorticity-Transport (VT) model [6] whose fidelity is between the CFD and the vortex based model. The model is based on the vorticity-vorticity form of the incompressible N-S equation with the lifting-line approach.

2.2.5 Ability of modelling double-rotor layouts

In this report, the focus is to model the influence between the two VAWT rotors when placed close together which is visualised in Figure 7.2. As a result, the abilities of the above models to model the influence between the rotors are discussed in this section. There are two different cases of the layout of the two rotors which will be discussed respectively as follows.

Outside the direct wake

The first case is neither of the rotors is in the direct wake of the other. For the ST model, due to the assumption that the flow in one streamtubes is independent of loadings outside this streamtube, the influence between the rotors is not able to be modelled. There will be

no difference whether placing the two rotors close together or infinitely far from each other. For the AC model, the induced velocities are dependent on the volume forces represented by distributed loadings on the rotors as well as geometry. As a result, there is the possibility of extending the model for multiple rotors which has been done by Ning [36]. However, detailed validations are needed to indicate whether the influence between the two rotors can be well modelled. The vortex based models and CFD models are able to model the double rotor setup because of their characteristics of being multiple body models if the models should be correctly applied. For example, the size of the mesh between the two rotors should be sufficiently small.

In the direct wake

The second case is one of the rotors is partially or entirely in the direct wake of another. The ST model is not able to model sufficiently as explained before. However, there is the possibility of the MST and DMST model to model the part that the rotor is in the direct wake. For the AC model, applying the non-expanding wake model by two extra terms in the equation of induced velocity in x -direction seems able to model the influence. However, the Mod-Lin correction method might not be sufficient because the interaction parts are significantly different from the other parts of the rotor. Thus, the method of applying the same correction factor to the whole rotor will not be sufficient. The vortex based models, as well as CFD methods, could model the effect well as long as the calculation is setup correctly.

2.3 Unsteady flow effects

The unsteady aerodynamic is of vital importance for the aerodynamics of the VAWT due to the inherent circular motion of the VAWT blades which cause the temporary variation of the flow properties and angle of attack. The azimuthal variation of the bound circulation will result in the continuous shedding of vortices, which will then cause the temporary variation of the aerodynamic forces [14]. In this section, the unsteady flow effects of dynamic stall, flow curvature and blade wake interaction will be introduced.

2.3.1 Dynamic stall effect

Firstly, the dynamic stall effect will be introduced. The term of *dynamic stall* typically represent the coupling effects of the trailing edge (TE) separation and the leading edge (LE) separation when the airfoil is experiencing very violent variations of the angle of attack with the variation rate above a certain limit. There are four stages for the dynamic stall effect, which are visualised in Figure 2.4 and listed as below:

- Onset of leading edge separation.

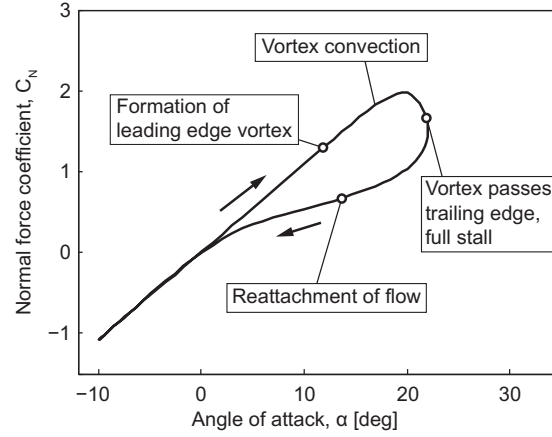


Figure 2.4: The onset of leading edge separation of the dynamic stall process with NACA0015 airfoil [11].

- Formation of the leading edge vortex.
- Convection of the leading edge vortex and formation of the trailing edge vortex.
- Breakdown of the leading edge vortex.

The LE separation will be dominant for the dynamic stall effects once it is initiated. The dynamic stall effect can be modelled with the three sub-effects which are the unsteady attached flow, trailing edge separation and leading edge separation. As a result, the term of *dynamic stall* in this thesis represents not only the stall-related effects but also the dynamics of the attached flow as well. The three sub-models are discussed as follows.

Attached flow Dynamics

The unsteady lift force of a flat plate with harmonic pitching and plunging motion of small amplitudes in an attached flow is approximated by Theodorsen [44]. It is assumed in the original Theodorsen's derivations that the free-stream velocity is constant. However, the arbitrary motion of the airfoil will result in the assumption of harmonic wake to fail. To solve this problem, different approximations to the Theodorsen function have been developed, and they are shown to have same results by Van der Wall [47] and Leishman [27].

In Theodorsen's functions, the unsteady lift is divided into a circulatory part which includes the memory effect of the vorticity shed previously and the non-circulatory part which is due to the acceleration of the added mass [44]. For the circulatory part of the lift function, there will be a delay for the variation of lift force with the change of angle of attack, which is directed related to the bound vortex. This delay effect is described with an indicial function in state space. The indicial function will be the Wagner function for a step-change of the angle of attack with the initial value of $\varphi(0) = 0.5$, which means half of the increment is *felt* instantaneously by the airfoil. Moreover, the function will be the Küssner function for

a sharp-edged gust with the initial value of $\varphi(0) = 0$ which means no increment will be *felt* by the airfoil instantaneously [27]. Both functions could be approximated by the response function with two time-lags as the equation below.

$$\phi(s) = 1 - A_1 e^{-b_1 s} A_2 e^{-b_2 s} \quad (2.4)$$

With $s = \frac{2}{c} \int_0^t U dt$, representing the distance travelled by the wake with the time-varying free-stream speed.

According to Bergami [4] and Hansen [18], the coefficients of A_i and b_i are dependent on the airfoils geometry and applications as well. It has been shown by Hansen [18] with the Risø A1-24 airfoil with 24% thickness with harmonic pitching motion that the lag effect of the lift is well modelled with the coefficients approximated for this airfoil. However, the results will have significant deviation when using the coefficients for the flat plate approximated by Jones [22].

Trailing edge separation

The stall for the 2D airfoil could be characterised by the decrease of the lift with the increment of the angle of attack after a certain value. This is due to the circulations are detached from the suction side of the airfoil near the trailing edge. The degree of the stall could be determined with the location of the separation point [18]. There will be delay effect for the unsteady flow with the stationary conditions due to the lag between the pressure and lift as well as the dynamics of the boundary layer that cause the separation point to lag behind the quasi-steady location of the separation [18]. As a result, when increasing the angle of attack, the unsteady lift is higher than that of decreasing the angle of attack which could also be visualised in Figure 2.4.

Leading edge separation

The leading edge separation will occur for very aggressive pitching of the airfoil and usually coupled with the trailing edge separation. There will be a separation bubble forms on the suction side of the airfoil near the leading edge. Due to the flow reversal phenomena in the boundary layer, the leading edge vortex will build up. The leading edge vortex will then detach from the airfoil and then convects downstream and meanwhile, a trailing edge vortex will be formed. With the interaction between the two vortices, the leading edge vortex will break down, and the trailing edge vortex will detach. For the airfoil with oscillatory motion, the flow will attach again when the angle of attack decreases below a certain value. This will result in a dynamic stall loop as in Figure 2.4. According to Leishman [27], the sudden forward movement of the separation point introduces an extra suction force and therefore increase in linear lift region. The lift coefficient is assumed to follow the linear relationship of the lift and angle of attack until the leading edge vortex detaches from the airfoil, which will result in an additional lift contribution.

2.3.2 Dynamic stall modelling

The dynamic stall model could be categorised into the resynthesize models and the semi-empirical models. The resynthesize models are fully based on wind tunnel measurement results for the 2D airfoil with oscillatory motions. The UTRC model by Carta [7] and Bielawa [5] as well as the Boeing-Vertol Gamma function method by Gross [17] and Gormont [16]. The semi-empirical models are consists of more physical equations with only some empirical coefficients based on the experimental results. This category includes the Beddoes' Time-Delay method [2], ONERA method [45] and the Beddoes-Leishman method [29].

The above methods are initially developed for the aviation industry and research. As a result, to apply the model for the wind turbine applications, the model should be a general method for multiple applications. The Beddoes-Leishman method is the most general one providing complete physical modelling of the unsteady aerodynamics. Also, Berg [3] further developed the widely used Gormont model for the application for the VAWTs.

Gormont model

The Gormont model [16] use the effective angle of attack to model the influence of the motion of the airfoil. The Gamma function is introduced for calculating the effective angle of attack from the geometric angle of attack. The Gamma function is dependent on the Mach number, and the relationship is from experimental data. The model is shown to have a positive impact than no dynamic stall model included according to Dyachuk [11].

Beddoes-Leishman model

The Beddoes-Leishman (B-L) model was originally derived in the form of indicial function due to the efficiency of computing. The model was gradually revised [27] and included the effect of the unsteady inviscid wake, trailing edge and leading edge separation as well as the compressibility which is similar to the Piston theory. The model was also revised with the state-space formulation for attached flow [28] and the complete model is introduced in [30]. The B-L model is consists of four sub-models which are:

1. Non-linear attached flow model.
2. Non-linear trailing edge separation model.
3. Dynamic stall onset model.
4. Vortex induced air loads model.

The sub-models are coupled with the ODEs [30]. For the flow in the linear region, the loads are calculated from the indicial response function. For the flow in the nonlinear region, the load is determined by the location of separation which is determined from the potential

Kirchhoff flow theory. The detailed comparison between the B-L model and the Gormont model is done by Dyachuk [11].

There are simplifications of the B-L model, which are the Risø model by Hansen et al.[18] and the L-N-K model by Larsen [24] The two models will be introduced in the followings respectively.

Risø model

The Risø model is a simplification of the B-L model with both state-space and indicial formulations intended, which is developed for wind turbine aeroelastic analysis. There are four aerodynamic state variables for the Risø model, two for the dynamics of the attached flow (x_1, x_2) and the other two for the dynamics of the trailing edge separation (x_3, x_4). The compressibility of the flow is not considered, and the leading edge separation is also neglected. The reason is that the typical maximum tip speed of $70 - 80 \text{ m/s}$ and the Mach number is too low to consider the compressibility. The variation of the angle of attack of the is relatively small for the HAWT blades, and these airfoils are relatively thick ($> 15\%$) which will result the leading edge separation effect could then be neglected. However, for the application of VAWT, the blade is more slender, and there will be violent variations of the angle of attack for low tip speed ratio, which will let the leading edge separation to occur. There is another issue when applying the Risø model for VAWT that the rotor can generate net torque in the condition of zero wind speed which is not physical. There is a modification to the Risø by Pirrung [39] to solve this issue.

Larsen-Nielsen-Krenk model

The Larsen-Nielsen-Krenk (L-N-K) model is also a simplification to the B-L model but with consideration of the leading edge separation. According to Larsen [24], this is because the blades of the HAWTs are getting slender, which increase the possibility of the LE separation. As a result, an additional aerodynamic state variable of (x_5) is used for modelling the describing the diminishing rate of the vortex lift of the LE separation with the angle of attack higher than the critical value of α_v .

The compressibility effect is neglected due to the relatively low relative wind speed for the wind turbine application which is same as Risø model. However, only one state variable is used for the dynamics of the trailing edge separation (x_3) instead of two state variables as that in the Risø model. It is shown that the L-N-K model performs well for both fully attached flow and dynamic stall conditions compared to the complete B-L model and the ONERA model which are more complicated than the L-N-K model.

2.3.3 Flow curvature effect

The Flow Curvature is another inherent phenomenon of the VAWT configuration. The individual blade sections will experience a curvilinear inflow due to the rotation of the rotor. This will result in the variation of the flow properties such as angle of attack along the chord. The flow curvature is validated to exist with the experiment that the minimum drag coefficient is not at the angle of attack at zero-degree for a symmetric airfoil mounted on the VAWT [33], this effect is typical for a cambered airfoil.

In order to model the flow curvature effect, one method is to transform the geometric airfoil in the curvilinear flow to a virtual airfoil in rectilinear flow with additional camber and incidence angle. This is illustrated in the Figure 5.2. According to Migliore [33], with the free wind speed and the rotational of the blades, the streamlines could be considered as con-centred circles with an offset of the origin. It is also demonstrated by Migliore [34] that the flow curvature properties are dependent on the chord to radius ratio c/R as well as the tip speed ratio λ . The influence of the chord to radius ratio is much stronger than the tip speed ratio. The added camber and incidence angle will vary for the azimuthal angle, and the mean value could be used for simplicity.

There are also other methods to model the flow curvature effect by transforming to a virtual airfoil. Such as Hirsch model [20], Zervos model [50] and Akimoto model [1]. According to Sander [46], all of the methods will have very similar results for a reasonable chord to radius ratio below 0.2 which is very high for VAWT applications. As a result, for a reasonable value of the solidity, all model will have reasonably good results.

2.3.4 Blade wake interaction

The blade-wake interaction (BWI) is an inherent feature for the VAWTs. With the rotational motion of the blades and their shedding of vortices in the wake, the blade in the downwind part travels through the wake generated in the upwind part [14]. For a one-bladed VAWT, the blade will travel through its own wake and for VAWT with two or more blades, the blade could cross its own wake as well as the wakes of other blades.

The effect of the BWI on the angle of attack and aerodynamic loadings is investigated by Scheurich [40]. The aerodynamic loadings will form a smooth curve for the upwind part, but there will be impulsive forces in the downwind part of the rotor due to the BWI effect. As a result, the flow unsteadiness in the downwind part is enhanced with impulsive changes of forces on the blades. This could be explained that when the blade travels through the wake, the induced velocity will be very high when the distance is very close to the wake and will suddenly change direction after passing the wake vortices. The BWI effect could also cause transients in the local angle of attack which could initiate a local dynamic stall process [40]. As a result, the BWI effect will cause the aerodynamic performance to decrease and more fatigue damages of the blade structures.

The ratio of the speed of the wake convection to rotational speed directly determines the amount of the wake crossed by the blade and their locations, which are represented by

the tip-speed-ratio λ and the upwind axial induction factor a_u . The analytical blade-wake interaction solution has been derived by Ferrer [15] for some specific values of the tip speed ratio λ .

Actuator Cylinder Model

In this chapter, the implementation of the Actuator Cylinder Model is presented. Firstly, there will be the details about the implementation of the original AC model as well as the validation of the implementation of the model with the results from HAWC2 code. After that, some important aspects of the AC model are discussed. Thirdly, the performance of the AC model on estimating the power coefficient and thrust coefficient for different tip speed ratio and solidity is validated with the result from the panel code. Finally, the performance of the AC model on calculating the value of the variables such as induced velocities, distributed normal and tangential loadings, angle of attack and relative wind speed is also validated with the panel code, and possible improvements to the AC model is given. The AC model in this chapter will not consider the unsteady effects of the VAWT. This chapter is the backbone of this report and serves as a prerequisite of the following works and researches.

3.1 Implementation procedure

In this section, there will be the detailed step-by-step procedure of the implementation of the original AC model for the single VAWT setup in a mathematical tool such as MATLAB. The method of implementation is based on that in the HAWC2 code [31] which combines the original AC model [32] with the airfoil aerodynamics and also Mod-Lin correction method. The term of *original* is to distinguish from the Cheng's modified AC model which will be introduced in subsection 3.3.3.

For the original AC model, the induced velocities are only dependent on the distributed normal loading Q_n on the Actuator Cylinder. With a given normal loading distribution of Q_n , the induced velocity in x - and y -direction at an arbitrary point (x, y) in the flow field is then able to be calculated with the following equations.

$$w_x(x, y) = -\frac{1}{2\pi} \int_0^{2\pi} Q_n(\phi) \frac{-(x + \sin \phi) \sin \phi + (y - \cos \phi) \cos \phi}{(x + \sin \phi)^2 + (y - \cos \phi)^2} d\phi - Q_n(\cos^{-1} y)^* + Q_n(-\cos^{-1} y)^{**} \quad (3.1)$$

$$w_y(x, y) = -\frac{1}{2\pi} \int_0^{2\pi} Q_n(\phi) \frac{-(x + \sin \phi) \cos \phi - (y - \cos \phi) \sin \phi}{(x + \sin \phi)^2 + (y - \cos \phi)^2} d\phi \quad (3.2)$$

The variables of x and y in the Equation 3.1 and 3.2 are the non-dimensional coordinate of point where the induced velocity to be evaluated. And the variable of ϕ represents the azimuthal angle of the location of the normal loading. The integral on the RHS is over the interval of $[0, 2\pi)$ which represents the induced velocity in x - and y -direction are dependent on the contribution of the normal loading distribution on the whole Actuator Cylinder. The integral is then divided by 2π , which represents the averaging the contributions from the loadings on the whole Actuator Cylinder.

The definition of the non-dimensioned coordinate system is consistent with the original AC model as in [32]. The origin is where the rotational axis of the rotor is located, the positive direction of x -axis coincides with the free wind direction, and the y -axis is 90° counter-clockwise perpendicular to it. The azimuthal angle is defined to be increasing in the counter-clockwise direction and is zero-valued when the location is on the positive y -axis. The coordinate is non-dimensioned with the radius of the rotor. As a result, the Actuator Cylinder will be a circle with the centre at the origin and radius equal to 1 in the non-dimensioned coordinate system, and it is where the normal and tangential loadings are located [32]. The non-dimensioned coordinate system and the direction of the loadings on the Actuator Cylinder are demonstrated in Figure 3.1. The normal loading Q_n is defined to be positive when pointing out from the centre of the AC, and the positive direction of tangential loading Q_t is 90° counter-clockwise perpendicular to it.

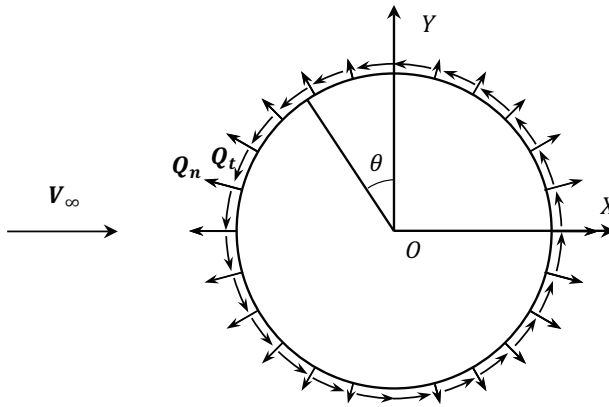


Figure 3.1: The distributed normal and tangential loadings in the non-dimensioned coordinate system of the Actuator Cylinder model.

For an arbitrary point in the flow field and the distance to the centre of AC is r and the azimuthal angle of θ , the corresponding non-dimensioned coordinate (x, y) could then be

calculated with the equations as below.

$$x = -r \sin \theta \quad (3.3)$$

$$y = r \cos \theta \quad (3.4)$$

In order to clarify the AC model, the whole flow field excluding the locations exactly on the Actuator Cylinder is divided into three regions which are demonstrated in Figure 3.2.

- Region 1: Outside the AC but not in the direct wake of it.
- Region 2: Inside the AC.
- Region 3: In the direct wake of AC.

The Actuator Cylinder is divided into two parts which are the windward part and the leeward part, with the region of the azimuthal angle to be $\theta \in [0^\circ, 180^\circ)$ and $\theta \in [180^\circ, 360^\circ)$ respectively, the term of *windward* and *leeward* are consistent with [32],

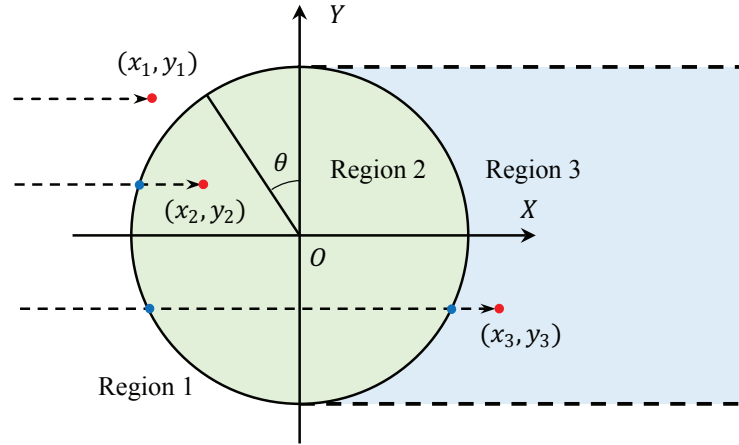


Figure 3.2: The regions and the integration path of the Actuator Cylinder model.

In Equation 3.1 of w_x , there are two extra terms of (*) and (**), the (*) term should be included when the location to be evaluated is inside the AC, which is the Region 2. Both of the two terms should be included when the location is in the direct wake of the AC, which is the Region 3. And no extra terms is needed if the location is outside of the AC but not in the direct wake, which is the Region 1. The reason to include the two extra terms is due to the integration path in Equation (7.3) which derives the Equation (3.1) [32]. The integration path is from $(-\infty, y)$ to (x, y) which is parallel to the x -axis with constant value of y , the path is demonstrated in Figure 3.2. The (*) term should be included when the integration path passes the windward part of the Actuator Cylinder, and the (**) term should be included when the integration passes the leeward part [32].

To be noted that the definition of the three regions above is also due to the aforementioned integration path and also implicitly determines the non-expanding wake modelling in the AC model. And it should also be noted that for the two extra terms in Equation

3.1, \cos^{-1} represents the arccosine function. As a result, the two extra terms represent the normal loading at the azimuthal angle of $\theta = \cos^{-1} y$ and $\theta = -\cos^{-1} y$ where the aforementioned integration path intersects with the windward and the leeward part of the Actuator Cylinder respectively.

The introducing of the extra terms will ensure continuity of the induced velocity in x -direction according to Madsen [32] and is of vital importance for the implementation of the AC model. There will be discussions about the details of including the extra terms in subsection 3.3.4, and the continuity of the induced velocity will be validated numerically and theoretically in subsection 3.3.5 and section 4.2.3 respectively.

In order to combine the AC model with airfoil aerodynamics and then implement the combined model in a computer code such as MATLAB, several aspects should be considered and summarised to four Modules as below.

3.1.1 Discretization method

The first Module is the discretization of the AC. The equations of the induced velocities are continuous functions with continuous integrals as in Equation (3.1) and (3.2). To calculate the results numerically with a computer code, the AC should be divided into several sections. The method introduced by Madsen [31] is straight forward that the AC is divided into N sections with uniform spacing of azimuthal angle, which is:

$$\Delta\theta = 2\pi/N \quad (3.5)$$

The control point of each section is selected to be the midpoint of this section arc, and piecewise constant of properties is assumed which means the property at the control point will represent the whole section. According to Madsen [31], a sufficient discretization method is with the number of the section to be $N = 36$ with azimuthal spacing $\Delta\theta = 10^\circ$, and the corresponding azimuthal locations of the control points to be:

$$\theta_i = (i - 1/2)\Delta\theta = (2i - 1)\pi/N, \quad i = 1, 2, \dots, N \quad (3.6)$$

With this discretization method, the locations at the connection points between the windward and leeward parts of the AC, whose azimuthal angle are $\theta = 0^\circ$ and $\theta = 180^\circ$, are not the control points. And another characteristic of this method is that for every control point on the windward part of the AC, there will be a corresponding control point in the leeward part of the AC with the same value of y , and vice-versa.

With the discretization method mentioned above, the integral part of the induced velocity in x - and y -direction are then written as:

$$w_x = -\frac{1}{2\pi} \sum_{i=1}^N Q_{n,i} \int_{\theta_i - \frac{1}{2}\Delta\theta}^{\theta_i + \frac{1}{2}\Delta\theta} \frac{-(x + \sin\phi) \sin\phi + (y - \cos\phi) \cos\phi}{(x + \sin\phi)^2 + (y - \cos\phi)^2} d\phi \quad (3.7)$$

$$w_y = -\frac{1}{2\pi} \sum_{i=1}^N Q_{n,i} \int_{\theta_i - \frac{1}{2}\Delta\theta}^{\theta_i + \frac{1}{2}\Delta\theta} \frac{-(x + \sin\phi) \cos\phi - (y - \cos\phi) \sin\phi}{(x + \sin\phi)^2 + (y - \cos\phi)^2} d\phi \quad (3.8)$$

One important thing to be noted is when evaluating the induced velocity at the control points of the AC, there will be singularity problems due to the denominator of the integrand in Equation (3.7) and (3.8) will become zero. In order to solve this issue, a practical method is to move the control points slightly to be just inside or outside of the AC by multiplying the coordinate of the point to be evaluated with a scaling factor f . According to Madsen, the value of $1 \pm 0.1\%$ to $1 \pm 1\%$ will be reasonable for the scaling factor of f . The coordinate of the control point number j after the shift is then as follows.

$$x_j = -f \sin \theta_j \quad (3.9)$$

$$y_j = f \cos \theta_j \quad (3.10)$$

With $j = 1, 2, \dots, N$

The choice of scaling factor f should be consistent throughout the windward and leeward parts respectively. This will make the physical meaning to be consistent and will also prevent the unnecessary issues during the implementation in the computer code. In addition, the choice of whether to move the control point inside or outside of the AC will determine what extra terms should be included will then determines the explicit form of the equation of the induced velocity in x -direction, and the detailed explanation will be in subsection 3.3.5. For the following contents in this chapter, if not specially mentioned, the scaling factor f is assumed to be slightly larger than 1 throughout the AC. This corresponds to moving the control points to be just outside the AC for both windward and leeward parts.

When evaluating the induced velocity at the control point number j which is just outside the AC, the induced velocities could then be rewritten into the forms as below.

$$w_{x,j} = -\frac{1}{2\pi} \sum_{i=1}^N Q_{n,i} I_{1,j,i} - (Q_{n,N+1-j})^* + (Q_{n,j})^{**} \quad (3.11)$$

$$w_{y,j} = -\frac{1}{2\pi} \sum_{i=1}^N Q_{n,i} I_{2,j,i} \quad (3.12)$$

The subscript of i and j represents the loading that inducing velocities is at the control point number i , and the induced velocity to be evaluated is at the control point number j . Both the (*) and (**) terms in Equation (3.11) should be included when the control point is on the leeward part of the AC, corresponds to the condition of $j > N/2$ which will let the azimuthal angle satisfies the condition of $\theta_j > 180^\circ$. The reason is that because the control points are shifted to be just outside of the AC, the control points in the leeward part are then in Region 3.

The explicit form of the (*) and (**) terms are derived as follows with Equation (3.10) and with the condition that scaling factor f is very close to 1.

$$y_i = f \cos \theta_j \cong \cos \theta_j \quad (3.13)$$

Because the control point is in the leeward part, the azimuthal angle satisfies $\theta_j > \pi$, the arc-cosine function is then:

$$\cos^{-1} y_j \cong 2\pi - \theta_j \quad (3.14)$$

The (*) and (**) terms in Equation 3.11 are then derived as follows.

$$Q_n(\cos^{-1} y) \cong Q_n(2\pi - \theta_j) = Q_{n,N+1-j} \quad (3.15)$$

$$Q_n(-\cos^{-1} y) \cong Q_n(-2\pi + \theta_j) = Q(\theta_j) = Q_{n,j} \quad (3.16)$$

3.1.2 The influence coefficients

The second Module is the calculation of the influence coefficients of $I_{1,j,i}$ and $I_{2,j,i}$ in Equation (3.11) and (3.12), with the explicit form as follows:

$$I_{1,j,i} = \int_{\theta_i - \frac{1}{2}\Delta\theta}^{\theta_i + \frac{1}{2}\Delta\theta} \frac{-(x_j + \sin \phi) \sin \phi + (y_j - \cos \phi) \cos \phi}{(x_j + \sin \phi)^2 + (y_j - \cos \phi)^2} d\phi \quad (3.17)$$

$$I_{2,j,i} = \int_{\theta_i - \frac{1}{2}\Delta\theta}^{\theta_i + \frac{1}{2}\Delta\theta} \frac{-(x_j + \sin \phi) \cos \phi - (y_j - \cos \phi) \sin \phi}{(x_j + \sin \phi)^2 + (y_j - \cos \phi)^2} d\phi \quad (3.18)$$

From the equations above, it could be concluded that the influence coefficients are purely geometric properties which are independent of the distribution of the loadings on the AC. As a result, the influence coefficients could be computed before and outside the iteration loop in subsection 3.1.5 to avoid repeating and wasting of computational efforts.

The integral can be calculated numerically with the integral interval of $[\theta_i - \frac{1}{2}\Delta\theta, \theta_i + \frac{1}{2}\Delta\theta]$ divided into N_s sub-sections with uniform spacing, and then use numerical integration method such as rectangle method.

$$I_{1,j,i} = \sum_{k=1}^{N_s} \frac{-(x_j + \sin \phi_k) \sin \phi_k + (y_j - \cos \phi_k) \cos \phi_k}{(x_j + \sin \phi_k)^2 + (y_j - \cos \phi_k)^2} \Delta\phi_k \quad (3.19)$$

$$I_{2,j,i} = \sum_{k=1}^{N_s} \frac{-(x_j + \sin \phi_k) \cos \phi_k - (y_j - \cos \phi_k) \sin \phi_k}{(x_j + \sin \phi_k)^2 + (y_j - \cos \phi_k)^2} \Delta\phi_k \quad (3.20)$$

For the discretization method in Equation (3.6) with $\Delta\theta = 10^\circ$, the value of $N_s = 100$ will be sufficient. With the interval divided into more sub-sections such as 1×10^3 or 1×10^4 , the results will have higher accuracy. However, the total computational effort of the influence coefficients will also increase linearly with N_s . Even though the calculation of the influence coefficients only needs to be done once for the whole computational process, the value of N_s for the numerical integration does not need to be too high to have a sufficient result. To be noted, the choice of the N_s should be dependent on the scaling factor f in Equation (3.11) and (3.12) as well, the details of this issue will be discussed in section 4.4. The calculation of the influence coefficients has also been simplified by the author in section 4.1 with some discussions about the results.

3.1.3 Calculate loadings at the control points.

The third Module is to calculate the distributed normal and tangential loadings at the control points. The relative wind speed should be firstly calculated. The relative wind

velocity is the vector sum of the free wind velocity, the induced velocity and the rotational velocity.

$$\vec{V}_{rel} = \vec{V}_{\infty} + \vec{V}_{ind} + \vec{V}_{rot} \quad (3.21)$$

To be noted that the vector sum of $(\vec{V}_{\infty} + \vec{V}_{ind})$ is the velocity of the wind with respect to the rotor axis and is noted as $\vec{V}_{W|R}$. The rotational velocity of \vec{V}_{rot} is defined to be the velocity of the rotor axis with respect to the blade which is $\vec{V}_{R|B}$. It is the opposite vector of the velocity of the blade with respect to the rotor axis $\vec{V}_{B|R}$, which is usually defined as the rotational velocity of the blade. According to Equation (3.21), the relative velocity \vec{V}_{rel} is then equal to the vector sum of $\vec{V}_{W|R}$ and $\vec{V}_{R|B}$, which is equal to $\vec{V}_{W|B}$. As a result, the relative velocity \vec{V}_{rel} is then the velocity of the wind with respect to the blade.

In Equation (3.21), the induced velocity at the control points are calculated with Equation (3.11) and (3.12), and the other two components of the velocity are also able to be easily calculated. The absolute value of the relative wind velocity is the relative wind speed.

To be noted that the VAWT can rotate in either counter-clockwise or clockwise direction. The explicit forms of the most equations are same, but some equations will have minor differences. For the following equations in this section, the condition of counter-clockwise rotation is assumed. And the condition of the clockwise rotation will be discussed in subsection 3.3.2 with the relationship of the value of the variables for two identical rotors with different rotational directions. The derivation of the following equations is according to [25] and [31].

Equations with dimensioned variables

To be noted that the following variables with upper case represent the dimensioned variables. For simplicity, the free wind velocity and the induced velocity are firstly summed together, and the components in x - and y -directions are as below.

$$V_x = V_{\infty}(1 + w_x) \quad (3.22)$$

$$V_y = V_{\infty}w_y \quad (3.23)$$

The normal and tangential relative wind speed with respect to the AC are then obtained as follows.

$$V_n = V_x \sin \theta - V_y \cos \theta \quad (3.24)$$

$$V_t = V_x \cos \theta + V_y \sin \theta + V_{rot} \quad (3.25)$$

The relative wind speed is then calculated from the normal and tangential relative wind velocity.

$$V_{rel} = \sqrt{V_n^2 + V_t^2} \quad (3.26)$$

The angle of attack is calculated with inverse trigonometric function of arctangent with the consideration of the pitch angle.

$$\alpha = \tan^{-1}(V_n/V_t) - \theta_p \quad (3.27)$$

The pitch angle of θ_p is defined to be positive when the blade pitches in the clockwise direction when the rotor is counter-clockwise rotating, which is consistent with the definition in [32].

The relationship of the aforementioned components of velocity as well as the angle of attack and pitch angle could be visualised in the Figure 3.3.

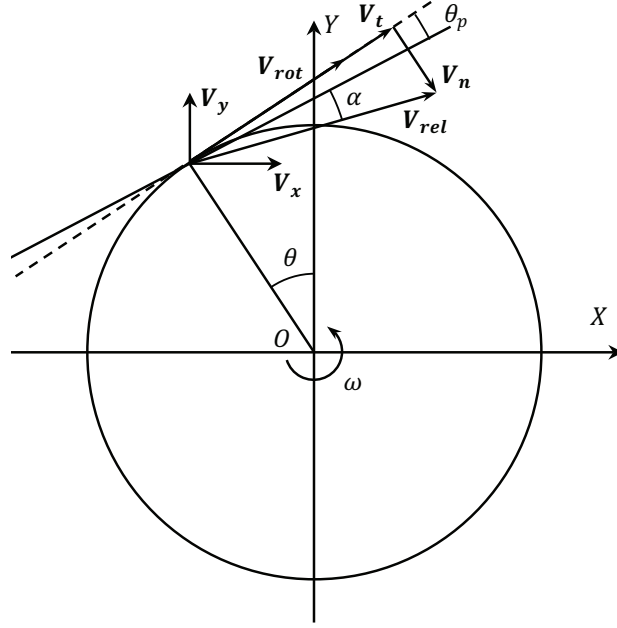


Figure 3.3: The velocity components and the angle of attack in the AC model for counter-clockwise rotating rotor.

With the airfoil aerodynamics, the lift and drag coefficients are obtained from a look-up table with the angle of attack α . The lift and drag forces are then calculated for a specified control point, when the blade is located exactly at this location, with the equations as below. Repeating this process will get the lift and drag forces for all the control points.

$$L(\theta) = \frac{1}{2} \rho V_{rel}^2(\theta) c C_L(\alpha) \quad (3.28)$$

$$D(\theta) = \frac{1}{2} \rho V_{rel}^2(\theta) c C_d(\alpha) \quad (3.29)$$

The lift and drag forces are then projected to normal and tangential components of the aerodynamic forces with respect to the airfoil.

$$F_n(\theta) = L(\theta) \cos \alpha + D(\theta) \sin \alpha \quad (3.30)$$

$$F_t(\theta) = L(\theta) \sin \alpha - D(\theta) \cos \alpha \quad (3.31)$$

The relationship of the different components of the aforementioned aerodynamic forces are demonstrated in Figure 3.4 which is zoomed in at the area of interest.

The normal and tangential loadings are the time-averaged non-dimensional aerodynamic forces on the AC. The normal and tangential aerodynamic forces are multiplied by the

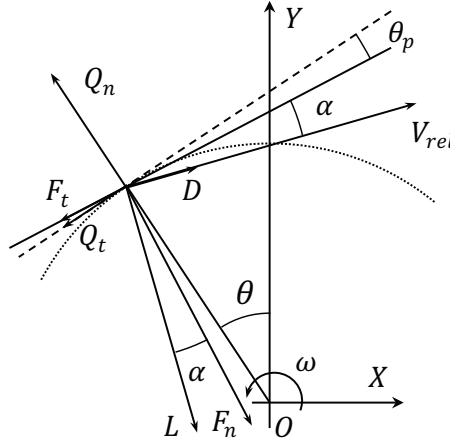


Figure 3.4: The components of the aerodynamic forces in the AC model for counter-clockwise rotating rotor.

number of blades B and then divided by $2\pi R$ which will serve as time-averaging in one revolution. And finally non-dimensioned with ρV_∞^2 which will then obtain the normal and tangential loadings.

$$Q_n(\theta) = \frac{B}{2\pi R \rho V_\infty^2} (F_n(\theta) \cos \theta_p - F_t(\theta) \sin \theta_p) \quad (3.32)$$

$$Q_t(\theta) = -\frac{B}{2\pi R \rho V_\infty^2} (F_n(\theta) \sin \theta_p + F_t(\theta) \cos \theta_p) \quad (3.33)$$

In the equations above, the normal and tangential loadings are the function of the variables of radius, density and free wind speed. However, the normal and tangential loadings are non-dimensioned values and should not be dependent on the aforementioned variables. As a result, the above equations are rewritten in the form of non-dimensioned variables as below.

Equations with non-dimensioned variables

Firstly, the different components of velocities from Equation (3.22) to (3.26) are non-dimensioned with the free wind speed V_∞ as below. The lower case represents the variables are non-dimensioned.

$$v_x = 1 + w_x \quad (3.34)$$

$$v_y = w_y \quad (3.35)$$

$$v_n = v_x \sin \theta - v_y \cos \theta \quad (3.36)$$

$$v_t = v_x \cos \theta + v_y \sin \theta + \lambda \quad (3.37)$$

$$v_{rel} = \sqrt{v_n^2 + v_t^2} \quad (3.38)$$

In Equation (3.37), the variable λ is the tip speed ratio defined as the ratio of the rotational speed to the free wind speed.

$$\lambda = \frac{V_{rot}}{V_\infty} = \frac{\omega R}{V_\infty} \quad (3.39)$$

The angle of attack in Equation (3.27) could then be written as the equation of the non-dimensioned velocities.

$$\alpha = \tan^{-1}(v_n/v_t) - \theta_p \quad (3.40)$$

The normal and tangential aerodynamic forces of Equation (3.30) and (3.31) are non-dimensioned with $\frac{1}{2}\rho V_{rel}^2 c$, and becomes the normal and tangential blade force coefficients.

$$C_n = C_L \cos \alpha + C_d \sin \alpha \quad (3.41)$$

$$C_t = C_L \sin \alpha - C_d \cos \alpha \quad (3.42)$$

The normal and tangential loading in Equation (3.32) and (3.33) could then be re-written into the form as below.

$$Q_n = \frac{\sigma}{2\pi} v_{rel}^2 (C_n \cos \theta_p - C_t \sin \theta_p) \quad (3.43)$$

$$Q_t = \frac{\sigma}{2\pi} v_{rel}^2 (C_n \sin \theta_p + C_t \cos \theta_p) \quad (3.44)$$

In the equation above, the variable of σ is the solidity of the rotor which is defined as below.

$$\sigma = \frac{Bc}{2R} \quad (3.45)$$

According to Equation (3.43) and (3.44), the explicit form of the normal and tangential loadings are only dependent on the non-dimensioned variables instead of dependent on the dimensioned variables as Equation (3.32) and (3.33). As a result, if the non-dimensioned variables are not changed, the normal and tangential loadings will not change.

3.1.4 Mod-Lin correction method

The fourth Module is the Modified linear (Mod-Lin) correction method. For the full AC model which consists of both linear and nonlinear parts of the solution, the computational efforts will be too heavy due to the requirement of including the influence from the whole flow field for the nonlinear part of the solutions. For the numerical calculation, the flow field should be discretized into mesh grids and with the value of the variables calculated on every grid point. For the linear part of the solution, only the volume forces, which are located on the AC, have the contribution to the induced velocities. With the discretization method in Equation (3.6), with only $N = 36$ sections will be sufficient for the calculation. This is much fewer than that needed for the mesh grid of the whole flow field for the nonlinear part of the full AC model.

There is a simple correction to the linear part of the solution introduced by Madsen [31]. The correction method is named *Mod-Lin* which stands for the modified linear method. With this correction method, the thrust coefficient and power coefficient are shown to have good agreements with the full AC model with almost no computational effort added due to this method. The modification is applied with a correction factor k_a multiplied to the induced velocities of all control points in both x - and y -directions calculated from Equation (3.11) and (3.12). The subscript of *Mod* in the following equations represents the induced velocities after Mod-Lin correction.

$$w_{x,Mod} = k_a w_x \quad (3.46)$$

$$w_{y,Mod} = k_a w_y \quad (3.47)$$

The explicit form of the correction factor k_a is as below.

$$k_a = \frac{1}{1-a} \quad (3.48)$$

The basis of this correction factor is the relationship of the linear solution of the thrust coefficient and the axial induction factor a for the VAWT with uniform loading is as below [31].

$$C_T = 4a_{lin} \quad (3.49)$$

And according to the momentum theory applied on the HAWT, the relationship of the thrust coefficient and the axial induction factor for not heavy loaded rotor is as follows [19].

$$C_T = 4a(1-a) \quad (3.50)$$

The correction factor of k_a in Equation (3.48) is then the ratio of Equation (3.49) and (3.50), which will let thrust coefficient from the linear solution from the AC model to have better agreements with the full AC model.

The thrust coefficient for the rotor can be calculated with the normal and tangential loadings with the equation below. The derivation is detailed in the Appendix A.1.1.

$$C_T = \int_0^{2\pi} (Q_n(\theta) \sin \theta + Q_t(\theta) \cos \theta) d\theta \quad (3.51)$$

The induction factor of a is calculated from the thrust coefficient C_T of the whole VAWT. One possible method of the relationship between the two variables is the polynomial function implemented in HAWC2 [25].

$$a = k_3 C_T^3 + k_2 C_T^2 + k_1 C_T + k_0 \quad (3.52)$$

With $k_0 = -0.0017$, $k_1 = 0.2511$, $k_2 = 0.0544$, $k_3 = 0.0892$

This polynomial function includes both the condition for $C_T = 4a(1-a)$ which is from the momentum theory for the case that the rotor is not heavily loaded with $a < 0.3$, as well as the heavily loaded case of $a > 0.3$ with the Glauert correction.

According to Cheng [8], the above method will result in significant deviation of the thrust and power coefficient for high loadings. Therefore, a modification to the Equation (3.52) is introduced with a piecewise equation which is identical for the not heavily loaded cases. And there is a correction for the heavily loaded cases which correspond to the case of high tip speed ratio and solidity.

$$k_a = \begin{cases} \frac{1}{1-a} & , a \leq 0.15 \\ \frac{1}{1-a} [0.65 + 0.35 \exp(-4.5(a - 0.15))] & , a > 0.15 \end{cases} \quad (3.53)$$

3.1.5 Iteration method for converged solutions

With the above four Modules, the converged solution could be obtained with a proper iteration method which will be introduced here. The iteration process is demonstrated in the flow chart in Figure 3.5.

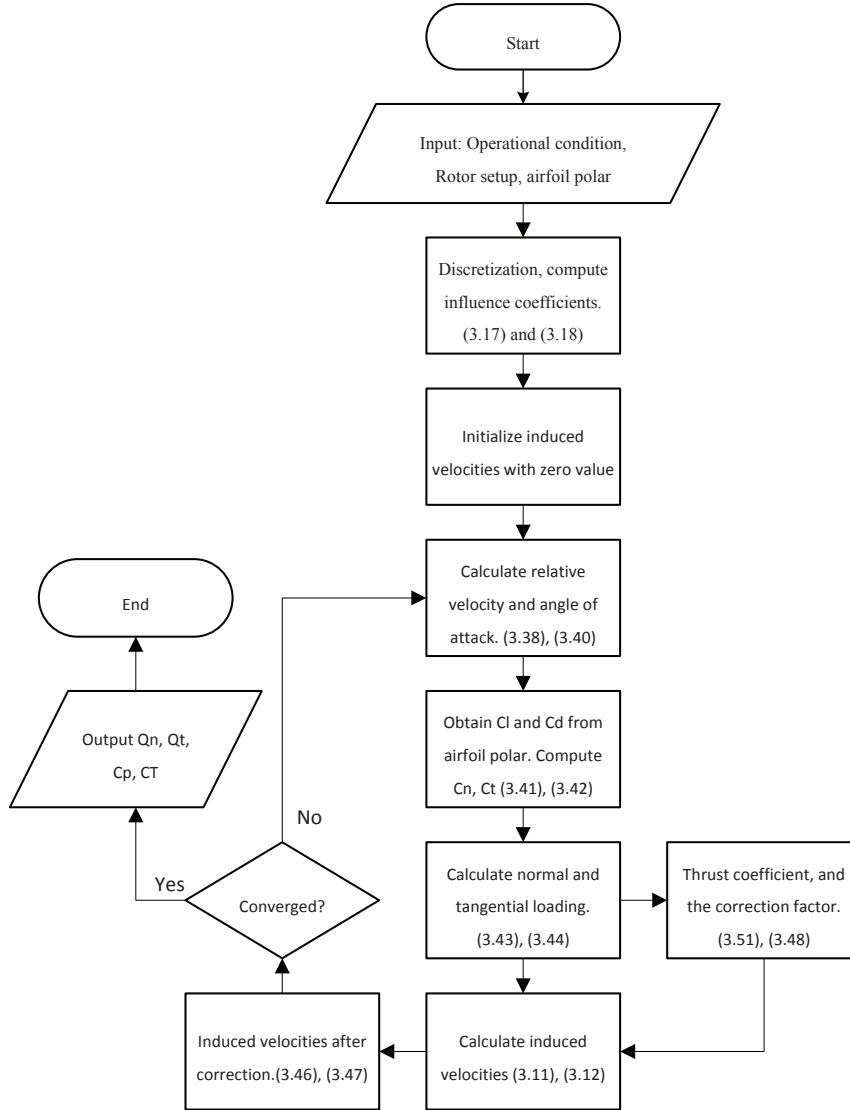


Figure 3.5: Flow chart of the iteration process for the Actuator Cylinder model.

Firstly, the input data is the operational condition, rotor setup and airfoil polar, which includes the tip speed ratio, solidity, pitch angle, mounting location, rotational direction. Secondly, the AC is discretized with the coordinate of the control points obtained with Equation (3.9) and (3.10), and the influence coefficients are purely geometric properties and are calculated with Equation (3.19) and (3.20). For the first iteration, the induced velocities are assumed to be zero-valued for all the control points in both x - and y -directions. Thirdly, the angle of attack and non-dimensioned relative wind speed are calculated with Equation (3.40) and (3.38). Fourthly, the lift and drag coefficient are obtained from the polar data with the angle of attack, and the normal and tangential aerodynamic force coefficients are calculated with Equation (3.41) and (3.42). The fifth step is to calculate normal and tangential loadings with Equation (3.43) and (3.44). The next step is to calculate the induced velocities in x - and y -direction with Equation (3.11) and (3.12) from the normal loadings calculated in the previous step. The induced velocities are then compared with

that from the previous step. If the error is within the tolerance, the converged solution is obtained. Otherwise, if the error is larger than the tolerance, the iteration should loop back to the step three with the new induced velocities and loop until the converged solution is reached. With the converged solution of the induced velocities obtained, the values of normal and tangential loading will also be the converged solution. To be noted that to prevent the divergence problems, a relaxation factor β of 0.1 or 0.2 is applied when updating the induced velocities for the next iteration, and the method is inherited from the widely-used method in the code of BEM method for HAWT applications.

3.1.6 Calculate the velocity at arbitrary points

With the converged solution of the normal and tangential loadings of the AC obtained with the iteration process according to the previous subsection, the induced velocities at an arbitrary point in the flow field could then be calculated with Equation (3.1) and (3.2). With the flow field discretized into a mesh grid, the velocities on the grid points could be obtained. The corresponding streamlines of the flow could then be calculated according to it, and the pressure field could also be obtained with the Bernoulli's equation.

When implementing the above two equations in the computer code, it could be done in a similar way as calculating the induced velocities on the control points. The explicit form of the equation of the integration part of the induced velocities are identical with Equation (3.7) and (3.8). However, attentions should be paid to the two additional terms of (*) and (**) in Equation (3.1) when the location (x, y) to be evaluated is inside or in the direct wake of AC which corresponds to Region 2 and Region 3 respectively. Because unlike when evaluating on the control points, the locations on the AC with the azimuthal angle of $\theta = \cos^{-1} y$ and $\theta = -\cos^{-1} y$ have very possibility that will not directly correspond to a certain control point of the AC. This is visualised in Figure 3.6.

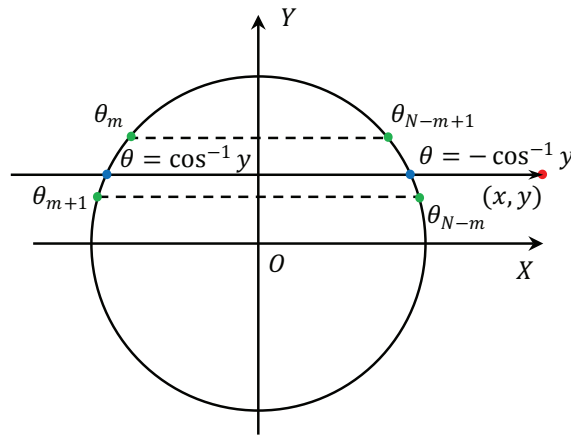


Figure 3.6: Interpolation of the variables on the Actuator Cylinder.

In order to obtain the loadings at the azimuthal angle of $\theta = \cos^{-1} y$ and $\theta = -\cos^{-1} y$, there are generally two methods which will be introduced as below.

Piecewise constant of loadings

The first method is to utilise the assumption of piecewise constant of properties of each section on the AC. For the control point number m , its corresponding section is then as follows according to Equation (3.6)

$$\theta_m - \frac{1}{2}\Delta\theta < \theta \leq \theta_m + \frac{1}{2}\Delta\theta \quad (3.54)$$

As a result, when the azimuthal angle of $\theta = \cos^{-1}y$ satisfies the Equation (3.54) which means it is in the section number m , the two extra terms could then be approximated with:

$$Q_n(\cos^{-1}y) \cong Q_{n,m} \quad (3.55)$$

$$Q_n(-\cos^{-1}y) \cong Q_{n,N+1-m} \quad (3.56)$$

Linear interpolation of loadings

The second method is to use linear interpolation to obtain the loadings at the azimuthal angle of $\theta = \cos^{-1}y$ and $\theta = -\cos^{-1}y$. For the azimuthal angle of $\theta = \cos^{-1}y$, it should be determined this azimuthal angle is between which two neighbouring control points instead of which section it is located as in the first method.

With the condition of $\theta_m < \cos^{-1}y < \theta_{m+1}$, the loadings at $\theta = \cos^{-1}y$ could be obtained with linear interpolation with the loadings at $Q_{n,m}$ and $Q_{n,m+1}$ as follows.

$$Q_n(\cos^{-1}y) = \frac{\theta_{m+1} - \cos^{-1}y}{\theta_{m+1} - \theta_m} Q_{n,m} + \frac{\cos^{-1}y - \theta_m}{\theta_{m+1} - \theta_m} Q_{n,m+1} \quad (3.57)$$

With the uniform spacing of the azimuthal angle be noted as $\Delta\theta$, the above equation could be then simplified to

$$Q_n(\cos^{-1}y) = k_m Q_{n,m} + k_{m+1} Q_{n,m+1} \quad (3.58)$$

With

$$k_{m+1} = (\cos^{-1}y - \theta_m) / \Delta\theta \quad (3.59)$$

$$k_m = 1 - k_{m+1} \quad (3.60)$$

And for the azimuthal angle of $\theta = -\cos^{-1}y$, the azimuthal angle then satisfies:

$$2\pi - \theta_{m+1} \leq 2\pi - \cos^{-1}y < 2\pi - \theta_m \quad (3.61)$$

The two corresponding points with the azimuthal angle of $\theta = \cos^{-1}y$ and $\theta = -\cos^{-1}y$ on the AC are having the same value of y . In addition, as mentioned in subsection 3.1.1, with the discretization method of Equation (3.6), for every control point on the AC, there will be a corresponding control point on the other part of the AC with the same value of y which will result in the following relationship:

$$\theta_{N-m+1} = 2\pi - \theta_m \quad (3.62)$$

$$\theta_{N-m} = 2\pi - \theta_{m+1} \quad (3.63)$$

The azimuthal $\theta = -\cos^{-1} y$ then satisfies:

$$\theta_{N-m} \leq 2\pi - \cos^{-1} y < \theta_{N+1-m} \quad (3.64)$$

The loading at the azimuthal angle of $\theta = -\cos^{-1} y$ could then be obtained by linear interpolation.

$$Q_n(-\cos^{-1} y) = \frac{\theta_{N-m+1} - (2\pi - \cos^{-1} y)}{\theta_{N-m} - \theta_{N+1-m}} Q_{n,N-m} + \frac{(2\pi - \cos^{-1} y) - \theta_{N-m}}{\theta_{N-m} - \theta_{N+1-m}} Q_{n,N-m+1} \quad (3.65)$$

The equation could be simplified with the relationship with Equation (3.58) as below.

$$\frac{\theta_{N-m+1} - (2\pi - \cos^{-1} y)}{\theta_{N-m} - \theta_{N+1-m}} = \frac{\cos^{-1} y - \theta_m}{\Delta\theta} = k_{m+1} \quad (3.66)$$

$$\frac{(2\pi - \cos^{-1} y) - \theta_{N-m}}{\theta_{N-m} - \theta_{N+1-m}} = \frac{\theta_{m+1} - \cos^{-1} y}{\Delta\theta} = k_m \quad (3.67)$$

The equation is then simplified as follows.

$$Q_n(-\cos^{-1} y) = k_{m+1} Q_{n,N-m} + k_m Q_{n,N-m+1} \quad (3.68)$$

In addition, another possible method is to calculate the induced velocities of two points which have the same radius as the location (x, y) but with the azimuthal angle of θ_m and θ_{m+1} . And then use linear interpolation to get the induced velocity in x - and y -direction.

3.2 Validation against HAWC2 code

The Actuator Cylinder model has been implemented in the aeroelastic code of HAWC2 which could be served as a tool to validate whether the AC model has been correctly implemented in the MATLAB code with the details above in section 3.1. The validation is done by comparing the results of induced velocities and angle of attack for different load cases.

Before the validation, some details about the implementation of the AC model in the HAWC2 are listed as below:

- The aerodynamic centre is assumed to be at the half chord point of the airfoil in the HAWC2 code after the version 12.3. This is according to the version log-file in the manual of the HAWC2 code [26].
- The number of sections for the discretization of the Actuator Cylinder is 36 in the HAWC2 code which is according to [31]. This could also be validated with the number of the output of induced velocities obtained from the HAWC2 output file.
- The rotor could only be clockwise rotating in the HAWC2 code according to Larsen [25].

- The discretization method actually used in the HAWC2 code is different from what is claimed in [25] but as follows.

$$\theta_i = (i - 1)\Delta\theta, i = 1, 2, \dots, N \quad (3.69)$$

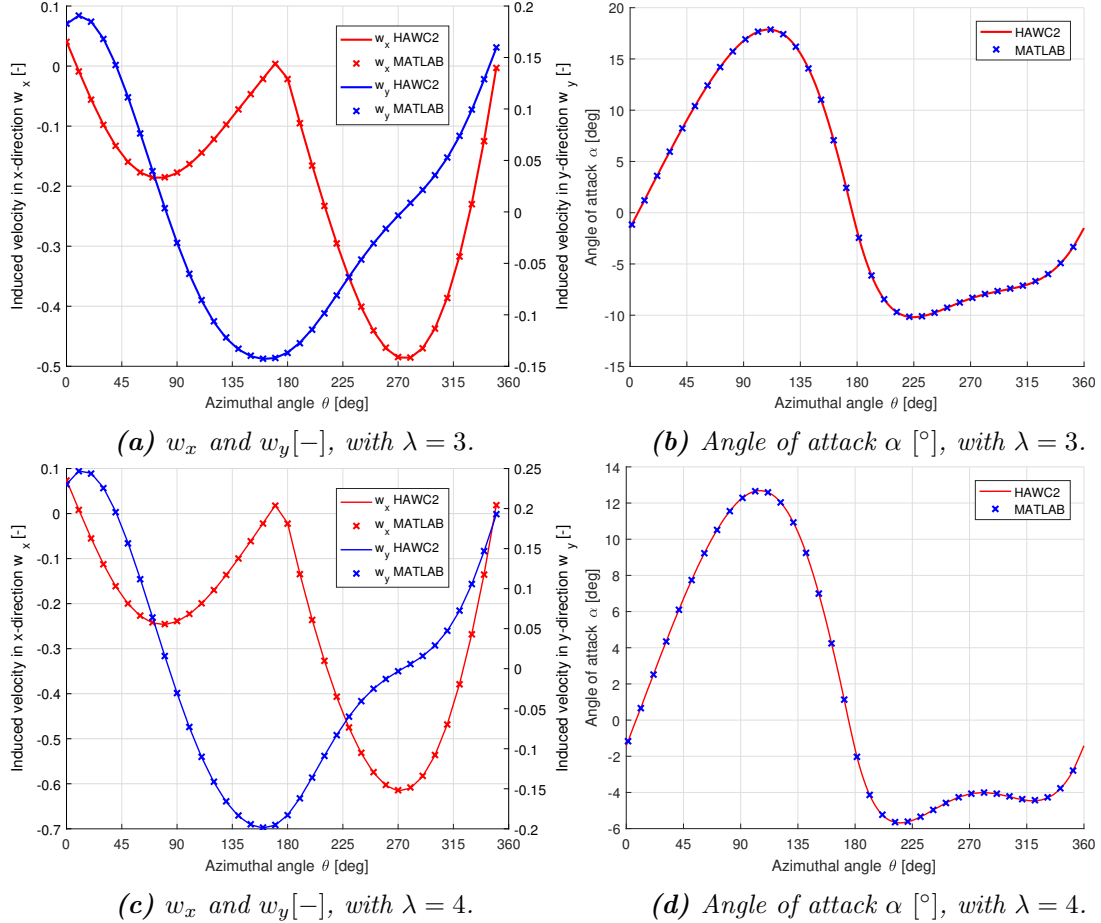


Figure 3.7: Validation of the induced velocities in x - and y -direction and angle of attack with HAWC2 code, with $\sigma = 0.1$, $B = 2$.

For the validation, the implementation of the AC model in the MATLAB code is adjusted to be consistent with the four points above. In addition, the mounting point is assumed to coincide with the aerodynamic centre, which is the half chord point, for the validation. The condition that the two points do not coincide with each other will be discussed in subsection 3.3.6. The implementation of clockwise rotation will be discussed in subsection 3.3.2 and the corresponding equations are used here for validation.

For the fourth point as above, it should be noted that the first control point is with the azimuthal angle of 0° and the corresponding first section is with the azimuthal angle from -5° to 5° . This is not consistent with the Equation (3.6), even though this method of the discretization in the HAWC2 code is given by [31]. If the method in Equation (3.6) is used, the result will not match with that from the HAWC2. By making sure that the implementation is without *bugs* and then trying out different possible methods, the exact method used in the HAWC2 is discovered to be the one in Equation (3.69). Because the

results will have very good agreements with that from the HAWC2 code if this method is used.

The results of two different load cases are calculated from the HAWC2 as well as the MATLAB code with the above four points adjusted, and the results are compared in Figure (3.7). From the figure, it could be observed that the results from the two codes have very good agreements with each other. As a result, it could be concluded that the AC model is correctly implemented in the MATLAB code. This could also verify that the aforementioned four points about the details of implementation are correct especially for the last point which is the discretization method.

3.3 Some aspects for the Actuator Cylinder model

There are several aspects of the Actuator Cylinder model and will be discussed in this section.

3.3.1 Matrix formulations

In Equation (3.11) and (3.12), the induced velocity at one control point is calculated with the summation of the product of normal loading Q_n and the corresponding influence coefficients for all of the control points of the AC. The calculation could also be achieved with the matrix product operation if the influence coefficients are correctly assembled to be an influence coefficient matrix. This is based on the method derived by Ning [36].

According to Equation (3.11) and (3.12), with the AC discretized into N sections, the induced velocity at one control point is dependent on loadings at all of the N control points on the AC which corresponds to N influence coefficients. As a result, in order to calculate the induced velocities at all of the control points of the AC in both x - or y -direction, $N \times N$ influence coefficients will be needed. This means the influence coefficient matrix is with the size of $[N, N]$ for either x - and y -direction.

Induced velocity in x -direction

The Equation (3.11) for the induced velocities in x -direction could be written as following matrix form:

$$\begin{bmatrix} w_{x,1} \\ w_{x,2} \\ \vdots \\ w_{x,N} \end{bmatrix} = \begin{bmatrix} A_{x,1,1} & A_{x,1,2} & \cdots & A_{x,1,N} \\ A_{x,2,1} & A_{x,2,2} & \cdots & A_{x,2,N} \\ \vdots & \vdots & \ddots & \vdots \\ A_{x,N,1} & A_{x,N,2} & \cdots & A_{x,N,N} \end{bmatrix} \begin{bmatrix} Q_{n,1} \\ Q_{n,2} \\ \vdots \\ Q_{n,N} \end{bmatrix} \quad (3.70)$$

With the matrix product of the influence coefficient matrix \mathbf{A}_x and the column vector of the normal loadings \mathbf{Q}_n , the result will be a column vector of the induced velocity in

x -direction w_x .

$$w_x = A_x Q_n \quad (3.71)$$

In order to take into account the integral parts as well as the additional terms of (*) and (**) in Equation (3.11) which corresponds to the location of inside and in the direct wake of the AC, the matrix A_x is thus written as the summation of the direct influence coefficient matrix of D_x and the wake coefficient matrix of W_x .

$$A_x = D_x + W_x \quad (3.72)$$

The direct influence coefficient matrix D_x corresponds to the integral parts of the Equation (3.11) which is then as follow.

$$D_x = -\frac{1}{2\pi} \begin{bmatrix} I_{1,1,1} & I_{1,1,2} & \cdots & I_{1,1,N} \\ I_{1,2,1} & I_{1,2,2} & \cdots & I_{1,2,N} \\ \vdots & \vdots & \ddots & \vdots \\ I_{1,N,1} & I_{1,N,2} & \cdots & I_{1,N,N} \end{bmatrix} \quad (3.73)$$

The direct influence coefficient matrix could then be assembled element by element with the method below, with the definition of i and j consistent with that in Equation (3.11).

$$D_x(j, i) = -\frac{1}{2\pi} I_{1,j,i} \quad (3.74)$$

The explicit form of the wake terms will be dependent on the choice of the direction of moving the control points which will be discussed in subsection 3.3.4. And here the control points in both windward and the leeward parts are moved just outside of the AC which is consistent with that in Equation (3.11).

For the windward part with the condition of $j \leq N/2$, no wake terms are needed according to Equation (3.11). As a result, the elements in the wake coefficient matrix which correspond to the windward of AC are all zero valued.

$$W_x(j, i) = 0 \quad , j \leq N/2 \quad (3.75)$$

For the leeward part with the condition of $j > N/2$, according to Equation (3.11), the non-zero elements of the matrix are as below:

$$W_x(j, N + 1 - j) = -1 \quad , j > N/2 \quad (3.76)$$

$$W_x(j, j) = 1 \quad , j > N/2 \quad (3.77)$$

Induced velocity in y -direction

The calculation of the induced velocity in y -direction with Equation (3.12) could also be transformed into matrix form. According to Equation (3.12), no extra terms are needed when calculating the induced velocity in y direction for the locations either inside or in the direct wake of the AC, which is different from calculating the induced velocity in x -direction. As a result, when calculating the induced velocities in y -direction, the influence

coefficient matrix \mathbf{A}_y is then identical to the direct influence coefficient matrix \mathbf{D}_y .

$$\begin{bmatrix} w_{y,1} \\ w_{y,2} \\ \vdots \\ w_{y,N} \end{bmatrix} = \begin{bmatrix} A_{y,1,1} & A_{y,1,2} & \cdots & A_{y,1,N} \\ A_{y,2,1} & A_{y,2,2} & \cdots & A_{y,2,N} \\ \vdots & \vdots & \ddots & \vdots \\ A_{y,N,1} & A_{y,N,2} & \cdots & A_{y,N,N} \end{bmatrix} \begin{bmatrix} Q_{n,1} \\ Q_{n,2} \\ \vdots \\ Q_{n,N} \end{bmatrix} \quad (3.78)$$

$$\mathbf{w}_y = \mathbf{A}_y \mathbf{Q}_n \quad (3.79)$$

Similar to the method of assembling the direction coefficient matrix in the x -direction as Equation (3.74), the influence coefficient matrix in y -direction could be assembled with the similar method as follows.

$$\mathbf{A}_y(j, i) = -\frac{1}{2\pi} I_{2,j,i} \quad (3.80)$$

Combination of the two matrices

With the influence coefficient matrix in x - and y -direction assembled, the induced velocity in x - and y -directions could be calculated separately with two matrix operations. An alternative method is to assemble the two matrices together into the total influence coefficient matrix \mathbf{A} with the size of $[2N, N]$, and the induced velocity in both x - and y -directions could be calculated together with a single matrix operation.

$$\mathbf{A} = \begin{bmatrix} \mathbf{A}_x \\ \mathbf{A}_y \end{bmatrix} \quad (3.81)$$

$$\mathbf{w} = \begin{bmatrix} w_x \\ w_y \end{bmatrix} = \mathbf{A} \mathbf{Q}_n \quad (3.82)$$

Induced velocity for arbitrary locations

According to subsection 3.1.6, the induced velocity at an arbitrary location in the flow field could be calculated with the converged solution of normal loading distributions on the control points with Equation (3.11) and (3.12). Similar to calculating the induced velocities at the control points on the AC, the calculation of the induced velocities at a set of arbitrary locations could also be done with matrix operation which needs to assemble the influence coefficient matrix.

For example, to calculate the influence coefficient of a set of N_E points in the flow field and with the AC discretized into N sections, there will be $N_E \times N$ influence coefficients needed for either the induced velocity in x - or y -direction. And the influence coefficient matrix in both x - and y -directions will have the size of $[N_E, N]$.

The matrix operation for the induced velocities in x -direction will be as below.

$$\begin{bmatrix} w_{x,1} \\ w_{x,2} \\ \vdots \\ w_{x,N_E} \end{bmatrix} = \begin{bmatrix} A_{x,1,1} & A_{x,1,2} & \cdots & A_{x,1,N} \\ A_{x,2,1} & A_{x,2,2} & \cdots & A_{x,2,N} \\ \vdots & \vdots & \ddots & \vdots \\ A_{x,N_E,1} & A_{x,N_E,2} & \cdots & A_{x,N_E,N} \end{bmatrix} \begin{bmatrix} Q_{n,1} \\ Q_{n,2} \\ \vdots \\ Q_{n,N} \end{bmatrix} \quad (3.83)$$

The influence coefficient could also be written as the sum of the direct influence coefficient matrix and the wake influence coefficient which is similar to Equation (3.72).

$$\mathbf{A}_x = \mathbf{D}_x + \mathbf{W}_x \quad (3.84)$$

The direct influence coefficient matrix could also be assembled element by element similar to Equation (3.74).

$$\mathbf{D}_x(j, i) = -\frac{1}{2\pi} I_{1,j,i} \quad (3.85)$$

To be noted the subscript of j and i represents the number of the location to be evaluated and the number of the control point that the normal loading is inducing velocity respectively which is consistent with definition in Equation (3.11).

For the wake coefficient matrix, the issue of the azimuthal angle of $\theta = \cos^{-1} y$ and $\theta = -\cos^{-1} y$ may not directly correspond to a control point has been explained before in section 3.1.6. And the two methods of obtaining the two wake terms in subsection 3.1.6 are also transformed to the matrix form as follows.

- For the first method which uses the assumption of piecewise constant of loadings on each section, and when the azimuthal angle satisfies $\theta_m - \frac{1}{2}\Delta\theta < \cos^{-1} y_i \leq \theta_m + \frac{1}{2}\Delta\theta$, the wake terms could be assembled as below. When the point j to be evaluated is in Region 2, the lines marked with (*) should be applied. And when the point j is in Region 3, both (*) and (**) lines should be applied.

$$(\mathbf{W}_x(j, m) = -1)^* \quad (3.86)$$

$$(\mathbf{W}_x(j, N + 1 - m) = 1)^{**} \quad (3.87)$$

- For the second method that the loading is calculated with linear interpolation, when the condition of $\theta_m < \cos^{-1} y_i \leq \theta_{m+1}$ is satisfied, the wake terms could be assembled as below.

$$(\mathbf{W}_x(j, m) = -k_m)^* \quad (3.88)$$

$$(\mathbf{W}_x(j, m + 1) = -k_{m+1})^* \quad (3.89)$$

$$(\mathbf{W}_x(j, n + 1 - m) = k_m)^{**} \quad (3.90)$$

$$(\mathbf{W}_x(j, N - m) = -k_{m+1})^{**} \quad (3.91)$$

With

$$k_{m+1} = (\cos^{-1} y_i - \theta_m) / \Delta\theta \quad (3.92)$$

$$k_m = 1 - k_{m+1} \quad (3.93)$$

The equation of the induced velocities in y -direction could also be written in the form of matrix operation which is similar to Equation (3.78) and (3.79) that the vector of the induced velocity in y -direction is the matrix product of the influence coefficient in y -direction with the vector of normal loadings.

$$\begin{bmatrix} w_{y,1} \\ w_{y,2} \\ \vdots \\ w_{y,N} \end{bmatrix} = \begin{bmatrix} A_{y,1,1} & A_{y,1,2} & \cdots & A_{y,1,N} \\ A_{y,2,1} & A_{y,2,2} & \cdots & A_{y,2,N} \\ \vdots & \vdots & \ddots & \vdots \\ A_{y,N,1} & A_{y,N,2} & \cdots & A_{y,N,N} \end{bmatrix} \begin{bmatrix} Q_{n,1} \\ Q_{n,2} \\ \vdots \\ Q_{n,N} \end{bmatrix} \quad (3.94)$$

$$\mathbf{w}_y = \mathbf{A}_y \mathbf{Q}_n \quad (3.95)$$

The influence coefficient matrix in y -direction could also be assembled element-wise which is similar to Equation (3.80) as below.

$$\mathbf{A}_y(j, i) = -\frac{1}{2\pi} I_{2,j,i} \quad (3.96)$$

3.3.2 Clockwise rotation and mirror effect

In the previous sections, the derivation of the equations is based on the assumption that the rotor is counter-clockwise rotating. However, the AC model is also able to model the clockwise rotating rotor as well, and the implementation in HAWC2 is an example. In this subsection, the case that the rotor is clockwise rotating is discussed and the mirror effect is also introduced.

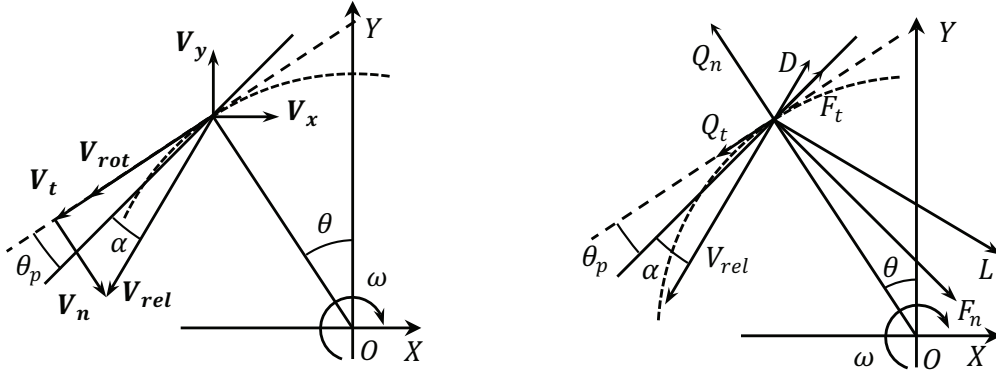
Clockwise rotation

For the case that the rotor is clockwise rotating, the components of the velocities and the forces are demonstrated in Figure 3.8b. The coordinate system, the direction of the normal and tangential loading and most of the equations are consistent with the counter-clockwise setup. The differences of the equations are listed below, which are corresponding to the Equation (3.25) and (3.32).

$$V_t = -V_x \cos \theta - V_y \sin \theta + V_{rot} \quad (3.97)$$

$$Q_t = -\frac{B}{2\pi R \rho V_\infty^2} (F_n \sin \theta_p + F_t \cos \theta_p) \quad (3.98)$$

Comparing the above equations with that of the counter-clockwise rotating, it could be concluded that there is change of sign for some terms in Equation (3.97) and (3.98). This is because of the definition of positive tangential loading direction is consistent with the definition by [32]. To be noted that the change of the rotational direction will not affect the influence coefficients because they are purely geometry properties.



(a) The velocity components and angle of attack. (b) The components of aerodynamic forces.

Figure 3.8: The components of velocities and aerodynamic forces for the clockwise rotating rotor.

Mirror effect

One of the important aspects when considering the different rotational directions is the *mirror effect* which is demonstrated in Figure 3.9.

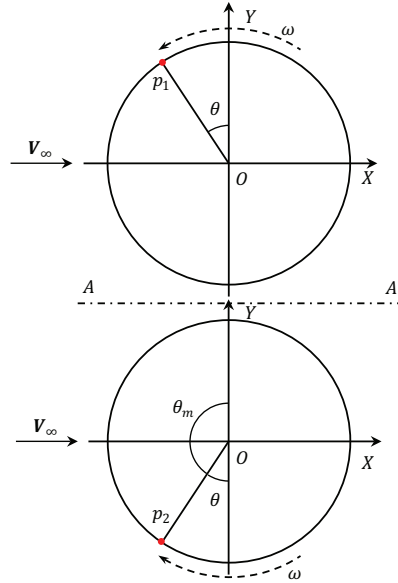


Figure 3.9: The mirror effect between two rotors with different rotational directions.

In the Figure 3.9, the two rotors are identical but the Rotor 1 is counter-clockwise rotating, and the Rotor 2 is clockwise rotating with same rotational speed. To be noted that this is not a double rotor setup, only one of the rotors is assumed to be in the flow field for each case, by plotting them together is only for demonstration purpose. The blade of Rotor 2 should be mounted correctly that letting the leading edge to encounter the rotational speed. It could be considered to be a 180° of pitch angle with respect to the Rotor 1 which is counter-clockwise rotating.

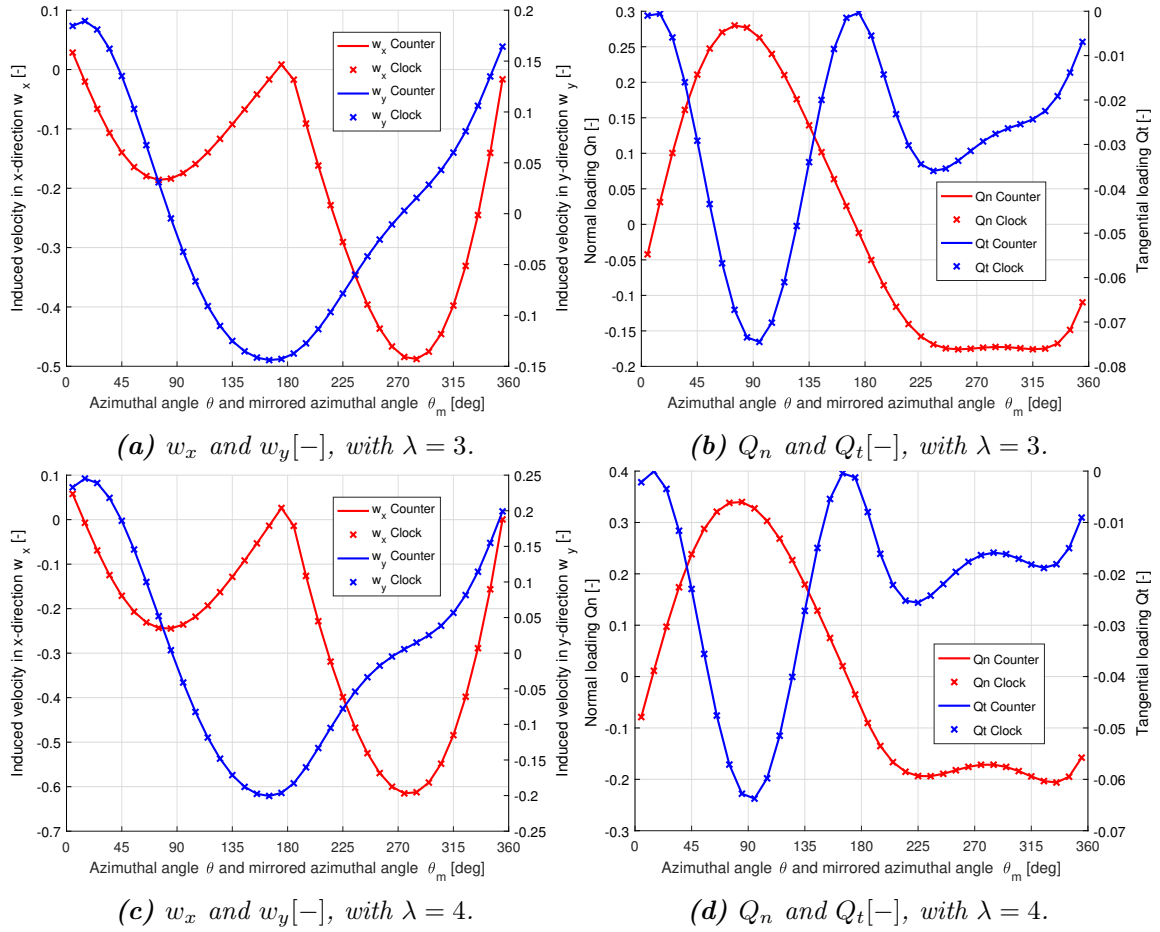


Figure 3.10: Validation of the mirror effect with induced velocities and distributed loadings, with $\sigma = 0.1$, $B = 2$.

And for the condition that two rotors are in the uniform inflow with same free wind speed, the property of an arbitrary point p_1 on Rotor 1 will be identical with the property of the point p_2 on Rotor 2 which is the *mirrored* point of p_1 with respect to the panel $A - A$ and vice versa. The *mirror effect* could be alternatively considered as a flip of the counter-clockwise rotating rotor with respect to the panel $A - A$ to get the corresponding clockwise rotating rotor and vice versa.

As a result, for the windward part, the property at the azimuthal angle of θ_1 on the Rotor 1 will be identical with the property at the azimuthal angle of $\theta_2 = \pi - \theta_1$ on the Rotor 2. And for the leeward part, the property at the azimuthal angle of θ_1 on the Rotor 1 will be identical with that at the azimuthal angle of $\theta_2 = 3\pi - \theta_1$ on the Rotor 2. The relationship of θ_1 and θ_2 are summarised as follows:

For the windward part,

$$\theta_1 + \theta_2 = \pi \quad (3.99)$$

And for the leeward part,

$$\theta_1 + \theta_2 = 3\pi \quad (3.100)$$

As a result, the value of the variables for the clockwise rotating rotor could be either calculated directly with the AC model for clockwise rotating rotors with modification of Equation (3.97) and (3.98), or could be calculated with the corresponding counter-clockwise rotating rotor which is only different in rotational direction with the clockwise rotating rotor to be calculated. And then the results of the counter-clockwise rotor are transformed to the mirrored clockwise rotating rotor with the Equation (3.99) and (3.100).

In order to validate the mirror effect, the results of two identical rotors with different rotational directions are calculated with the AC model. And then, the converged solution of the induced velocities and loadings on the control points of the counter-clockwise rotating rotor are compared with that of the corresponding clockwise rotating rotor on the *mirrored* control points. The results are plotted in the Figure 3.10. To be noted that the x -axis in the figure is the azimuthal angle for the counter-clockwise rotor and is the mirrored azimuthal angle for the clockwise rotating rotor for comparison purposes. The counter-clockwise rotation and clockwise rotational cases are noted as *Counter* and *Clock* in the legend of the figure respectively.

According to the Figure 3.10, it could be visualised that the value of the variables of the counter-clockwise rotating rotor are identical with that of the corresponding mirrored points of the clockwise rotating rotor. The results then verified the mirror effect of the two rotors with different rotational directions. The results could also verify that the AC model for the clockwise rotating setup with the modification of Equation (3.97) and (3.98) are correct and is correctly implemented in the MATLAB code.

According to the *mirror effect*, the performance of the rotor will not be influenced by choice of the rotational direction of the VAWT rotor. This is similar to that of the HAWT where the performance does not rely on the rotational direction, be it counter-clockwise or clockwise. Thus, a clockwise rotating rotor can be modelled either by using the modified AC model for clockwise rotation or by using the counter-clockwise rotating setup together with the *mirror effect*. As such, the *mirror effect* will be a tool to relate the counter-clockwise rotor with its corresponding clockwise rotating rotor, and also a good indication for the sanity check of the implementation of the AC model. The modelling of the clockwise rotating is necessary for the Double Actuator Cylinder (DAC) model and the mirror effect is of vital importance to relate the two rotors in the double rotor setup which will be discussed in Chapter 7.

3.3.3 Cheng's modified Actuator Cylinder model

In the original AC model, the induced velocity is only dependent on the normal loadings as Equation (3.1) and (3.2). According to Cheng [8], the linear solution of the induced velocities is derived again and shown to be dependent on loadings in both normal and tangential directions. In order to distinguish with the original AC model by Madsen [32], this modified AC model is named Cheng's modified AC model in the following. The explicit form of equations for the linear parts as well as detailed derivation could be found in Cheng's paper [8].

Explicit formulation

Firstly, the explicit form of the equations for the induced velocities in x - and y -directions are as below:

$$\begin{aligned}
 w_x(x, y) = & -\frac{1}{2\pi} \int_0^{2\pi} Q_n(\phi) \frac{-(x + \sin \phi) \sin \phi + (y - \cos \phi) \cos \phi}{(x + \sin \phi)^2 + (y - \cos \phi)^2} d\phi \\
 & - \frac{1}{2\pi} \int_0^{2\pi} Q_t(\phi) \frac{-(x + \sin \phi) \cos \phi - (y - \cos \phi) \sin \phi}{(x + \sin \phi)^2 + (y - \cos \phi)^2} d\phi \\
 & - Q_n(\cos^{-1} y)^* + Q_n(-\cos^{-1} y)^{**} - (Q_t(\cos^{-1} y) \frac{y}{\sqrt{1-y^2}})^* - (Q_t(-\cos^{-1} y) \frac{y}{\sqrt{1-y^2}})^{**}
 \end{aligned} \quad (3.101)$$

$$\begin{aligned}
 w_y(x, y) = & -\frac{1}{2\pi} \int_0^{2\pi} Q_n(\phi) \frac{-(x + \sin \phi) \cos \phi - (y - \cos \phi) \sin \phi}{(x + \sin \phi)^2 + (y - \cos \phi)^2} d\phi \\
 & + \frac{1}{2\pi} \int_0^{2\pi} Q_t(\phi) \frac{-(x + \sin \phi) \sin \phi + (y - \cos \phi) \cos \phi}{(x + \sin \phi)^2 + (y - \cos \phi)^2} d\phi
 \end{aligned} \quad (3.102)$$

Similar to original AC model, with AC discretized into N sections and the assumption of piecewise constant of property, the integral parts of the equations of induced velocities are then:

$$\begin{aligned}
 w_x = & -\frac{1}{2\pi} \sum_{i=1}^N Q_{n,i} \int_{\theta_i - \frac{1}{2}\Delta\theta}^{\theta_i + \frac{1}{2}\Delta\theta} \frac{-(x + \sin \phi) \sin \phi + (y - \cos \phi) \cos \phi}{(x + \sin \phi)^2 + (y - \cos \phi)^2} d\phi \\
 & - \frac{1}{2\pi} \sum_{i=1}^N Q_{t,i} \int_{\theta_i - \frac{1}{2}\Delta\theta}^{\theta_i + \frac{1}{2}\Delta\theta} \frac{-(x + \sin \phi) \cos \phi - (y - \cos \phi) \sin \phi}{(x + \sin \phi)^2 + (y - \cos \phi)^2} d\phi
 \end{aligned} \quad (3.103)$$

$$\begin{aligned}
 w_y = & -\frac{1}{2\pi} \sum_{i=1}^N Q_{n,i} \int_{\theta_i - \frac{1}{2}\Delta\theta}^{\theta_i + \frac{1}{2}\Delta\theta} \frac{-(x + \sin \phi) \cos \phi - (y - \cos \phi) \sin \phi}{(x + \sin \phi)^2 + (y - \cos \phi)^2} d\phi \\
 & + \frac{1}{2\pi} \sum_{i=1}^N Q_{t,i} \int_{\theta_i - \frac{1}{2}\Delta\theta}^{\theta_i + \frac{1}{2}\Delta\theta} \frac{-(x + \sin \phi) \sin \phi + (y - \cos \phi) \cos \phi}{(x + \sin \phi)^2 + (y - \cos \phi)^2} d\phi
 \end{aligned} \quad (3.104)$$

When evaluating the induced velocity on the control points, it is assumed that the control points are moved just outside of the AC which is consistent with subsection 3.1.1 for simplicity. The (*) and (**) terms should be added when the control points are in the leeward part of the AC.

$$\begin{aligned}
 w_{x,j} = & -\frac{1}{2\pi} \sum_{i=1}^N Q_{n,i} I_{1,j,i} - \frac{1}{2\pi} \sum_{i=1}^N Q_{t,i} I_{2,j,i} - (Q_{n,N+1-j})^* + (Q_{n,j})^{**} \\
 & - (Q_{t,N+1-j})^* \frac{y_j}{\sqrt{1-y_j^2}} - (Q_{t,j})^{**} \frac{y_j}{\sqrt{1-y_j^2}}
 \end{aligned} \quad (3.105)$$

$$w_{y,j} = -\frac{1}{2\pi} \sum_{i=1}^N Q_{n,i} I_{2,j,i} + \frac{1}{2\pi} \sum_{i=1}^N Q_{t,i} I_{1,j,i} \quad (3.106)$$

The explicit form of the influence coefficients of $I_{1,j,i}$ and $I_{2,j,i}$ are identical to that of the original AC model with Equation (3.17) and (3.18). It could be concluded from Equation (3.105) and (3.106) that the induced velocity consists of two parts which are the contribution due to the normal loadings and tangential loadings respectively. The part that due to the normal loadings is in the identical formulation as the original AC model. Thus, if setting the tangential loadings of the control points on the AC to be all zero-valued, there is then no contribution due to the tangential loading, the equations for Cheng's AC model will then be identical to Equation (3.11) and (3.12) for the original AC model.

Matrix formulation

Similar to the original AC model, the calculation of the induced velocity in x - and y -direction for the Cheng's modified AC model could also be calculated with matrix operation. The difference is that the induced velocities are now dependent on both normal and tangential loadings.

Firstly, for the induced velocity in x -direction, the calculation could be written as the following form.

$$\mathbf{w}_x = \mathbf{A}_x \begin{bmatrix} \mathbf{Q}_n \\ \mathbf{Q}_t \end{bmatrix} \quad (3.107)$$

The total influence coefficient matrix for x -direction is the summation of the direct influence coefficient matrix and the wake coefficient matrix for x -direction which is similar to that of the original AC model.

$$\mathbf{A}_x = \mathbf{D}_x + \mathbf{W}_x \quad (3.108)$$

Each of the above three matrices consists of two parts which are the coefficients corresponding to the normal loading and to the tangential loadings, the two parts are noted with the subscript of n and t standing for *normal* and *tangential* respectively.

$$[\mathbf{A}_{x,n} \quad \mathbf{A}_{x,t}] = [\mathbf{D}_{x,n} \quad \mathbf{D}_{x,t}] + [\mathbf{W}_{x,n} \quad \mathbf{W}_{x,t}] \quad (3.109)$$

The direct influence coefficient matrix in x -direction due to normal loadings is identical to the direct influence coefficient matrix in x - and y -direction of the original AC model and the explicit equations are identical to Equation (3.74) and (3.80).

With the assumption that the control points are moved outside of the AC for all the control points, the explicit form of the equation of the induced velocity in x -direction is given by Equation (3.105). The wake influence coefficient matrix due to normal loadings $\mathbf{W}_{x,n}$ is corresponding to the first two (*) and (**) terms in Equation (3.105), and the

wake influence coefficient matrix due to tangential loadings $\mathbf{W}_{x,t}$ is corresponding to the last two (*) and (**) terms in Equation (3.105). The four extra (*) and (**) terms should be included only for the control points in the leeward part of the AC. As a result, when $j \leq N/2$, all elements in the j -th row of the four wake influence coefficient matrices are zero valued. And when $j > N/2$, the nonzero terms could be obtained according to Equation (3.105) in the similar way to Equation (3.76) and (3.77) as follows.

$$\mathbf{W}_{x,n}(j, N+1-j) = -1 \quad (3.110)$$

$$\mathbf{W}_{x,n}(j, j) = 1 \quad (3.111)$$

$$\mathbf{W}_{x,t}(j, N+1-j) = -\frac{y_j}{\sqrt{1-y_j^2}} \quad (3.112)$$

$$\mathbf{W}_{x,t}(j, j) = -\frac{y_j}{\sqrt{1-y_j^2}} \quad (3.113)$$

To be noted that the equations of wake influence coefficient due to normal loadings for the Cheng's AC model in Equation (3.110) and (3.111) are identical to the wake influence coefficient for the original AC model defined in Equation (3.76) and (3.77).

The induced velocities in y -direction for the Cheng's AC model could also be rewritten in the matrix form as below.

$$\mathbf{w}_y = \mathbf{A}_y \begin{bmatrix} \mathbf{Q}_n \\ \mathbf{Q}_t \end{bmatrix} \quad (3.114)$$

Similar to the original AC model, the total influence coefficient in y -direction is equal to the direct influence coefficient matrix. And similar to the Equation (3.109) for the induced velocities in x -direction, the total influence coefficient for y -direction \mathbf{A}_y is also consists of two parts which are due to the normal and tangential loadings respectively.

$$\mathbf{A}_y = [\mathbf{A}_{y,n} \quad \mathbf{A}_{y,t}] \quad (3.115)$$

The influence coefficient matrices that due to tangential loadings could be directly obtained from the direct influence coefficient matrices due to the normal loadings. The relationship could be determined according to Equation (3.105) and (3.106) and are shown as below.

$$\mathbf{A}_{y,t} = -\mathbf{D}_{x,n} \quad (3.116)$$

$$\mathbf{D}_{x,t} = \mathbf{A}_{y,n} \quad (3.117)$$

As a result, it is not necessary to assemble the influence coefficient matrix of $\mathbf{D}_{x,t}$ and $\mathbf{A}_{y,t}$ which will save the computational efforts and will also show the relationship between the matrix \mathbf{A}_x and \mathbf{A}_y

3.3.4 The explicit form of the wake terms

In the previous sections, to avoid singularity problems of the integral for the influence coefficient, all the control points are assumed to be moved slightly outside of the AC for

simplicity. However, the control points could also be moved slightly inside the AC as well, the details about the direction of moving the control points is investigated in this subsection.

In order to simplify the problem, the direction to shift the control points is consistent throughout the windward and leeward parts of the AC respectively. This means for the windward and leeward part, the control points are assumed that could only be moved either inside or outside of the AC. As a result, there will be four different cases of moving the control points for the whole AC which are summarised in the table as below.

Table 3.1: Four different cases of moving all the control points on the Actuator Cylinder.

#	Windward part	Leeward part
1	Outside	Outside
2	Inside	Inside
3	Outside	Inside
4	Inside	Outside

According to Equation (3.17) and (3.18) in subsection 3.1.2, the influence coefficients as well as the additional terms are purely geometric properties and to be more precise they are only dependent on the location of the point to be evaluated. It could then be concluded that the choice of the direction of moving the control point of the windward part will not influence the explicit form of the equation for the leeward part, and vice versa. As a result, the control points on the windward and the leeward part could be considered separately. And with the assumption that the control point could be only moved either outside or inside of the AC for both the windward and the leeward part, there will be four different cases that an arbitrary control point is located which are summarised as below.

Table 3.2: Four different cases of moving one control point on the Actuator Cylinder.

#	Location of control point	Direction
1	Windward	Outside
2	Windward	Inside
3	Leeward	Outside
4	Leeward	Inside

The induced velocities in y -direction do not have the additional terms. Thus the explicit form of the equation will not change when evaluating just outside or inside of the AC, and will be Equation (3.12) for the original AC model and will be Equation (3.106) for the Cheng's AC model. Thus, it will not be discussed for different cases as follow.

The explicit form of the equations of the induced velocities in x -direction for the four different cases will be shown as below in the same order as Table 3.2. In order to let the equations presented in a more general, the equation for the original AC model and the Cheng's AC model are written together in the same equation for each case. In the following equations, the (*) term corresponds to the influence on the induced velocity in x -direction due to tangential loadings which should only be included for the Cheng's AC model and should not be included in the original AC model.

Case 1: Windward part and outside the AC

For Case 1, the control point is on the windward part of the AC and is moved to be just outside of the AC. The control point is then outside but not in the direct wake of the AC which corresponds to Region 1 as defined in section 3.1. As a result, there will be no extra terms to be included, and the explicit form of the induced velocity in x -direction is then as follows.

$$w_{x,j} = -\frac{1}{2\pi} \sum_{i=1}^N Q_{n,i} I_{1,j,i} + \left(-\frac{1}{2\pi} \sum_{i=1}^N Q_{t,i} I_{2,j,i} \right)^* \quad (3.118)$$

Case 2: Windward part and inside the AC

For Case 2 that when the control point is on the windward part of the AC and is moved to be just inside the AC. The control point is then inside the AC which corresponds to the Region 2, thus the (*) terms in Equation (3.101) should be included. Because the control point is in the windward part, the azimuthal angle then satisfied that $0 \leq \theta_j < \pi$, the azimuthal angle corresponding to the control point number j on the AC with the y coordinate of y_j could then be simplified with Equation (3.10) as follows.

$$\cos^{-1} y_j = \cos^{-1}(f \cos \theta_j) \approx \theta_j \quad (3.119)$$

The extra terms of (*) in Equation (3.101) could then be simplified as follows.

$$Q_n(\cos^{-1} y_j) \approx Q_{n,j} \quad (3.120)$$

$$Q_t(\cos^{-1} y_j) \frac{y_j}{\sqrt{1-y_j^2}} \approx Q_{t,j} \frac{y_j}{\sqrt{1-y_j^2}} \quad (3.121)$$

The induced velocity in x -direction is then:

$$w_{x,j} = -\frac{1}{2\pi} \sum_{i=1}^N Q_{n,i} I_{1,j,i} - Q_{n,j} + \left(-\frac{1}{2\pi} \sum_{i=1}^N Q_{t,i} I_{2,j,i} - Q_{t,j} \frac{y_j}{\sqrt{1-y_j^2}} \right)^* \quad (3.122)$$

Case 3: Leeward part and outside the AC

For Case 3, the control points are on the leeward part of the AC and are moved to be just outside of the AC. The control points are then in the direct wake of the AC which corresponds to Region 3 as defined in section 3.1, and the (*) and (**) terms in Equation (3.105) should be included. For the control points in the leeward part of the AC, the explicit form of the normal loading at the azimuthal angle of $\theta = -\cos^{-1} y_j$ and $\theta = -\cos^{-1} y_j$ have been derived to be Equation (3.15) and (3.16). And when only consider the normal loadings, the explicit form has been derived as in Equation (3.11). Similarly, when considering the tangential loadings, the extra terms could be obtained similarly as

below:

$$Q_t(\cos^{-1} y_j) \frac{y_j}{\sqrt{1-y_j^2}} \cong Q_{t,N+1-j} \frac{y_j}{\sqrt{1-y_j^2}} \quad (3.123)$$

$$Q_t(-\cos^{-1} y_j) \frac{y_j}{\sqrt{1-y_j^2}} \cong Q_{t,j} \frac{y_j}{\sqrt{1-y_j^2}} \quad (3.124)$$

The induced velocity in x -direction is then:

$$w_{x,j} = -\frac{1}{2\pi} \sum_{i=1}^N Q_{n,i} I_{1,j,i} - Q_{n,N+1-j} + Q_{n,j} + \left(-\frac{1}{2\pi} \sum_{i=1}^N Q_{t,i} I_{2,j,i} - Q_{t,N+1-j} \frac{y_j}{\sqrt{1-y_j^2}} - Q_{t,j} \frac{y_j}{\sqrt{1-y_j^2}} \right)^* \quad (3.125)$$

Case 4: Leeward part and inside the AC

For Case 4, when the control point is on the leeward part of the AC and is moved to be just inside of the AC. The control point is then inside the AC which corresponds to the Region 2, and the (*) terms in Equation (3.105) should be included. This case could be related to the Case 3 by neglecting the extra terms in Equation (3.125) which corresponding to the (**) terms in Equation (3.101). The explicit form of the induced velocity in x direct could then be obtained as follows.

$$w_{x,j} = -\frac{1}{2\pi} \sum_{i=1}^N Q_{n,i} I_{1,j,i} - Q_{n,N+1-j} + \left(-\frac{1}{2\pi} \sum_{i=1}^N Q_{t,i} I_{2,j,i} - Q_{t,N+1-j} \frac{y_j}{\sqrt{1-y_j^2}} \right)^* \quad (3.126)$$

3.3.5 The continuity of velocity

Another important aspect will be the continuity of velocity when passing the AC. If the velocity is continuous when passing the AC, there will be no difference of evaluating the control points to be just outside or inside the AC as long as the distance of moving the control points is small enough. The converged solutions of moving the control points in either of the directions will converge to the same value. However, if the velocity is not continuous when passing the AC, there will be an apparent difference when evaluating at the control points which are just inside or outside of the AC and could not be neglected. According to Equation (3.21), the only possible source of discontinuity of the velocity will be from the induced velocity. Thus, the continuity of the induced velocity will be investigated. To be noted that the validation should be done for both the original AC model as well as the Cheng's AC model.

There are two possible methods for evaluating the continuity of the induced velocity which are listed as follows.

- The first method is straight forward by calculating the induced velocities along a line which is parallel to the x -axis and passing the AC. In order to have sufficient results which are the premise for a correct conclusion, the spacing of the points on the line should be small enough when the passing the windward and leeward part of the AC. Thus, the induced velocities at the locations of just outside and inside the AC could be sufficiently calculated. By repeating this process for multiple parallel lines passing all the control points, the continuity of the induced velocities could then be verified.
- The second method is to calculate the induced velocities of two sets of control points, with the first set to be all the control points of the AC are moved just outside of the AC and the second set is all the control points are moved just inside of the AC. The two scaling factors could then be chosen to be $1 + \delta$ and $1 - \delta$ respectively, for example 1.001 and 0.999. And for the same load case, the converged solutions of induced velocities are calculated for the two set of control points. By comparing the converged solutions, whether the induced velocity is continuous when passing the AC could then be determined. This method is able to verify the continuity of all of the control points on the AC at once instead of multiple calculations as the first method. Thus, the second method will be used for the investigation of the continuity of velocity in the followings of this section.

Validation for original AC model

Firstly, the induced velocities in x - and y -direction of the two sets of control points for two load cases are calculated using the original AC model that the induced velocities are only dependent on the normal loadings. The results for two load cases are plotted respectively in the Figure 3.11. From the figures, it could be visualised that the induced velocities for the two set of control points have very good agreements with each other for both x - and y -directions. It could then be concluded that the induced velocity calculated from the original AC model is continuous when passing the AC.

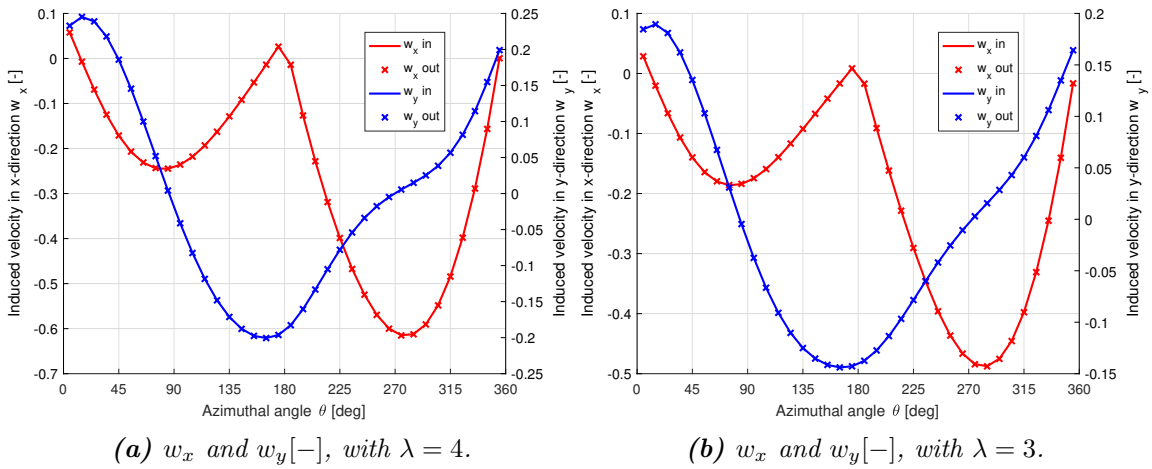


Figure 3.11: Validation of the continuity of the induced velocities from the original AC model, with $\sigma = 0.1$, $B = 2$.

Validation for Cheng's AC model

Then, the induced velocities in x - and y -directions for the two set of control points are calculated with the Cheng's AC model that the induced velocities are dependent on both the normal and tangential loadings. The results for two different load cases are plotted in Figure 3.12.

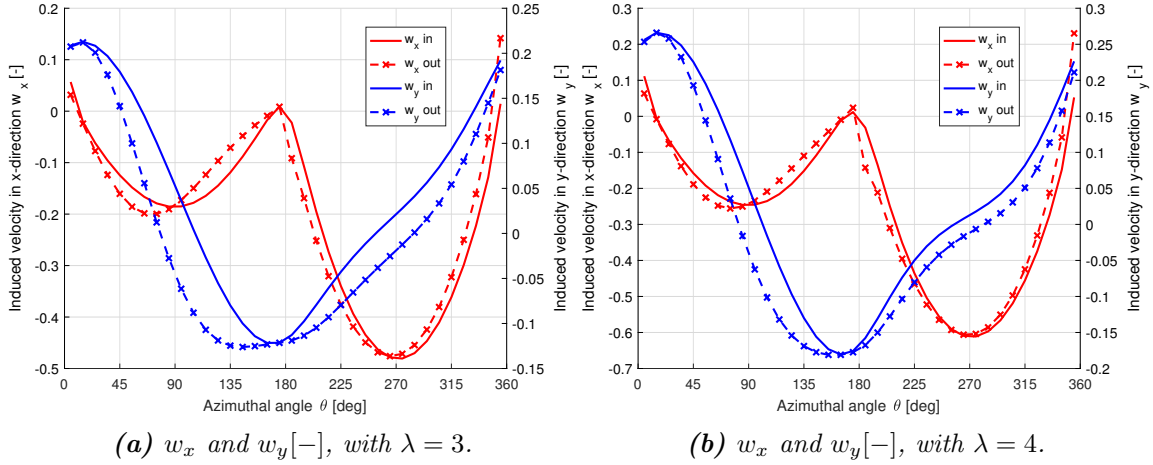


Figure 3.12: Validation of the continuity of the induced velocities from the Cheng's modified AC model, with $\sigma = 0.1$, $B = 2$.

From the figure, it could be concluded that the induced velocities for two sets of control points calculated from the Cheng's AC model do not coincide with each other in either x - or y -direction. As a result, the induced velocities are not continuous when passing the AC. Thus, the converged solution of induced velocities, loadings as well as the angle of attack will be dependent on whether evaluating the control points to be just outside or inside of the AC. The source of the discontinuity of induced velocity should then be investigated.

Contribution due to normal and tangential loadings

According to the above results, the induced velocities from the original AC model are continuous when passing the AC, but the result from the Cheng's AC model is discontinuous when passing the AC. And according to Equation (7.20) and (7.21), the explicit equation of the induced velocities of the original AC model is identical to that of the parts of the induced velocities due to normal loadings in the Cheng's AC model. As a result, the discontinuity should be due to the contribution of the tangential loadings on the induced velocities. In order to validate the above reasoning, the induced velocities due to the contribution of the normal and tangential loadings for the two sets of control points are calculated and plotted in the Figure 3.13. The superscripts of n and t represent the contribution due to normal and tangential loadings.

From the figure, it could be concluded that the contribution of the normal loadings to the induced velocity is continuous in both x - and y -directions when passing the AC, and the discontinuity comes from the contribution of the tangential loadings. For the induced

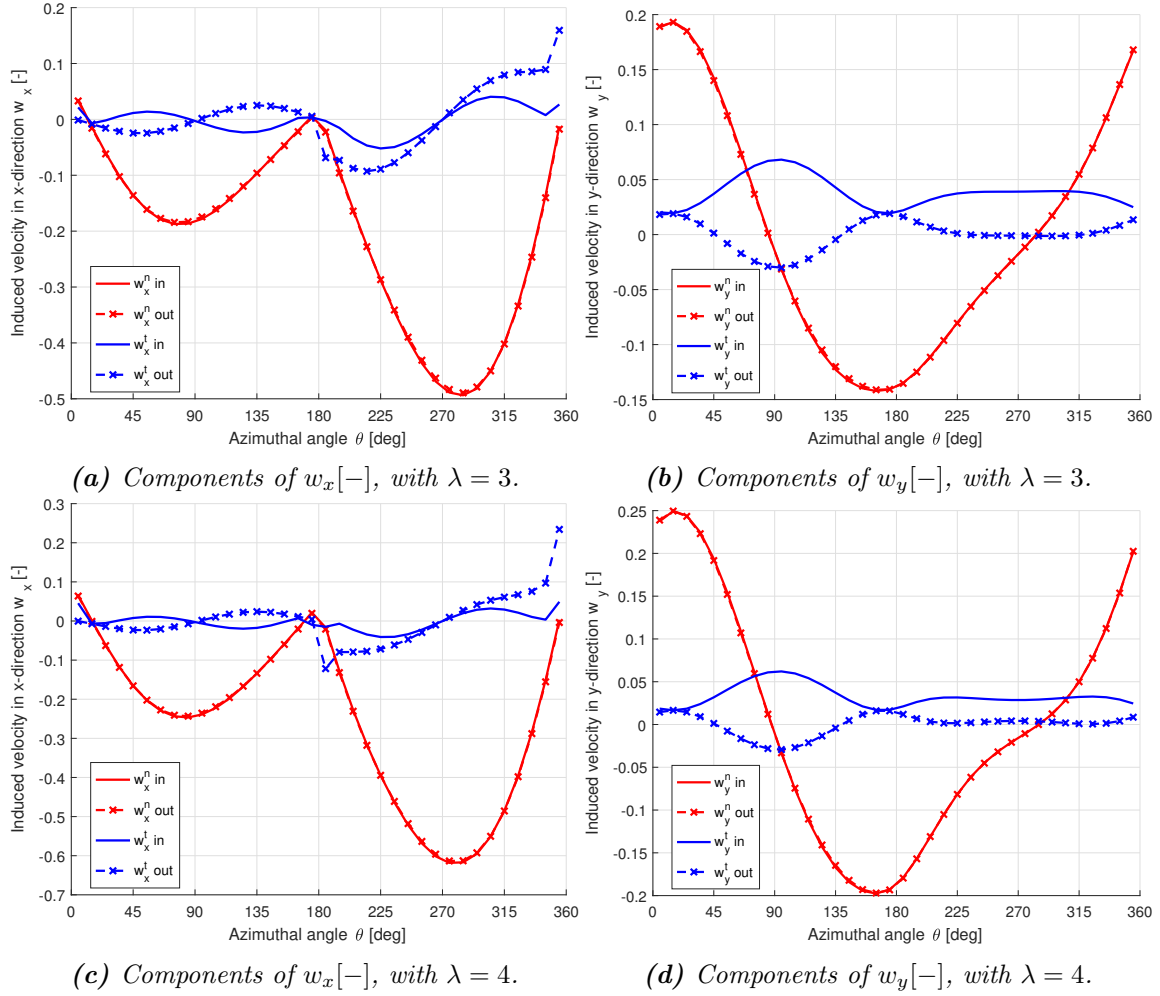


Figure 3.13: The components of the induced velocity due to normal and tangential loadings, with $\sigma = 0.1$, $B = 2$.

velocity in x -direction due to tangential loadings, when evaluating just outside of the AC for the leeward part will have a sudden change of values near the azimuthal angle of 180° and 360° which are the connection between the windward and leeward part. And when evaluating just inside of the AC, the induced velocities does not have a sudden change with the azimuthal angle. It could also be visualised that the induced velocities in y -direction due to tangential loadings when evaluating just outside and inside the AC are having a change of sign with respect to a constant value of y . For the aforementioned two cases, the constant values are $w_y = 0.019$ and $w_y = 0.016$ respectively. However, the above results of the discontinuity of induced velocities are not sufficient enough for a solid conclusion, further investigation is needed.

Normal and tangential induced velocities

For further investigation of the discontinuity of induced velocity due to tangential loadings, the normal and tangential induced velocities w_n and w_t are defined, whose positive direction

is in the opposite direction of normal and tangential loading respectively. The term of *normal* and *tangential* are then with respect to the AC, and the relationship of the induced velocities are demonstrated in Figure 3.14.

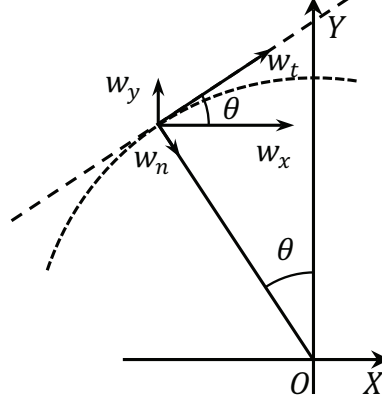


Figure 3.14: The definition of the normal and tangential induced velocities.

The variables are able to be calculated with vector projection with Equation (3.127) and (3.128), the results are calculated and are plotted in Figure 3.15.

$$w_n = w_x \sin \theta - w_y \cos \theta \quad (3.127)$$

$$w_t = w_x \cos \theta + w_y \sin \theta \quad (3.128)$$

From Figure 3.15, it could be observed that the normal induced velocity w_n is continuous when passing the AC, and the discontinuity is only in the tangential direction with w_t . Since the induced velocity in x - and y -direction due to normal loading, which are w_x^n and w_y^n , are continuous when passing the AC, the induced velocity in normal and tangential direction due to normal loading, which are w_n^n and w_t^n , should also be continuous. And because the total normal induced velocity w_n is continuous when passing the AC, the contribution to the normal induced velocity due to tangential loading w_n^t should then also be continuous when passing the AC. As a result, the discontinuity of induced velocity is only due to the tangential loading and in the tangential direction, which is w_t^t .

The influences of the tangential loadings on the normal and tangential induced velocities are then investigated. Firstly, the influence of the tangential loadings on the normal induced velocity is investigated. Since w_n^n and w_t^t are all continuous when passing the AC, the results will then be the same whether moving the control points inside or outside, which could be represented by either case. Thus, the converged solution of the normal induced velocities due to normal loading, tangential loading and the total value, which are w_n^n , w_n^t and w_n , with the control points moved outside the AC are calculated and plotted in Figure 3.16.

From Figure 3.16, it could be visualised that the tangential loadings will let the normal induced velocities to have a general phase lead in the leeward part when the rotor is counter-clockwise rotating. For the windward part, the influence due to tangential loadings will

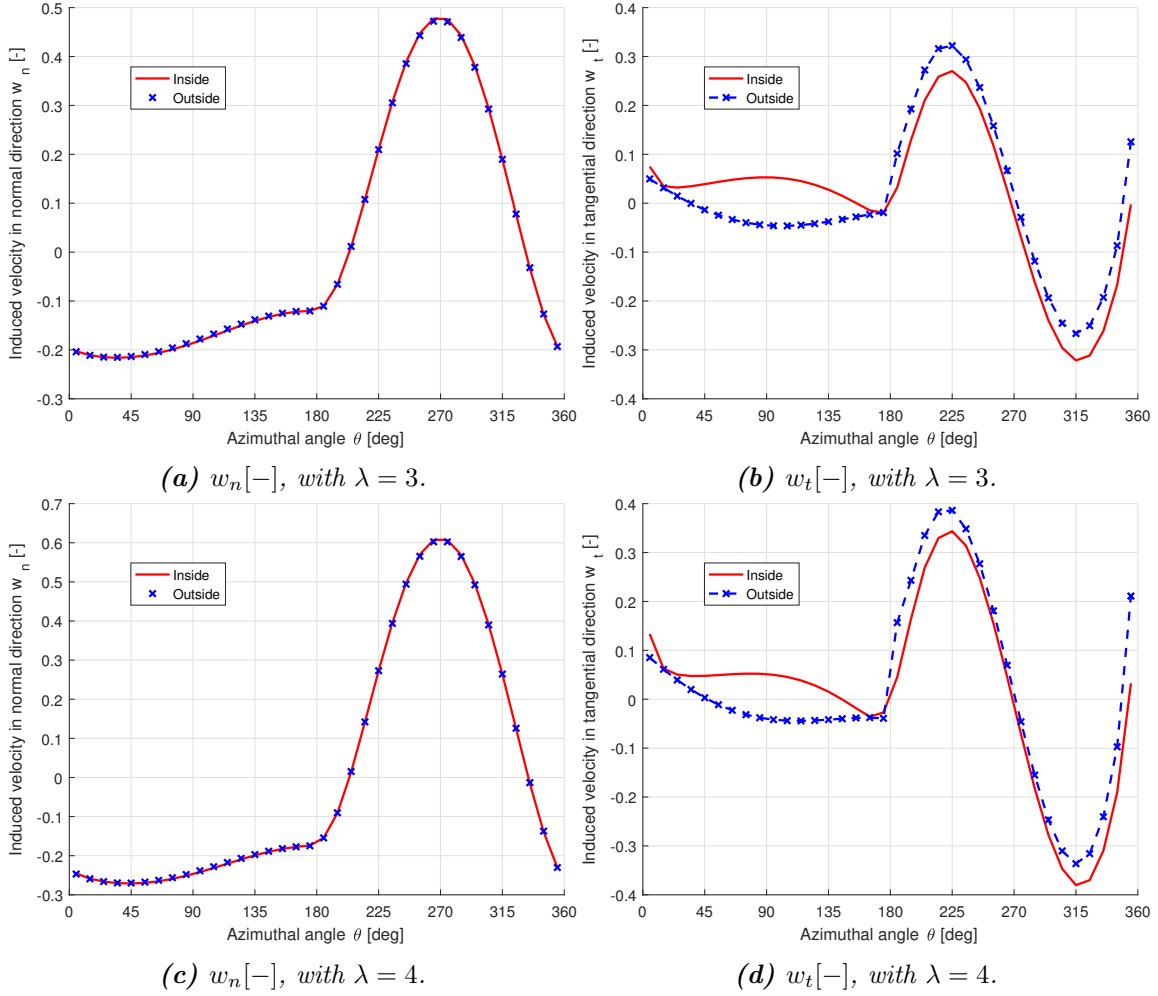


Figure 3.15: Validation of the continuity of the normal and tangential induced velocities, with $\sigma = 0.1$, $B = 2$.

result in a decrease of normal induced velocity for the first half of the windward part with the azimuthal angle of $0^\circ < \theta < 90^\circ$, and an increase for the second half of the windward part with condition of $90^\circ < \theta < 180^\circ$. This could be considered as re-distribution of the normal induced velocity in the first and second half of the windward part.

Secondly, the influence of the tangential loadings on the tangential induced velocity is investigated. It is different from the normal induced velocity, the tangential induced velocity is not continuous when passing the AC. As a result, the two cases of moving the control points outside and inside will have different results which will be calculated and plotted separately in the Figure 3.17.

From the Figure 3.17(a) and (c) it could be concluded that when evaluating just outside of the AC, the tangential loading will result a decrease of tangential induced velocity in the windward part with the maximum decrement near the azimuthal angle of $\theta = 90^\circ$ which is the centre of the windward part. The magnitude of the decrements is decreasing when moving away from this location and the decrements will be zero-valued when approaching

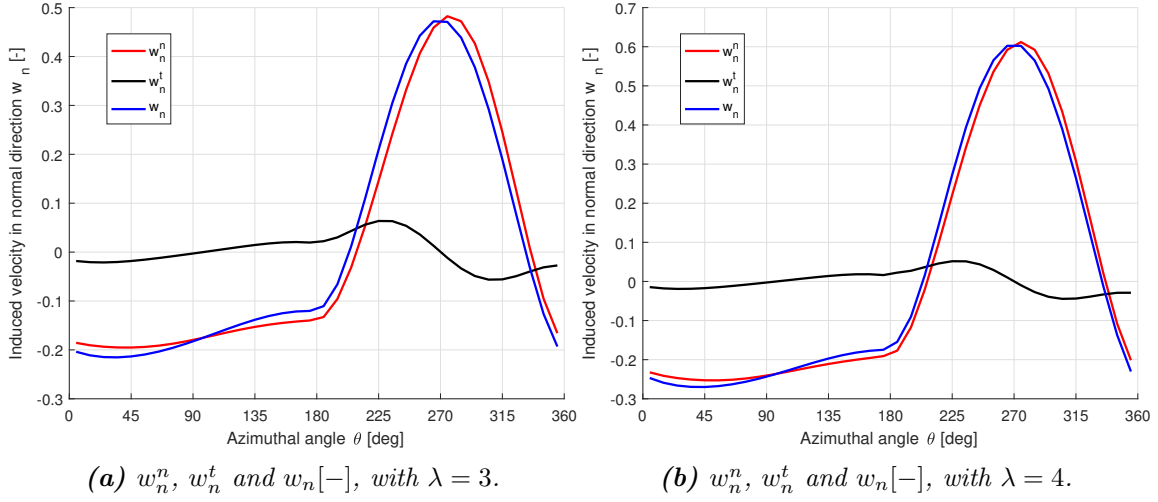


Figure 3.16: Components of normal induced velocity w_n [-], with $\sigma = 0.1$, $B = 2$.

the azimuthal angle of $\theta = 0^\circ$ and $\theta = 180^\circ$ which are the connection points between the windward part and the leeward part. For the leeward part of the AC, the tangential loading will result in the tangential induced velocity to increase, where the maximum increments are near the azimuthal angle of $\theta = 0^\circ$ and $\theta = 180^\circ$. The influence due to tangential loading will decrease when approaching azimuthal angle of $\theta = 270^\circ$ which is the centre of the leeward part and the influence is disappeared at this location. The tangential loadings will generally amplify the induced velocities in the leeward part which results in the maximum magnitude to increase, but will not cause visible phase difference.

According to Figure 3.17(b) and (d), it could be concluded that when evaluating just inside of the AC, the tangential loadings will result an increase of the induced velocities in the windward part. And for the leeward part, the tangential loading will result in a small phase lead for the induced velocity in tangential direction but will not cause the magnitude to have a significant change as evaluating outside of the AC.

Summary of the continuity

To sum up, there will be discontinuity of induced velocity for the Cheng's AC model when passing the AC only in tangential direction and only due to the tangential loadings. It could then be concluded that the choice of moving the control points to be just inside or outside of the AC will not influence the results from the original AC model but will have different results when calculating with Cheng's AC model. However, the choice of whether the control points should be moved to be just outside or inside of the rotor for the windward and leeward parts could not be determined yet. Some differences of influence due to tangential loadings when moving the control points to be just outside or inside of the AC are discussed above, but it is premature to have a convincing conclusion that which method of moving the control points is reasonable.

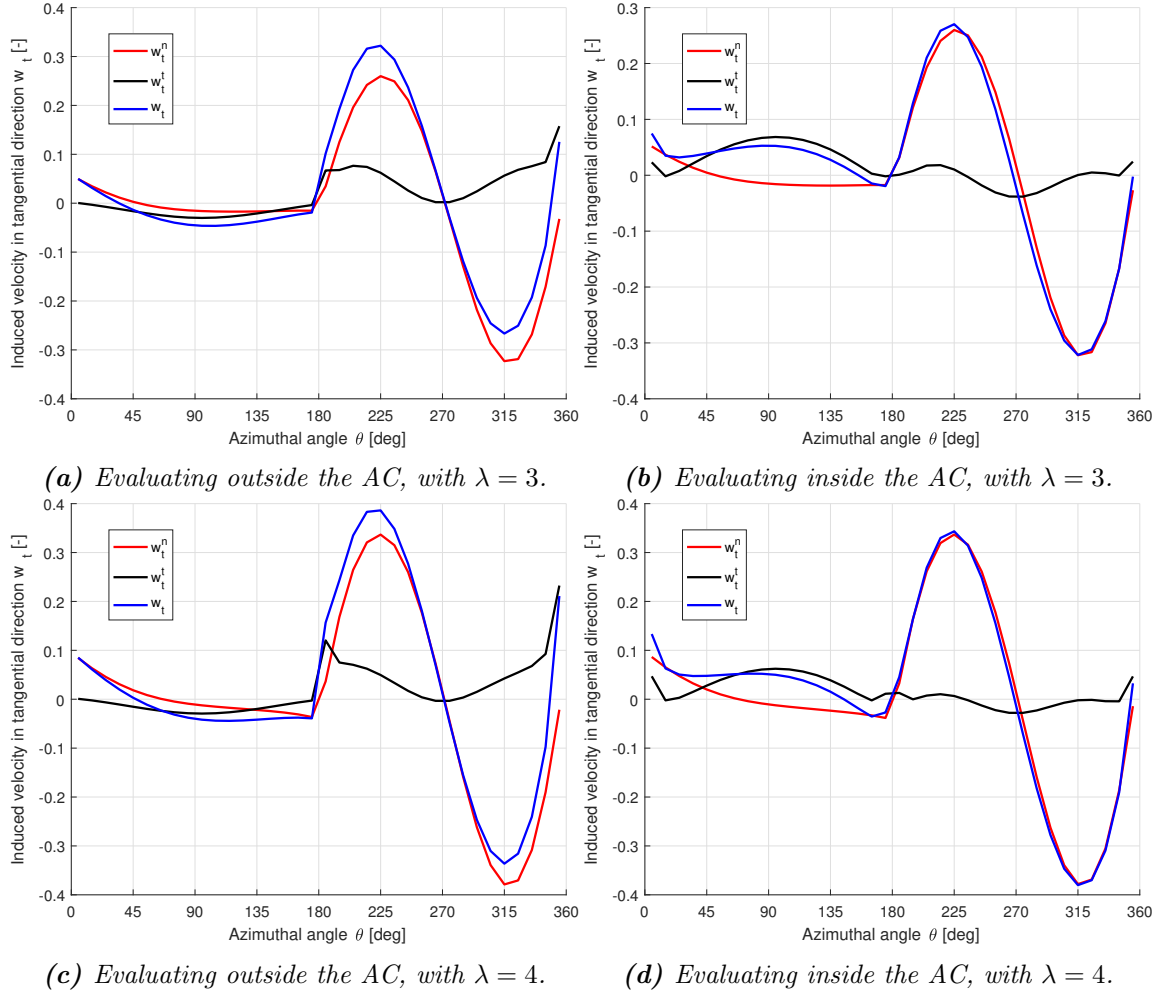


Figure 3.17: Components of tangential induced velocity $w_t[-]$, with $\sigma = 0.1$, $B = 2$.

3.3.6 The mounting point

In the previous sections, the blade mounting location is not able to be modelled. For the rotor with very small solidity, the location of the mounting point will not result in significant influence and could be neglected. However, when the solidity is relatively large, the location of the mounting point will have a significant influence on the results. Thus the location of the mounting point should be modelled.

Definition of two locations

To clarify the problem to be discussed in this section, two terms are defined as below which correspond to two locations on the airfoil.

- The first one is the *mounting point* which is defined as where the airfoil connected to the beam, it is demonstrated as the point M as shown in the Figure 3.18. The

beam $M-O$ is connected to the rotational axis point O on the other side. The pitch angle is the included angle between the chord line of the airfoil and the tangential direction of the AC which is perpendicular to the beam of $M-O$. The pitch angle is then defined to be with respect to the mounting point M since the airfoil is mounted here which is reasonable.

- The second one is the *evaluation point* where the flow properties are calculated. It is demonstrated as the point E in the Figure 3.18. This could be the aerodynamic centre of the airfoil which is usually assumed to be the quarter chord point according to the thin airfoil theory [23]. To be noted that the aerodynamic centre is assumed to be the half chord point in HAWC2 code.

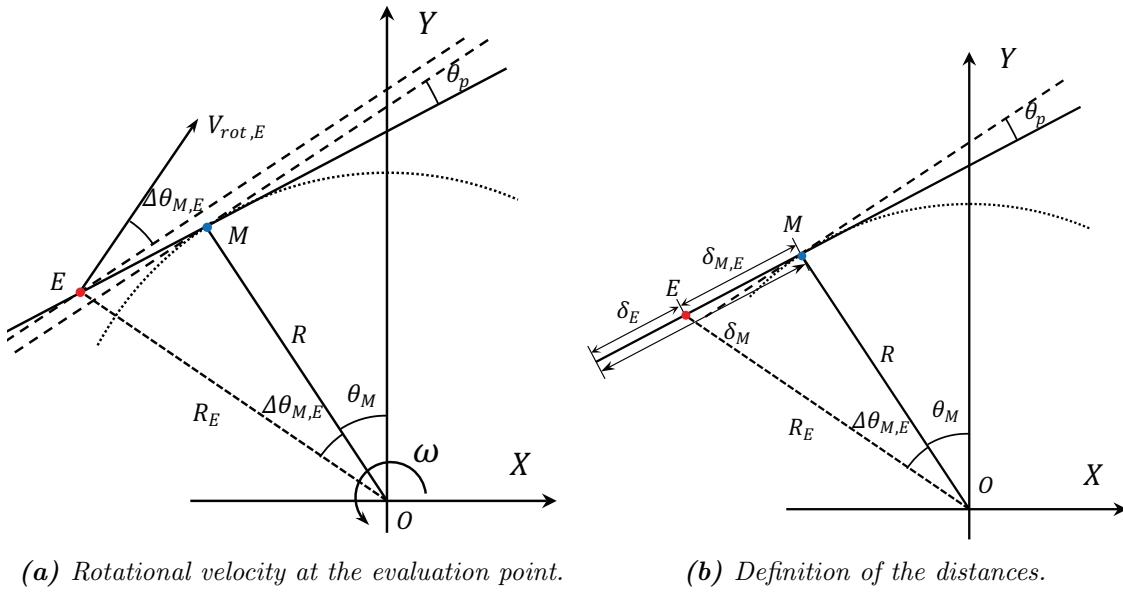


Figure 3.18: The mounting point and the evaluation point of the VAWT blade.

For the implementation of the AC models in the previous sections, there is no distinguishing of the two points in the original AC model nor Cheng's AC model. As a result, it is implicitly assumed in the previous implementations that the two points coincide with each other, which corresponds to the special condition that the blade is mounted at the aerodynamic centre. For the condition that the two points do not coincide with each other, the flow properties such as angle of attack will be different at the two locations on the airfoil which is according to the flow curvature effect [33]. If the AC models implemented previously are used for the calculation, the results will then be insufficient.

Modelling the mounting point

To model the difference between the mounting point and the evaluation point, the relative velocity at the evaluation point should be determined. To be noted that the constant pitch angle condition is assumed for simplicity which means there is no azimuthal variation of pitch angle. The relative wind speed at the evaluation point then does not have components

due to the pitching motion and is then consisted of three components which are identical with Equation (3.21). For simplicity, the induced velocity and the free wind speed are summed together, and the components in x - and y -directions are V_x and V_y which are consistent with Equation (3.22) and (3.23).

According to Figure 3.18(a), the rotational velocity of the evaluation point E is perpendicular to the line of $O-E$. And if the two points of E and M do not coincide with each other, the rotational velocity will have both normal and tangential components with respect to the AC. This will result in the explicit form of the normal and tangential relative wind speed to be different from Equation (3.24) and (3.25). The projection of the rotational velocity of the evaluation point could be done with one additional variable of $\Delta\theta_{M,E}$ which represents the difference of the azimuthal location of the two points. The Equation of (3.24) and (3.25) are then modified to the equations as below:

$$V_n = V_x \sin \theta_M - V_y \cos \theta_M + V_{rot,E} \sin \Delta\theta_{M,E} \quad (3.129)$$

$$V_t = V_x \cos \theta_M - V_y \sin \theta_M + V_{rot,E} \cos \Delta\theta_{M,E} \quad (3.130)$$

In the above equations, the variable of θ_M is the azimuthal angle for the mounting point and $V_{rot,E}$ is the rotational speed at the evaluation point. The azimuthal angle used for the vector projection of V_x and V_y is at the mounting point instead of the azimuthal angle at the evaluation point M because of the definition of the pitch angle as explained above.

According to subsection 3.1.1, the properties of the rotor are represented by the values of the variables at the control points of the AC. As a result, the control points will then correspond to the evaluation points whose azimuthal angle is then defined with Equation (3.6). And then the azimuthal angle at the mounting point θ_M could be calculated by subtracting the angular difference of $\Delta\theta_{M,E}$. Thus, in order to consider the difference between the mounting point and the evaluation point, the only modification to the AC model will then be the Equation (3.129) and (3.130) while all other equations will remain identical.

Rotational velocity at evaluation point

For the Actuator Cylinder model, the loadings are located on an infinitely thin annulus with the radius non-dimensioned to be 1. For the case that the mounting point M coincides with the evaluation point E , which is the case that the blade is mounted at the quarter chord point, the length used for non-dimensioning is the length between the rotational axis and the mounting point which is defined as the radius of the rotor. However, when the two points are not coincided with each other, which is the case that the blade is not mounted at the quarter chord point, the length used for non-dimensioning is the distance from the mounting point M to the rotational axis and is demonstrated in Figure (3.18) as line $O-M$. The evaluation point E is then not on the AC with the distance to the rotational axis noted as R_E .

For the zero-pitch angle condition,

$$R_E = \frac{R}{\cos \Delta\theta_{M,E}} = \sqrt{R^2 + \delta_{M,E}^2} \quad (3.131)$$

And for the case that the pitch angle is not zero,

$$R_E = \frac{\delta_{M,E}}{\sin \Delta\theta_{M,E}} \cos \theta_p \quad (3.132)$$

In the Equation (3.131) and (3.132), the variable of $\delta_{M,E}$ is the distance between the mounting point and the evaluation point which could be calculated as follows according to Figure 3.18(b).

$$\delta_{M,E} = \delta_E - \delta_M \quad (3.133)$$

The variables of δ_M and δ_E are the distance from the leading edge to the mounting point M and to the evaluation point E respectively.

The difference of the azimuthal angle of the evaluation point and the mounting point $\Delta\theta_{M,E}$ could be calculated as follows for two conditions.

- If there is no pitch angle, the azimuthal difference could be directly calculated with the arc-tangent function:

$$\Delta\theta_{M,E} = \tan^{-1}(\delta_{M,E}/R) \quad (3.134)$$

- If there is a constant pitch angle, the azimuthal angle difference could then be calculated with the law of sine:

$$\Delta\theta_{M,E} = \tan^{-1} \left(\frac{\delta_{M,E} \cos \theta_p}{R - \delta_{M,E} \sin \theta_p} \right) \quad (3.135)$$

Simplification method

In reality, the distance between the mounting point and the evaluation point is small compared to the radius of the rotor especially when the solidity of the rotor is not too large. The following relationship could then be obtained.

$$\frac{\delta_{M,E}}{R} < \frac{c}{R} \ll 1 \quad (3.136)$$

The two conditions of no pitch and constant pitch angle which corresponds to Equation (3.134) and (3.135) will be discussed separately as follows.

- For the condition of zero-pitch angle, the radius of the evaluation point R_E and the azimuthal difference could then be simplified as follows.

$$R_E \approx R \quad (3.137)$$

$$\Delta\theta_{M,E} \approx \delta_{M,E}/R \quad (3.138)$$

For example, for a two bladed VAWT with the solidity of $\sigma = 0.1$ and the mounting point is at the three-quarter chord which is already very far from the evaluation point of quarter chord point, the relative error of the two radii is then:

$$\frac{R_E - R}{R} = 1.25 \times 10^{-3} \quad (3.139)$$

This indicates that there will be only about 0.1% of relative error which could then be neglected.

- For the case that there is a constant small-pitch angle, the radius of the evaluation point R_E could also be replaced by the radius of the rotor.

For example, a constant 10° of pitch angle is applied to the case as above, the relative error of the radius is also shown to be very small with the value of 7.46×10^{-3} , which is still small enough to be neglected.

As a result, the radius of the evaluation point could be assumed to be identical with the radius of the rotor. With the conclusion above, Equation (3.135) could be simplified with the help of Equation (3.136) to be as follows.

$$\Delta\theta_{M,E} \approx \sin^{-1} \left(\frac{\delta_{M,E}}{R} \cos \theta_p \right) \approx \frac{\delta_{M,E}}{R} \cos \theta_p \quad (3.140)$$

And finally, the variable of $V_{rot,E}$ is the rotational speed of the valuation point which could also be approximated with the rotational speed of the mounting point as follows.

$$V_{rot,E} = \omega R_E \approx \omega R \quad (3.141)$$

A sanity check of the Equation of (3.138) and (3.140) could be done with the special condition that the mounting point is coincided with the evaluation point, it will result $\delta_{M,E} = 0$ and then $\Delta\theta_{M,E} = 0$, the Equation (3.129) and (3.130) will then be identical to Equation (3.24) and (3.25) which does not consider the difference of the two points.

Validation

In order to validate the modification which considers the difference between the mounting point and the evaluation point, the results are compared with that from the HAWC2 code. To be noted that the aerodynamic centre is at the half chord in the HAWC2 code which has been validated before, as a result, the evaluation point in the MATLAB code is also set to be the half chord point for the validation. Even though, the evaluation point E is chosen to be the half chord point instead of the quarter chord, it is still able to validate whether the above modification can model the difference between the evaluation point E and the mounting point M correctly.

There will be three different locations of mounting point for the validation which will be the quarter chord point, half chord point and three-quarter chord point of the airfoil. And the corresponding notations are 1/4, 1/2 and 3/4 for abbreviation. The angle of attack α

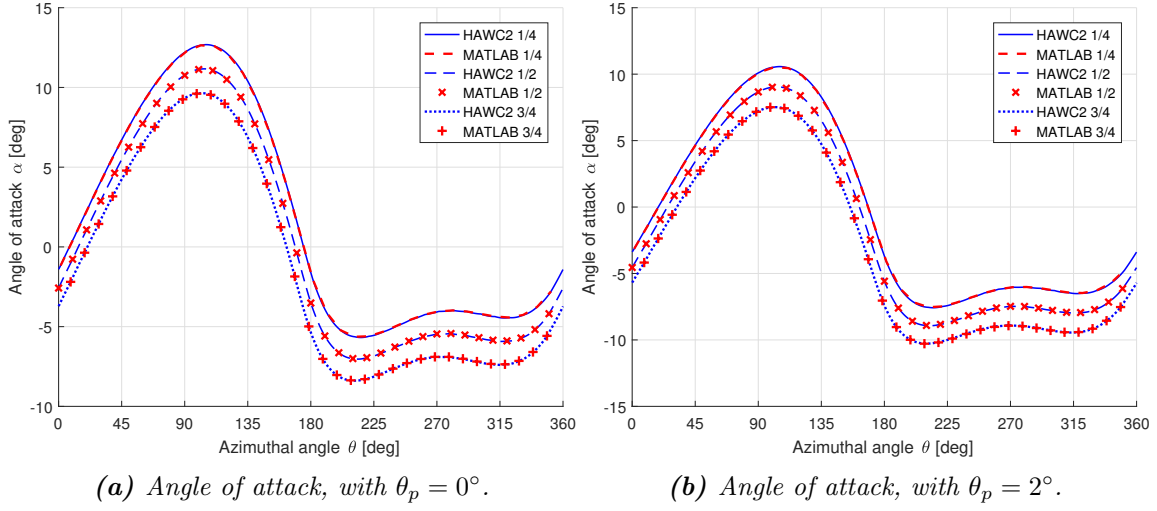


Figure 3.19: Validation of the implementation with the angle of attack against the HAWC2 code for different mounting points, with $\lambda = 4$, $\sigma = 0.1$, $B=2$.

will be used for the validation because it is directly related to V_n and V_t , which could then validate Equation (3.129) and (3.130).

Firstly, the zero-pitch angle case is validated and the results of the angle of attack are plotted in Figure 3.19(a). From the figure, it could be concluded that the both the aforementioned modification and the HAWC2 code can model the difference between the mounting point and the evaluation point because the two models are having the identical results. However, there is no explicit distinguish between the two points in the literature and manual for the HAWC2 code, the two points might have been implicitly distinguished with the vector transformations as in [25] since the HAWC2 is a multibody code itself. To be noted that the induced velocities in x - and y -directions are also validated to have the same results but will not be plotted here for concision.

Secondly, the case with constant pitch angle is validated with a constant 2° pitch angle applied for all the three cases above. The results from the MATLAB code as well as the HAWC2 code are calculated and compared in Figure 3.19(b). From the figure, it could be concluded that the constant pitch angle is implemented correctly in the MATLAB code. To be noted that for the case that the mounting point is at the half chord point which is coincided with the evaluation point, the model is then identical to that without the consideration of the difference of the two points of M and E . It could then validate that the pitch angle in Equation (3.27) is also correctly implemented.

From mounting location to constant pitch

The difference between the mounting point and the evaluation point could be directly linked to an additional constant pitch angle, the relationship is obtained as follows. For simplicity, it is assumed that the rotor is counter-clockwise rotating for all the cases.

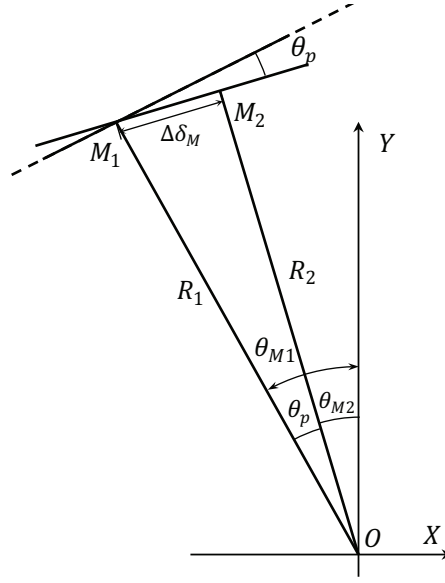


Figure 3.20: Relate the mounting location to a constant pitch angle.

As demonstrated in Figure 3.20, the airfoil is mounted at point M_1 with zero pitch angle for the case 1. And for the case 2, another airfoil is also mounted at the point M_1 with a constant pitch angle of θ_p . The line of $O-M_2$ is perpendicular to the airfoil of the case 2, and it could then be considered that the airfoil of the case 2 is mounted at the point M_2 with zero pitch angle and with the same angular velocity as case 1. The distance from the leading edge to the point M_1 and M_2 are noted as δ_{M1} and δ_{M2} respectively. The distance between the two mounting points is then the difference between the two variables.

$$\Delta\delta_M = \delta_{M2} - \delta_{M1} \quad (3.142)$$

The pitch angle then equals to the inverse trigonometric function of arcsine according to Figure 3.20.

$$\theta_p = \sin^{-1} \frac{\Delta\delta_M}{R_1} \quad (3.143)$$

The radius of the rotor for the case 2 will be different with the case 1 with following relationship.

$$R_2 = R_1 \cos \theta_p \quad (3.144)$$

To sum up, there will be three effects with different mounting points.

- Firstly, there will be a difference of the radius with Equation (3.144).
- Secondly, there will be an additional pitch angle with Equation (3.143).
- Thirdly, there will be a phase different of the azimuthal angle. For the cases above that the rotors are counter-clockwise rotating, the rotor of case 2 will have lag in phase which equals to the pitch angle of θ_p .

For example, if the case 1 is a two bladed VAWT with the solidity of 0.1 mounted at the quarter chord point with zero pitch angle, the corresponding case 2 rotor that mounted at the three-quarter chord point will have a phase lag of 2.87° , and the relative difference of the two radii is:

$$\frac{R_1 - R_2}{R_1} = 1.25 \times 10^{-3} \quad (3.145)$$

To be noted that letting the chord length to be identical but with different radius, there will be different solidity and tip speed ratio for the two cases. However, since the difference of the radius is very small and could be neglected, the difference of the solidity and tip speed ratio of the two cases could then also be neglected.

The influence of the mounting point is then the pitch angle and the phase difference. To be noted that according to Ferreira [12], for the inviscid flow, a constant pitch angle will only transport the loadings between the windward and the leeward part which will not influence the total power coefficient. As a result, changing the mounting point will also not influence the total aerodynamic power for the inviscid flow condition.

3.4 Validation against the panel code

The AC model and the extensions which are introduced previously in this chapter should then be validated with the results from the panel code of U2DiVA. The validation will show the performance of the current AC model and also indicate whether the model requires further improvements.

3.4.1 The choice of airfoil and airfoil polar

The choice of the airfoil for the validation with panel code is the NACA0015 airfoil which is consistent with the validation of the implementation of the AC model with the result from HAWC2 code as in section 3.2. The details about the airfoil polar are explained as follows.

Importance of correct airfoil polar

It is important to obtain the correct airfoil polar for the validation with panel code and the reason is explained as follows. For the validation of the implementation of the AC model with HAWC2 code, there are no specific requirements for the airfoil polar. If the AC models implemented in the MATLAB code is identical with that in the HAWC2 code, the results from the two models will be identical with each other, as long as the input airfoil polar is the same. However, for the panel code, the aerodynamic forces are directly calculated from the pressure forces which are determined from the velocity potential according to the bound and shed vortices in the flow field. The lift and drag forces are not determined from a look-up table according to the angle of attack as that used in the AC model. As a result,

the airfoil polar obtained from the panel code is dependent on the airfoil shape data and is not able to use an arbitrary polar as the validation with the HAWC2 code. As a result, it is necessary to determine the airfoil polar and use it as the input of the AC model for the validation.

Inviscid NACA0015 airfoil polar

According to Ferreira [13], the inviscid airfoil polar for the NACA0015 airfoil is as below.

$$C_L = 2\pi \times 1.11 \sin \alpha \quad (3.146)$$

$$C_d = 0 \quad (3.147)$$

The Equation (3.146) of the lift coefficient is different from the theoretical lift coefficient for an infinitely thin airfoil which is also called flat plate with the explicit form as follows [23].

$$C_L = 2\pi\alpha \quad (3.148)$$

There are two differences for the lift coefficient polar. The first one is there is a factor of 1.11 for the NACA0015 airfoil in Equation (3.146). The second difference is the lift coefficient is proportional to the sine value of the angle of attack for the NACA0015 airfoil, while the flat plate is linearly proportional to the angle of attack. The above two differences are due to the finite thickness of the airfoil of NACA0015.

Verification

In order to verify the inviscid lift coefficient of Equation (3.146) for the NACA0015 airfoil, the steady lift coefficient for the angle of attack from 0° to 20° with the spacing of 2° are calculated with the panel code of U2DiVA. In order to obtain the steady solution of lift coefficients, one simulation should correspond to one angle of attack. And the simulation time is set to be long enough to let the wake to be fully developed. The results are plotted together with the Equation (3.146) and (3.148) in the Figure 3.21(a). And the zero drag condition is also validated in Figure 3.21(b).

From the figure, it could be visualised that the result from the panel code of U2DiVA is having a very good agreement with Equation (3.146). However, the result will have a relatively large deviation with the theoretical lift coefficient of the flat plate with Equation (3.148). As a result, the inviscid lift coefficient is verified to be Equation (3.146) which is then used for the validation in this section. Despite the drag coefficient is not exactly equal to zero, the value is very small which is only 5×10^{-4} when the angle of attack of 20° and can be neglected. Thus the Equation (3.147) is also verified.

3.4.2 Power coefficient and thrust coefficient

The total performance of the rotor could be represented by the power coefficient and thrust coefficient. As a result, the performance of the two AC models are validated by comparing

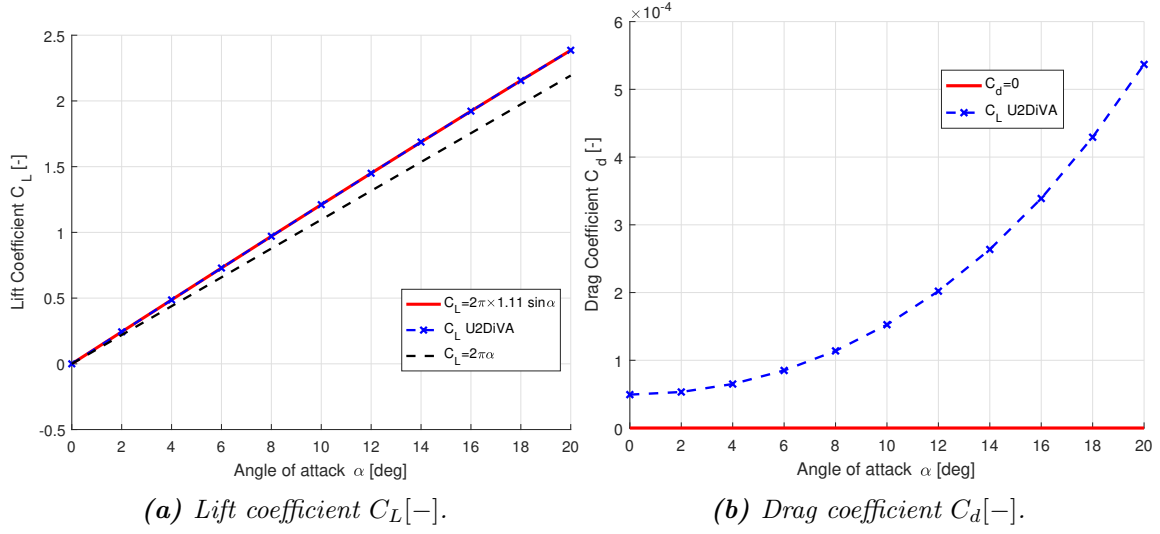


Figure 3.21: Verification of the NACA0015 airfoil polar for the inviscid flow with panel code.

the thrust and power coefficient with that from the panel code for different cases of solidity and tip speed ratios, the results are plotted in Figure 3.22.

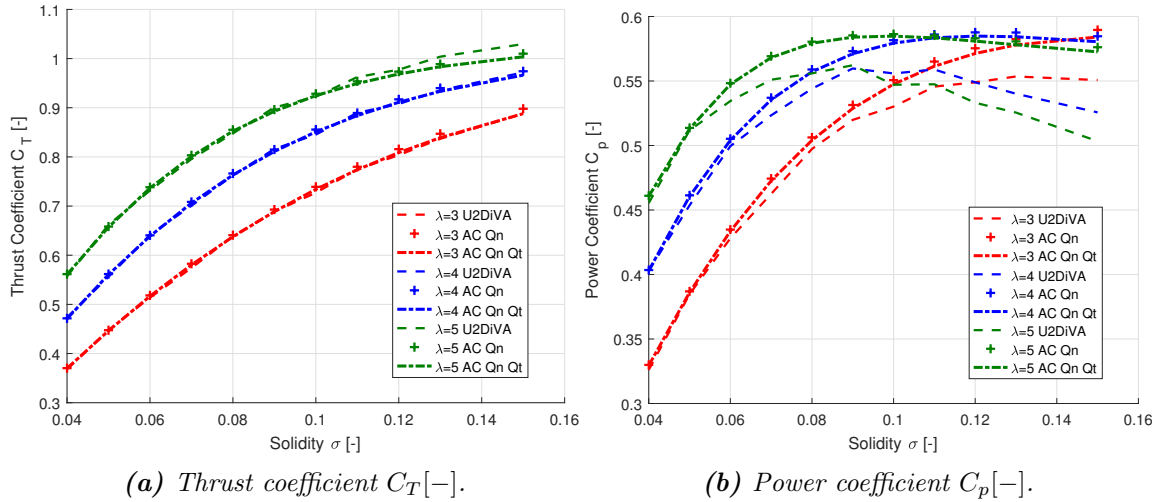


Figure 3.22: Validation of thrust coefficient and power coefficient for different tip speed ratio and solidity.

Thrust coefficient

For the AC model, the thrust coefficient is calculated with Equation (3.51). For the panel code, the aerodynamic forces in x - and y -direction are obtained for different azimuthal locations. The thrust coefficient is then the non-dimensioned averaged aerodynamic force in x -direction in one revolution. From Figure 3.22(a), it could be visualised that the thrust coefficient calculated from the two AC models are having good agreements with

the result from the panel code. The thrust coefficient from Cheng's AC model is slightly lower than that from the original AC model which indicates that the influence of the tangential loadings on the induced velocities will not have significant influences on the thrust coefficient. For the cases that the rotor is not heavily loaded, which corresponds to $C_T < 1$, the two AC models slightly over estimates the thrust coefficient compared with that from the panel code. And for the cases that the rotor is heavily loaded, with $C_T > 1$, the two AC models will slightly underestimate the thrust coefficient.

Power Coefficient

For the AC model, with the tangential loadings located on the AC, the power coefficient could be calculated with the following equation, the derivation is detailed in Appendix A.1.2.

$$C_p = \lambda \int_0^{2\pi} Q_t(\theta) d\theta \quad (3.149)$$

For the panel code, there will be both aerodynamic forces and aerodynamic torque at the aerodynamic centre of quarter chord point. The aerodynamic torque M with respect to the rotational axis is firstly calculated. Secondly, the aerodynamic power is calculated with Equation (A.10). Thirdly, the mean aerodynamic of the whole rotor in one revolution is calculated with Equation (A.12) and non-dimensioned with Equation (A.13) to be the mean power coefficient of the rotor in one revolution. The method mentioned above is used to calculate the power coefficient from the panel code for the validation in this report if not explicitly stated.

There is also another method to calculate the power coefficient from the panel code. When evaluating the tangential loadings Q_t from the AC model against the panel code, the tangential loading from the panel code is calculated by vector projection of the aerodynamic forces in the tangential direction with respect to the rotor and then non-dimensioned. When using the calculated tangential loading Q_t to calculate the power coefficient with Equation (3.149), the contribution of the aerodynamic torque at the aerodynamic centre is then neglected. The power coefficient calculated from this method will then deviate from the real one calculated from the previous method. This will be investigated in subsection 7.4.1.

From Figure 3.22(b), it could be visualised that the two AC models overestimate the power coefficients compare to the panel code. The difference will increase with the increase of the thrust coefficient. For the case of $\lambda = 3$ and $\sigma = 0.07$, the relative error is about 1.5%. However, for the heavily loaded case of $\lambda = 5$ and $\sigma = 0.15$, the relative error will be 7% which is too large for sufficient estimation. The Cheng's AC model also underestimates the power coefficient compared to the original AC model. As a result, the results from Cheng's AC model will then have slightly better agreements with that from the panel code.

Summarise the thrust and power coefficient

To sum up, the thrust coefficient could be well modelled with the AC model and is having good agreement with the panel code. However, the two AC models will overestimate the power coefficient compared to the result from panel code, and the over estimation is significant when the rotor is heavily loaded. It could also be concluded that considering the influence of the tangential loadings on the induced velocities will only have little influence on the thrust and power coefficient. Thus it is not the reason for the overestimation of power coefficient.

3.4.3 Detailed validation against panel code

For the detailed validation of the AC model with the panel code, the results of induced velocities, loadings, angle of attack and relative wind speed are calculated from the original AC model as well as the Cheng's modified AC model and compared with that from the panel code. The results for a typical two-bladed counter-clockwise VAWT are plotted in Figure 3.23. The mounting point is the quarter chord point, and the variables from the panel code for the validation are also calculated at the quarter chord point. The results for other operational conditions are also calculated and are plotted in Figure B.1 and B.2 in the Appendix B.

From Figure 3.23(a) and (b), it could be visualised that magnitude of the induced velocity in x -direction is significantly underestimated by the AC model near the azimuthal angle of 0° and 180° which are the connection between the windward and the leeward part of the rotor. And the magnitude of the induced velocity in y -direction is overestimated by the AC model at the azimuthal angle between 100° and 250° . According to Figure 3.23(c) and (d), it could be visualised that for curve of the normal loadings calculated from the AC model, there is a general downward *shift* compared to the result from the panel code. The magnitude of the tangential loading is generally underestimated by the AC model in the windward part and is generally overestimated by the AC model in the leeward part. This could be considered as a transfer between the windward part and the leeward part. For the angle of attack and the relative wind speed that plotted in Figure 3.23 (e) and (f), the result of the angle of attack from the two AC models are having generally good agreements with that from the panel code especially in the windward part. The relative wind speed calculated from the two AC models underestimate the magnitude near the azimuthal angle of $\theta = 180^\circ$ and there is an overestimation near the azimuthal angle of $\theta = 0^\circ$. This could be due to the underestimation of the magnitude of induced velocity in x - and y -directions near these two locations which are the connection between the windward and the leeward part of the AC.

Comparing the results from the original AC model and the Cheng's AC model, there is not much difference between the two results. It seems that the angle of attack from the Cheng's AC model is having better agreement with the panel code and the trend of the tangential loading could be modelled better than the original AC model. However, it is still premature here to conclude which model is better, because neither of the current two models could have good agreements of normal and tangential loadings with that from the

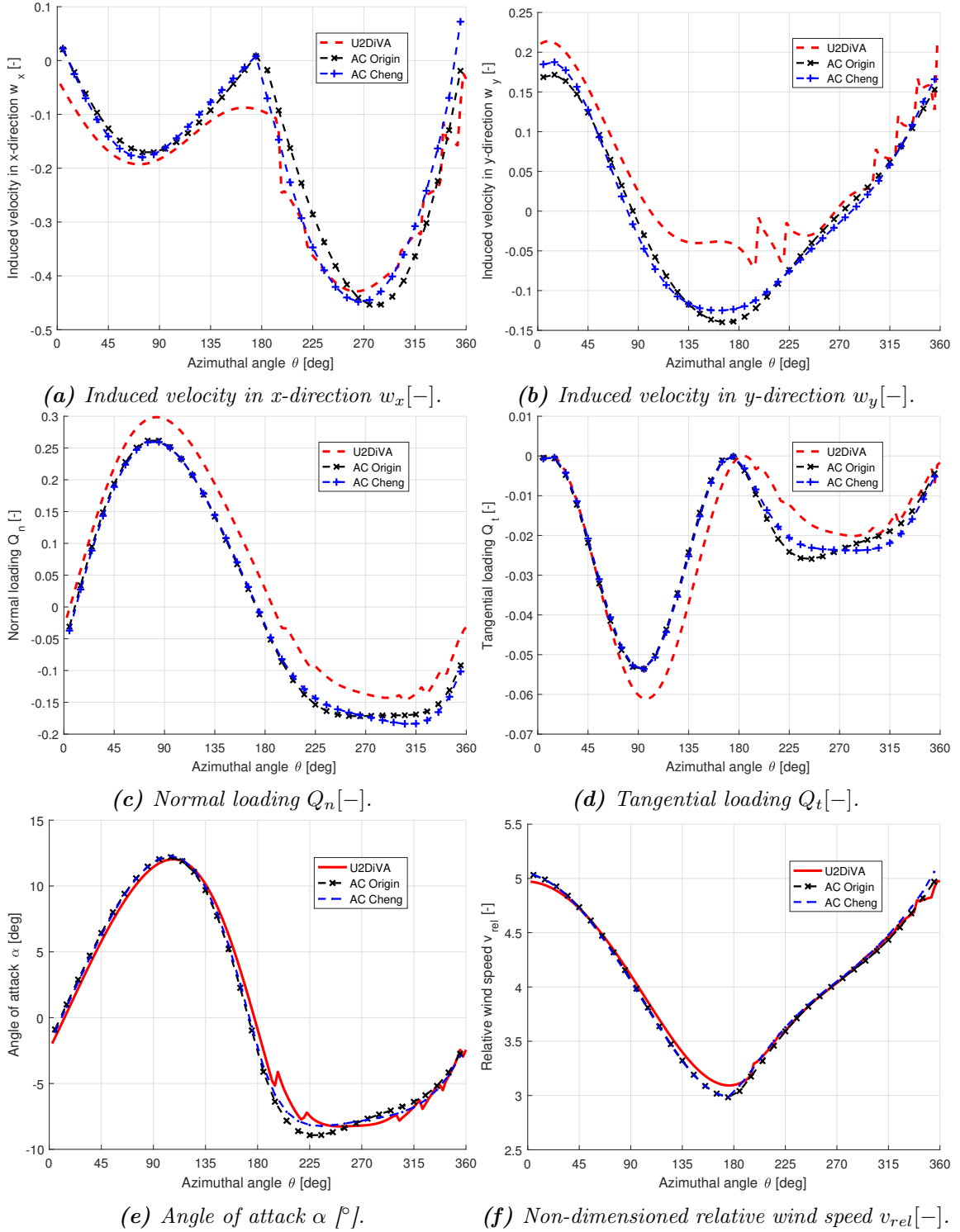


Figure 3.23: Validation of the AC model with the panel code, with $\lambda = 4$, $\sigma = 0.07$, $B = 2$, $\theta_p = 0$, mounted at $1/4c$.

panel code.

It should be noted that the most important results from the calculation should be the normal and tangential loadings because they are dominant for the design, optimisation and evaluation of the VAWT. The normal and tangential loadings are also directly linked to the thrust coefficient and the power coefficient. Even though the result of the total power and thrust coefficients match well with the AC model according to Figure 3.22, those two variables only represent the total performance of the rotor which is the averaged value for the whole rotor. The reason for there is still good agreements of the thrust coefficient and power coefficient with that from the panel code could be due to the errors are cancelled out during the averaging for the whole rotor. However, the significant difference of the loadings as in Figure 3.23(c) and (d) indicate the current AC models is not sufficient for the designing and optimisation purposes of the VAWT.

3.4.4 Reasons of loading deviations

In order to investigate the reason of the deviation of the normal and tangential loadings calculated from the AC methods with that from the panel code, the lift and drag coefficient are then calculated from both methods and are plotted against the angle of attack in Figure 3.24. To be noted that only the original AC model is used for validation instead of using both two AC models to make the figures more clearly.

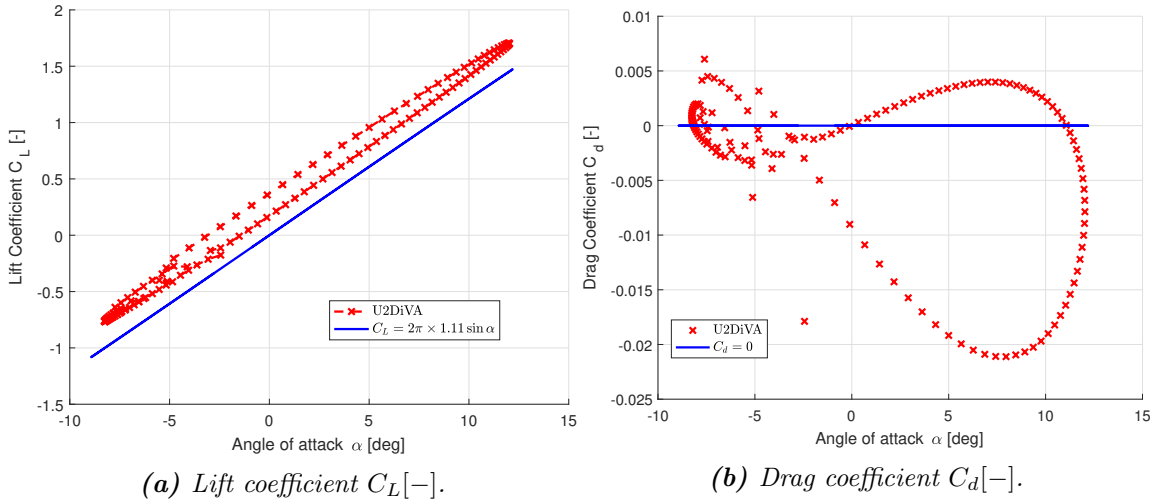


Figure 3.24: Validate the inviscid lift and drag coefficient used in the AC model against that calculated from the panel code.

From the Figure 3.24, two effects could be observed which are the flow curvature effect and the unsteady aerodynamic effects.

- The curve of the lift coefficient from the panel code has a generally up-shift compare to the inviscid airfoil polar with the Equation (3.146) which is used in the AC model. This could be due to the flow curvature effect because the flow properties at different locations on the airfoil will be different according to Migliore [33].

- There is a lag effect of the lift coefficient calculated from the panel code whose shape is a loop instead of the almost linear relationship corresponding to the steady lift curve. This effect corresponds to the unsteady aerodynamics of the airfoil which is due to the azimuthal variation of the angle of attack and relative wind speed in one revolution. This could also be visualised by the non-zero value of the drag coefficient which forms a horizontal asymmetric ‘8’ shaped loop due to the lag effects.

3.4.5 Possible improvements

According to previously in this section, the current AC models could model the total performance of the rotor well especially for the not heavily loaded rotor. However, the normal and tangential loadings could not be sufficiently predicted by the current AC models. The reason has been determined to be two effects which are the flow curvature and unsteady aerodynamic effects. If the two effects of the VAWT could be sufficiently modelled and included in the AC model, the modified AC model will then have the potential to let the normal and tangential loadings from the AC model to have better agreements with that from the panel code. Thus, the AC models will then be a more sufficient tool for the calculation of the VAWT.

3.5 Conclusions of the chapter

In this chapter, the detailed implementation method of the Actuator Cylinder model has been described with the validation with the HAWC2 code. Some important aspects of the model are also investigated. And finally, the performance of the AC model is validated with the panel code. The main conclusions of this chapter are listed as below.

- With the validation of the implementation of the AC model with Mod-Lin correction with the HAWC2 code, the results not only indicated the AC model is implemented correctly in the MATLAB code but also discovered the method that actually used in the HAWC2 code for the implementation of the AC model. In the HAWC2 code, the aerodynamic centre is set to be at the half chord point of the airfoil, and the discretization method of the AC is different from what claimed by [25].
- The induced velocities from the Cheng’s AC model are different from that from the original AC model, and the reason is the Cheng’s AC model takes into account the contribution due to both normal and tangential loadings, instead of only the normal loadings as the original AC model. The converged solutions of the normal and tangential loadings as well as the angle of attack calculated from the two models are almost identical in the windward part and are having some difference in the leeward part.
- The matrix formulation of the induced velocities is also derived for both the original AC model and Cheng’s AC model, which clarifies the relationship between the influence coefficients and the induced velocities.

- The mirror effect of the VAWT rotor indicates the relationship between the counter-clockwise rotating rotor and the corresponding clockwise rotating rotor, which could be used as a tool for the verification of the implementation. The value of the variables on one rotor will be identical to that on the mirrored point of the identical rotor with different rotational direction. Thus, the performance of the rotor is independent of the rotational direction setup.
- The additional wake terms in the equation of the induced velocity in x -direction for the control points are dependent on the direction of the shift of the control points with respect to the AC. The explicit form of the additional wake terms is derived for the conditions that the control points on the windward or leeward part that moves to be just inside or outside of the AC. This enables different methods of implementing the AC model with the control points could be moved either just outside or inside the AC.
- The induced velocity calculated from the original AC model is continuous when passing the AC. For the Cheng's AC model, the induced velocity due to the contribution of the normal loadings is continuous when passing the AC, while the components due to the tangential loadings are not continuous. The discontinuity of the induced velocities is only due to the tangential loading in the tangential direction.
- The condition that the mounting point of the VAWT blade does not coincide with the aerodynamic centre is also modelled by implementing a modification to distinguish the two points. The modification is verified with the results from the HAWC2 code which also indicates that the HAWC2 code is also able to model this effect. Besides, it is derived that changing the mounting point is equivalent to applying an additional constant pitch angle and having a lead of phase with this pitch angle. There will also be a slight change of the radius which could be neglected.
- The thrust coefficients from the two AC models are close to each other and are having good agreements with that from the panel code when the rotor is not heavily loaded, with $C_T < 1$. And the AC models will underestimate the thrust coefficient when the rotor is heavily loaded, with $C_T > 1$. The two AC models will over estimate the power coefficient while the Cheng's AC model is having slightly better agreements with the panel code.
- The normal and tangential loadings from the two AC models are not having good agreements with that from the panel code. There is transfer of the values of the loadings between the windward and leeward part of the AC. The reason for the deviation is because of the flow curvature effect, and the unsteady aerodynamics are not modelled in the current AC models. There is then the possibility to improve the AC model by modelling the aforementioned two effects.

Simplifications and analytical Solutions

In this chapter, a simplified method is developed by the author in order to calculate the integral in the influence coefficient analytically instead of using numerical integration method. The analytical solution of the induced velocity in x -direction due to arbitrary normal loading form is also derived. The properties of the influence coefficients are also obtained. This will result in a decrease of the computational efforts and will also help to have a more clear physical representation of the influence coefficient as well as the relationship of induced velocity and the loadings in the AC model.

4.1 Analytical solutions of influence coefficients

In this section, there will be the derivation of the analytical solution of the influence coefficient of I_1 and I_2 , the derivation is done with the polar coordinate system which will then be firstly introduced.

4.1.1 Transformation to polar coordinate system

The derivation of the analytical solution relies on the polar coordinate system which is due to the circular shape of the Actuator Cylinder. The explicit equation of the influence coefficient is in non-dimensioned Cartesian coordinate system of (x, y) . As a result, the non-dimensioned coordinate of the location to be evaluated (x, y) should then be transformed to the non-dimensioned polar coordinate of (r, β) where r is the non-dimensioned distance from the point to be evaluated to the centre of the AC and the β is the azimuthal angle of this point which is defined the same way as in the original AC model by Madsen [32].

The transformation from the polar coordinate system to Cartesian coordinate system is given in Equation (3.3) and (3.4), but the backwards transformation from the Cartesian coordinate system to the polar coordinate system is not given. The method of backwards transformation is dependent on the Inverse trigonometric function, and the detail will be in the Appendix A.2, attention should be made to the domain of definition and the range of the inverse trigonometric function.

4.1.2 Analytical solution of I_1

Firstly, the analytical solution of the influence coefficient of I_1 is derived. The influence coefficient $I_1(x, y)$ in Equation (3.17) is corresponding to the influence of loadings on the section number i of the AC on the induced velocity at the point (x, y) in the flow field. In order to calculate the analytical solution of the $I_1(x, y)$, the coordinate (x, y) should be transformed into the polar coordinate system (r, θ) with the coordinate of (r, β) . The transformation method is given in the Appendix A.2. Substitute the variables of x and y in Equation (3.17) with the polar coordinate of (r, β) , the explicit form of the influence coefficient of $I_{1,i}(r, \beta)$ is then as follows. It represents the influence of the loading at section number i of the AC on the induced velocity at the location with the polar coordinate of (r, β) .

$$I_{1,i}(r, \beta) = \int_{\theta_i - \frac{1}{2}\Delta\theta}^{\theta_i + \frac{1}{2}\Delta\theta} \frac{r \cos(\phi - \beta) - 1}{r^2 - 2r \cos(\phi - \beta) + 1} d\phi \quad (4.1)$$

The equation could then be further simplified by letting $\varphi = \phi - \beta$, to be noted that the value of β is constant during the integration.

$$I_{1,i}(r, \varphi) = \int_{\theta_i - \beta - \frac{1}{2}\Delta\theta}^{\theta_i - \beta + \frac{1}{2}\Delta\theta} \frac{r \cos \varphi - 1}{r^2 - 2r \cos \varphi + 1} d\varphi \quad (4.2)$$

Let the function to be integrated which is called the integrand noted as $f_1(r, \varphi)$, the explicit form is then as follows.

$$f_1(r, \varphi) = \frac{r \cos \varphi - 1}{r^2 - 2r \cos \varphi + 1} \quad (4.3)$$

The indefinite integral of $f_1(r, \varphi)$ which is noted as $I_{1in}(r, \varphi)$ is then defined as below.

$$I_{1in}(r, \varphi) = \int f_1(r, \varphi) d\varphi \quad (4.4)$$

There will be singularity problem for the indefinite integral with the condition of $\varphi = 0$. By assuming that $\varphi \neq 0$, the indefinite integral could be derived analytically to be:

$$I_{1in}(r, \varphi) = -\tan^{-1} \left(\frac{r-1}{r+1} \cot \frac{\varphi}{2} \right) - \frac{\varphi}{2} + C_1 \quad , \quad \varphi \neq 0 \quad (4.5)$$

In order to calculate the definite integral as Equation (4.2), there will be two different cases which are whether the point of $\varphi = 0$ is inside or outside the integration interval of $[\theta_i - \beta - \frac{1}{2}\Delta\theta, \theta_i - \beta + \frac{1}{2}\Delta\theta]$.

- If the singular point of $\varphi = 0$ is outside of the integration interval $[\theta_i - \beta - \frac{1}{2}\Delta\theta, \theta_i - \beta + \frac{1}{2}\Delta\theta]$, which means that the condition of $\varphi \neq 0$ is satisfied throughout the region. This is equivalent to the condition for the azimuthal angle of β satisfies $\beta < \theta_i - \frac{1}{2}\Delta\theta$ or $\beta > \theta_i + \frac{1}{2}\Delta\theta$. For this case, the influence coefficient could then be directly calculated from the analytical solution of the indefinite integral with Equation (4.5) as follows.

$$I_{1,i}(r, \beta) = I_{1in}(r, \theta_i - \beta + \frac{1}{2}\Delta\theta) - I_{1in}(r, \theta_i - \beta - \frac{1}{2}\Delta\theta) \quad (4.6)$$

- If the singular point of $\varphi = 0$ is inside the integration region $[\theta_i - \beta - \frac{1}{2}\Delta\theta, \theta_i - \beta + \frac{1}{2}\Delta\theta]$ which means that the condition of $\varphi \neq 0$ is not satisfied throughout the region. This is equivalent to the condition that the azimuthal angle of β satisfies $\theta_i - \frac{1}{2}\Delta\theta < \beta < \theta_i + \frac{1}{2}\Delta\theta$. For this case, the issues due to the singularity point should be specially considered. The integral could be calculated with the Cauchy principal value of the integration and the detailed derivation is in the Appendix A.3.

$$I_{1,i}(r, \beta) = \begin{cases} I_{1in}(r, \theta_i - \beta + \frac{1}{2}\Delta\theta) - I_{1in}(r, \theta_i - \beta - \frac{1}{2}\Delta\theta) + \pi & , r > 1 \\ I_{1in}(r, \theta_i - \beta + \frac{1}{2}\Delta\theta) - I_{1in}(r, \theta_i - \beta - \frac{1}{2}\Delta\theta) - \pi & , r < 1 \end{cases} \quad (4.7)$$

There is singularity for the condition of $r = 1$ which could not be calculated analytically. The continuity of the induced velocities when passing the AC which is the condition of $r = 1$ will be discussed in section 4.2.3.

4.1.3 Analytical solution of I_2

Secondly, the analytical solution of the influence coefficient of I_2 is also derived. Similar to the derivation of the analytical solution of I_1 as above, the variable of x and y in Equation (3.18) is substituted with the polar coordinate of (r, β) and the explicit form of the influence coefficient of $I_{2,i}(r, \beta)$ is then as follows. To be noted that the definition of i , r and β are consistent with that in Equation (4.1) and the influence coefficient of $I_{2,i}(r, \beta)$ represents the influence of the loading at section number i of the AC on the induced velocity at location of (r, β) .

$$I_{2,i}(r, \beta) = \int_{\theta_i - \frac{1}{2}\Delta\theta}^{\theta_i + \frac{1}{2}\Delta\theta} \frac{r \sin(\phi - \beta) - 1}{r^2 - 2r \cos(\phi - \beta) + 1} d\phi \quad (4.8)$$

Similar to Equation (4.8), the above equation could also be simplified by letting $\varphi = \phi - \beta$.

$$I_{2,i}(r, \varphi) = \int_{\theta_i - \beta - \frac{1}{2}\Delta\theta}^{\theta_i - \beta + \frac{1}{2}\Delta\theta} \frac{r \sin \varphi - 1}{r^2 - 2r \cos \varphi + 1} d\varphi \quad (4.9)$$

Let the integrand of the above function noted as $f_2(r, \varphi)$ and the explicit form is as follows.

$$f_2(r, \varphi) = \frac{r \sin \varphi - 1}{r^2 - 2r \cos \varphi + 1} \quad (4.10)$$

The indefinite integral of $f_2(r, \varphi)$ is noted as $I_{2in}(r, \varphi)$ and could be derived to be as below.

$$I_{2in}(r, \varphi) = -\frac{1}{2} \log(r^2 - 2r \cos \varphi + 1) + C_2 \quad (4.11)$$

In the above equation, the function \log stands for the Natural logarithm. Thus the condition of $r^2 - 2r \cos \varphi + 1 > 0$ should be satisfied. And this condition is violated only when $r = 1$ and $\varphi = 0$ and if the control points are moved to be just inside or outside of the AC, this point will be not reached. As a result, it is not necessary to consider the special case of the singularity point, and the analytical solution of the influence coefficient of I_2 could then be calculated as follows.

$$I_{2,i}(r, \beta) = I_{2in}(r, \theta_i - \beta + \frac{1}{2}\Delta\theta) - I_{2in}(r, \theta_i - \beta - \frac{1}{2}\Delta\theta), \quad r \neq 1 \quad (4.12)$$

4.1.4 Analytical solution of I_1 for control points

In order to obtain the converged solution from the AC model, it is necessary to calculate the induced velocities on the control points of the AC, which then requires the influence coefficient on the control points to be calculated. For the control points on the AC, the condition corresponds to $r = 1$ in Equation (4.1). However, there is singularity problem for the condition that the control points are on the AC, with $r = 1$. To prevent the singularity problem, the control points are assumed to be moved just outside or inside of the AC model for the numerical integration.

In this section, the analytical solution of the influence coefficient of $I_{1,j,i}$ for the control points will be derived. There will be two different conditions which corresponds to the two conditions in the subsection 4.1.2 and will be considered separately as follows.

- For the condition of $i \neq j$ which means the influence coefficient of $I_{1,j,i}$ corresponds to the influence at the control point j due to loadings on control point i which is different from point j . As a result, the condition of $\varphi \neq 0$ is then satisfied in Equation (4.2), there will be no singularity problem. Thus, the condition of $r = 1$ could be applied in Equation (4.5), the indefinite integral could then be derived as follows.

$$I_{1in}(r, \varphi) = -\frac{1}{2}\varphi + C_1, \varphi \neq 0 \quad (4.13)$$

The influence coefficient of $I_{1,j,i}$ could then be calculated as follows.

$$I_{1,j,i} = I_{1in}(1, \theta_i - \theta_j + \frac{1}{2}\Delta\theta) - I_{1in}(1, \theta_i - \theta_j - \frac{1}{2}\Delta\theta) = -\frac{1}{2}\Delta\theta \quad (4.14)$$

- For the condition of $i = j$ which means that the influence coefficient of $I_{1,j,i}$ corresponds to the influence at the control point j due to the loading at the point itself. And then the condition of $\varphi \neq 0$ will not be satisfied throughout the integration interval in Equation (4.2). As a result, the condition of $r = 1$ could not be applied in Equation (4.5). The control point should then be shifted to be just inside or outside the AC as explained before.

- For the case of moving the control point j to be just outside the AC, apply $r = 1 + 0^+$ in Equation (4.7), the influence coefficient is then as follows.

$$I_{1,j,i} = \pi - \frac{1}{2}\Delta\theta \quad (4.15)$$

- For the case of moving the control point j to be just inside the AC, the variable of r is then $r = 1 + 0^-$, the influence coefficient is then as follows according to Equation (4.7).

$$I_{1,j,i} = -\pi - \frac{1}{2}\Delta\theta \quad (4.16)$$

It could be concluded that it is not necessary to move all of the control points to be inside or outside of the AC to prevent singularities. It is only necessary to move the control point j when evaluating the influence of the loading on control point j inducing on itself.

4.2 Analytical solutions of w_x^n

With the analytical solution of the influence coefficient of I_1 at the control points, the analytical solution of induced velocity w_x^n could then be derived. The variable of w_x^n is the induced velocity in x -direction due to normal loading in the Cheng's AC model and is also the induced velocity on the control points in the x -direction in the original AC model which could be calculated with Equation (3.11).

4.2.1 Derivation of the analytical solution

Firstly, the derivation of the analytical solution of the induced velocity of w_x^n is presented here. It is assumed that for both windward and the leeward part, the control points are moved just outside of the AC when calculating the induced velocity at the control point j due to the loading at this control point which corresponds to the condition of $j = i$.

Windward part

For the windward part which corresponds to the condition of $j \leq N/2$, substitute the influence coefficient in Equation (3.11) with the analytical solution in Equation (4.14) and (4.15), the induced velocity in x -direction due to normal loading is then as follows.

$$w_{x,j}^n = -\frac{1}{2\pi} \sum_{i=1}^N Q_{n,i} I_{1,j,i} = -\frac{1}{2} Q_{n,j} - \frac{1}{2\pi} \sum_{i=1}^N \left(-\frac{1}{2} Q_{n,i} \Delta\theta \right) \quad (4.17)$$

Substitute the azimuthal angular spacing $\Delta\theta$ with the definition in Equation (3.5), the analytical solution is then:

$$w_{x,j}^n = -\frac{1}{2} Q_{n,j} + \frac{1}{2N} \sum_{i=1}^N Q_{n,i} \quad (4.18)$$

The equation indicates that the induced velocity of w_x^n at the section number j in the windward part of the AC is dependent on the normal loadings at the control points of all sections. The second term in the equation could be further simplified with the mean value of the normal loading of the whole AC which is defined as follows.

$$\overline{Q}_n = \frac{1}{N} \sum_{i=1}^N Q_{n,i} \quad (4.19)$$

By substituting Equation (4.19) into Equation (4.18), the analytical solution of w_x^n could be further simplified as follow.

$$w_{x,j}^n = -\frac{1}{2}(Q_{n,j} - \overline{Q}_n) \quad (4.20)$$

According to Equation (4.20), the analytical solution of the induced velocity of w_x^n for the control point j in the windward part is in a very simple form, which is equal to negative one half of the difference between the normal loading at this control point and the mean value of the normal loadings at all control points .

Leeward part

For the control points in the leeward part of the AC which corresponds to the condition of $j > N/2$, the analytical solution could be obtained with similar method as that for the case that the control point is in the windward part of the AC as above. By substituting the analytical solution of influence coefficient of Equation (4.14) and (4.15) into the Equation (3.11), will get the analytical solution of the induced velocities in x -direction due to normal loadings.

$$w_{x,j}^n = -\frac{1}{2}Q_{n,j} + \frac{1}{2N} \sum_{i=1}^N Q_{n,i} - Q_{n,N+1-j} \quad (4.21)$$

The equation could be simplified with the definition of the mean normal loading as Equation (4.19).

$$w_{x,j}^n = \frac{1}{2}Q_{n,j} + \frac{1}{2}\overline{Q}_n - Q_{n,N+1-j} \quad (4.22)$$

The equation of w_x^n for the leeward part is then in the different form as that for the windward part in Equation (4.20). As a result, the Equation (4.22) is then re-arranged to the form as below with the first term to be identical with that for the windward case.

$$w_{x,j}^n = -\frac{1}{2}(Q_{n,j} - \overline{Q}_n) - (Q_{n,N+1-j} - Q_{n,j}) \quad (4.23)$$

There will be an extra term compared with the Equation (4.20), which is the difference between the normal loadings at control point number j , which is the point to be evaluated in the leeward part, and number $(N+1-j)$, which is the corresponding control point in the windward part in the direct upstream of control point j with same value of y coordinate.

Difference between $w_{x,j}^n$ and $w_{x,N+1-j}^n$

For an arbitrary control point j in the windward part with $j \leq N/2$, there will be a control point $(N + 1 - j)$ in the leeward part in the direct downstream with point j with the same value of y . With the analytical solution of the induced velocity in x -direction at the control points due to normal loadings which has been derived above, the difference of w_x^n between two control points with the same value of y is then derived as below.

$$w_{x,j}^n - w_{x,N+1-j}^n = \frac{1}{2}(Q_{n,j} - Q_{n,N+1-j}) \quad (4.24)$$

From the equation above, it could be concluded that the difference of induced velocity of w_x^n for the two control point of j and $N + 1 - j$ with same y value is equal to one half of the difference of the normal loadings at the two control points.

4.2.2 Validation of the analytical solutions

The analytical solution of w_x^n derived previously in this section is named the *new* analytical solution and will be validated here with the analytical solutions of the induced velocity derived by Madsen [32]. The Madsen's analytical solutions are for a certain form of normal loading following a sine function as below. To be noted that the analytical solutions by Madsen are corresponding to the original AC model which could also be considered as the induced velocities due to the contribution of the normal loadings in the Cheng's AC model.

$$Q_n(\theta) = Q_{n,m} \sin \theta \quad (4.25)$$

For the validation, the induced velocity of w_x^n for the control points on the windward part and on the leeward part of the AC for the normal loading in the form of Equation (4.25) is calculated from both the Madsen's analytical solution and the *new* analytical solution derived in this report.

Madsen's analytical solutions

The analytical solution derived by Madsen [32] is corresponding to the induced velocity at an arbitrary point in the flow field with the load case of Equation (4.25). The analytical solution is a piecewise function with three pieces which correspond to the three different regions as defined in section 3.1. It has been verified by Madsen that this analytical solution of induced velocity is continuous when passing the AC. It has also been validated numerically in subsection 3.3.5 that w_x^n is continuous when passing the AC. As a result, the control points are then assumed to be just inside the AC for simplicity, because then only one of the three pieces in function is needed for all the control points in both windward

and leeward part of the AC. This analytical solution is as follows according to Madsen [32].

$$w_x^n = -Q_{n,m} \left(\frac{1}{2}x + \sqrt{1-y^2} \right) \quad (4.26)$$

The non-dimensioned coordinate of (x, y) in Equation (4.26) could be transformed to polar coordinates with Equation (3.3) and (3.4). And the condition of $r = 1$ is applied due to the continuity of the induced velocity of w_x^n . The analytical solution of w_x^n is then:

$$w_x^n = -Q_{n,m} \left(-\frac{1}{2} \sin \theta + \sqrt{1 - \cos^2 \theta} \right) \quad (4.27)$$

This equation could be further derived and transformed into a piecewise function for the windward and the leeward part of the AC, which corresponds to the azimuthal angle of $[0, \pi)$ and $[\pi, 2\pi)$ respectively, and is as follows.

$$w_x^n = \begin{cases} -\frac{1}{2}Q_{n,m} \sin \theta & , 0 < \theta \leq \pi \\ \frac{3}{2}Q_{n,m} \sin \theta & , \pi < \theta \leq 2\pi \end{cases} \quad (4.28)$$

New analytical solutions

The *new* analytical solution derived in this report is the induced velocity on the control points for an arbitrary form of the normal loadings, which is different from Madsen's analytical solutions. The analytical solution is also a piecewise function with the two pieces to be Equation (4.20) and (4.22).

$$w_{x,j}^n = \begin{cases} -\frac{1}{2}(Q_{n,j} - \overline{Q}_n) & , j < N/2 \\ \frac{1}{2}Q_{n,j} + \frac{1}{2}\overline{Q}_n - Q_{n,N+1-j} & , j \geq N/2 \end{cases} \quad (4.29)$$

The mean value of the normal loadings will be zero because the normal loadings is in the form of a sine function as Equation (4.25), which is also an odd function.

$$\overline{Q}_n = 0 \quad (4.30)$$

The normal loadings of $Q_{n,j}$ and $Q_{n,N+1-j}$ are then obtained from Equation (4.25) to be as follows.

$$Q_{n,j} = Q_{n,m} \sin \theta_j \quad (4.31)$$

$$Q_{n,N+1-j} = Q_{n,m} \sin(2\pi - \theta_j) = -Q_{n,m} \sin \theta_j \quad (4.32)$$

Subtracting Equation (4.30), (4.31) and (4.32) in Equation (4.29), the analytical solution of w_x^n could then be rewritten in the following form.

$$w_x^n(\theta_j) = \begin{cases} -\frac{1}{2}Q_{n,m} \sin \theta_j & , 0 < \theta_j \leq \pi \\ \frac{3}{2}Q_{n,m} \sin \theta_j & , \pi < \theta_j \leq 2\pi \end{cases} \quad (4.33)$$

The result is identical with that derived from Madsen's analytical solution in Equation (4.28). As a result, the *new* analytical solution of the induced velocity of w_x^n due to normal loadings in x -direction is validated.

4.2.3 Analytical validation of the continuity of w_x^n

The induced velocities in x -direction due to normal loadings have been verified numerically to be continuous when passing the AC. And the continuity is also verified with Madsen's analytical solution for the sine form of the normal loading as Equation (4.25). However, Madsen's analytical solution is only for a certain load case while the *new* analytical solution is able to calculate the induced velocity of w_x^n on the control points for an arbitrary normal loading distribution, which is then used for the validation of the continuity of w_x^n .

In the previous derivation of the *new* analytical solution of w_x^n , the control points are assumed to be just outside of the AC. And for the following validation, the control points now are assumed to be just inside of the AC. The continuity of w_x^n could then be validated by checking if the explicit form of the analytical solutions for the control points to be just inside the AC are identical to that of just outside of the AC, for the windward and leeward part respectively.

Windward part

For the control points in the windward part and are moved to be just inside the AC, the equation of the induced velocity could then be obtained with Equation (3.122).

$$w_{x,j}^n = -\frac{1}{2\pi} \sum_{i=1}^N Q_{n,i} I_{1,j,i} - Q_{n,j} \quad (4.34)$$

Since the control points are just inside the AC, substituting the influence coefficient of I_1 with the analytical solution in Equation (4.14) and (4.16), the Equation (4.34) is then as follows.

$$w_{x,j}^n = \frac{1}{2} Q_{n,j} - \frac{1}{2\pi} \sum_{i=1}^N \left(-\frac{1}{2} Q_{n,i} \Delta\theta \right) - Q_{n,j} \quad (4.35)$$

The equation could be further simplified with the mean normal loadings defined with Equation (4.19).

$$w_{x,j}^n = \frac{1}{2} (Q_{n,j} + \bar{Q}_n) - Q_{n,j} = -\frac{1}{2} (Q_{n,j} - \bar{Q}_n) \quad (4.36)$$

The Equation (4.36) is identical with Equation (4.20) which is with the control points moved just outside the AC. As a result, the induced velocity of w_x^n is verified analytically to be continuous when passing the windward part of the AC.

Leeward part

For the control points in the leeward part and are moved to be just inside the AC, the equation of the analytical solution could be obtained according to Equation (3.126).

$$w_{x,j}^n = -\frac{1}{2\pi} \sum_{i=1}^N Q_{n,i} I_{1,j,i} - Q_{n,N+1-j} \quad (4.37)$$

Similar to the windward case, the influence coefficient of I_1 is substituted with the analytical solution in Equation (4.14) and (4.16).

$$w_{x,j}^n = \frac{1}{2}Q_{n,j} - \frac{1}{2\pi} \sum_{i=1}^N \left(-\frac{1}{2}Q_{n,i}\Delta\theta \right) - Q_{n,N+1-j} \quad (4.38)$$

With the definition of mean normal loadings, the analytical solution of $w_{x,j}^n$ is then rewritten as follows.

$$w_{x,j}^n = \frac{1}{2}(Q_{n,j} + \overline{Q}_n) - Q_{n,N+1-j} \quad (4.39)$$

The Equation (4.39) is identical with Equation (4.22) which means the induced velocity of w_x^n is validated analytically to be continuous when passing the leeward part of the AC.

Comments on the continuity

The conclusion of the continuity of w_x^n from the analytical solution is consistent with that from the numerical validation in subsection 3.3.5. To be noted that the influence coefficient of $I_{1,j,j}$, which corresponds to the influence of the normal loading at control point j on the induced velocity of w_x^n at the control point itself, is not continuous and is having a jump of $\pm 2\pi$ when passing the AC depending on the direction. This discontinuity is eliminated by the extra terms of (*) and (**) in Equation (3.1), which results the induced velocity of w_x^n is continuous when passing the AC.

Because of the continuity of w_x^n when passing the AC, it is not necessary to really move the control points to be just inside or outside of the AC when calculating the induced velocity of w_x^n due to normal loadings. It is only necessary to *virtually* move the control points and then obtain the corresponding analytical solution of influence coefficient I_1 . The extra terms in Equation (3.1) should then be included depending on the direction of the *virtually* shift of the control points, and the analytical solution of induced velocity of w_x^n will be obtained.

4.2.4 Continuous analytical solution of w_x^n

The AC model was initially derived with continuous functions, and for the purpose of the numerical calculation that the AC is discretized into sections which are represented by the properties of the control points. The analytical solution of the induced velocity in x -direction due to the normal loadings is derived into a continuous function.

With the increase of the number of sections, the Equation (4.20) and (4.22) will approach that for the continuous function, and when the number of sections is infinitely large, the resulting induced velocity of w_x^n is then as below.

$$w_x^n(\theta) = \begin{cases} \frac{1}{2}(Q_n(\theta) + \overline{Q}_n), & 0 \leq \theta < \pi \\ \frac{1}{2}Q_n(\theta) + \frac{1}{2}\overline{Q}_n - Q_n(2\pi - \theta), & \pi \leq \theta < 2\pi \end{cases} \quad (4.40)$$

With the mean value of the normal loadings defined to be as follows.

$$\bar{Q}_n = \frac{1}{2\pi} \int_0^{2\pi} Q_n(\theta) d\theta \quad (4.41)$$

Similar to subsection 4.2.2, it could be verified that analytical solution of w_x^n for the sine form of normal loading in Equation (4.25) will also be identical with the analytical solution by Madsen.

4.3 Properties of the influence coefficients

With the analytical solution of the influence coefficients of I_1 and I_2 derived in the previous sections, the properties of the two influence coefficients of I_1 and I_2 as well as their impact on the induced velocities on the control points are investigated.

4.3.1 Influence coefficient I_1

Firstly, the properties of the influence coefficient of I_1 is investigated. For simplicity, the condition that the control points are moved just outside of the AC is assumed. When assembling the influence coefficient matrix of $\mathbf{D}_{x,n}$ with the influence coefficient of $I_{1,j,i}$, there will be $N \times N$ elements when the AC is discretized into N sections. For a certain control point j , the influence coefficient of $I_{1,j,i}$ only have two different conditions which correspond to two values with Equation (4.15) and (4.14). Thus, when assembling the j -th column of matrix $\mathbf{D}_{x,n}$, there will be only two values which correspond to the condition of $j = i$ and $j \neq i$. Furthermore, the explicit form of the analytical solution of the influence coefficient of I_1 is independent on j which means for any column, the elements will only have two possible values which are identical for all columns. As a result, it is not necessary to calculate $N \times N$ influence coefficients to assemble the matrix of $\mathbf{D}_{x,n}$, instead only two different values of the elements need to be calculated, and the matrix could be then assembled.

The impacts of the influence coefficient of I_1 on the induced velocity of w_x^n are then investigated for the windward and leeward part of the AC respectively.

Windward part

For the condition that the control points on the windward part of the AC and are moved just outside of the AC, there will be no extra terms in the equation of the induced velocity of w_x^n according to Equation (3.118). The influence coefficient of $I_{1,j,i}$ could then represent the weight of the contribution of the normal loading at control point i to the induced velocity of w_x^n at control point j . According to the analytical solution of $I_{1,j,i}$, the value is constant and equals to $-\frac{1}{2}\Delta\theta$ when $j \neq i$, and is equal to $\pi - \frac{1}{2}\Delta\theta$ when $j = i$. It could then be concluded that the contribution to w_x^n at control point j due to the normal loadings on

other control points are having the same weight, and weight of the contribution due to the normal loading on the control point itself is different and with much larger absolute value. The conclusion could also be obtained from the analytical solution of w_x^n in Equation (4.20) that the induced velocity of w_x^n is proportional to the difference of the normal loading on the control point to be evaluated and the mean value of the normal loadings for all the control points.

Leeward part

For the condition that the control points on the leeward part of the AC are moved just outside of the AC, the corresponding influence coefficient will have the same form as that in the windward part. However, two extra terms are needed for the induced velocity of w_x^n , then the influence coefficient could not fully represent the weight of the contribution to the induced velocity of w_x^n due to normal loadings. The property of w_x^n could then be determined by Equation (4.22). It could be concluded that the contribution due to the normal loadings at all other control points are with the same weight, except for the control point j which is itself and the control point $N + 1 - j$ which is the corresponding control point in the direct upstream of it. The weight of the contribution due to the normal loadings at the aforementioned two control points are having much larger absolute value than other control points.

4.3.2 Influence coefficient I_2

With the analytical solution of I_2 in Equation (4.12), three properties could be obtained and are listed as below.

- For the condition of $j = i$ or $j = N + 1 - i$, the influence coefficient of $I_{2,j,i}$ will be zero-valued.

$$I_{2,j,i} = 0 \quad , \text{ if } j = i \quad \text{ or } \quad j = N + 1 - i \quad (4.42)$$

This indicates that the induced velocity in y -direction due to normal loading w_y^n of a certain control point j is independent on the normal loading of this point j itself as well as the control point of $N + 1 - j$ which is having a 180° difference of azimuthal angle with respect to it.

- The influence coefficient of I_2 for the influence on control point j due to the loadings at the control point $j - k$ and $j + k$ will be additive inverses of each other.

$$I_{2,j,j-k} = -I_{2,j,j+k} \quad (4.43)$$

This indicates that the contribution of the induced velocity of w_y^n due to the normal loadings at two control points with the same distance with respect to the control point j to be evaluated will have the same weight but in different directions due to the difference of the sign.

- The influence coefficient of I_2 has the property of:

$$I_{2,j+1,i+1} = I_{2,j,i} \quad (4.44)$$

This indicates the relationship of the influence coefficient of I_2 for different control points.

According to Equation (3.73), the direct influence coefficient matrix of $\mathbf{A}_{y,n}$ is consist of $N \times N$ elements which could be assembled with influence coefficient of $I_{2,j,i}$ as Equation (3.80). According to the third property as above, it indicates that the elements in the $(j+1)$ -th of matrix $\mathbf{A}_{y,n}$ could be directly obtained from the elements in the j -th column. Repeating this process, the influence matrix of $\mathbf{A}_{y,n}$ could be obtained with one column of the matrix with the N elements instead of calculating the Equation (3.18) $N \times N$ times to get all elements for matrix $\mathbf{A}_{y,n}$. The number of the influence coefficients needed to be calculated could be further decreased to be $N/2$ because the second half of the column could be obtained from the additive inverses of the corresponding elements of the first half according to the second property as above. As a result, the assembly of the matrix $\mathbf{A}_{y,n}$ only needs $N/2$ different elements with some matrix assembly techniques.

4.4 Issues of numerical integration method

According to subsection 3.1.1, in order to avoid singularity problems, the control points are shifted about 0.1% to 1% to be just outside or inside of the AC. The integrals for the influence coefficients are calculated numerically by discretizing the region of integration into N_s sub-sections in the azimuthal direction. The numerical integration method such as rectangle method and trapezoidal rule could be used, and the former is used in Equation (3.19) and (3.20). For the numerical integration, there will be two issues which are the accuracy and convergence which will be discussed respectively as follows.

Accuracy of the method

The first issue is the accuracy of the numerical integration. With the increase of the number of sub-sections N_s for each integration region, the accuracy of the numerical integration will also increase. However, the computational efforts will also increase linearly with the number of sub-sections N_s , and will cost too much CPU-time when the number of sub-sections is too large.

As a result, the convergence study should be done for the numerical integration of the influence coefficient. According to the analytical solution in Equation (4.20) and (4.22), the influence coefficient of $I_{1,j,i}$ with the condition of $j = i$ is the most important for the induced velocities in x -direction due to normal loadings. As a result, the influence coefficient of $I_{1,j,j}$ is used for the convergence study. The scaling factor is chosen to be $f_o = 1 + \delta = 1.01$ and $f_i = 1 - \delta = 0.99$ representing moving the control point just outside

and inside respectively, and the corresponding analytical solutions could be calculated with Equation (4.5) and are as follows.

$$I_{1,analy,o} = I_{1,j,j} = -2 \tan^{-1} \left[\frac{\delta}{2+\delta} \cot \left(\frac{1}{4} \Delta \theta \right) \right] - \frac{1}{2} \Delta \theta \quad (4.45)$$

$$I_{1,analy,i} = I_{1,j,j} = 2 \tan^{-1} \left[\frac{\delta}{2-\delta} \cot \left(\frac{1}{4} \Delta \theta \right) \right] - \frac{1}{2} \Delta \theta \quad (4.46)$$

The relative error of the numerical solution $I_{1,num}$ with respect to the analytical solution of $I_{1,analy}$ is defined as below.

$$\epsilon = \left| \frac{I_{analy} - I_{1,num}}{I_{1,analy}} \right| \quad (4.47)$$

For the convergence study, the numerical solution $I_{1,num}$ is calculated for different number of sub-sections N_s in the region of integration, and the relative error is calculated and plotted against the number of sub-sections in the Log-log plot in Figure 4.1.

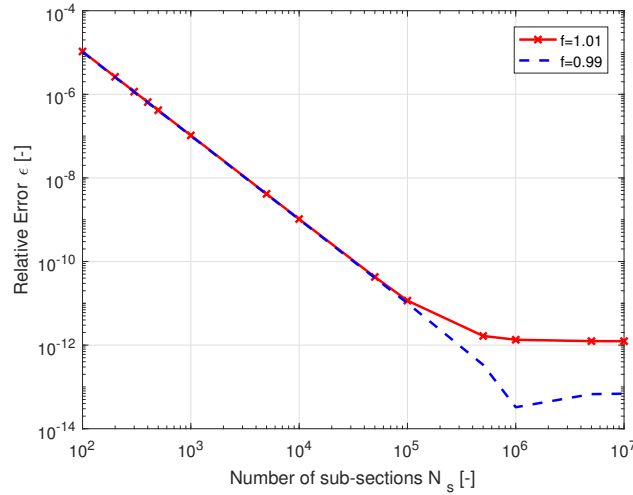


Figure 4.1: Relative error of the influence coefficient from numerical integration method with $\delta=0.01$ versus number of sub-sections N_s .

From the figure, it could be concluded that the logarithmic of the relative error decrease linearly with the logarithmic of the number of sub-sections until $N_s = 1 \times 10^5$ and $N_s = 1 \times 10^6$ for the condition of $f = 1.01$ and $f = 0.99$ respectively. There will then be a trade-off between the accuracy of the numerical solution and the computational efforts. With the number of sub-section to be 1×10^2 , the relative error is small enough to be only 1×10^{-5} which is sufficient for obtaining the converged solution. This value of the number of sub-section is also used in Chapter 3.

The convergence problem

The second issue is encountered when letting the number of sub-sections N_s not changed and the scaling factor f getting closer to 1, the convergence issue will then rise that the

numerical integration method will not have sufficient results. For demonstration of this issue, the influence coefficient of $I_{1,j,j}$ is calculated with the scaling factor to be $f_o = 1 + \delta = 1.0001$ and $f_i = 1 - \delta = 0.9999$. The relative error of the numerical solutions with respect to the analytical solutions are calculated with different number of sub-sections and plotted in the Log-log plot in Figure 4.2.

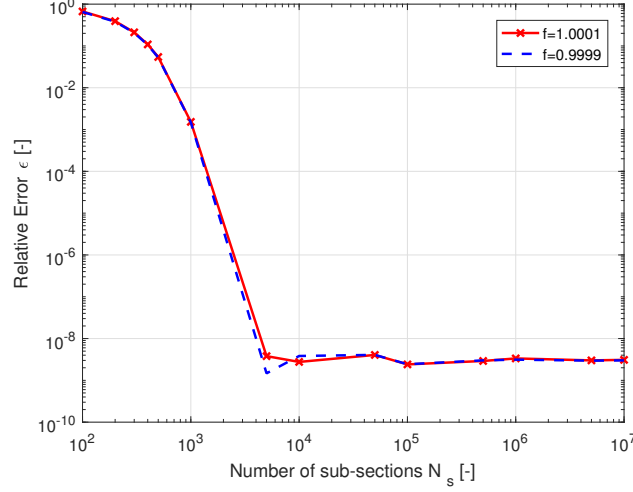


Figure 4.2: Relative error of the influence coefficient from numerical integration method with $\delta=0.0001$ versus number of sub-sections N_s .

From the figure, it could be concluded that when the distance δ of moving the control point is very small, the number of sub-sections should be large enough for the sufficient numerical solutions. For the case of $\delta = 0.0001$, The value of N_s should be at least $N_s = 1 \times 10^3$ for sufficient results. With a parameter study of different values of δ and N_s , it could be concluded that for a sufficient result, the following condition should be satisfied.

$$\delta N_s > 0.1 \quad (4.48)$$

This could be explained by Equation (A.26) in the Appendix that in order to use the Cauchy principal value of the integration. In Equation (A.26) the value of ϵ is assumed to be much smaller than $(r - 1)$. As a result, if keeping the value of ϵ constant and decrease the value of $(r - 1)$, the condition will be not satisfied anymore after some certain value. As a result, the choice of the scaling factor f and the number of sub-sections N_s should be correctly chosen in pairs if using the numerical integration method.

4.5 Conclusions of the chapter

In this chapter, the analytical solution of the influence coefficients as well as the induced velocity w_x^n on the control points in x -direction due to normal loadings are derived. The main findings and major conclusions are listed as follows.

- With the analytical solution of the influence coefficients derived, the influence coefficients could then be calculated analytically instead of using the numerical integration methods. The computational effort of the AC model is then decreased.
- The properties of the influence coefficients are also obtained from the analytical solutions. When calculating the induced velocities on the control points, with the AC discretized into N sections, it is not necessary to calculate $N \times N$ different influence coefficients for both x - and y -directions. There are only three different values of $I_{1,j,i}$ and $N/2$ different values for $I_{2,j,i}$. This will further decrease the computational efforts.
- With the analytical solution of I_1 for the special case that evaluating on the control points, the analytical solution of the induced velocities w_x^n on the control points in x -direction due to arbitrary normal loadings is obtained. The analytical solution is verified with the Madsen's analytical solution [32] which is for the induced velocity w_x^n at an arbitrary point with a sine form normal loading. The continuity of w_x^n is validated analytically which is shown to have the identical conclusion with that from the numerical validation.
- The analytical solution of w_x^n is in simple formulation and the difference of the value between one control point in the windward part and the corresponding one in the leeward part in its direct downstream is also obtained. These solutions are beneficial for a deeper understating of the AC model.
- The convergence issue of calculating the influence coefficient I_1 with the numerical integration is also investigated. The conclusion is that with the distance of moving the control points to be just inside or outside of the AC decreases, the sub-section number for the numerical integration should increase accordingly. In practical, the condition of $\delta N_s > 0.1$ should be satisfied.

Flow curvature effect

According to the validation of the results from the AC models with the panel code of U2DiVA in Chapter 3, the flow curvature effect is shown to have a significant influence on the results of normal and tangential loading distributions which is of vital importance for the designing and optimisation of the VAWT. In this Chapter, the flow curvature effect is firstly modelled with the conformal mapping method, and the characteristic is investigated. After that, the method of evaluating at the three-quarter chord is introduced and implemented in AC models as a modification. The performance of the modified AC models is then validated to determine whether this method is sufficient to model the flow curvature effect.

5.1 Conformal mapping method

There are multiple methods to model the flow curvature effect, and most of the methods are to transform the airfoil in the curvilinear flow, which is due to the rotation of the rotor, into a virtual airfoil in the rectilinear flow.

5.1.1 Migliore's method

One of the methods to model the flow curvature effect is to transform the airfoil geometry with the conformal mapping method, and Migliore [33] is one of the first to develop this method. According to Migliore, the local angle of attack should remain the same for all locations on the airfoil after transforming with the conformal mapping method. In the derivation of the model, the streamlines are derived from the velocity potential and are shown to in the form of concentric circles whose centre is having an offset with the rotational

axis of the rotor. As a result, a polar coordinate system is then used to transform the concentric circular streamlines, which correspond to the curvilinear flow, into the parallel straight streamlines which correspond to the rectilinear flow. The coordinate systems in this method are demonstrated in the Figure 5.1.

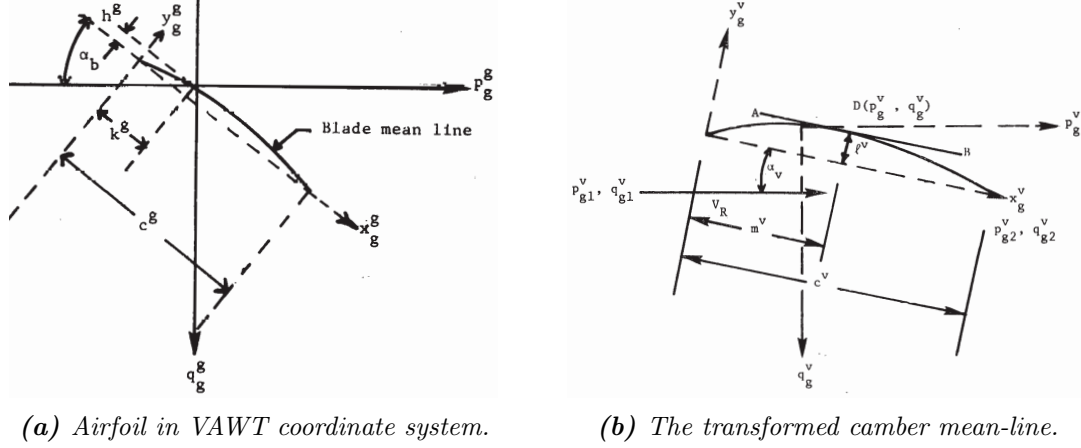


Figure 5.1: Coordinate systems for the conformal mapping method [33].

Coordinate systems

There are mainly two sets of coordinate systems in the model, which are the airfoil coordinate system of (x, y) and the VAWT coordinate system of (p, q) . For the variables in the figures and the following equations in this section, the superscripts of g and v represent the variables are corresponding to the geometric airfoil and virtual airfoil respectively. The subscripts of g , v and R represent the length used for the non-dimensioning is the geometric chord c^g , virtual chord c^v and the radius of the rotor R respectively.

The definition of the airfoil coordinate system of (x_g^g, y_g^g) and (x_v^v, y_v^v) are consistent with the standard NACA airfoil coordinate system that the leading edge is at the origin and the trailing edge is at the coordinate of $(1, 0)$. The x -axis is along the chord line pointing to the leading edge, and the y -axis is 90° counter-clockwise with respect to it. The VAWT coordinate system of (p, q) is a non-inertial coordinate system that rotates about the rotational axis of the rotor with the same angular velocity of the rotor. The origin is at the blade mounting point, and the q -axis coincides with the line connecting the centre of the rotor and the mounting point of the blade, and the positive direction is from the rotor axis pointing to the mounting point. The p -axis is 90° clockwise rotation with respect to the q -axis. For the clockwise rotating rotor, the positive p direction is identical with the rotational velocity encounter at the mounting point.

Transforming procedure

Firstly, the coordinate of the geometric airfoil in the non-dimensioned airfoil coordinate system of (x_g^g, y_g^g) is transformed into the VAWT coordinate system of (p_g^g, q_g^g) with the

pitch angle of θ_p and mounting point to be (k_g^g, h_g^g) which could be visualised in Figure 5.1(a).

$$p_g^g = (x_g^g - k_g^g) \cos \theta_p + (y_g^g - h_g^g) \sin \theta_p \quad (5.1)$$

$$q_g^g = (x_g^g - k_g^g) \sin \theta_p - (y_g^g - h_g^g) \cos \theta_p \quad (5.2)$$

Secondly, the geometry of the original airfoil is transformed into the virtual airfoil in the rectilinear flow by transforming the coordinate in (p_g^g, q_g^g) plane into the (p_g^v, q_g^v) plane with the following equations which are according to Migliore [34].

$$\gamma = \epsilon \cos \theta \quad (5.3)$$

$$\lambda = 1 - \epsilon \sin \theta \quad (5.4)$$

$$\Gamma = \frac{p_g^g}{R_g} + \gamma \quad (5.5)$$

$$\Lambda = \frac{q_g^g}{R_g} + \lambda \quad (5.6)$$

$$\frac{q_g^v}{R_g} = \sqrt{\Gamma^2 + \Lambda^2} - \sqrt{\gamma^2 + \lambda^2} \quad (5.7)$$

$$\frac{p_g^v}{R_g} = \sqrt{\Gamma^2 + \Lambda^2} \left[\tan^{-1} (\Gamma/\Lambda) - (\gamma/\lambda) \right] \quad (5.8)$$

In the above equations, the variable of ϵ is the inverse of the tip speed ratio and θ is the azimuthal angle of the rotor. To be noted that the definition of the azimuthal angle is different from that in the AC model, the azimuthal here is defined to increase in the clockwise direction and is zero-valued when the q -axis is opposite to the incoming wind. With the virtual airfoil geometry obtained in the (p_g^v, q_g^v) plane, the virtual angle of attack and the virtual chord line could then be calculated with Equation (5.9) and (5.10). To be noted that in the aforementioned two equations, the subscript of 1 and 2 represent the properties at the leading edge and trailing edge respectively. Finally, the virtual airfoil data is transformed into the coordinate system of (x_v^v, y_v^v) which is identical to the NACA coordinate system.

$$\alpha_v = \tan^{-1} \left(\frac{q_{g2}^v - q_{g1}^v}{p_{g2}^v - p_{g1}^v} \right) \quad (5.9)$$

$$\frac{c^v}{c^g} = \sqrt{(p_{g2}^v - p_{g1}^v)^2 + (q_{g2}^v - q_{g1}^v)^2} \quad (5.10)$$

$$x_g^v = [(p_g^v - p_{g1}^v) \cos \alpha_v + (q_g^v - q_{g1}^v) \sin \alpha_v] \quad (5.11)$$

$$y_g^v = [(p_g^v - p_{g1}^v) \sin \alpha_v + (q_g^v - q_{g1}^v) \cos \alpha_v] \quad (5.12)$$

$$x_v^v = \frac{c^g}{c^v} x_g^v \quad (5.13)$$

$$y_v^v = \frac{c^g}{c^v} y_g^v \quad (5.14)$$

To be noted that for the virtual airfoil in the (x_g^v, y_g^v) plane, because the coordinate is non-dimensioned by the geometric chord length c^g which is different from the virtual chord length c^v , the coordinate of the trailing edge is not (1,0). And with the virtual airfoil transformed to the (x_v^v, y_v^v) plane with Equation (5.13) and (5.14), the trailing edge is

then at the coordinate of $(1, 0)$. From the above equations, it could be concluded that the properties of the virtual airfoil such as the virtual airfoil geometry and the virtual angle of attack are dependent on the tip speed ratio λ and chord-to-radius ratio c/R which is directly linked with solidity σ . And according to Equation (5.1) and (5.2), the properties are also dependent on the mounting point location and the pitch angle.

5.1.2 Virtual camber and virtual incidence

According to the result from the conformal mapping method, there will be two effects which are the additional virtual camber and the virtual incidence angle. The two effects which will be discussed in details respectively as follows.

Additional virtual camber

With the conformal mapping method as above, the virtual airfoil could be then obtained. The airfoil geometry and camber mean-line of the original NACA0015 airfoil and its virtual airfoil for a certain case are plotted in the non-dimensioned coordinate system of (x_g^g, y_g^g) and (x_v^v, y_v^v) respectively in Figure 5.2. The camber mean-line is defined to be the line that equidistant to the upper and lower surface of the airfoil.

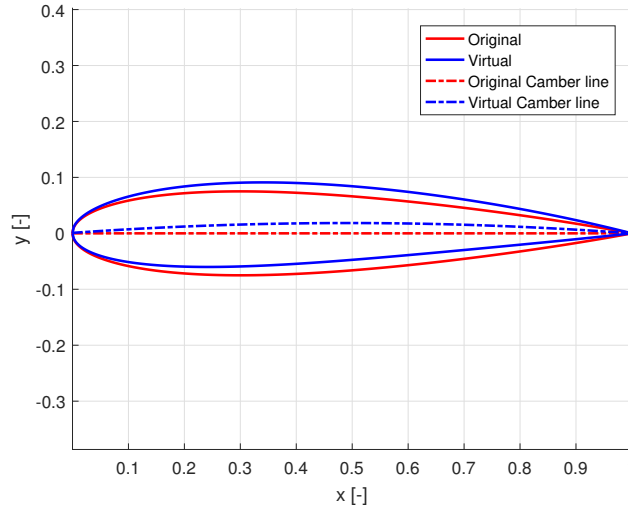


Figure 5.2: The original NACA0015 airfoil and its virtual airfoil, with $\lambda = 3$, $c/R=0.1$, $\theta = 90^\circ$, $\theta_p = 0^\circ$, mounted at $1/4$ c .

It could be visualised from Figure 5.2 that the camber mean-line of the virtual airfoil is curved and different from that of the NACA0015 airfoil which coincides with the x -axis. It could then be concluded that there is an additional virtual camber of the virtual airfoil.

In order to quantify the virtual camber, the variable of y_c is introduced, which is the maximum distance between the camber mean-line and the chord line. The virtual camber is defined as the ratio of the y_c and the chord to the rotor c which is then y_c/c [33].

Virtual incidence

The virtual incidence angle is the difference between the virtual angle of attack α_v and the geometric angle of attack α_g at the mounting point with the following equation.

$$\alpha_i = \alpha_v - \alpha_g \quad (5.15)$$

The geometric angle of attack at the mounting point could be obtained from the following equation according to Migliore [33].

$$\alpha_g = \tan^{-1} \left(\frac{\epsilon \cos \theta}{1 - \epsilon \sin \theta} \right) \quad (5.16)$$

The incidence angle α_i could be considered as an additional pitch angle due to the flow curvature effect.

Azimuthal variation of camber and incidence

As explained before, the incidence angle and the additional camber will vary with the azimuthal angle. The results for one revolution with the azimuthal angle from 0° to 360° are then calculated. The setup is set to be consistent with one of the cases demonstrated by Migliore [33] and will then serve as validation of the implementation.

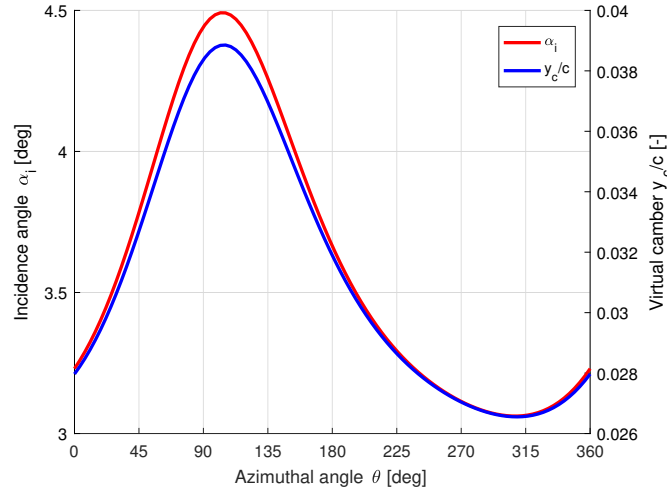


Figure 5.3: The incidence angle α_i and the camber y_c/c for NACA0015 airfoil, with $c/R=0.26$, $\lambda = 5.5$, $\theta_p = 0^\circ$ mounted at $1/4 c$.

By comparing the results in Figure 5.3 with that calculated by Migliore in [33], the results of the variation of incidence angle and the virtual camber with the azimuthal angle are having good agreements. It is then indicated the Migliore's model is correctly implemented in the MATLAB code.

5.1.3 Investigate virtual camber with panel code

With the Migliore's conformal mapping method, the incidence angle α_i and the virtual camber y_c/c could be obtained. And it is then necessary to determine the influence on the airfoil polar due to the two effects. The incidence angle α_i could be directly calculated from Equation (5.15) and could be considered as a virtual pitch angle whose influence could be directly modelled by horizontally shifting the lift curve leftwards with α_i . However, for the additional virtual camber, which is represented by the ratio of y_c/c , the influence could not be directly determined as that for the incidence angle. According to Migliore [33], with the examination of sectional lift data at zero angle of attack, there is an upward shift of 0.10 of the lift curve for every 1% of camber. Even though this method might be a good approximation, it is an empirical formulation, and the validation is needed as well.

The additional virtual camber is also able to be investigated by directly comparing the airfoil polar of the original airfoil and the virtual airfoil. The virtual airfoil in the non-dimensioned coordinate system of (x_v^v, y_v^v) is used as the airfoil data input, which does not include the incidence angle α_i , thus only the additional virtual camber is considered. For the virtual airfoil obtained from the aforementioned conformal mapping method, the lift and drag coefficient for a certain angle of attack could be calculated with the panel code of U2DiVA. In the panel code, the virtual airfoil is placed with a constant angle of attack in the uniform flow, and the simulation time is set to be long enough for the wake to be fully developed, the converged solution is then obtained. Repeating this process for different angle of attacks, the lift polar of this virtual airfoil is then obtained. In this report, the simulation is done for the angle of attack from -10° to 10° with the spacing of 2° , which will be 11 simulations. Since the virtual airfoil as well as the virtual camber are dependent on the azimuthal angle, the process mentioned above should be repeated for virtual airfoil for different azimuthal angles. In this report, the calculation is done the azimuthal angles from 0° to 350° with the spacing of 10° , which will then be 36 different cases. As a result, there will be $36 \times 11 = 396$ simulations for one case of the tip speed ratio λ and chord to radius ratio c/R .

The converged solution of the drag coefficient for the virtual airfoil is very close to zero for different angle of attacks, which corresponds to the drag coefficient for the inviscid flow in Equation (3.147). The lift polar of a certain virtual airfoil is plotted in Figure 5.4 together with the inviscid lift polar of the original NACA0015 airfoil with Equation (3.146) for comparison.

From the figure, it could be observed that there is a significant difference of the lift curve of the virtual airfoil and that of the original airfoil which is due to the additional virtual camber. It could also be visualised from the figure that the two lift curves seem parallel to each other. As a result, it could be considered that the lift curve of the original airfoil having an upward or leftward shift to get the lift curve of the virtual airfoil. This is with the similar idea as the empirical method of shifting the lift curve upwards according to the camber ratio of y_c/c .

The above two methods are then investigated and discovered that the difference of the lift coefficient for the two airfoils is constant for an arbitrary angle of attack. And the difference

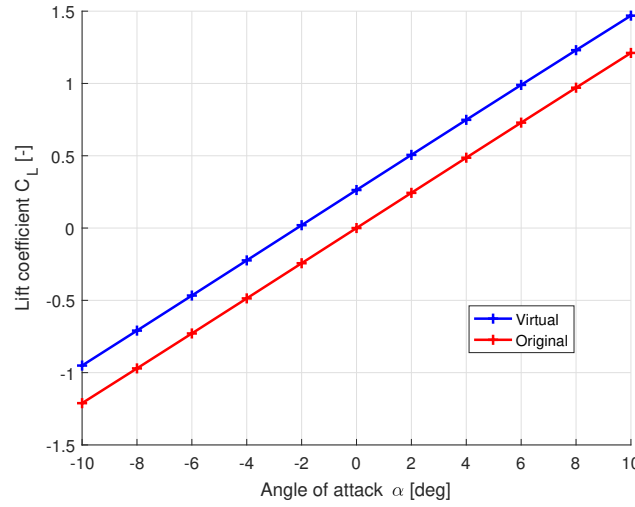


Figure 5.4: Comparison of the lift coefficient for the virtual and original airfoil, with $c/R=0.1$, $\lambda = 3$, $\theta_p = 90^\circ$ mounted at $1/4$ c .

of the angle of attack of the two airfoils corresponding to an arbitrary lift coefficient is also constant. As a result, the lift curve of the virtual airfoil could be represented by a leftward shift of $\Delta\alpha_c$ or could be represented by an upward shift of $\Delta C_{L,c}$. The two methods are demonstrated for a certain virtual airfoil in Figure 5.5 that the original lift curve after shifted with the aforementioned two methods will both coincide with the virtual lift curve.

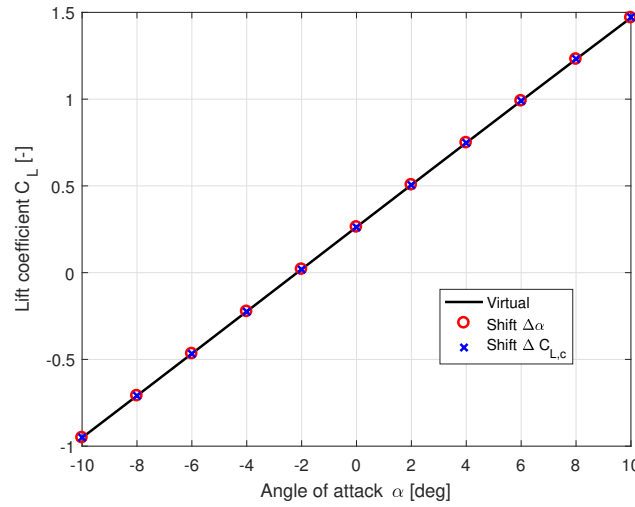


Figure 5.5: Validation of the method of shifting the lift coefficient curve, with $c/R=0.1$, $\lambda = 3$, $\theta_p = 90^\circ$ mounted at $1/4$ c .

And the next step is to calculate the two values, which represent the shift of the lift curve, for different azimuthal angles. With the original airfoil of NACA0015 being symmetric and has zero lift coefficient at zero angle of attack, a practical method of obtaining the $\Delta\alpha_c$ could then be using the negative value of the angle of attack which corresponds to the zero lift coefficient. And the value of $\Delta C_{L,c}$ could be obtained with the lift coefficient for zero angle of attack. The verification of the two methods could be done by calculating the maximum absolute value of the difference between the lift coefficient of the virtual airfoil

and the original airfoil after the shift. The verification is done for different azimuthal angles which correspond to different virtual airfoils, the absolute error is plotted against the azimuthal angle in Figure 5.6. From the figure, it could be visualised that the difference between the lift polar of the virtual airfoil and that of the original airfoil after shift with the aforementioned two methods are very small. Thus both of the two methods are sufficient.

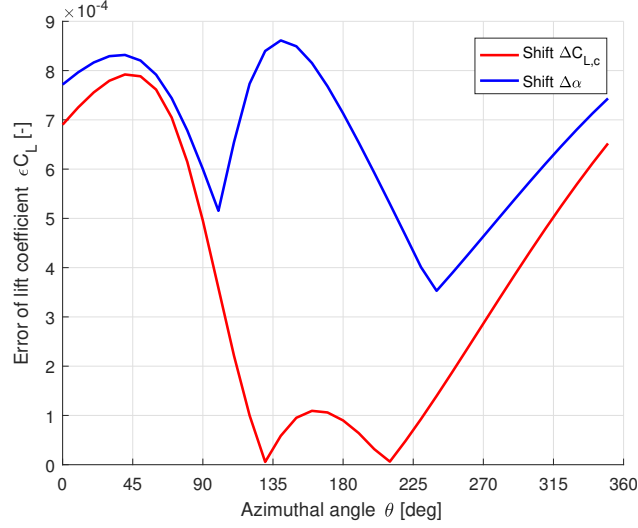


Figure 5.6: The error of the lift coefficient for the two methods of shifting the lift curve, with $c/R=0.1$, $\lambda = 4$, $\theta_p = 0^\circ$ mounted at $1/4$ c .

For the two methods, the shift of angle of attack $\Delta\alpha_c$ is chosen to represent the camber effect. The relationship between the lift coefficient and the virtual angle of attack is then as follows.

$$C_L = 2\pi \times 1.11 \sin(\alpha_v + \Delta\alpha_c) \quad (5.17)$$

5.1.4 Local angle of attack at three-quarter chord point

The previous subsection indicates that the additional camber effect could be represented by the horizontal shift of the lift curve with $\Delta\alpha_c$, which could be calculated with the panel code. However, this method is very complicated and impractical because both the conformal mapping method and the panel code are needed. Since the virtual airfoil varies with the azimuthal angle, which should be firstly calculated with the conformal mapping method for different azimuthal angles. The shift of angle of attack $\Delta\alpha_c$ for every virtual airfoil should then be calculated from the panel code. The computational effort will then be too heavy for the flow curvature modelling and is not favourable for implementing as a modification of the AC model.

According to the literature review in Chapter 2, in the B-L type dynamic stall model such as the Risø dynamic stall model, the lift coefficient is calculated from the effective angle of attack which is calculated from the angle of attack at three-quarter chord point of the

airfoil. According to the flow curvature effect, the flow properties at the three-quarter chord point is different from that of the mounting point if the two points do not coincide with each other. As a result, the property of the virtual airfoil at the three-quarter chord point should then be investigated. There is a conjecture that the virtual camber could be represented by the local slope of the camber mean-line at the three-quarter chord point with the equation as follows.

$$\Delta\alpha_{c,3/4} \approx \tan \Delta\alpha_{c,3/4} = \frac{dx_v^v}{dy_v^v} \quad (5.18)$$

In the equation above, the variable of $\Delta\alpha_{c,3/4}$ could be considered as the difference of the local angle of attack at the three-quarter chord point and the angle of attack of the airfoil. To be noted that this angle is obtained from the virtual airfoil geometry in the non-dimensioned coordinate system of (x_v^v, y_v^v) which will then only model the virtual camber but not the incidence angle α_i . The results of $\Delta\alpha_{c,3/4}$ are calculated for different azimuthal angles and compared with the shift of angle of attack $\Delta\alpha_c$ in Figure 5.7.

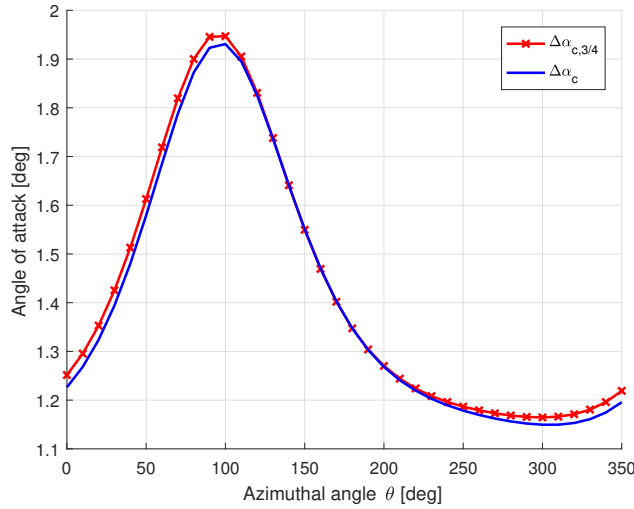


Figure 5.7: The relationship of the camber and local angle of attack at the three-quarter chord point, with $c/R=0.1$, $\lambda = 4$, $\theta_p = 0^\circ$ mounted at $1/4$ c .

It could be visualised from the figure that the results of two angles are having good agreements with each other. As a result, the virtual camber could be sufficiently modelled by the angle of $\Delta\alpha_{c,3/4}$ from the camber mean-line with Equation (5.18). This will then reduce the computational efforts because the camber mean-line could be calculated directly from the virtual airfoil data which is from the conformal mapping method, the panel code of U2DiVA is then not necessary for the modelling the virtual camber.

The conclusion indicates that there is a possibility to model the flow curvature effect by evaluating the local angle of attack at the three-quarter chord point of the airfoil. This method will then be investigated in the next section that whether the modified AC model with this method will sufficiently model the flow curvature effect. To be noted that there is another reason to validate the aforementioned method because when implementing the Risø dynamic stall model in the AC model, the method of evaluating at the three-quarter chord point is implicitly implemented. Thus, there will then be *double-consideration* of

the flow curvature effect if both the Risø dynamic stall model and the conformal mapping method are implemented in the AC model, which will then not be able to have sufficient results.

5.2 Evaluate at three-quarter chord point

The reason for investigating the method of evaluating at the three-quarter chord of the airfoil has been introduced in the previous section that this method has the possibility to model the flow curvature effect. The details of implementing this method in the AC model will be introduced in this section.

It has been mentioned in the previous section that this method has been implicitly included in the Risø dynamic stall model. It will be introduced in Chapter 6 that the Risø dynamic stall model consists of four different aerodynamic state variables representing the dynamic effects which could be partially or fully applied, resulting in different levels of modelling the dynamic effects. If none of the four aerodynamic state variables are used, the dynamics of the attached flow as well as the trailing edge separation will be neglected. The Risø dynamic stall model then becomes a steady model and the only thing left in the model is evaluating the angle of attack at the three-quarter chord point. As a result, this method of evaluating at the three-quarter chord point could be considered as the Risø dynamic stall model with all the dynamic effects neglected.

5.2.1 The evaluation point and aerodynamic centre

For the AC model implemented in Chapter 3, there is no distinguish of the aerodynamic centre and the evaluation point because the induced velocity and the angle of attack are evaluated at the aerodynamic centre, which is usually assumed to be the quarter chord point, but is assumed to be the half chord point in the HAWC2 code. With the method of evaluating at the three-quarter chord point, the aerodynamic centre and the evaluation point should then be distinguished. There will then be three different points of interest on the airfoil, which are the aerodynamic centre, mounter point and the evaluation point. The three points are demonstrated in Figure 5.8 and are noted with A , E and M respectively.

For the method of evaluating at the three-quarter chord point, the evaluation point E is then at the three-quarter chord point and the aerodynamic centre A is at the quarter chord point of the airfoil. This will be throughout the following of this chapter.

5.2.2 Implementation of the method in AC model

The details of implementing the method of evaluating at the three-quarter chord point of the airfoil in the AC model will then be introduced in two parts as follows, which are

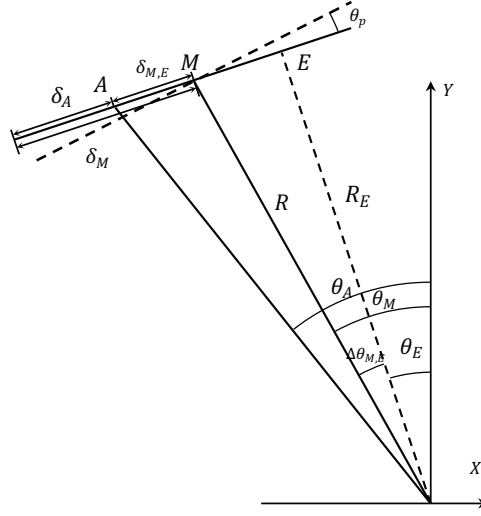


Figure 5.8: The mounting point M , evaluation point E and the aerodynamic centre A on the airfoil.

calculating the angle of attack at three-quarter chord point and calculating the lift and drag coefficients.

Angle of attack at three-quarter chord point

Firstly, the local angle of attack at the three-quarter chord point $\alpha_{3/4}$ which is also the evaluation point should be calculated, and the explicit form is as follows.

$$\alpha_{3/4} = \tan^{-1}(V_{n,3/4}/V_{t,3/4}) - \theta_p \quad (5.19)$$

The Equation (5.19) is similar to Equation (3.27) but with the subscript of 3/4 which represents the value of the variables are at the three-quarter chord point, in order to distinguish from that at the quarter chord point which is the aerodynamic centre. The variable of $V_{n,3/4}$ and $V_{t,3/4}$ are then normal and tangential relative wind speed at the three-quarter chord point. To be noted the aforementioned normal and tangential directions are the normal and tangential direction with respect to the AC at the mounting point M . This is because of the definition of the pitch angle θ_p is with respect to the mounting point which has been explained in Chapter 3. The explicit form of the equations of $V_{n,3/4}$ and $V_{t,3/4}$ are as follows which are very similar to Equation (3.129) and (3.130) with only the subscript of E replace by 3/4.

$$V_{n,3/4} = V_{x,3/4} \sin \theta_M - V_{y,3/4} \cos \theta_M + V_{rot,3/4} \sin \Delta \theta_{M,E} \quad (5.20)$$

$$V_{t,3/4} = V_{x,3/4} \cos \theta_M - V_{y,3/4} \sin \theta_M + V_{rot,3/4} \cos \Delta \theta_{M,E} \quad (5.21)$$

The variable of $\Delta \theta_{M,E}$ is the angular difference of the azimuthal angle at the mounting point and the evaluation point which could calculated from Equation (3.135). The variable of θ_M is the azimuthal angle of the mounting point M which is needed for the calculation.

Since the loadings are located at the aerodynamic centre A , which then corresponds to the control points with the discretization method of Equation (3.6). With the azimuthal angular difference of the aerodynamic centre A and the mounting point M to be $\Delta\theta_{A,M}$ as in Figure 5.8, the azimuthal angle θ_M could then be obtained with the following equation.

$$\theta_M = \theta_A - \Delta\theta_{A,M} \quad (5.22)$$

The variable of $V_{rot,3/4}$ is the rotational speed at the three-quarter chord point which could be approximated with the rotational speed at the mounting point V_{rot} because the value of R_E is very close to the value of R according to Chapter 3.

$$V_{rot,3/4} \approx V_{rot} = \omega R = \lambda V_\infty \quad (5.23)$$

The variable of $V_{x,3/4}$ and $V_{y,3/4}$ are the sum of the free wind velocity and induced velocity at the three-quarter chord point in x - and y -direction respectively with the following equations.

$$V_{x,3/4} = V_\infty(1 + w_{x,3/4}) \quad (5.24)$$

$$V_{y,3/4} = V_\infty w_{y,3/4} \quad (5.25)$$

The induced velocity at the three-quarter chord point, which are $w_{x,3/4}$ and $w_{y,3/4}$, are then needed for the calculation. However, the induced velocity calculated with Equation (3.105) and (3.106) are at the control points which corresponding to the aerodynamic centre A . It has been shown that the distance from the evaluation point E to the rotational axis, which is R_E , is approximately equal to the distance from the mounting point M to the rotational axis, which is R , in Equation (3.137). It could also be concluded with the similar method that value of R_A which is the distance from the aerodynamic centre A to the rotational axis is also approximately equal to the aforementioned two variables of R_E and R . With this assumption, the three points are then assumed to be all located on the AC when calculating the induced velocities. The induced velocity at point E could then be directly calculated from the induced velocity that has been calculated at the control points which is also the point A as well as quarter chord point. There will then be two methods which are using the piecewise constant of properties and using interpolation which will be introduced respectively as follows. Before that, the azimuthal angle of the evaluation point θ_E should be firstly calculated according to Figure 5.8 with the following equation.

$$\theta_E = \theta_M - \Delta\theta_{M,E} \quad (5.26)$$

- The first method is to utilise the assumption of piecewise properties of each section on the AC. It should be determined which section is the azimuthal angle of θ_E located in and the induced velocity of the control point in this section will be used for the evaluation point E . It should be noted that when the solidity of the rotor is not too large, and the AC is not discretized into too many sections, the three-quarter chord point will be located in the same section as the quarter chord point. For example, with the number of section $N = 36$, the point E and A will then be in the same section if the chord to radius ratio satisfies $c/R < 0.17$ which is a relatively large value. To be noted that for a two bladed rotor setup, the ratio of c/R is equal to the solidity σ which is defined in Equation (3.45).

- The second method it to use interpolation method such as linear interpolation method to obtain the induced velocity at the three-quarter chord point with that at the quarter chord point which corresponds to the control points. The induced velocity of the evaluation point E could then be considered as the induced velocity at the aerodynamic centre A with a lag effect with the angular difference of $\Delta\theta_{A,E}$. And with the assumption that the rotational speed of the two points is identical, the relative wind speed at the evaluation point is then also with a lag effect of that at the quarter-chord point with the same angular difference.

There is another method that the induced velocity at the evaluation point is directly calculated with Equation (3.1) and (3.2). However, this method requires to calculate the induced velocity at the quarter chord point as well as three-quarter chord point, the computational effort is then doubled. As a result, this method will not be used and the aforementioned first and second method will then be investigated.

The difference between the two methods is that the second method is able to model the phase lag while the first model is not able. In order to evaluate the performance of the above two methods, a straight forward method is to compare the relative wind speed at the three-quarter chord point $V_{rel,3/4}$ from the AC model with the result from the panel code. However, the relative wind speed calculated from the AC model and the panel code are having some difference, this method is then insufficient to evaluate the performance of the two methods. As a result, an alternative method is introduced which is to compare the difference of the relative wind speed at the quarter-chord point $V_{rel,1/4}$ and at the three-quarter chord point $V_{rel,3/4}$ which are calculated from the AC model and the panel code. The results are plotted in the Figure 5.9.

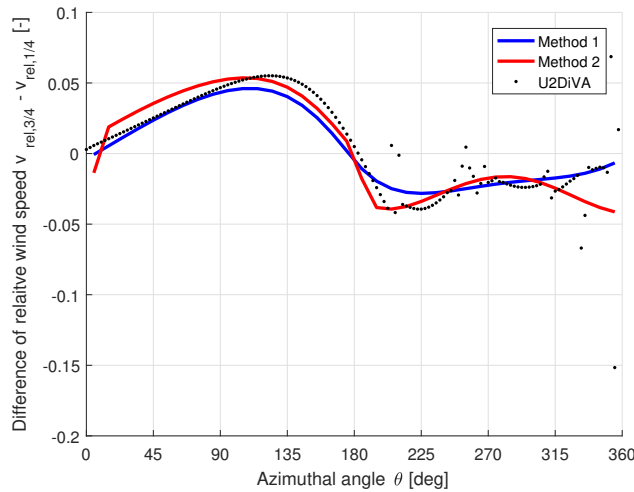


Figure 5.9: Comparison of the difference of relative wind speed at $1/4$ c point and $3/4$ c point.

From the figure above, it could be visualised that the Method 2 is having better agreement with the result from the panel code comparing with the Method 1. As a result, the second method which is the linear interpolation method is chosen.

Calculate lift and drag coefficient

Secondly, with the angle of attack at the three quarter chord point $\alpha_{3/4}$ calculated, the corresponding lift and drag coefficient should also be obtained. With the airfoil polar, the lift and drag coefficient corresponding to a certain angle of attack, which is $\alpha_{3/4}$ here, could be obtained. For the inviscid NACA0015 polar, the lift and drag coefficient are as follows which are according to Equation (3.146) and (3.147).

$$C_L = 2\pi \cdot 1.11 \sin \alpha_{3/4} \quad (5.27)$$

$$C_d = 0 \quad (5.28)$$

The aerodynamic force should then be applied at the aerodynamic centre A which is the quarter chord point of the airfoil. The magnitude of the lift and drag forces could be calculated with the lift and drag coefficient, but the directions of apply the forces are not clarified yet. There are two possible methods to apply the lift force, the first one is the lift force is perpendicular to angle of attack at the quarter chord point $\alpha_{1/4}$ which is visualised in Figure 5.10(a), and the second one is the lift force is perpendicular to the angle of attack at the three-quarter chord point $\alpha_{3/4}$ which is visualised in Figure 5.10(b).

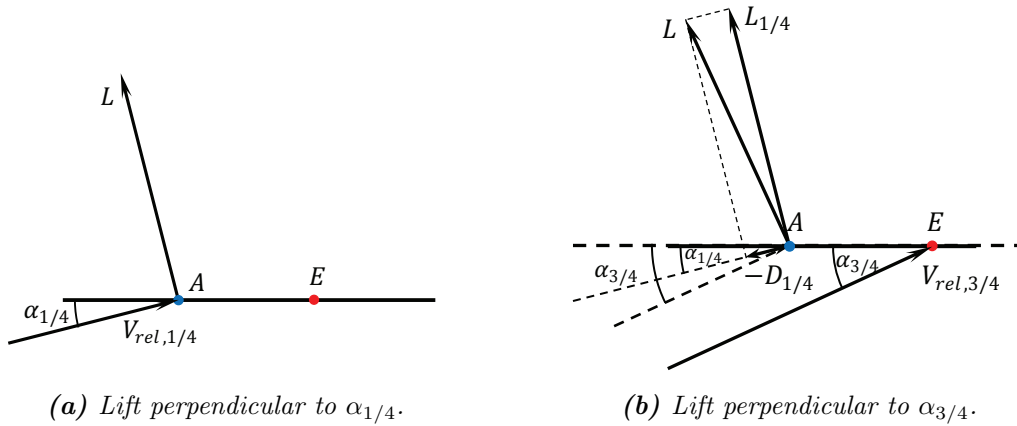


Figure 5.10: The direction of the aerodynamic forces.

In order to compare the two methods, the lift and drag forces for the second method is projected to the direction corresponding to the first method that the lift force is perpendicular to $\alpha_{1/4}$ with the equations as below, with the subscript of 1/4.

$$C_{L,1/4} = C_L \cos(\alpha_{1/4} - \alpha_{3/4}) \quad (5.29)$$

$$C_{d,1/4} = C_L \sin(\alpha_{1/4} - \alpha_{3/4}) \quad (5.30)$$

Because the difference between the angle of attack at the quarter-chord point and the three-quarter chord point is small, the lift coefficient could be simplified to as follows.

$$C_{L,1/4} \approx C_L = 2\pi \times 1.11 \sin \alpha_{3/4} \quad (5.31)$$

Comparing with Equation (5.27) and (5.28), it could be concluded that the mainly difference of the two methods is the drag coefficient. For the inviscid flow, there will be not drag components in the direction of $\alpha_{1/4}$ for the first method but will be an induced drag component for the second method in that direction. There will be the detailed investigation on which method should be chosen in Chapter 6 and the conclusion is used here that the first method should be chosen which is to apply the lift perpendicular to $\alpha_{1/4}$ and there should be no drag component in this direction for the inviscid flow.

5.3 Validation against panel code

With the details of the implementation of the method of evaluating angle of attack at the three-quarter chord point into the AC model in the previous section, the modified original AC model and modified Cheng's AC model could then be obtained. In this section, the performance of the method of evaluating at the three-quarter chord point is evaluated by comparing the converged solution for a certain load case calculated from the two modified AC models with that from the panel code of U2DiVA with the same load case.

5.3.1 Validate normal and tangential loadings

Firstly, the normal and tangential loadings are validated to indicate if the flow curvature effect could be sufficiently modelled. The normal and tangential loadings from the different models are plotted in the Figure 5.11.

From the Figure 5.11, it could be visualised that the normal and tangential loadings from the two modified AC models which evaluate angle of attack at the three-quarter chord point are having much better agreements with the panel code comparing to the AC models that evaluate at the quarter chord point as in Figure B.1 and B.2. The transportation of the value of the normal and tangential loadings between the windward and leeward part of the rotor are generally eliminated. It could then be concluded that the modified AC models are sufficient to model the flow curvature effect. However, further validation of the lift coefficient is needed in order to determine whether the upward shift of the lift coefficient as in Figure 3.24(a) could be modelled.

It could also be visualised from the Figure 5.11 that for the results of the loadings calculated from the two modified AC models, there is not much difference in the windward part and there is apparent difference in the leeward part. It seems that the loadings calculated from the modified Cheng's AC model will have a better agreement with that from the panel code, but it is still premature to have the conclusion at this stage.

According to Figure 5.11, it could be observed that both the normal and tangential loadings calculated from the panel code are having a lag in phase compared to the results from the two AC models. The reason of the phase lag is due to the unsteady aerodynamics of the rotor which could be directly modelled by the panel code with the modelling of the bound and shed vortices. However, the AC models currently are lacking unsteady aerodynamic

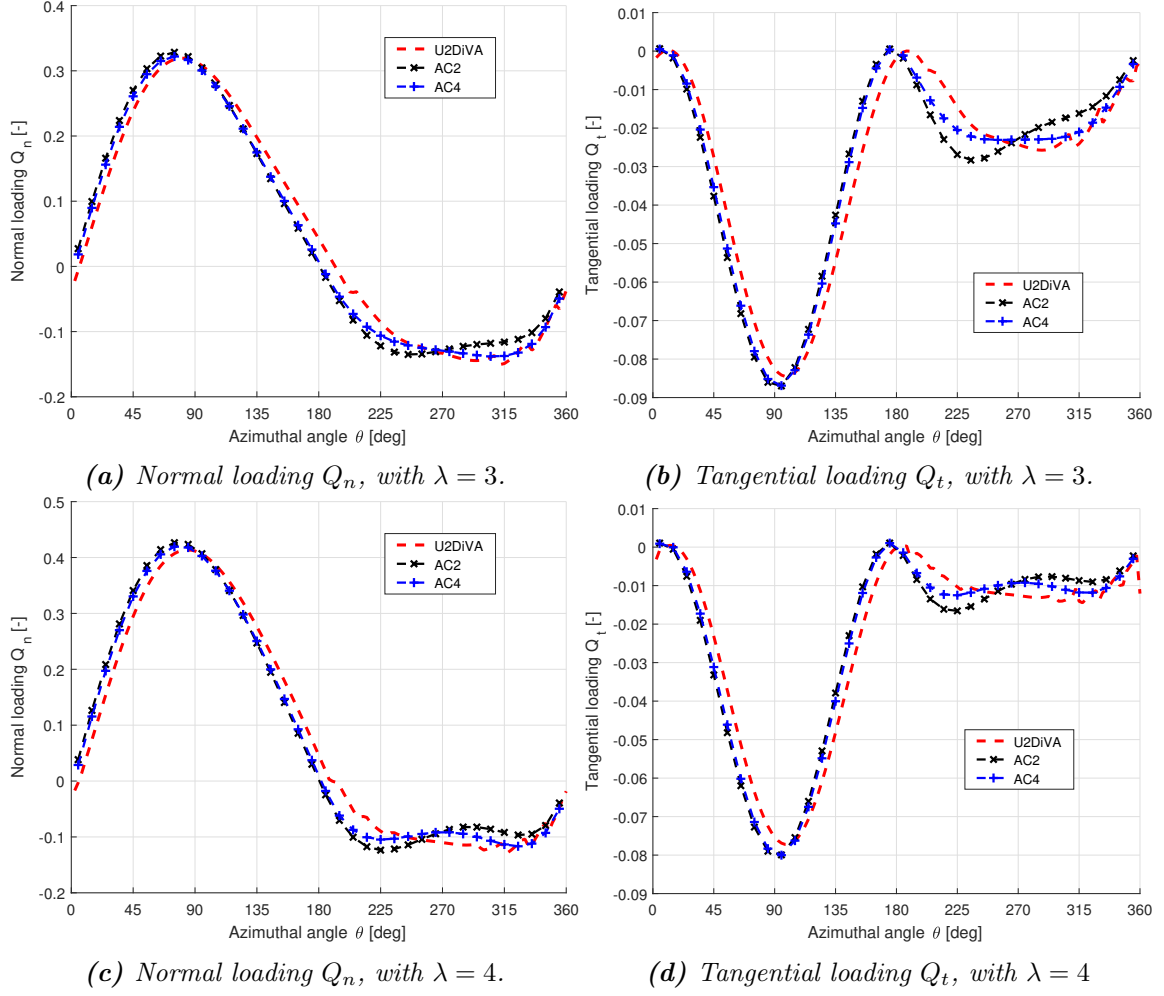


Figure 5.11: Validation of the normal and tangential loading, with $\sigma = 0.1$, $B=2$, mounted at $1/4$ c.

models. As a result, if the unsteady effects could be modelled by including a proper unsteady aerodynamic model in the AC model, the results from the AC model will have the potential of having even better agreements with that from the panel code.

5.3.2 Validate lift and drag coefficient

Besides the normal and tangential loadings, the lift and drag coefficient are also strong indications for the validation. There are two different angle of attacks which are the angle of attack at the quarter chord point $\alpha_{1/4}$ and at the three-quarter chord point $\alpha_{3/4}$. The lift and drag coefficients corresponding to $\alpha_{1/4}$ are in Equation (5.27) and (5.28) which is having zero drag component for the inviscid flow.

For validation purpose, the lift and drag coefficient corresponding to the direction of $\alpha_{3/4}$ are obtained as follows with vector projection and is demonstrated in Figure 5.12.

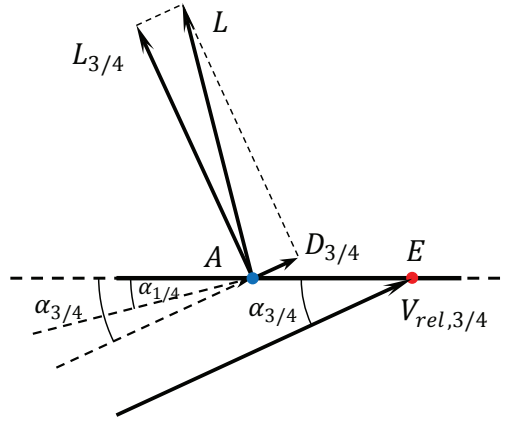


Figure 5.12: The decomposition of lift force in $\alpha_{1/4}$ direction to lift and drag in $\alpha_{3/4}$ direction.

The corresponding equations are then as follows.

$$C_{L,3/4} = C_L \cos(\alpha_{3/4} - \alpha_{1/4}) \quad (5.32)$$

$$C_{d,3/4} = C_L \sin(\alpha_{3/4} - \alpha_{1/4}) \quad (5.33)$$

Similar to Equation 5.31, because the difference between $\alpha_{3/4}$ and $\alpha_{1/4}$ is a small value, the lift coefficient $C_{L,3/4}$ could be approximated with the following equation.

$$C_{L,3/4} \approx C_L = 2\pi \times 1.11 \sin \alpha_{3/4} \quad (5.34)$$

It could then be concluded that the lift coefficient corresponding to $\alpha_{1/4}$ and $\alpha_{3/4}$ are almost identical. With the above variables, the lift and drag coefficient are validated respectively as follows.

Validate lift coefficient

The lift coefficient calculated from the two modified AC models are compared with that from the panel code for the validation. Firstly, with the result from the AC models and panel code, the lift coefficient C_L is plotted versus the angle of attack at the quarter chord point $\alpha_{1/4}$ in Figure 5.13a. It could be visualised from the Figure 5.13(a) that unlike Figure 3.24(a), there is no general shift of lift curve. As a result, the flow curvature effect is well modelled in both of the AC models with the method of evaluating angle of attack at the three-quarter chord point. To be noted that the curve of the C_L versus $\alpha_{1/4}$ from either of the AC models is having a *loop* which means there could be two values of lift coefficient C_L corresponds to one value of $\alpha_{1/4}$. This *loop* is different from the that due to the dynamic effects. The reason is that the lift coefficient is the function of $\alpha_{3/4}$ as in Equation (5.27) instead $\alpha_{1/4}$.

For further validation, with the results from the AC models as well as panel code, the lift coefficient C_L is plotted versus the angle of attack at three-quarter chord point $\alpha_{3/4}$ in the Figure 5.13(b). It could be concluded from the figure that there is no *loop* of the lift curve

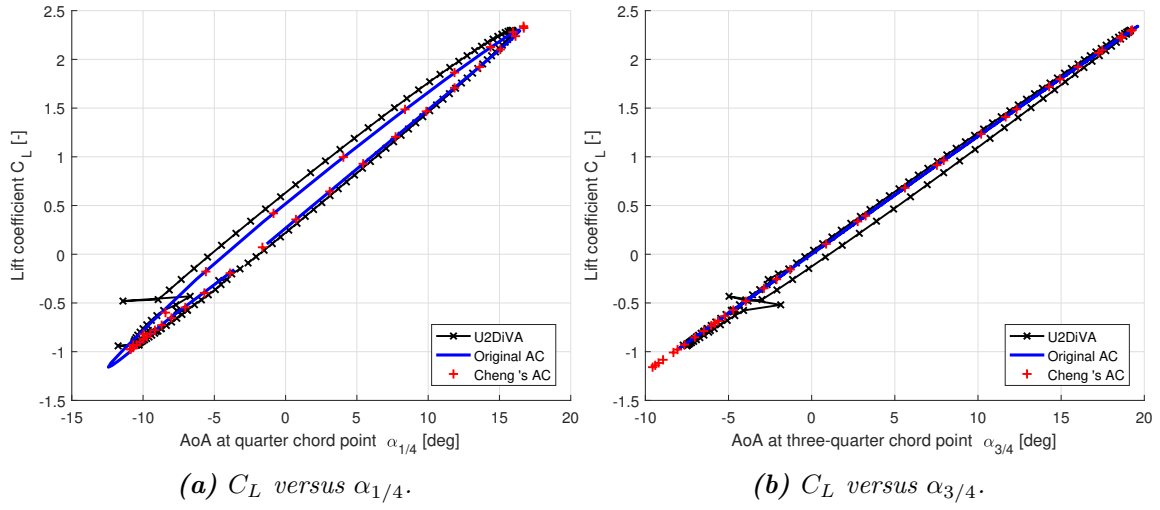


Figure 5.13: Validation of the lift coefficient C_L versus angle of attack at $1/4 c$ and $3/4 c$.

of C_L versus $\alpha_{3/4}$ from either of the AC models. The lift coefficient C_L is the function of $\alpha_{3/4}$ with Equation (5.27) which is almost linear. And there is no general shift of lift curve from the AC models compared to that from the panel code which means the flow curvature effect is well modelled.

Despite the results from the AC models and the panel code does not coincide with each other, the general shift of the lift curve has been eliminated which means the flow curvature effect has been sufficiently modelled. This is already an improvement of the AC model towards a more sufficient modelling. According to Figure 5.13(b), the lift curve from the panel code is having a *loop* which is due to the lag effect due to the unsteady aerodynamics. The conclusion is then identical to subsection 5.3.1 that the unsteady effects of the VAWT are favourable to be modelled in the AC model for better agreements with the panel code.

Validate drag Coefficient

For the validation with drag coefficient, the drag coefficient C_d is plotted versus the angle of attack $\alpha_{1/4}$ in Figure 5.14(a). The drag coefficient C_d from the AC models is zero-valued constantly which follows Equation (5.28). The figure is then almost identical with Figure 3.24(b). As a result, new conclusions can not be obtained with this figure.

For further investigation, the induced drag coefficient $C_{d,3/4}$ calculated with which is corresponding to $\alpha_{3/4}$ is plotted versus $\alpha_{3/4}$ in Figure 5.14(a). It could be visualised that there is generally good agreements between the result from the two AC models and the panel code. The drag coefficient of $C_{d,3/4}$ is generally increase with the increasing of $\alpha_{3/4}$ which is consistent with Equation (5.28).

Comparing Figure 5.14(a) and (b), it could then be validated that the lift coefficient is perpendicular to the $\alpha_{1/4}$ instead of $\alpha_{3/4}$. With the results from the panel code, the drag

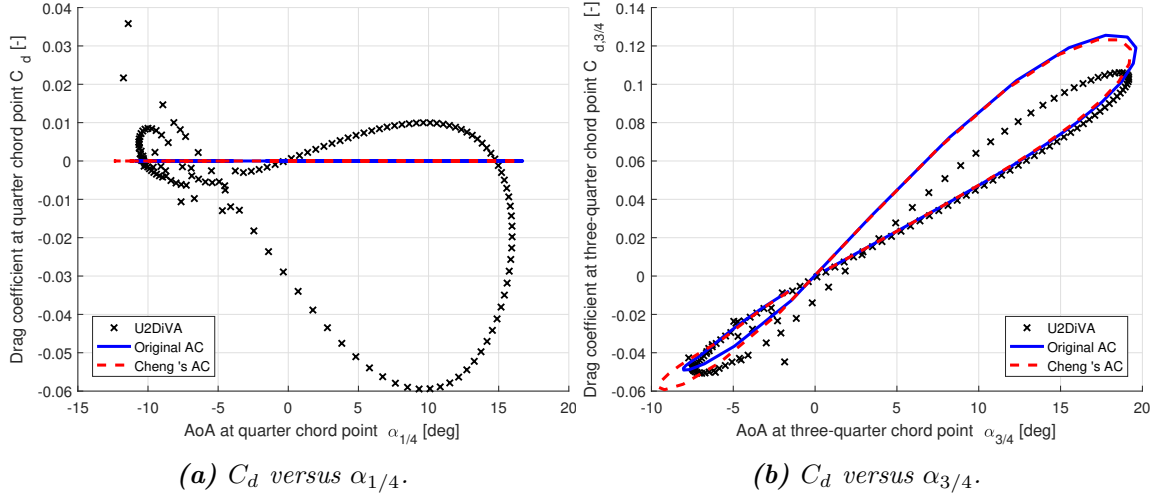


Figure 5.14: Validation of the drag coefficient C_L versus angle of attack at $1/4$ c and $3/4$ c.

coefficient in the direction $\alpha_{1/4}$ is around zero value and not generally increase with $\alpha_{1/4}$, but the drag coefficient in the direction $\alpha_{3/4}$ is generally increasing with $\alpha_{3/4}$ instead. To be noted that the loop of the drag coefficient $C_{d,3/4}$ from the two AC models are not corresponding to the dynamic effects but because of the variation of the angular difference of $(\alpha_{3/4} - \alpha_{1/4})$.

5.4 Four different AC models

Thus far, four different AC models have been introduced in this report and are named AC1 to AC4 for abbreviation. The specifications of the four models are listed in Table 5.1 as below.

Table 5.1: Four different Actuator Cylinder Models.

Name	Dependence of Loading	Evaluation point
AC1	Q_n	$1/4$ c
AC2	Q_n, Q_t	$3/4$ c
AC3	Q_n	$1/4$ c
AC4	Q_n, Q_t	$3/4$ c

The second column represents what loadings are the induced velocity dependent on. The induced velocity in the original AC model is only dependent on the normal loadings Q_n while the Cheng's AC model also takes into account the influence on the induced velocities due to tangential loadings Q_t . The third column is where the angle of attack is evaluated, with the abbreviation of $1/4$ and $3/4$ represents the quarter chord point and the three-quarter chord point. It has been validated that when evaluating on the three-quarter chord point, the flow curvature effect could be modelled. Thus the aforementioned two different evaluation point then represents with and without modelling of flow curvature effect.

In conclusion for the four models, the AC1 and AC3 corresponds to the original AC model and Cheng's AC model without flow curvature modelling which are introduced in Chapter 3. And the AC2 and AC4 models are corresponding to the AC1 and AC3 models but with flow curvature effect modelled which are introduced in this Chapter. To be noted that the above four models do not consider the unsteady aerodynamics of the airfoil.

5.5 Conclusions of the chapter

The flow curvature effect is investigated and the modelling is implemented in the AC model in this chapter, the findings and conclusions are summarised as below.

- The flow curvature effect can be modelled with the conformal mapping method by transforming the geometric airfoil to a virtual airfoil with incidence angle and additional virtual camber. The former is calculated directly with the conformal mapping method, while the latter is not able to be directly obtained and is calculated with the panel code instead. It is verified that the virtual camber can be represented by either shifting the lift curve horizontally with $\Delta\alpha_c$ or vertically with ΔC_L . It is also discovered that the horizontal shift of curve $\Delta\alpha_c$ is having good agreements with the difference between the local angle of attack at three-quarter chord point and the geometric angle of attack. And this is the reason for the possibility to model the flow curvature effect by evaluating the angle of attack at three-quarter chord point.
- With the method of evaluating the angle of attack at the three-quarter chord point implemented in the AC model, the results indicate the flow curvature has been well modelled because there is no general shift of the lift coefficient curve. The normal and tangential loadings are also having much better agreements with that from the panel code, instead of having transportation of the value of the loadings between the windward and leeward part of the rotor.
- It is also verified that despite the lift force is calculated with the angle of attack at the three-quarter chord point, the lift force should not be applied perpendicular to this angle of attack, but should be applied perpendicular to the angle of attack at quarter chord point instead, which is assumed to be the aerodynamic centre.
- Despite the results from the modified AC model are having much better agreements with that from the panel code, the results of normal and tangential loadings from the panel code still have a visible phase lag compared to that from the AC model. The phase lag can also be observed from the shape of the lift and drag coefficient against the angle of attack. The reason is the unsteady aerodynamics is not included in the AC model. There is then the possibility to further improve the AC model by implementing the unsteady aerodynamics in the model.

Unsteady Aerodynamics

It has been concluded from the previous chapters that the unsteady aerodynamics for the VAWT is favourable to be included in the AC model. In this chapter, the Risø dynamic stall model is firstly introduced with the application for different flow conditions as well as the relationship to the flow curvature modelling. Secondly, Pirrung's simplification and modification to the Risø model is introduced. Thirdly, the inviscid part of the model is validated with the panel code for harmonic pitching. Then, the Risø dynamic stall model is coupled with the AC model to be the dynamic AC model. Finally, the performance is validated with the panel code and possible issues of the coupled dynamic AC model is investigated.

6.1 Risø dynamic stall model

In this section, the Risø dynamic stall model will be introduced in details. Firstly, the steady lift decomposition which is the pre-processing of the steady lift data is introduced. Secondly, the dynamics of the attached flow and dynamics of the trailing edge separation are modelled with the coupled set of ODEs. And thirdly, there will be the indicial formulation of the equations as well as the discretization method. Finally, the Risø dynamic stall model with different complexities for modelling different flow conditions is introduced.

6.1.1 Steady lift decomposition

The decomposition of the steady lift polar data should be firstly done for the Beddoes-Leishman (B-L) type model which is a pre-processing progress for the modelling of trailing edge separation. The algorithm is according to Hansen [18] and is summarised as follows.

According to the basic assumption in the B-L type model for the trailing edge separation, the static lift coefficient could be represented by the expression of a flat plate in potential Kirchhoff flow [43].

$$C_L^{st} = C_{L,\alpha} \left(\frac{1 + \sqrt{f^{st}(\alpha)}}{2} \right)^2 (\alpha - \alpha_0) \quad (6.1)$$

In the Equation (6.1), α_0 is the angle of attack corresponding to zero lift, $C_{L,\alpha}$ is the slope of the linear part of the lift curve with the definition of $C_{L,\alpha} = \max\{C_L^{st}/(\alpha - \alpha_0)\}$ and f^{st} is the separation function which is an indication of the non-dimensioned distance between the leading edge and the trailing edge separation point. With the steady lift coefficient data as the input, the separation function f^{st} could be inversely calculated with the equation below.

$$f^{st}(\alpha) = \left(2 \sqrt{\frac{C_L^{st}}{C_{L,\alpha}(\alpha - \alpha_0)}} - 1 \right)^2 \quad (6.2)$$

The separation function f^{st} has to follow the condition below in order to satisfy the physical meaning of it.

$$0 \leq f^{st} \leq 1 \quad (6.3)$$

There will then be two special conditions for the separation function f^{st} which are the two ends of the interval:

- The condition of $f^{st} = 1$ represents the fully attached flow which corresponds to the linear part of the static lift curve, the Equation (6.1) then becomes

$$C_L^{st} = C_{L,\alpha}(\alpha - \alpha_0) \quad (6.4)$$

- The condition of $f^{st} = 0$ corresponds to the fully separated flow, the Equation (6.1) then becomes

$$C_L^{fs} = C_L^{st} = \frac{1}{4} C_{L,\alpha}(\alpha^{fs} - \alpha_0) \quad (6.5)$$

The static lift coefficient C_L^{st} will then be the full separation lift coefficient C_L^{fs} , and the angle of attack will be the fully separation angle of attack α^{fs} .

To be noted that for the angle of attack exceed the full separation angle α^{fs} , the Equation (6.1) will not be valid anymore. In order to solve this problem, the static lift coefficient is written in the following form which is the weighted sum of the lift coefficient of the fully attached flow and the fully separated flow.

$$C_L^{st} = C_{L,\alpha}(\alpha - \alpha_0)f^{st} + C_L^{fs}(\alpha)(1 - f^{st}) = C_{L,att}(\alpha)f^{st} + C_L^{fs}(\alpha)(1 - f^{st}) \quad (6.6)$$

The fully separated flow lift coefficient is then calculated as follows.

$$C_L^{fs} = \frac{C_L^{st} - C_{L,\alpha}(\alpha - \alpha_0)f^{st}}{1 - f^{st}} \quad (6.7)$$

It should be noted that the condition of $f^{st} = 1$ which corresponds to the fully attached flow is a singular point for the Equation (6.7). The corresponding fully separation lift coefficient should then be calculated with the following Equation according to Hansen [18].

$$C_L^{fs}(\alpha) \rightarrow C_L^{st}/2, \text{ for } C_L^{st}(\alpha) \rightarrow C_{L,\alpha}(\alpha - \alpha_0) \quad (6.8)$$

6.1.2 Dynamics of attached flow and trailing edge separation

The state-space formulation of the Risø B-L type dynamic stall model is consisted of four aerodynamic state variables which are x_1 to x_4 . The state variables are coupled by four nonlinear ordinary differential equations (ODEs) with the explicit form as below.

$$\dot{x}_1 + T_u^{-1}(b_1 + c\dot{U}/(2U^2))x_1 = b_1 A_1 T_u^{-1} \alpha_{3/4} \quad (6.9)$$

$$\dot{x}_2 + T_u^{-1}(b_2 + c\dot{U}/(2U^2))x_2 = b_2 A_2 T_u^{-1} \alpha_{3/4} \quad (6.10)$$

$$\dot{x}_3 + T_p^{-1}x_3 = T_p^{-1}(C_{L,\alpha}(\alpha_E - \alpha_0) + \pi T_u \dot{\alpha}) \quad (6.11)$$

$$\dot{x}_4 + T_f^{-1}x_4 = T_f^{-1}f^{st}(x_3/C_{L,\alpha} + \alpha_0) \quad (6.12)$$

The input variables required in the above set of ODEs are the flow properties, which are the angle of attack at the three-quarter chord point $\alpha_{3/4}$ and the free-stream velocity U , as well as the airfoil motion, which are the pitch rate of $\dot{\alpha}$ and the acceleration of the free-stream velocity \dot{U} . To be noted that for VAWT applications, the free-stream velocity U defined above corresponds to the relative wind speed of V_{rel} in the AC model which is calculated from Equation (3.26). The variable of T_u , T_p and T_f in the ODEs are three time coefficients which are defined as follows.

$$T_u = c/(2U) \quad (6.13)$$

$$T_p = \tau_p c/(2U) = \tau_p T_u \quad (6.14)$$

$$T_f = \tau_f c/(2U) = \tau_f T_u \quad (6.15)$$

The three time coefficients correspond to the velocity, lag in pressure and lag in the boundary layer respectively. The non-dimensional time constants of τ_p and τ_f are dependent on the airfoil geometry. However, for the airfoils for wind energy applications, the value for the flat plate will have good agreements and could be used. To be noted that the above three variables are named *time constants* in [18] which is confusing because the free-stream speed U varies with time, and thus the three variables are not constant values.

For the coupled set of ODEs, the first two aerodynamic state variables of x_1 and x_2 are corresponding to the dynamics of the attached flow. The effective angle of attack α_E is calculated with the two state variables with the following equation.

$$\alpha_E = \alpha_{3/4}(1 - A_1 - A_2) + x_1(t) + x_2(t) \quad (6.16)$$

The unsteady lift coefficient for the attached flow is C_L^p which corresponds to the inviscid part of the unsteady lift and is as follows, where the last term is the torsion rate lift.

$$C_L^p = C_{L,\alpha}(\alpha_E - \alpha_0) + \pi T_u \dot{\alpha} \quad (6.17)$$

The last two variables are corresponding to the dynamic behaviour of the trailing edge separation. The variable of x_3 is used to model the time-lag effect between the pressure and the lift with $C_L^{p'} = x_3(t)$ which corresponding to an equivalent quasi-steady separation point $f' = f^{st}(x_3/C_{L,\alpha} + \alpha_0)$. And the fourth variable x_4 is to model the dynamics of the boundary layer which will cause the unsteady separation point of $f'' = x_4$ to lag behind the equivalent quasi-steady separation point of f' .

The dynamic lift coefficient could then be calculated as follows which is consisted of the circulatory part and the non-circulatory part.

$$C_L^{dyn} = C_{L,\alpha}(\alpha_E - \alpha_0)x_4(t) + C_L^{fs}(\alpha_E)(1 - x_4(t)) + \pi T_u \dot{\alpha} \quad (6.18)$$

$$C_L^{dyn} = C_{L,circ} + C_{L,tor} \quad (6.19)$$

The circulatory part is the weighted sum of the unsteady attached flow and the fully separated flow with the separation point $x_4 = f''$. And the non-circulatory part is due to the acceleration of the added mass, only the torsion rate is considered in the Risø model, and the other two terms are assumed to be much smaller compared to it [18]. For the dynamic drag coefficient, the explicit form of the equation is as follows.

$$C_d^{dyn} = C_D^{st}(\alpha_E) + (C_D^{st} - C_{D0}) \left(\frac{\sqrt{f^{st}(\alpha_E) - \sqrt{x_4}}}{2} - \frac{f^{st}(\alpha_E) - x_4}{4} \right) + (\alpha - \alpha_E) C_L^{dyn} \quad (6.20)$$

The dynamic drag coefficient consists of three parts, the first part is the steady drag coefficient corresponding to the effective angle of attack obtained from the airfoil polar. The second part is the contribution due to the trailing edge separation. And the third part is the induced drag which is due to the difference between the effective angle of attack α_E and geometric angle of attack α . The equation of the dynamic drag coefficient is then written as the sum of the three parts as follows.

$$C_d^{dyn} = C_{d,E} + C_{d,sep} + C_{d,ind} \quad (6.21)$$

6.1.3 Indicial formulation

The ODEs in the previous subsection is transformed into implicit indicial formulations in order to obtain the numerical solution with the computer code. The Duhamels integrals are employed, and the response of the state variables of current time-step is obtained from the value at the previous time-step with a decaying factor as well as an increment. The derivations are according to Hansen [18] and are summarised as follows.

General solution

The ODES are consisted of linear first order differential equations with the following form, the subscript i is from 1 to 4 representing the variables are corresponding to the equation of each state variable.

$$\dot{x}_i + P_i x_i = Q_i \quad (6.22)$$

With the general solution at time $t = t_e$ and $t = t_e + \Delta t$, it could be shown that the solution in the next time-step could be written as the solution in the current time-step with a decaying factor $C_{dec,i}$ and an increment factor $I_{new,i}$ as follows.

$$x_i(t_e + \Delta t) = C_{dec,i} x_i(t_e) + I_{new,i} \quad (6.23)$$

where

$$C_{dec,i} = e^{-\int_{t_e}^{t_e+\Delta t} P_i dt} \quad (6.24)$$

$$I_{new,i} = \int_{t_e}^{t_e+\Delta t} Q_i e^{-\int_{t_e}^{t_e+\Delta t} P_i d\tau} dt \quad (6.25)$$

Discretization

There are several discretization methods available, the most simple one is to assume the piecewise constant of P_i and Q_i , and there are also more complex methods with the assumption of linear or parabolic of P_i and Q_i . In this report, the assumption of piecewise constant of properties is used for simplicity. The Equations below are according to [18] with small modifications.

$$C_{dec,i} = e^{-\bar{P}_i \Delta t} \quad (6.26)$$

$$I_{new,i} = \frac{\bar{Q}_i^j}{\bar{P}_i^j} (1 - e^{-\bar{P}_i \Delta t}) \quad (6.27)$$

The piecewise constant values are approximated with the mean value of the time step $j-1$ and time step j .

$$\bar{P}_i^j = 0.5(P_i^{j-1} + P_i^j) \quad (6.28)$$

$$\bar{Q}_i^j = 0.5(Q_i^{j-1} + Q_i^j) \quad (6.29)$$

For the first two aerodynamic state variables of x_1 and x_2 , it could be obtained as follows.

$$\bar{P}_i^j = b_i \frac{U^j + U^{j-1}}{c} + \frac{\dot{U}^j + \dot{U}^{j-1}}{U^j + U^{j-1}} \quad (6.30)$$

$$\bar{Q}_i^j = \frac{b_i A_i}{c} (U^{j-1} \alpha_{3/4}^{j-1} + U^j \alpha_{3/4}^j) \quad (6.31)$$

The effective angle of attack at time-step j could then be calculated according to Equation (6.16) and is as follows.

$$\alpha_E^j = \alpha_{3/4}^j (1 - A_1 - A_2) + x_1^j + x_2^j \quad (6.32)$$

The dynamic lift coefficient corresponding to the attached flow is then.

$$C_L^{p,j} = C_{L,\alpha} (\alpha_E^j - \alpha_0) + \pi T_u \dot{\alpha}^j \quad (6.33)$$

For the last two aerodynamic state variables of x_3 and x_4 , the equations are then as follows.

$$\bar{P}_3^j = 0.5 \left(\frac{1}{T_p^j} + \frac{1}{T_p^{j-1}} \right) \quad (6.34)$$

$$\bar{Q}_3^j = 0.5 \left(\frac{C_L^{p,j}}{T_p^j} + \frac{C_L^{p,j-1}}{T_p^{j-1}} \right) \quad (6.35)$$

$$\bar{P}_4^j = 0.5 \left(\frac{1}{T_f^j} + \frac{1}{T_f^{j-1}} \right) \quad (6.36)$$

$$\bar{Q}_4^j = 0.5 \left[\frac{f_{st}(x_3^j / C_{L,\alpha} + \alpha_0)}{T_f^j} + \frac{f_{st}(x_3^{j-1} / C_{L,\alpha} + \alpha_0)}{T_f^{j-1}} \right] \quad (6.37)$$

6.1.4 Application in different flow conditions

The Risø dynamic stall model introduced previously in this section could be partially or fully applied depends on the application for different assumptions of the flow in the model. There will then be three different flow conditions which are summarised below in the order of increasing complexity.

- **Steady flow:** The first condition is the steady flow which means that none of the four aerodynamic state variables are used. Thus the unsteady effects are not modelled. And the only thing left in the Risø dynamic stall model is to evaluate the angle of attack at the three-quarter chord point which is equivalent to the method of modelling the flow curvature effect as in Chapter 5.
- **Dynamics of attached flow:** The second condition is the dynamics of the attached flow which corresponding to the inviscid flow. For this condition, the first two aerodynamic state variables of x_1 and x_2 are included and used to calculate the effective angle of attack α_E . And taking into account the torsion rate lift, the lift coefficient corresponding to dynamics of the attached flow could be calculated with Equation (6.17)
- **Dynamics of attached flow and TE separation:** The third condition is to take into account the dynamics of the attached flow as well as the dynamics of trailing ledge separation which is corresponding to the full Risø dynamic stall model. All the four aerodynamic state variables should be used, and the dynamic lift coefficient could be calculated with Equation (6.18).

6.2 Pirrung's extended Risø model

According to Pirrung [39], when applying the Risø dynamic stall model on the VAWT, there will be an issue that the wind turbine is generating net power even with the zero incoming wind speed condition. In order to solve this issue, a modification to the original Risø dynamic stall model for the VAWT application is introduced by Pirrung [39], and it has been validated analytically the extended model is able to solve this issue. The explicit formulation of the original Risø model is also simplified in [39] with a different formulation from the original Risø model in [18] which will be discussed in this section.

6.2.1 Pirrung's simplification

According to Pirrung [39], the calculation of the effective angle of attack α_E could also be written in the following form.

$$\alpha_E = \alpha_{3/4}(1 - A_1 - A_2) + \frac{y_1(t)}{U} + \frac{y_2(t)}{U} \quad (6.38)$$

The indicial formulations of the aerodynamic state variables of y_1 and y_2 are given as follows.

$$y_i(t) = y_i(t - \Delta t)e^{-b_i \Delta t / T_u} + \frac{1}{2}(\alpha_{3/4}(t - \Delta t) + \alpha_{3/4}(t))A_i U(t)(1 - e^{-b_i \Delta t / T_u}) \quad (6.39)$$

The detailed derivation is not given by Pirrung [39] but the detailed derivation will be done by the author in the Appendix A.4 according to the steps of the derivation of the original Risø model in [18]. The Equation (6.38) is equivalent to the Equation (6.16) and the difference is what the aerodynamic state variables are used. The relationship of the aerodynamic state variables is $y_i = U x_i$.

To be noted that the aerodynamic state variables of y_1 and y_2 in Equation (6.38) are noted as x_1 and x_2 by Pirrung [39] which may cause confusion. In this report, the notation of y_1 and y_2 used with the definition to be identical with that in [18] to avoid confusions.

6.2.2 Pirrung's modification

The Risø dynamic stall model is modified by Pirrung for the VAWT applications to deal with the issue that the rotor is generating net torque with zero wind speed condition. The modification could be summarised into four different parts which are summarised as follows.

Formulation of effective angle of attack

The first part is the formulation of the effective angle of attack which is different from that of Equation (6.16). The equation of the effective angle of attack for the Pirrung's modification method is as below.

$$\alpha_E = \alpha_{3/4} - \frac{g_1(t)}{U} - \frac{g_2(t)}{U} \quad (6.40)$$

The corresponding indicial formulation of the state variables are given and are as below.

$$g_i(t) = g_i(t - \Delta t)e^{-b_i \Delta t / T_u} + (w_{3/4}(t) - w_{3/4}(t - \Delta t)) \frac{A_i}{b_i} \frac{T_u}{\Delta t} (1 - e^{-b_i \Delta t / T_u}) f_{scale} \quad (6.41)$$

The Equation (6.40) is not in the same form as Equation (6.16) or Equation (6.38) with the terms of $(1 - A_1 - A_2)$ disappeared. The aerodynamic state variables of g_1 and g_2 are noted as x_1 and x_2 by Pirrung [39] which may cause confusion. Thus, the notation of g_i is used to distinguish from x_i and y_i .

According to Pirrung [39], the extended method will be almost identical to the original Risø model when letting the variable of $f_{scale} = 1$. The details of the derivation of the equations with similar method as that in [18] will be in the Appendix A.5.

Introducing a scaling factor

There is a scaling factor introduced which is equal to the trailing edge separation position of the previous time step.

$$f_{scale} = f_{sep}(t - \Delta t) = x_4(t - \Delta t) \quad (6.42)$$

According to Pirrung [39], the additional shed vorticity in full stall condition is removed by introducing the scaling factor, and thus reduces the prediction of the lag of angle of attack.

Dynamic lift coefficient.

The total dynamic lift coefficient is then consisted of three different parts as follows.

$$C_L^{dyn} = C_{L,circ} + C_{L,tor} + C_{L,acc} \quad (6.43)$$

The first term in the RHS of Equation (6.43) is the circulatory lift which is identical to the first term in the RHS of Equation (6.18), and is as follows.

$$C_{L,circ} = C_{L,\alpha}(\alpha_E - \alpha_0) \quad (6.44)$$

And the non-circulatory part of the lift is consisted of the contribution due to the torsion rate and due to the acceleration of the blade. The second term in the RHS of Equation (6.43) is the torsion lift which is defined different with that in Equation (6.18). Both the torsion rate due to the variation of angle of attack and due to the variation of the azimuthal angle are taken into consideration. And the notation of $\dot{\vartheta}$ is used instead of $\dot{\theta}$ as in [39] to avoid confusion with the azimuthal angle.

$$C_{L,tor} = \pi T_u \dot{\vartheta} = \pi T_u (\dot{\alpha} - \omega) \quad (6.45)$$

The last term in the RHS of Equation (6.43) is the contribution due to the acceleration. According to Pirrung [39], the airfoil is having a constant acceleration \ddot{y} perpendicular to the chord towards the rotational centre due to the circular motion of the VAWT blades. The explicit form of the contribution is as follows.

$$C_{L,acc} = -\pi T_u \frac{\ddot{y}}{U} \quad (6.46)$$

Dynamic drag coefficient

The drag coefficient in the Pirrung's extended dynamic stall model is as follows.

$$C_d^{dyn} = C_{d,E} + C_{d,sep} + C_{d,ind} + C_{d,tor} \quad (6.47)$$

$$C_{d,ind} = C_{L,circ}(\alpha_{3/4} - \alpha_E) \quad (6.48)$$

$$C_{d,tor} = -C_{L,circ} T_u \dot{\vartheta} \quad (6.49)$$

There are two differences between the original formulation in Equation (6.20) and the equation above. The first difference is the induced drag coefficient is based on the circulatory lift coefficient instead of the complete dynamic lift coefficient. And the second difference is the drag coefficient due to torsion rate is introduced.

6.3 Validation of the inviscid part of Risø model

In this section, the step response of the NACA0015 airfoil is firstly investigated with the panel code, and the coefficients of the airfoil are obtained numerically. The performance of the inviscid part of the Risø dynamic stall model is then validated for the harmonic pitching motion by comparing the results from the inviscid Risø model with that from the panel code of U2DiVA.

6.3.1 Investigation with step response

In the first two equations of the coupled set of ODES in Equation (6.9) and (6.10) for the first two aerodynamic state variables, the four variables of A_1, A_2, b_1, b_2 are four coefficients which are dependent on the airfoil geometry. For the infinitely thin airfoil which is also called the *flat plate*, the response of the step change of angle of attack was solved analytically by Wagner[48] and is usually approximated by two time-lags as follows.

$$\phi(s) = 1 - A_1 e^{-b_1 s} - A_2 e^{-b_2 s} \quad (6.50)$$

The most commonly used approximation to the Wagner function is by Jones [22] with the coefficients listed in Table 6.1. However, for the airfoils in reality with finite thickness, the response will be different from the flat plate. The step response of the Risø A1-24 airfoil with 24% thickness is calculated with the panel code by Hansen [18] and is shown to have a significant difference from that of the flat plate. The step response of the Risø A1-24 airfoil with finite thickness is lagging behind that of the flat plate. The coefficients for the A1-24 airfoil could be obtained numerically by minimising RMS of the error between the approximation response curve with two time-lags and the response curve from the panel code.

Table 6.1: *Approximated coefficients for the inviscid step response.*

	A_1	A_2	A_3	A_4
Flat plate (Jones [22])	0.1650	0.3350	0.0455	0.3000
NACA0015 airfoil	0.2072	0.3474	0.0525	0.2612

The airfoil used in this report is NACA0015 with the thickness of 15% which is smaller than the Risø A1-24 airfoil. The step response of the NACA0015 airfoil for a step change of angle of attack is calculated with the panel code of U2DiVA. The coefficients for this airfoil could also be obtained numerically by minimising the RMS of the error between the approximated response curve with the two time-lags with the response curve from the panel code. The method is similar to that in [18], and the approximated coefficients are

listed in Table 6.1. The step response of the NACA0015 airfoil from the panel code is plotted together with the numerical approximation of it calculated above as well as the Jones approximation for the flat plate in Figure 6.1. To be noted that the x -axis is the non-dimensioned time τ which is defined as $\tau = 2Ut/c$. It could be concluded from the figure that the approximated curve is having good agreements with that from the panel code with the maximum relative error to be 0.83%. As a result, the numerical method of minimising the RMS error is sufficient.

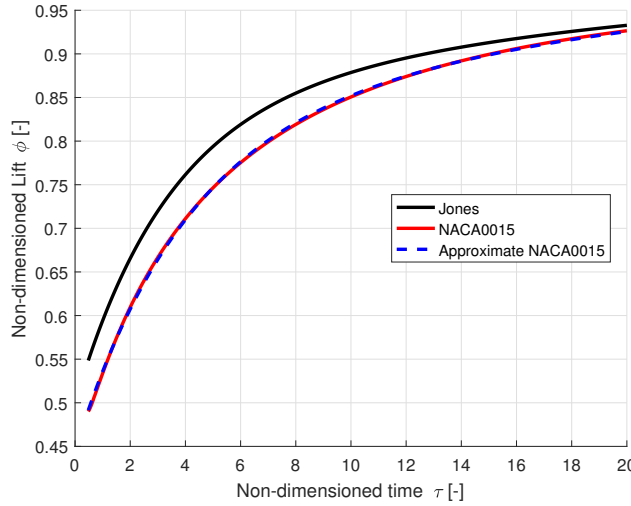


Figure 6.1: The step response of the NACA0015 airfoil and the flat plate.

The instantaneous response of the step change of angle of attack corresponds to the condition of $s = 0$ in Equation (6.50) which is then $\phi(0) = 1 - A_1 - A_2$. For the flat plate with Jones approximation which is listed in Table 6.1, the instantaneous response is $\phi(0) = 0.5$ which means that half of the change of the lift is obtained instantaneously. For the NACA0015 airfoil, the instantaneous response is $\phi(0) = 0.4454$ which could be calculated from the coefficients in Table 6.1. This means that less than half of the change is obtained instantaneously for the NACA0015 airfoil. It could also be visualised from Figure 6.1 that the response curve of the NACA0015 airfoil which has finite thickness lag behind that of the flat plate. This lag effect could also be visualised for the Risø A1-24 airfoil in [18] which also have finite thickness.

6.3.2 Validation with harmonic pitching

As mentioned by Hansen [18], the method of using downwash at the three-quarter chord point is developed for the infinitely thin airfoil, and it is not theoretically proven whether this method could be used for the airfoil with finite thickness. The performance of the model should then be validated and the harmonic pitching motion is favourable for the validation due to its simplicity.

The full Risø dynamic stall model has been validated with the response of the Risø A1-24 airfoil with harmonic pitching motion by Hansen [18]. In that validation, two sets of

coefficients are used in the dynamic stall model which are the approximated coefficients for the Risø A1-24 airfoil calculated with minimising RMS method and the Jones approximation for the flat plate. The results are validated by comparing the response with that calculated from the Navier-Stokes solver of *EllipSys2D*. In the validation, it is concluded there will be significant derivation when using the Jones approximation for the flat plate, but the results will have good agreements with results from N-S solver when using the approximated coefficients for the Risø A1-24 airfoil.

For the validation in this report, instead of validating the full Risø dynamic stall model using the N-S solver, the inviscid part of the Risø dynamic stall model is validated with the panel code of U2DiVA. The details of the validation will be introduced as follows.

Setup of the harmonic pitching

For the validation, the airfoil is set to pitch about the zero angle of attack with a sine function as below. The variable of ω_p is the angular frequency for the harmonic pitching motion, with the subscript of p representing pitching, the notation is to avoid confusion with angular speed of the rotor ω .

$$\alpha_g = \alpha_m \sin \omega_p t \quad (6.51)$$

The angular frequency ω_p is determined by the reduced frequency k which is defined as follows.

$$k = \omega_p c / (2V_\infty) \quad (6.52)$$

Additional angle of attack due to pitching

According to Hansen [18], the geometric angle of attack should take into account the motions of the airfoil. For the setup in this validation, the pitching axis is located at the quarter chord point. As a result, there is no extra motion at the quarter chord point due to pitching. However, there will be additional motion at the location of the three-quarter chord point due to pitching which is visualised in Figure 6.2.

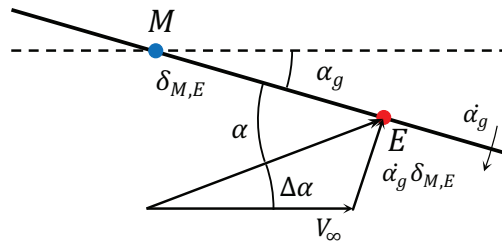


Figure 6.2: The additional angle of attack due to pitching motion.

When the additional velocity of $\alpha_g \delta_{M,E}$ is small compared to the free wind speed of V_∞ and the amplitude of the pitching angle is small, the additional angle of attack could be

estimated with the following equation.

$$\Delta\alpha \approx \frac{\dot{\alpha}_g \delta_{M,E}}{V_\infty} = \frac{\alpha_m \omega_p \cos(\omega_p t) \delta_{M,E}}{V_\infty} \quad (6.53)$$

To be noted that the variable of $\delta_{M,E}$ is the distance between the mounting point and the evaluation point which is the three-quarter chord point. And for the current setup with the mounting point to the quarter chord point, $\delta_{M,E} = c/2$ and the Equation (6.53) could then be simplified as follows.

$$\Delta\alpha = \frac{\omega_p c}{2V_\infty} \alpha_m \cos(\omega_p t) = k \alpha_m \cos(\omega_p t) \quad (6.54)$$

When the additional velocity of $\dot{\alpha}_g \delta_{M,E}$ is not small enough or the amplitude of the pitching is large, the result should then be determined with the law of sine as well as inverse trigonometric function as follows.

$$\Delta\alpha = \tan^{-1} \left(\frac{1}{\frac{V_\infty}{\dot{\alpha}_g \delta_{M,E} \cos \alpha_g} + \tan \alpha_g} \right) \quad (6.55)$$

Comparison of the results

The results that calculated with the inviscid part of the dynamic stall model with the two different sets of the coefficients, which are Jones approximation for flat plate and the numerical approximation for NACA0015 airfoil. The results are compared with that calculated from the panel code of U2DiVA for the validation.

Firstly, the effective angle of attack calculated from the inviscid part of dynamic stall model with the two sets of coefficients are compared with the angle of attack at quarter chord point as well as the three-quarter chord point calculated from the panel code. The results are plotted in Figure 6.3. It should be noted that the angle of attack from the panel code will take into account of the motion of the airfoil as well as the downwash. As a result, the variable will then corresponding to the effective angle of attack at the aforementioned two points.

It could be visualised from the figure that when using the approximated coefficients for NACA0015 airfoil, the effective angle of attack from the dynamic stall model will have good agreements with the angle of attack at three-quarter chord point from the panel code. However, the result will have visible differences when using the coefficients for the Jones approximation for the flat plate.

Secondly, the inviscid lift coefficient from the dynamic stall model is calculated with Equation (6.17) for the two sets of coefficients and are compared with that from the panel code. The lift coefficient for the angle of attack at quarter chord point as well as three-quarter chord point are calculated from the panel code. It could be determined from the results that there are only small differences and the values of the two variables are almost identical. This conclusion is consistent with that in subsection 5.3.2. As a result, the lift coefficient at quarter chord point from the panel code is used for the validation. The results are plotted in the Figure 6.4.

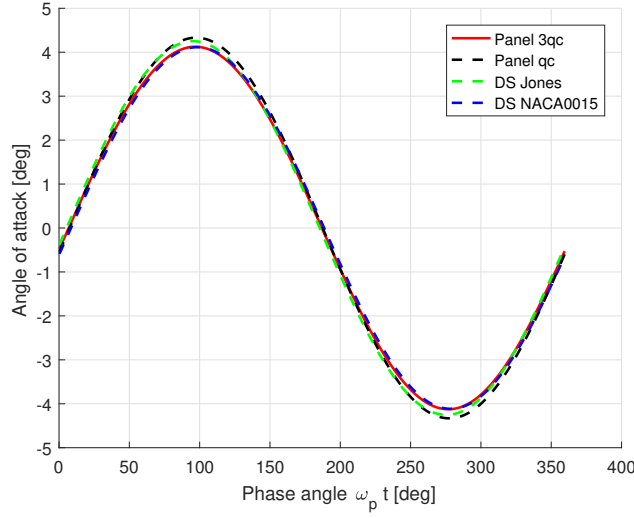


Figure 6.3: Validation of the inviscid part of Risø dynamic stall model with the azimuthal variation of angle of attack.

It could be visualised from Figure 6.4 that the lift coefficient calculated from the inviscid part of the dynamic stall model with the approximated coefficients for the NACA0015 airfoil is having good agreements with that from the panel code. However, there is a significant difference when using the Jones approximation for the flat plate.

In conclusion, the inviscid part of the dynamic stall model is sufficient to model the dynamics of the attached flow with the coefficients obtained for the airfoil. When using the Jones approximation for the flat plate, there will be some difference of the results compare to that of the panel code.

6.4 Coupling dynamic stall model with AC model

In this section, the method of coupling the dynamic stall model with the Actuator Cylinder model is introduced. The coupled model is named dynamic Actuator Cylinder model. There will be the flowchart illustrating the calculation procedure followed by some specifications of the implementation.

6.4.1 The flow chart of implementation

The flowchart of the coupled dynamic AC model is in Figure 6.5 as follows.

According to the flowchart, the dynamic stall model that coupled with the AC model could be considered as a modification to the AC model that the lift and drag coefficients are calculated from the dynamic stall model. Thus the dynamic effects are taken into consideration. This is different from the previous AC models that the lift and drag coefficients are directly determined from the airfoil polar with the geometric angle of attack.

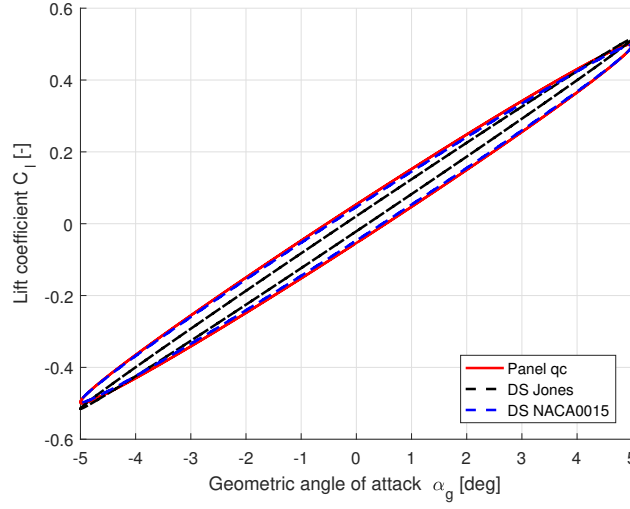


Figure 6.4: Validation of the inviscid part of Risø dynamic stall model with the lift coefficient versus angle of attack.

With the dynamic stall model coupled with the AC model, the AC model will then become a quasi-steady model instead of a *dynamic* model. This is because for a variation of the flow in the upstream of the rotor, there will be instantaneous effects on the downstream of the rotor which is the inherent characteristic of the AC model. In reality, there will be a lag effect due to the shed of vortices which could not be modelled with this quasi-steady model.

6.4.2 Transform between discretization methods

To be noted that in the Risø dynamic stall model with the indicial formulations as in subsection 6.1.3, the calculation is based on the variables at the current time step and the previous time step. This requires the time t to be discretized into time steps with the spacing of Δt . For the AC model, the azimuthal angle is discretized into sections whose properties are represented by the control points with the azimuthal spacing of $\Delta\theta$. With the AC discretized into N sections, the period of the rotation for one revolution should also be discretized into N sections. The relationship between the spacing of Δt and $\Delta\theta$ could then be obtained with Equation (6.56).

$$\Delta t = \frac{T}{N} = \frac{2\pi}{\omega N} = \frac{\Delta\theta}{\omega} = \frac{R\Delta\theta}{\lambda V_\infty} \quad (6.56)$$

With this relationship, the azimuthal location of the control points could then be transformed to the corresponding time steps.

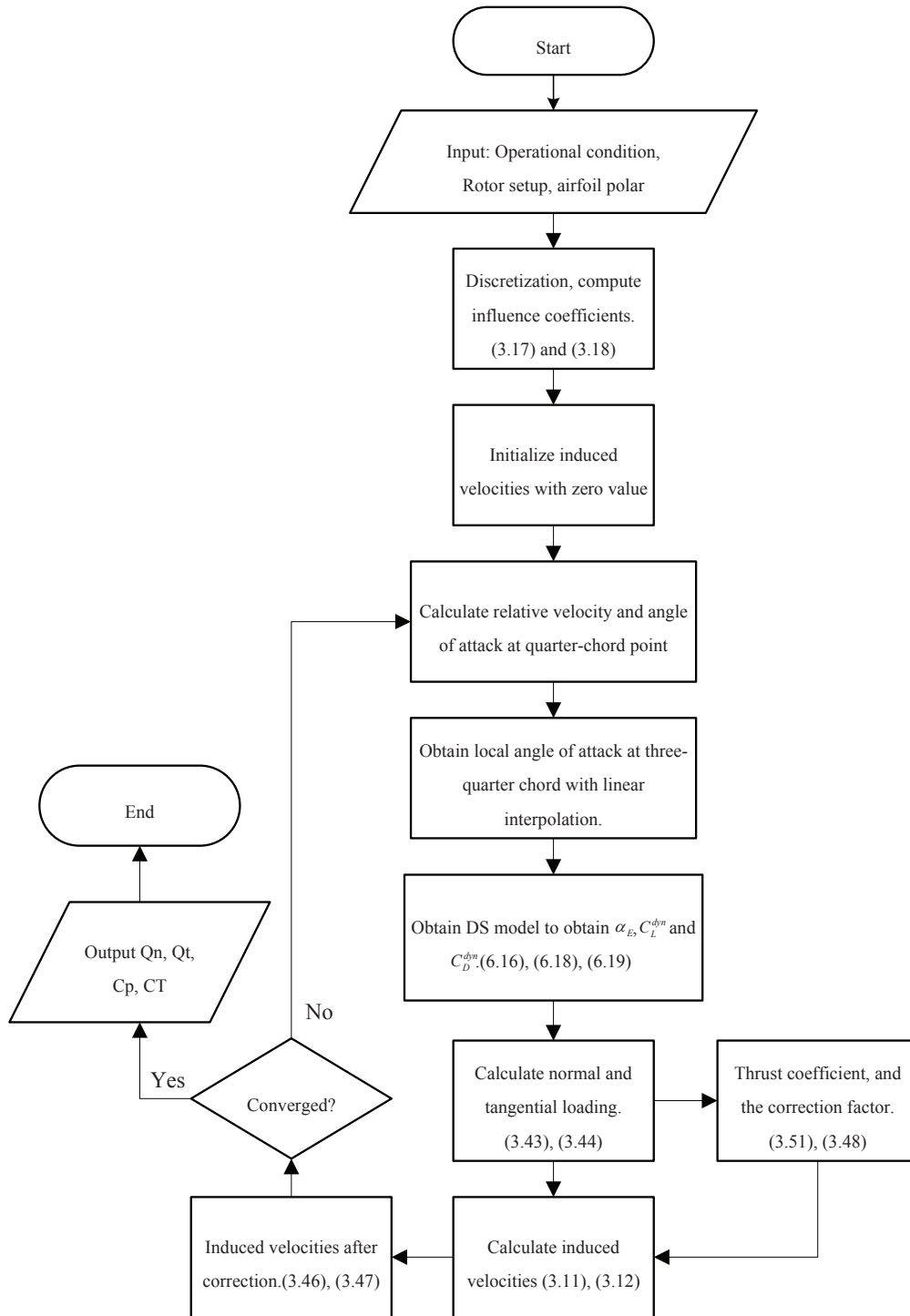


Figure 6.5: Flowchart of the iteration process for the coupled dynamic Actuator Cylinder model.

6.4.3 Two different dynamic AC models

With the dynamic stall model coupled with the AC model, the coupled dynamic AC model is then obtained. Even though there are four different AC models according to section 5.4, there will only be two dynamic AC models which correspond to the AC2 and AC4 model. The two models are named AC_2^{dyn} and AC_4^{dyn} for abbreviation. This is because of the requirement of evaluating the angle of attack at three-quarter chord point which is not applicable for AC1 and AC3 model. The AC_2^{dyn} and AC_4^{dyn} model then corresponds to the original AC model and Cheng's AC model respectively, the induced velocities for the two models are then dependent on only normal loading and normal as well as tangential loadings respectively.

6.5 Direction of applying the lift force

There is an important aspect to be determined when coupling the dynamic stall model in the AC model which is the direction to apply the lift force. This issue of determining the lift force direction is also encountered in the previous chapter when applying the flow curvature model but used the conclusion obtained in this chapter. The details of determining the direction of applying the lift force will be discussed in this section.

For simplicity, the inviscid flow condition is assumed in this section. For the airfoil in the uniform inviscid flow, there will be zero drag force in the direction of the incoming wind. For the VAWT blade, the local angle of attack varies along the airfoil due to the flow curvature effect. However, the total aerodynamic force of the whole airfoil will still be a single vector in a certain direction. For the inviscid flow, the total aerodynamic force is then the lift force and is perpendicular to the local relative wind speed at a certain location on the airfoil. Thus, there will be no drag components in the direction of the local relative wind speed at this location. This location on the airfoil should then be determined.

6.5.1 Definition of two types of angle of attack

In order to clarify the problem, two types of angle of attacks are firstly defined here.

- The type-one angle of attack α_1 is defined as the local angle of attack on the airfoil that the total lift force $C_{L,1}$ is perpendicular to it. There will be zero drag component in the direction of α_1 for the inviscid flow.
- The type-two angle of attack α_2 is defined as the local angle of attack at an arbitrary point on the airfoil. The lift and drag coefficient of $C_{L,2}$ and $C_{d,2}$ corresponding to this angle of attack α_2 is then the decomposition of the total lift coefficient $C_{L,1}$ corresponding to type-one angle of attack α_1 and is visualised in Figure 6.6.

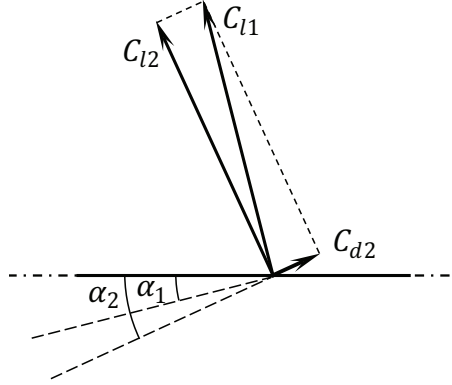


Figure 6.6: Decomposition of the total lift for the type-one angle of attack to lift and drag for the type-two angle of attack.

The decomposition is as follows which is similar to that of Equation (5.29) and (5.30).

$$C_{L,2} = C_{L,1} \cos(\alpha_2 - \alpha_1) \quad (6.57)$$

$$C_{d,2} = C_{L,1} \sin(\alpha_2 - \alpha_1) \quad (6.58)$$

Similar to subsection 5.3.2, if the difference between the two types of the angle of attacks of α_1 and α_2 is relatively small, the lift coefficient of $C_{L,2}$ and $C_{L,1}$ will then be approximately equal. And the difference is then mainly the drag coefficient. For the implementation in the AC model, the results are only dependent on the type-one angle of attack α_1 but not on the type-two angle of attack α_2 . This is because the lift and drag coefficients for the type-two angle of attack is the decomposition of that corresponding to the type-one angle of attack. And the choice of α_2 is arbitrary as long as the corresponding lift and drag coefficients are calculated correctly with Equation (6.57) and (6.58). As a result, the type-one angle of attack should be determined correctly. Otherwise, the drag coefficients will not be correctly determined which results in the derivation of the normal and tangential loadings.

It should be noted that in Equation (6.57) and (6.58), the transformation of the lift and drag forces are directly written in the form of lift and drag coefficient which means it is implicitly assumed that the relative wind speed corresponding to the two locations are identical. In reality, the relative wind speed at the two locations will have a small phase difference according to subsection 5.2.2 but is neglected in this section for simplicity.

6.5.2 Different possible type-one angle of attacks

There are different possibilities for the choice of the type-one angle of attack. Thus, different possible methods should be investigated in detail.

Risø dynamic stall model

Firstly, the details about the direction of applying the lift force in the Risø dynamic stall model is investigated. In the model, the dynamic lift force is applied perpendicular to the direction of the effective angle of attack of α_E , and the corresponding drag force will be zero for the inviscid flow condition [18]. This could be visualised in Figure 6.7. As a result, it could be indicated that the type-one angle of attack is the effective angle of attack α_E which is calculated from the geometric angle of attack at three-quarter chord point.

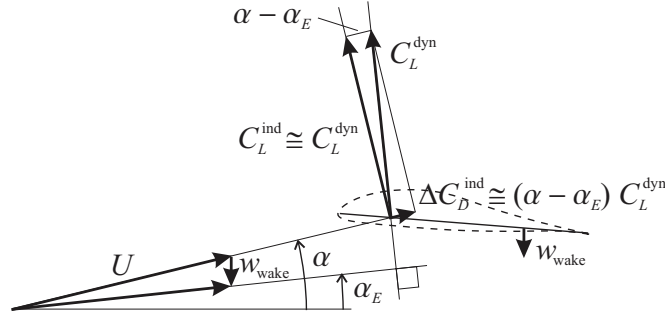


Figure 6.7: The decomposition of the lift and drag coefficient in Risø dynamic stall model [18].

In the Risø model, the terms of induced lift and drag force are introduced which are corresponding to the geometric angle of attack α , and are calculated from the decomposition of the dynamic lift coefficient C_L^{dyn} which could be visualised in Figure 6.7. The induced lift and drag coefficients are calculated with the following equations.

$$C_L^{ind} = C_L^{dyn} \cos(\alpha - \alpha_E) \approx C_L^{dyn} \quad (6.59)$$

$$C_d^{ind} = C_L^{dyn} \sin(\alpha - \alpha_E) \approx C_L^{dyn} (\alpha - \alpha_E) \quad (6.60)$$

The equations of the induced lift and drag coefficients are in the same form of the lift and drag coefficients as that of the type-two angle of attack in Equation (6.57) and (6.58). As a result, the geometric angle of attack α in the Risø model is then the type-two angle of attack α_2 .

Geometric AoA at three-quarter chord point

There is another method which is to let the type-one angle of attack to be $\alpha_{3/4}$ which is the local geometric angle of attack at three-quarter chord point.

Geometric AoA at quarter chord point

Another possible method is to let α_1 to be the local geometric angle of attack $\alpha_{1/4}$ which could be considered as a modification to the Risø dynamic stall model. This method has

been validated in Chapter 5 for the case of neglecting all the aerodynamic state variables in the Risø dynamic stall model, which is for steady flow condition. However, whether this method is still valid for the inviscid part of the Risø dynamic stall model should be validated.

Effective AoA at quarter chord point

There is also another possible method that the type-one angle of attack is the *effective* angle of attack at the quarter chord point $\alpha_{E,1/4}$. The effective angle of attack α_E defined previously is corresponding to the effective downwash at the three-quarter chord point which could be calculated from the local geometric angle of attack at the three-quarter chord point $\alpha_{3/4}$ and the dynamic effects are modelled by aerodynamic state variables as in Equation (6.16). The effective angle of attack at quarter chord point $\alpha_{E,1/4}$ is defined to be corresponding to the angle of attack at quarter chord point with dynamic effects due to the wake.

The reason of introducing this variable is to correspond to the angle of attack at the quarter chord point calculated from the panel code which is different from the geometric angle of attack. Similar to the angle of attack at three-quarter chord point calculated from the panel code, the angle of attack at quarter chord point from the panel code will also take into consideration of dynamic effects due to the downwash due to the wake. However, the value of $\alpha_{E,1/4}$ could not be calculated directly because the dynamic effects at the quarter chord point could not be calculated directly with the current dynamic stall model. There is a possible method which is to assume the difference between the effective angle of attack and the geometric angle of attack at the quarter chord point is approximately equal to that at the three-quarter chord point.

$$\alpha_E - \alpha_{E,1/4} \approx \alpha_{3/4} - \alpha_{1/4} \quad (6.61)$$

The effective angle of attack at quarter chord point $\alpha_{E,1/4}$ could then be approximated as follows.

$$\alpha_{E,1/4} \approx \alpha_E - (\alpha_{3/4} - \alpha_{1/4}) \quad (6.62)$$

6.5.3 Reasoning with the bound vortex

The Risø dynamic stall model is a B-L type dynamic stall model which is derived from the Theodorsen theory for the flat plate. The vortex distribution on the flat plate can be modelled with a lumped-vortex element located at the aerodynamic centre which is the quarter chord point [23]. This vortex is then the bound vortex for the lifting line model. The collocation point is the three-quarter chord point which satisfies the boundary condition of the airfoil. The strength of the bound vortex is then estimated with the downwash $w_{3/4}$ calculated at the collocation point which is the three-quarter chord point [23]. With the Kutta-Joukowski theorem, the lift is then directly calculated from the bound vortex, and the direction is perpendicular to the local relative velocity at the quarter chord point of the airfoil where the bound vortex is located. In the Risø dynamic stall model, the

lift coefficient is determined with the effective angle of attack α_E , which is equivalent to determine the strength of the bound vortex with the downwash at the three-quarter chord point as mentioned before. The direction of the lift force should then be perpendicular to the angle of attack at quarter chord point, which is then the type-one angle of attack.

For the first two methods as above, the type-one angle of attack is assumed to be the effective and geometric angle of attack at three-quarter chord point of the airfoil respectively, which do not coincide with the reasoning with the bound vortex. For the last two methods, the type-one angle of attack is the geometric and effective angle of attack at the quarter chord point which satisfies the reasoning in this subsection.

6.6 Validation of the direction of lift force

According to the previous section, there are four different methods of choosing the type-one angle of attack which could be the local geometric or effective angle of attack at quarter chord point or three-quarter chord point. The different methods are validated, and finally, the method with the best agreements with the panel code will be chosen for the implementation in the coupled dynamic AC model. To be noted that only the inviscid part of the dynamic stall model is included in the coupled dynamic AC model in this section in order to be validated with the panel code.

6.6.1 Validation of drag coefficient from panel code

According to the definition of the type-one angle of attack, there is no drag force component corresponding to this angle of attack. The drag coefficient from the panel code is then able to be used to verify which is the type-one angle of attack. The drag coefficient from the panel code in both the directions of the angle of attack at quarter chord point and at the three-quarter chord point should then be plotted versus the corresponding angle of attack, which has already been done previously in Figure 5.14b and 3.24b respectively. It could then be concluded that the drag coefficient corresponding to the angle of attack at quarter chord point is generally around zero value, while the drag coefficient corresponding to the angle of attack at three-quarter chord point is generally increasing with this angle of attack. It could then be concluded that the type-one angle of attack is neither the geometric nor effective angle of attack at the three-quarter chord point. The conclusion is identical with the reasoning with the bound vortex in subsection 6.5.3.

As a result, the direction of applying the lift force in the Risø dynamic stall model is not sufficient. There are then two possible methods for the modification to the Risø model which are letting the type-one angle of attack to be the geometric or the effective angle of attack at the quarter chord respectively. The two methods are named M_1 and M_2 respectively for abbreviation of modified method of 1 and 2. The two methods should then be further validated.

6.6.2 Validation of loadings from the AC model

The two methods of M_1 and M_2 are able to be validated by comparing the normal and tangential loadings calculated from the corresponding modified dynamic AC models and compared with that from the panel code. It has been introduced previously in subsection 6.4.3 that there are two dynamic AC models which are AC_2^{dyn} and AC_4^{dyn} respectively, both of them are used for the validation. To be noted that, there are two different Mod-Lin correction methods which are the original one with Equation (3.48) as well as the Cheng's modified Mod-Lin correction method with Equation (3.53). In order to obtain sufficient conclusion, the results from both of the methods are validated.

Original Mod-Lin correction method

Firstly, the two methods of M_1 and M_2 are validated with the original Mod-Lin correction. The results of normal and tangential loadings from the two corresponding modified AC models are compared with that from the panel code in Figure 6.8.

It could be visualised from the figure that the results of the normal loadings from the two methods of M_1 and M_2 are almost identical with each other, and the results are also having good agreements with the panel code. The two modified dynamic AC models underestimate the normal loadings at the azimuthal angle about 90° as well as about 270° . For the tangential loading, the results from the two methods of M_1 and M_2 have some difference. Upon initial inspection for the windward part, the magnitude of tangential loading is underestimated by the M_2 method while the M_1 method is having good agreement with panel code. However, it could not be concluded that the M_2 method is more sufficient than M_1 model. This is because the aim of applying the dynamic stall model is to model the lag effects due to the unsteady aerodynamics as in Figure 5.11. There is visible phase lead of the tangential loading from the M_1 method compare with that from the panel code, which indicates the phase lag is not sufficiently modelled with the M_1 method. The phase lag effect is well modelled with the M_2 method. As a result, the conclusions could not be made yet. Further validation of the M_1 and M_2 method with Cheng's modified Mod-Lin correction is favourable.

Cheng's Mod-Lin correction method

Secondly, the results of normal and tangential loadings calculated with the M_1 and M_2 methods with the Cheng's modified Mod-Lin correction method are compared with that from the panel code in Figure 6.9.

From the figure, it could be visualised that the normal loadings from the M_1 and M_2 methods are also almost identical with each other and are having good agreements with that from the panel code. The tangential loadings from the two methods are having some difference. The M_1 method overestimates the amplitude of the tangential loading for both the windward and leeward part of the rotor. And with the M_1 method, the phase lag of

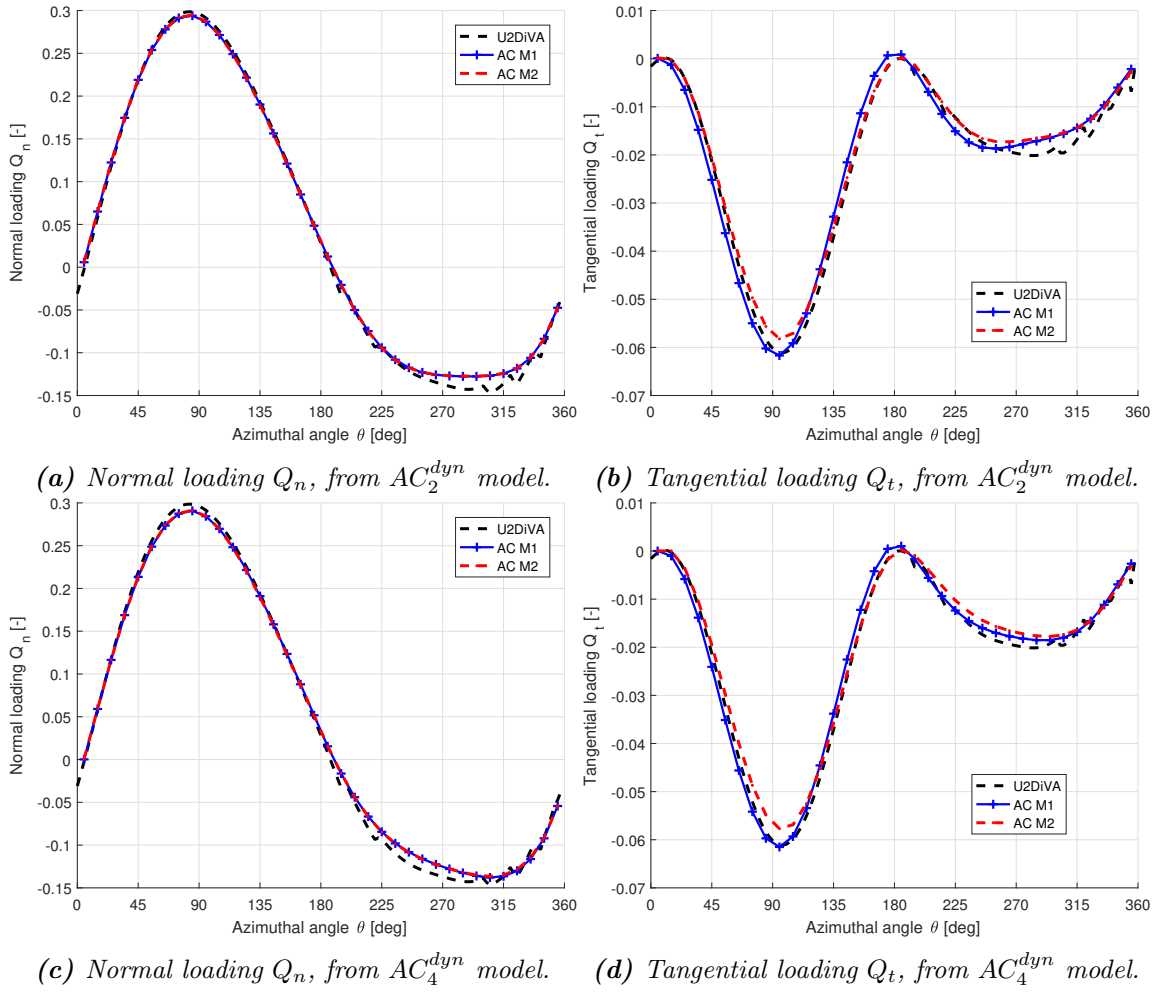


Figure 6.8: Validation of the normal and tangential loading for the M_1 and M_2 method with original Mod-Lin correction, with $\lambda = 4$, $\sigma = 0.07$, $B = 2$.

the tangential loading could not be well modelled. The tangential loading calculated with M_2 method is having good agreements with that from the panel code with phase lag effect well modelled.

Summarising the validation of the M_1 and M_2 in this section, it is concluded that the M_2 method is more sufficient than the M_1 method because the phase lag of the tangential loadings is more sufficiently modelled with the M_2 method. As a result, the type-one angle of attack should then be the effective angle of attack at quarter chord point. It can also be concluded that the results of the loadings will have better agreements if using Cheng's modified Mod-Lin correction method. As a result, the M_2 and Cheng's Mod-Lin correction methods are then implemented in the dynamic AC model, and the performance of this model will be further validated.

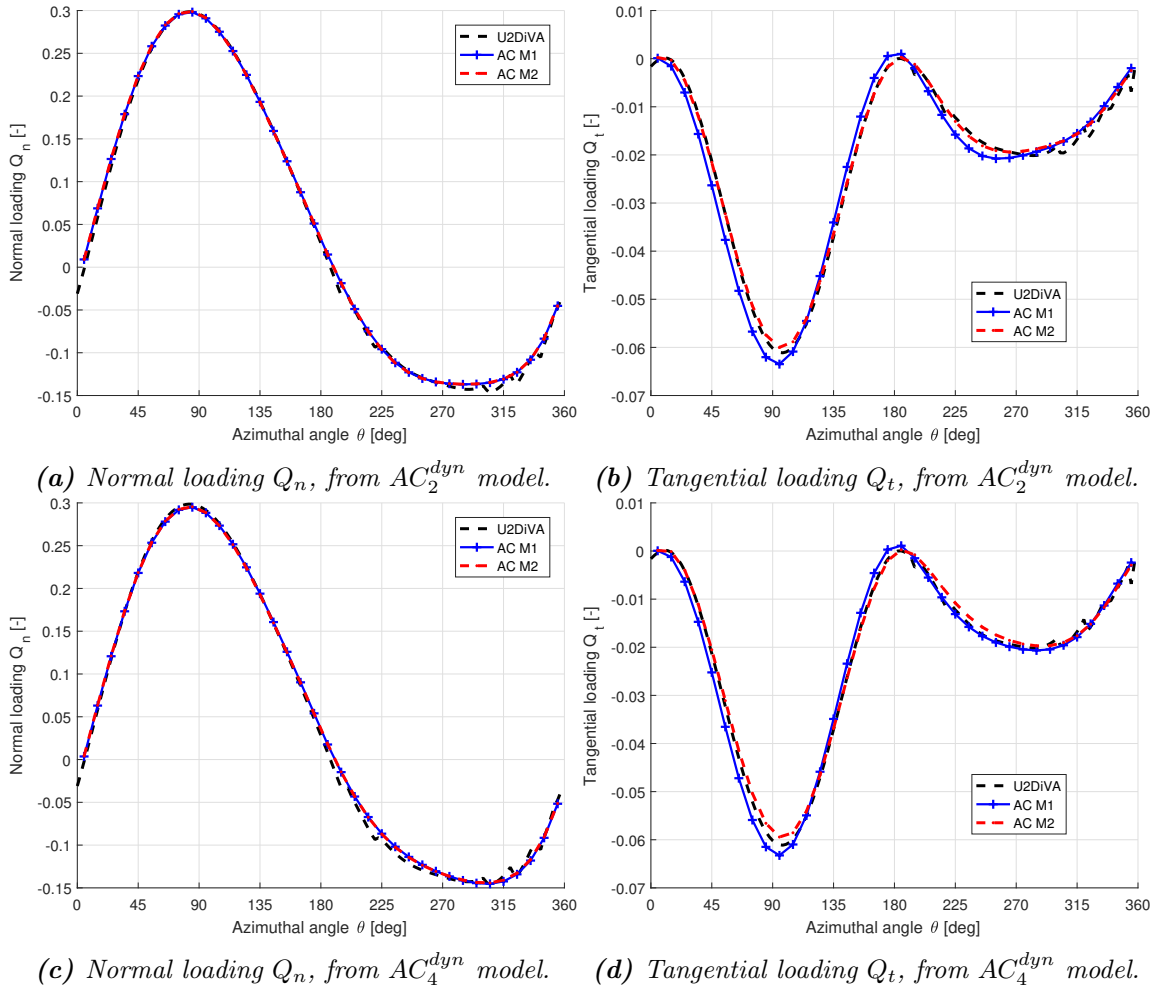


Figure 6.9: Validation of the normal and tangential loading for the M_1 and M_2 method with Cheng's Mod-Lin correction, with $\lambda = 4$, $\sigma = 0.07$, $B = 2$.

6.7 Performance of dynamic AC model

With the coupled dynamic AC model obtained in the previous section, the performance of the inviscid part of the coupled model will be investigated in this section by comparing with the panel code. Firstly, the two possible dynamic AC models which are according to subsection 6.4.3 will be compared. It will also be determined which model is having better agreements with the panel code and this model will then be chosen. Secondly, the performance of the chosen dynamic AC model is investigated with detailed comparison of the variables with that from the panel code and conclusions will be made. To be noted that only the inviscid part of the dynamic stall model is coupled with the AC model, which is for the validation with the panel code.

6.7.1 Comparison of two dynamic AC models

There are two different dynamic AC models according to subsection 6.4.3 which are AC_2^{dyn} and AC_4^{dyn} . For the comparison, the type-one angle of attack is the effective angle of attack at quarter chord point and the Cheng's modified Mod-Lin correction method is used, which is consistent with the conclusion of the validation in subsection 6.6.2. The normal and tangential loadings are calculated from the two dynamic AC models and are compared with that from the panel code for different load cases in Figure 6.10. There are more results of the normal and tangential loading for different load cases in Figure B.7 in the Appendix.

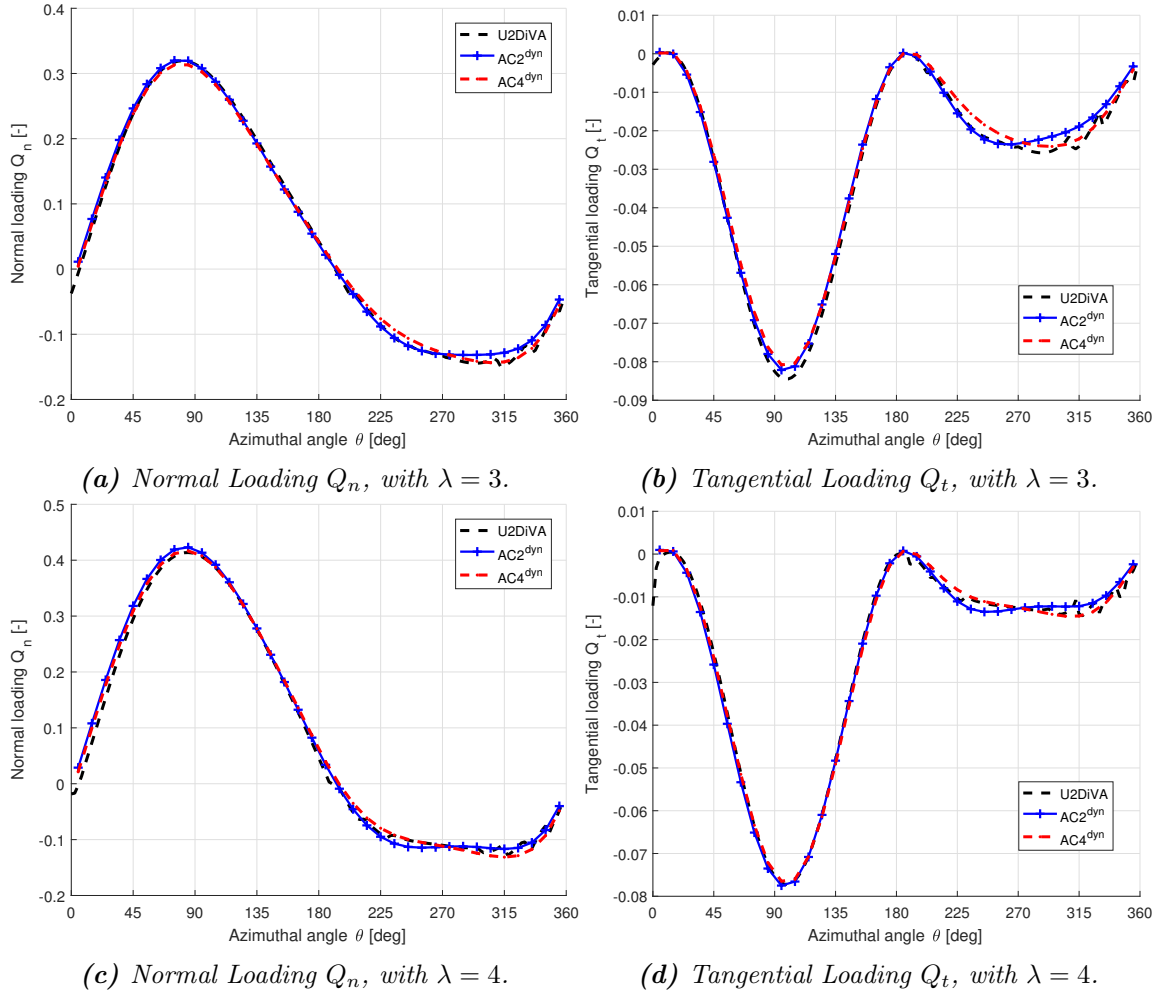


Figure 6.10: Comparison of the normal and tangential loading from two dynamic AC models, with $\sigma = 0.1$, $B = 2$.

It could be visualised from the figure that in the windward part, the normal and tangential loadings from the two dynamic AC models are almost identical and are having good agreements with that from the panel code. There is small difference of the magnitudes of the loadings that the magnitude calculated from the AC_2^{dyn} model will be slightly higher than that from the AC_4^{dyn} model, but the difference is small enough to be neglected. For

the leeward part, the loadings calculated from the two models are different, which are then validated with the panel code. Firstly, the trend of both normal and tangential loadings is better modelled by the AC_4^{dyn} model than the AC_2^{dyn} model. Secondly, the azimuthal location corresponding to the maximum magnitude of the tangential loading in the leeward part could be well modelled by the AC_4^{dyn} model but not the AC_2^{dyn} . As a result, the loadings calculated from the AC_4^{dyn} model is having better agreements with the panel code than the AC_2^{dyn} especially for the tangential loadings. The performance of the AC_4^{dyn} model will be then be investigated in detail.

6.7.2 Validation of the induced velocities

The induced velocities are firstly calculated from the AC_4^{dyn} and are compared with that from the panel code to evaluate the performance of the coupled dynamic AC model.

Steady induced velocities

Firstly, the steady induced velocities in x - and y -directions are evaluated, where *steady* is to distinguish from the dynamic induced velocities which will be introduced later. The steady induced velocities of w_x and w_y at the quarter chord point are calculated from Equation (3.105) and (3.105). The steady induced velocities at the three-quarter chord point are also calculated with linear interpolation method from w_x and w_y according to subsection 5.2.2. The results are compared with that from the panel code and are plotted in Figure 6.11. To be noted that the induced velocities are directly calculated from the panel code. The induced velocities are calculated inversely with Equation (3.21) by subtracting the free wind velocity \vec{V}_∞ and the rotational velocity \vec{V}_{rot} from the relative velocity \vec{V}_{rel} .

It could be visualised from the figure that there is significant differences between the results of the steady induced velocities from the dynamic AC model and the induced velocities from the panel code. The reason for the difference is that the induced velocity of w_x and w_y from the AC model are steady values while the results of the induced velocities from the panel code are with the unsteady effects which are then corresponding to the dynamic values. It could also be considered as the steady induced velocities are corresponding to the geometric angle of attack while the dynamic induced velocities are corresponding to the effective angle of attack. The dynamic induced velocities of w_x^{dyn} and w_y^{dyn} should then be calculated for the comparison with the results from the panel code.

Dynamic induced velocities

For the dynamic AC model, the dynamic induced velocities of w_x^{dyn} and w_y^{dyn} could not be calculated directly as the steady induced velocities. In order to obtain the dynamic induced velocities, it should be obtained inversely from the effective angle of attack α_E . To be noted that even though the term of *dynamic induced velocity* is used, the variables

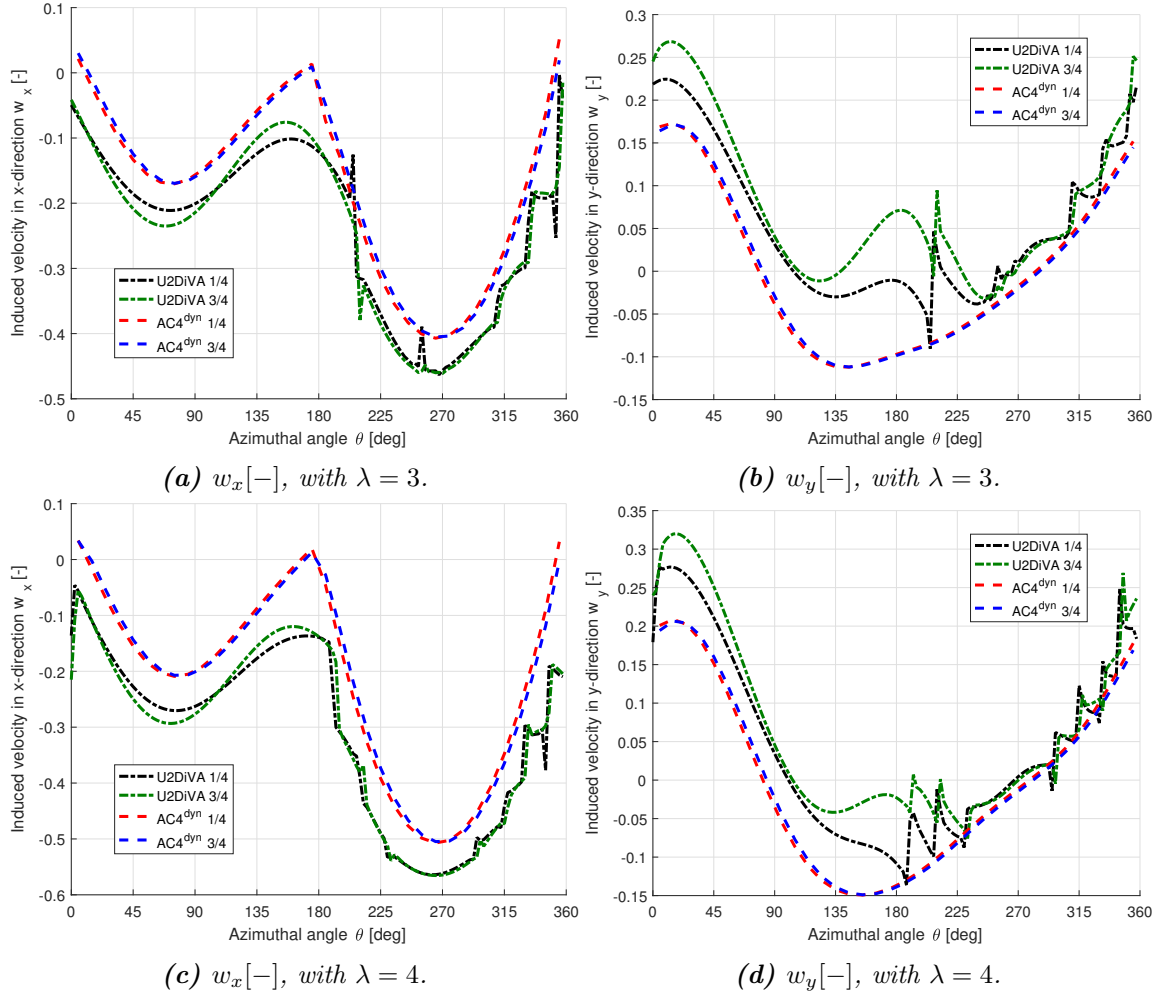


Figure 6.11: Validation of the steady induced velocity in x - and y -directions, with $\sigma = 0.1$, $B = 2$.

are actually corresponding to the quasi-steady values because of the dynamic AC model is actually a quasi-steady model according to section 6.4.

Before deriving the equation of the dynamic induced velocities, the relationship between the steady induced velocities and the effective angle of attack is summarised here, and the reason for the dynamic induced velocities to be different from the steady induced velocities is explained. Firstly, the steady induced velocity at the three-quarter chord point $w_{x,3/4}$ and $w_{y,3/4}$ are calculated with linear interpolation from the values at the quarter chord point $w_{x,1/4}$ and $w_{y,1/4}$. Secondly, the normal and tangential relative wind speed at the three-quarter chord point $V_{n,3/4}$ and $V_{t,3/4}$ are calculated with Equation (5.20) and (5.21), the corresponding geometric angle of attack $\alpha_{3/4}$ could then be calculated with Equation (5.19). Thirdly, the effective angle of attack α_E which is due to the downwash $w_{3/4}$, is then obtained by applying the inviscid part of the dynamic stall model. The steady relative velocity $V_{rel,3/4}$ is also changed to the dynamic relative velocity $V_{rel,3/4}^{dyn}$ due to the downwash $w_{3/4}$, with the direction determined by α_E . According to Equation (3.21), because the relative velocity $\vec{V}_{rel,3/4}$ is changed and the free wind velocity \vec{V}_∞ as well as

the rotational velocity $\vec{V}_{rot,3/4}$ remains unchanged, the induced velocity $\vec{V}_{ind,3/4}$ is then changed. Similarly, the induced velocity $\vec{V}_{ind,1/4}$ is then also changed.

In order to obtain the dynamic induced velocities, the relative wind velocity at the three-quarter chord point after the downwash should then be obtained. The steady relative wind velocity could be easily determined with $V_{n,3/4}$ and $V_{t,3/4}$, and the magnitude of the downwash $w_{3/4}$ could also be determined with the difference of α_E and $\alpha_{3/4}$. However, the direction of the downwash is not explicitly given in the dynamic stall model. There is a possible method which is to assume that the downwash only changes the direction of the relative wind velocity but not change the magnitude. The dynamic relative wind speed $V_{rel,3/4}^{dyn}$ is then equal to the steady value $V_{rel,3/4}$ and the direction is determined by the effective angle of attack α_E . The corresponding normal and tangential dynamic relative wind speed could then be calculated with the following steps and the corresponding equations.

Firstly, the dynamic value of the normal and tangential relative wind speed are calculated from the dynamic relative wind speed according to Figure 3.4.

$$V_{n,3/4}^{dyn} = V_{rel,3/4} \sin(\alpha_E + \theta_p) \quad (6.63)$$

$$V_{t,3/4}^{dyn} = V_{rel,3/4} \cos(\alpha_E + \theta_p) \quad (6.64)$$

$$(6.65)$$

The dynamic induced velocity of $w_{x,3/4}^{dyn}$ and $w_{y,3/4}^{dyn}$ could then be calculated inversely by re-arranging Equation (5.20) and (5.21), and the explicit form is as follows.

$$w_{x,3/4}^{dyn} = \frac{V_{t,3/4}^{dyn}}{V_\infty} \cos \theta_m + \frac{V_{n,3/4}^{dyn}}{V_\infty} \sin \theta_m - 1 \quad (6.66)$$

$$w_{y,3/4}^{dyn} = \frac{V_{t,3/4}^{dyn}}{V_\infty} \sin \theta_m + \frac{V_{n,3/4}^{dyn}}{V_\infty} \cos \theta_m - 1 \quad (6.67)$$

In the equations above, the variable of θ_M is the corresponding azimuthal angle at the mounting point, and the reason of using this value has been explained in subsection 5.2.2. The dynamic induced velocities at the quarter chord point $w_{x,1/4}^{dyn}$ and $w_{y,1/4}^{dyn}$ could be calculated with similar method as above with the effective angle of attack at quarter chord point $\alpha_{E,1/4}$ which is approximated with Equation (6.62).

With the aforementioned method, the dynamic induced velocities in x - and y -direction at the quarter chord point as well as the three-quarter chord point are calculated and are compared with that from the panel code in the Figure 6.12.

It could be visualised from the figure that the dynamic induced velocities are now having better agreements with that from the panel code than the steady induced velocities as in Figure 6.11. For the induced velocity in x -direction, the results are having better agreements near the azimuthal angle of 90° and 270° . However, there are still significant differences near the azimuthal angle of 0° and 180° where the windward and leeward part of the AC are connected. For the induced velocity in y -direction, the general W shape of the curve calculated from the panel code could also be obtained, instead of a V shape

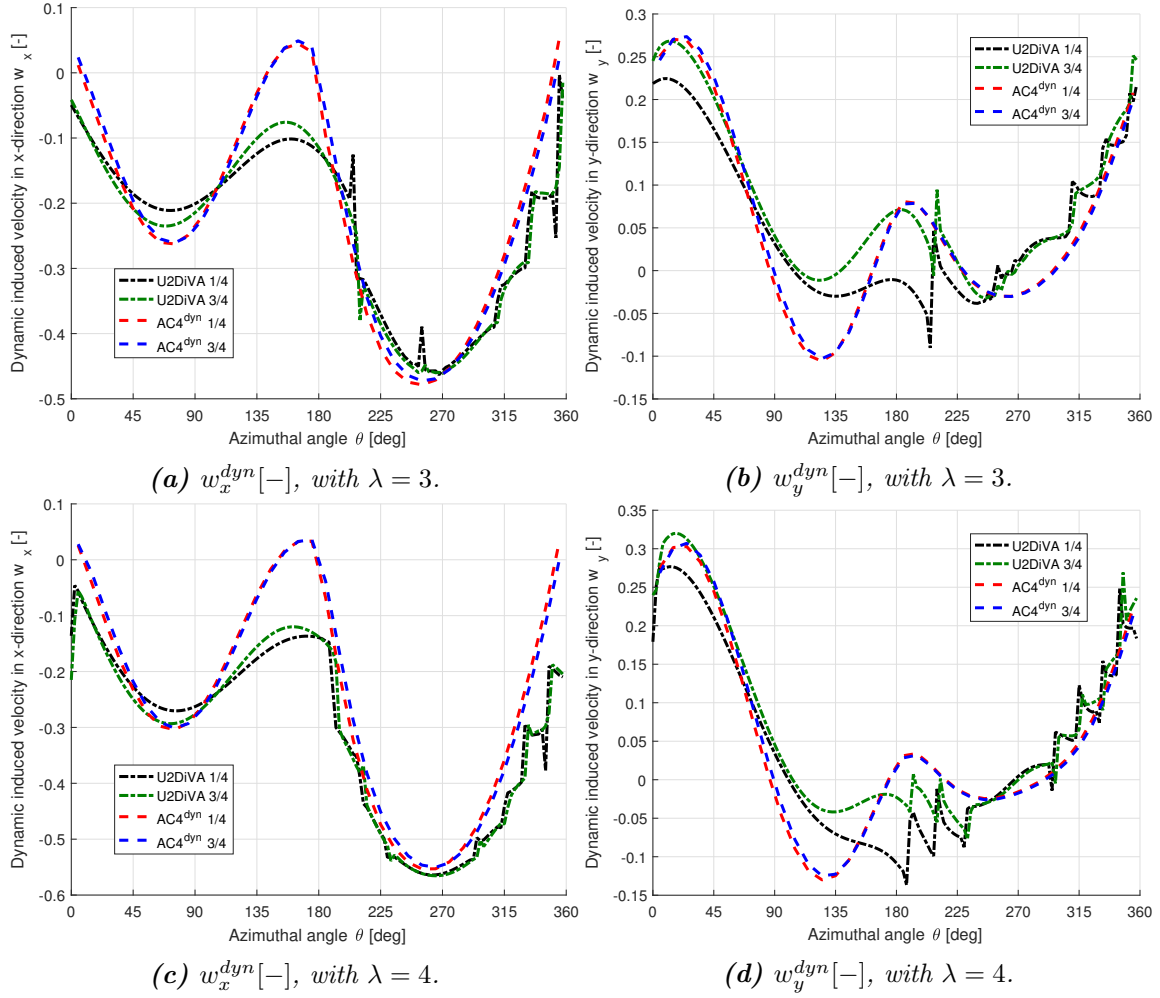


Figure 6.12: Validation of the dynamic induced velocity in x - and y -direction, with $\sigma = 0.1$, $B = 2$.

as in Figure 6.11(b) and (d). However, there are still some differences especially in the windward part of the rotor. The difference might be due to the assumption that the downwash only changes the direction but not the magnitude of the relative wind speed. Further investigations of the induced velocities are required.

Normal and tangential dynamic induced velocities

Similar to the Chapter 3, the induced velocity is also decomposed in the normal and tangential direction with respect to the Actuator Cylinder with respect to the azimuthal location at the mounting point. Both the values of the normal and tangential dynamic results of w_n^{dyn} and w_t^{dyn} are calculated. The dynamic results of induced velocities at quarter chord point as well as three-quarter chord point are compared with the results from the panel code and plotted in the Figure 6.13.

From Figure 6.13 (a) and (c), it could be visualised that for the leeward part, the dynamic

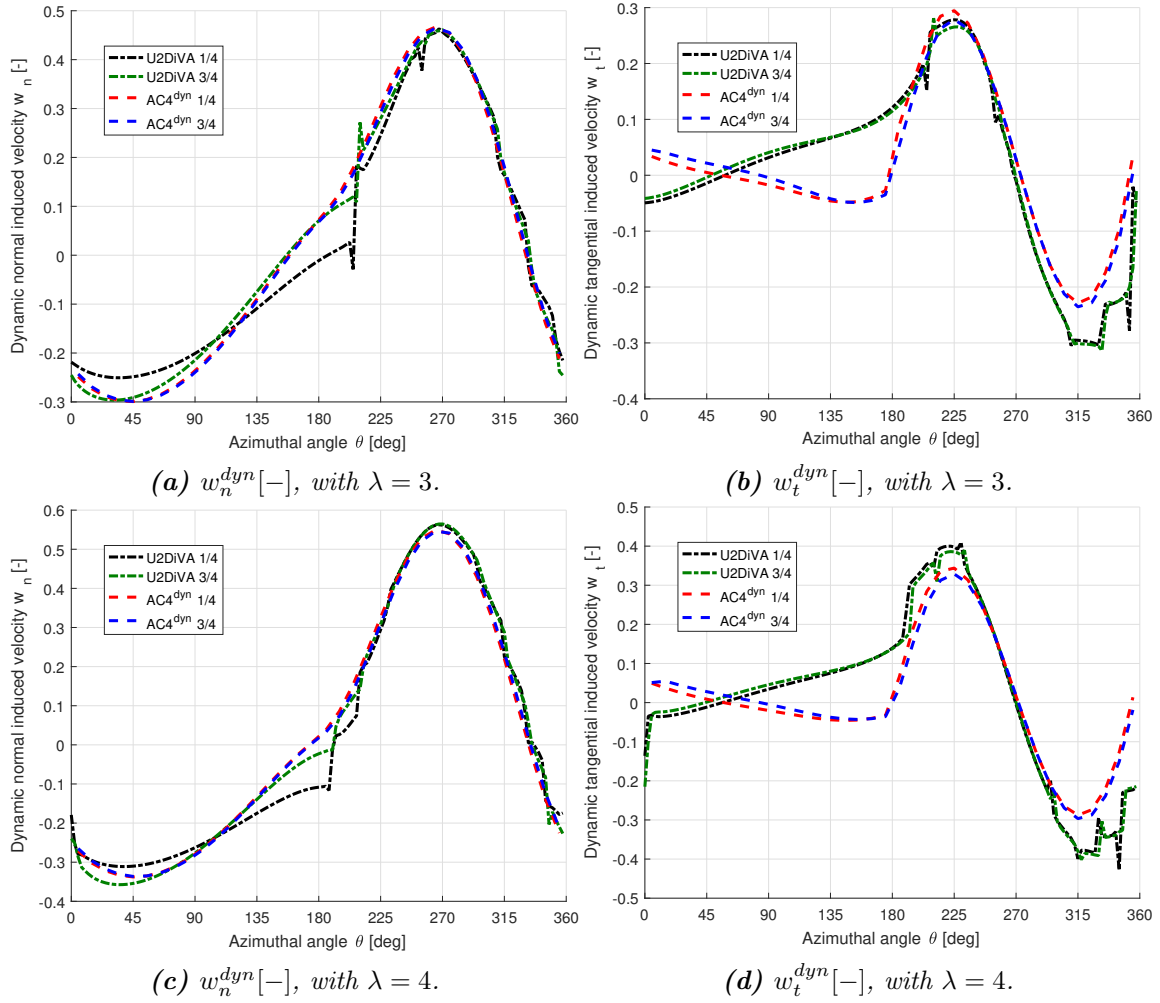


Figure 6.13: Validation of the dynamic normal and tangential induced velocity, with $\sigma = 0.1$, $B = 2$.

normal induced velocity at the quarter chord point $w_{n,1/4}^{dyn}$ and three-quarter chord point $w_{n,3/4}^{dyn}$ calculated from the AC model are having good agreements with that from the panel code. For the windward part, the value of $w_{n,3/4}^{dyn}$ from the AC model is having some difference with that from the panel code, and the value of $w_{n,1/4}^{dyn}$ is having significant differences with that from the panel code. There is then another validation to indicate whether the difference between $w_{n,1/4}^{dyn}$ and $w_{n,3/4}^{dyn}$ is able to be correctly modelled with the dynamic AC model. For the leeward part, the values of $w_{n,1/4}^{dyn}$ and $w_{n,3/4}^{dyn}$ calculated from the panel code is also identical which could be correctly modelled with the dynamic AC model. However, for the windward part, the values of $w_{n,1/4}^{dyn}$ and $w_{n,3/4}^{dyn}$ from the panel code are having significant differences from each other which could not be modelled with the dynamic AC model.

It could be visualised from Figure 6.13b and d in the leeward part, that the magnitudes of the dynamic tangential induced velocities of $w_{t,1/4}^{dyn}$ and $w_{t,3/4}^{dyn}$ from the AC model are having the same trend as that from the panel code but the magnitude is underestimated

when $\theta > 270^\circ$. For the windward part, there is significant between the results from the dynamic AC model and the panel code and seems like a change of sign. The code has been checked multiple times to be without *bugs* in the implementation. The difference of the dynamic tangential induced velocities could be due to the assumption previously in this section that the magnitude of relative wind speed does not change after the downwash.

According to Equation 5.19, the induced velocity in the normal direction is more important than the tangential induced velocity for the result of the angle of attack because of the characteristic of arctangent function. As a result, the effective angle of attack α_E is able to be well modelled with the AC model because the value of $w_{n,3/4}^{dyn}$ is well modelled. However, the difference between the dynamic tangential direction from the AC model and the panel code will influence the relative wind speed which will then influence the normal and tangential loadings.

6.7.3 Effective angle of attack and relative wind speed

The effective angle of attack α_E and the relative wind speed at the quarter chord point $V_{rel,1/4}^{dyn}$ which are directly linked to the induced velocities are calculated and compared with that from the panel code in Figure 6.14. To be noted that the effective angle of attack α_E is compared with the angle of attack at three-quarter chord point from the panel code.

The difference between the relative wind speed at the quarter chord point and the three-quarter chord point is a phase lag according to subsection 5.2.2. The difference between the two variables is shown to have good agreements with that from the panel code in Figure 5.9. As a result, only the relative wind speed at the quarter chord is validated here. From the figure, it could be visualised that the effective angle of attack α_E for different load cases are having good agreements with that from the panel code. This is consistent with the reasoning in the previous subsection that the dynamic normal induced velocity at the three-quarter chord point w_n^{dyn} is well modelled. The relative wind speed calculated from the AC model is having some difference with the result from the panel code at the locations near the azimuthal angle of 0° and 180° which are the connection between the windward and leeward part. The source of the difference is mainly due to the difference of the tangential induced velocity as explained in subsection 6.7.2. For the azimuthal angle near 90° and 270° which are at the centre of the windward and leeward part, the results have good agreements.

6.7.4 Normal and tangential loadings

The normal and tangential loadings, which directly determine the performance of the rotor, have been plotted previously in Figure 6.10. It could be visualised from the figure that the normal loading Q_n is having good agreements with the panel code for both load cases. However, the magnitude of the tangential loadings Q_t from the AC model is smaller than the panel code near the azimuthal angle of 100° and 270° which is more significant especially for the second load case. The difference of the tangential loadings calculated

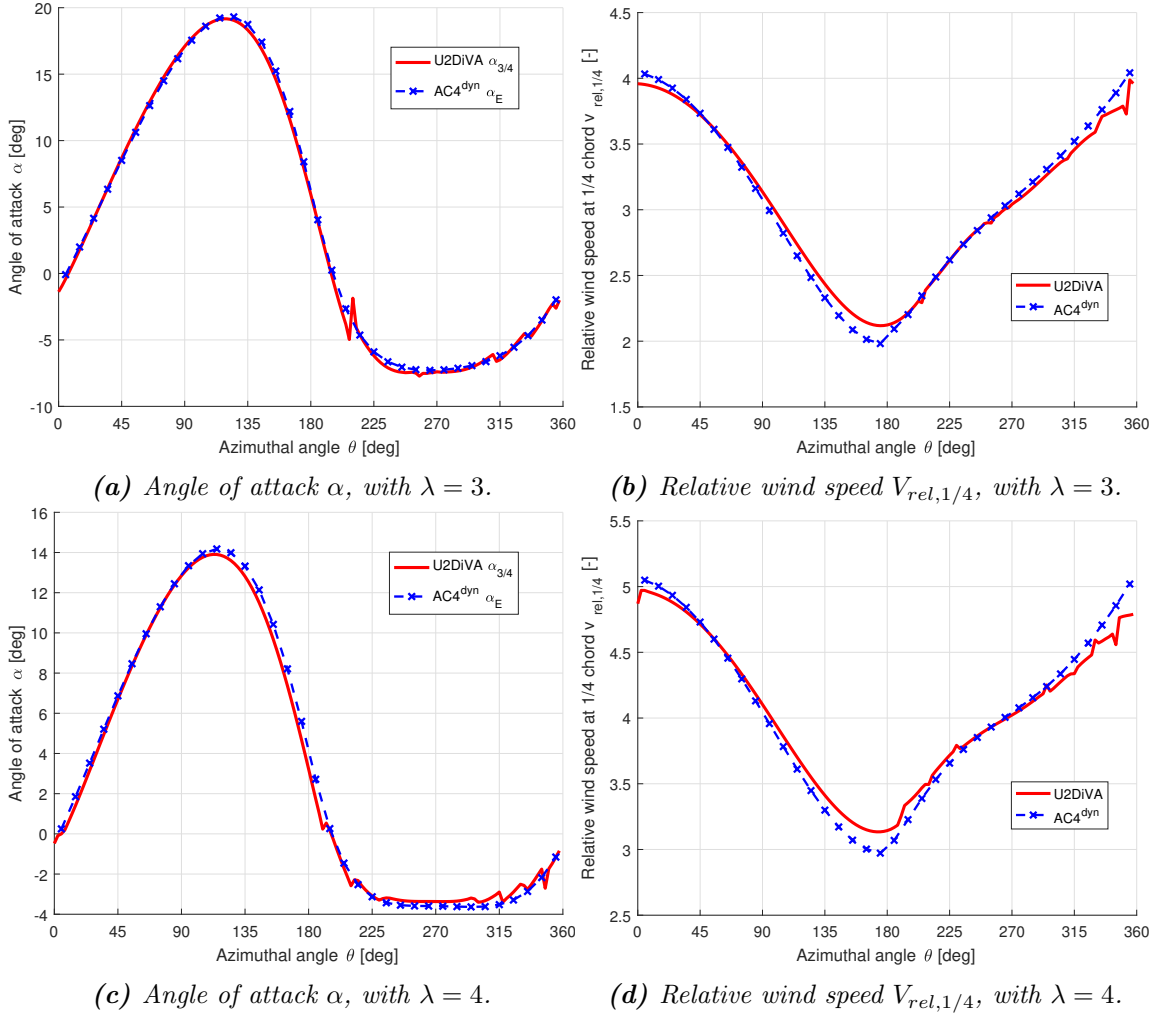


Figure 6.14: Validation of the angle of attack and relative wind speed, with $\sigma = 0.1$, $B = 2$.

from AC model and the panel code could be due to the Mod-Lin correction method.

6.7.5 Thrust and power coefficient

Before determining whether the Cheng's modified Mod-Lin correction method is sufficient, the thrust coefficient should be validated. Besides, the power coefficient is also validated. The results are calculated with the dynamic AC model for different cases with different tip speed ratio and solidity and are plotted together with the results from the panel code in Figure 6.15.

By comparing the results of thrust coefficient in Figure 6.15 and 3.22, it could be concluded that the thrust coefficient from the AC model in Chapter 3 without dynamic stall model is having better agreements with the results from panel code. The thrust coefficient from the dynamic AC model is not having very good agreements with that from the panel code

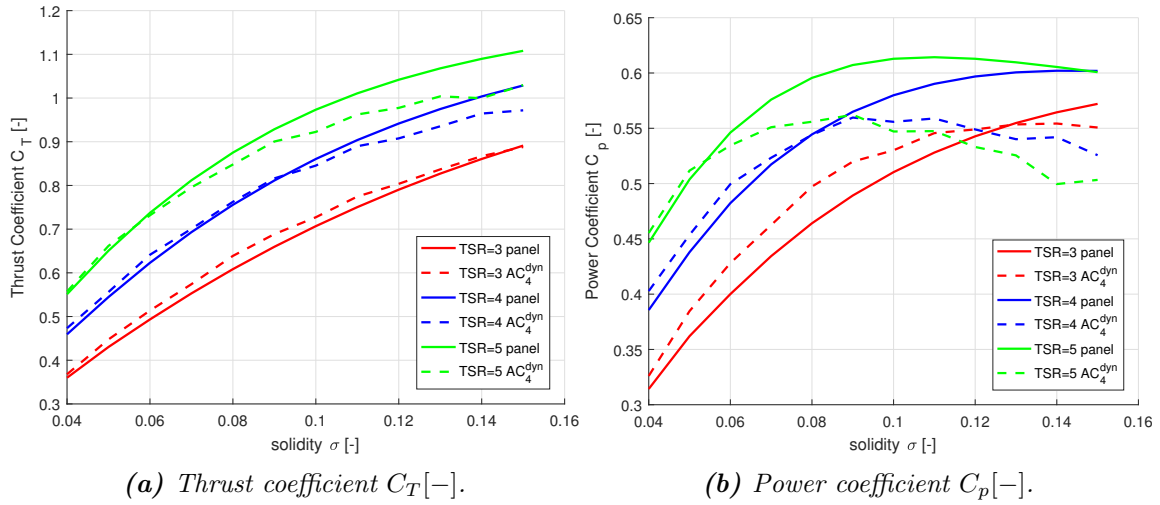


Figure 6.15: Validation of the thrust and power coefficient from the dynamic AC model.

which means the thrust coefficient is not well predicted by the dynamic AC model. It could also be concluded that the dynamic AC model is also worse than the AC model without dynamic stall modelling in predicting the power coefficient. However, it should be noted that the dynamic AC model could predict the azimuthal loading distribution which is very important for the design and optimisation. The reason for some difference could then due to the Cheng's modified Mod-Lin correction maybe still not sufficient.

6.7.6 The influence of Mod-Lin method

The influence due to the Mod-Lin correction should then be investigated. The possible issues of the Mod-Lin correction method will be firstly discussed. And then, the possibility of the improvements is demonstrated by *forcing* the thrust coefficient to have good agreements with that from the panel code which corresponds to a virtual *perfect* Mod-Lin correction method.

Possible issues of Mod-Lin correction

There are two different possible issues for the Mod-Lin correction method which are as follows.

- The first possible issue is the correction factor k_a is not applied correctly. For the dynamic AC model, the correction factor k_a is applied to the steady induced velocities w_x and w_y which is with the same method as that for the AC model without dynamic stall modelling. However, in order to maintain the physical meaning of the Mod-Lin correction, the correction factor k_a should be applied to the *real* induced velocities which are the quasi-steady values w_x^{dyn} and w_y^{dyn} calculated from Equation (6.66) and (6.67). It should be noted that this method may not be possible because the dynamic

induced velocities could not be directly calculated. The dynamic induced velocities after the correction could not be directly transformed to the steady induced velocities. Thus, it is not able to form a sufficient iteration process to obtain converged solutions.

- The second possible issue is the polynomial function between the thrust coefficient C_T and axial induction a is not sufficient enough for the correction. This issue will directly cause the thrust coefficient from the dynamic AC model is not as sufficient as the AC models without dynamic stall modelling. With Cheng's modified Mod-Lin correction, there are some improvements but still not sufficient enough to let the thrust coefficient to have good agreements with panel code. As a result, further improvements are needed.

Demonstrate the possibility of improvements

It will be demonstrated whether there are possible improvements for the current polynomial functions to solve the second issue previously in this subsection. For the demonstration here, it is then not necessary to obtain a more sufficient polynomial function to show the possibility of improvements. This means that the relationship between the correction factor k_a and the induction factor a which is calculated from the thrust coefficient C_T is not necessary to be explicitly known.

What needs to be demonstrated is that for a certain load case, when the correction factor k_a is chosen that the thrust coefficient C_T from the dynamic AC model is having good agreements with that from the panel code, whether the normal and tangential loadings will have good agreements with that from the panel code. Because the thrust coefficient C_T calculated from the AC model in Chapter 3 which does not take into consideration of the unsteady effects is having good agreements with that from the panel code according to Figure 3.22, the steady AC model could be firstly applied to calculate the thrust coefficient C_T . And this value is then set to be the *aim* of the following calculations, and is noted at C_T^{aim} .

Then the dynamic AC model is applied and the thrust coefficient C_T^{dyn} is then calculated. The value is compared with the *aim* thrust coefficient C_T^{aim} which is calculated before. And the new correction factor should then be adjusted according to the relationship of the C_T^{dyn} and C_T^{aim} . Because of the thrust coefficient increases with the increasing of the correction factor k_a . Thus, for the condition of $C_T^{dyn} > C_T^{aim}$, the correction factor k_a should be decreased. And for the condition of $C_T^{dyn} < C_T^{aim}$, the correction factor k_a should increase. The process should iterate until the difference between the two thrust coefficients is within a certain tolerance. The above iteration process could be achieved with Newton's method. The initial value of the lower and upper boundary of k_a could be set to be $k_a^{low} = 1$ and $k_a^{high} = 2$ respectively which will ensure the converged solution of the correction factor k_a is inside this region. With the method implemented in the MATLAB code, the converged solution is reached with approximately 8 to 10 iterations and the total CPU time is less than 5 seconds which is very fast.

To be noted that with this method, the thrust coefficient from the dynamic AC model is

forced to have good agreements with that from the panel code which could be considered as applying a virtual *perfect* Mod-Lin correction method whose explicit form is unknown.

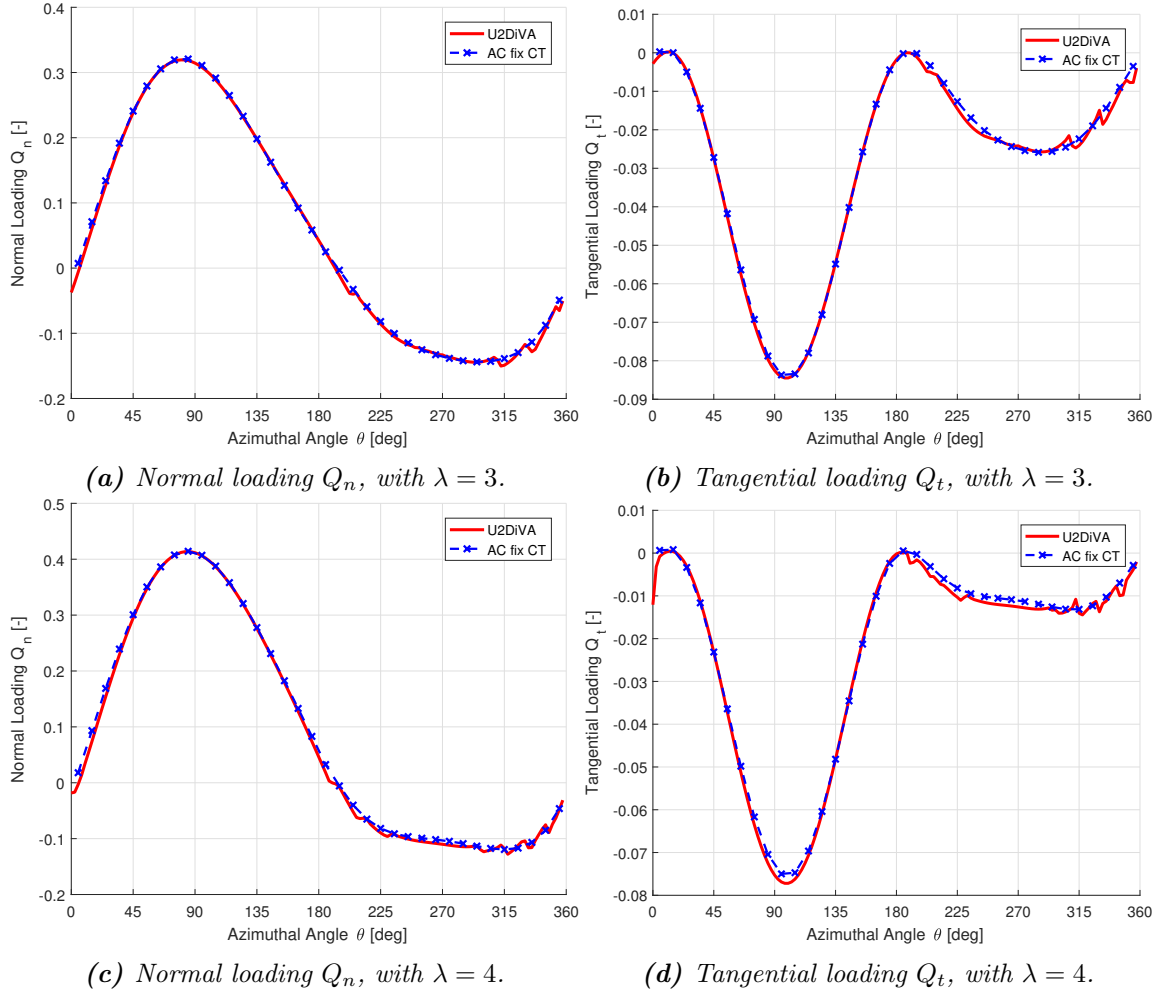


Figure 6.16: Demonstration of further improvements to the Mod-Lin correction method with the normal and tangential loadings, with $\sigma = 0.1$, $B = 2$.

The results of the normal and tangential loadings for the load cases which are identical to that in Figure 6.10 are plotted in Figure 6.16.

It could be visualised from Figure 6.16 that the normal and tangential loadings are having very good agreements with that from the panel code. There is significant improvements to the case of using Cheng's modified Mod-Lin correction as in Figure 6.10. It could then be concluded that there is still possible improvements that could be done to the polynomial function of the Mod-Lin correction.

To be noted that the in above method, the thrust coefficient from the dynamic AC model is *forced* to be a certain value which is calculated from the AC model without dynamic stall modelling. Thus, this method is not well physically based and is not considered as a new modification to the AC model. Instead, this method is only considered for the demonstration of whether the issue is from the polynomial function and whether there

is any possibilities of improvements could be made to let the loadings to have better agreements with panel code.

6.8 Relationship with Pirrung's extended model

The Pirrung's extended Risø dynamic stall model is introduced in section 6.2, the relationship between Pirrung's extended model and the modified method used in this report is discussed in this section. The latter is named *new* modified model for abbreviation. For simplicity, the condition of inviscid flow is assumed, then only the dynamics of the attached flow is modelled. The converged solution of the inviscid part of the dynamic AC model with the inviscid NACA0015 airfoil in section 6.7 is used for the investigation.

6.8.1 Investigation of Pirrung's extended model

According to section 6.5, the type-one angle of attack α_1 which is defined in that section should be determined. If the type-one angle of attack α_1 and the lift coefficients of the two methods are identical with each other, the two methods are then equivalent to each other. For the *new* modified method in this report, the type-one angle of attack is the *effective* angle of attack at the quarter chord point which is approximated with Equation (6.62). For Pirrung's extended model, the lift is applied at the quarter chord point but perpendicular to the geometric angle of attack of $\alpha_{3/4}$ at the three-quarter chord point, which is the type-two angle of attack because there is drag component in this direction.

Dynamic lift coefficient

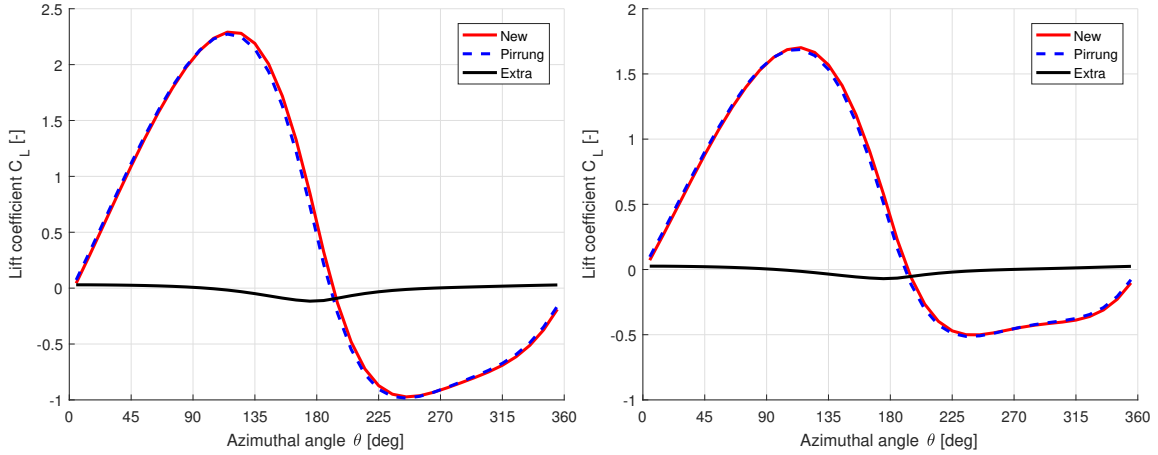
Firstly, lift coefficient from Pirrung's extended model is investigated. According to Pirrung [39], the dynamic lift in Pirrung's extended model is consisted of three parts according to Equation (6.43). The circulatory lift $C_{L,circ}$ is calculated from the effective angle of attack α_E with Equation (6.44). The torsion lift $C_{L,tor}$, which takes into account the variation of the angle of attack as well as azimuthal angle, is calculated with Equation (6.45). And the lift due to acceleration $C_{L,acc}$ is calculated with Equation (6.46). With the assumption of fixed pitch angle, the equation is rewritten in the following form.

$$C_{L,acc} = -\pi T_u \frac{-\omega^2 R}{V_{rel}} = -\pi T_u \frac{-\omega^2}{v_{rel}} \quad (6.68)$$

Substituting Equation (6.68) and (6.45) in to Equation (6.43), the dynamic lift coefficient C_L^{dyn} is then:

$$C_L^{dyn} = C_{L,circ} + \pi T_u \dot{\alpha} + \pi T_u \frac{\omega(\omega - v_{rel})}{v_{rel}} \quad (6.69)$$

In Equation (6.69), the first two terms are identical with Equation (6.17) which is identical to that from the *new* modified model. The difference is that there is an extra term in the RHS of Equation (6.69). The contribution of this term is investigated with the converged solutions obtained in section 6.7, the azimuthal variation of the lift coefficient calculated from Equation (6.69) and (6.17) as well as the extra term are plotted in Figure 6.17, and are noted as *Pirrung*, *New* and *Extra* respectively in the figure.



(a) Comparison of lift coefficient C_L , with $\lambda = 3$. (b) Comparison of lift coefficient C_L , with $\lambda = 4$.

Figure 6.17: Comparison of the unsteady lift coefficient of the attached flow from Pirrung's extended model and Risø dynamic stall model, with $\sigma = 0.1$, $B = 2$.

From the figure, it could be visualised that there is small difference of the unsteady lift coefficient calculated from the two methods. The lift coefficient from Pirrung's extended model with Equation (6.69) will have a small phase lead compared to that from the *new* modified model with Equation (6.17).

Dynamic drag coefficient

Secondly, the drag coefficient from Pirrung's extended model is investigated. There is an induced drag term in Equation (6.48) which is proportional to the difference between α_E and $\alpha_{3/4}$. Referring to section 6.5 and Equation (6.57) and (6.58), the Pirrung's extended method is able to be transformed to an equivalent method. If letting the type-two angle of attack to be the effective angle of attack α_E , the induced drag term is disappeared. And the lift coefficient is approximately not changed because the difference between α_E and $\alpha_{3/4}$ is small. And for the inviscid NACA0015 airfoil polar with constant zero drag coefficient, the first two terms in Equation (6.47) are then equal to zero. The dynamic drag coefficient for α_E is then equal to the torsion rate drag.

$$C_d^{dyn} = C_{d,tor} = -C_{L,circ} T_u \dot{\theta} \quad (6.70)$$

6.8.2 Comparison of the two methods

For comparison purpose, instead of finding what is the type-one angle of attack for Pirrung's extended model and compare with $\alpha_{E,1/4}$, the type-two angle of attack for both Pirrung's extended model and the *new* modified model are both set to be the effective angle of attack α_E . The corresponding lift coefficients for this angle from the two methods are then approximately equal to each other according to Figure 6.17 and Equation (6.57). The drag coefficient for this angle of attack from Pirrung's extended model has been derived in Equation (6.70), and now the value from *new* modified model should be derived and compared with Equation (6.70).

For the *new* modified model, the drag coefficient for α_E is as follows according to Equation (6.58).

$$C_d^{dyn} = C_L^{dyn} \sin(\alpha_E - \alpha_{E,1/4}) = C_L^{dyn} \sin(\alpha_{3/4} - \alpha_{1/4}) \quad (6.71)$$

Preliminary analytical comparison

Comparing with Equation (6.70), there are two differences. The first one is the lift coefficient in Equation (6.70) is the circulatory lift coefficient $C_{L,circ}$ while in Equation (6.71) is the dynamic lift coefficient C_L^{dyn} . The second difference is the term multiplied by the lift coefficient is $T_U \dot{\vartheta}$ in Equation (6.70) and is $\sin(\alpha_{3/4} - \alpha_{1/4})$ in Equation (6.71). For a preliminary comparison, the two lift coefficients are assumed to be approximately equal to each other with $C_{L,circ} \approx C_L^{dyn}$. The second difference motioned above is then investigated.

For Equation (6.70) from Pirrung's extended model, if neglecting the variation of the angle of attack and assuming the rotational wind speed v_{rot} is approximately equal to the relative wind speed v_{rel} , it can be simplified as follows.

$$C_{d,tor} \approx C_{L,circ} T_u \omega \approx C_{L,circ} c/2 \quad (6.72)$$

For Equation (6.71) from the *new* modified model, if neglecting the difference of the induced velocities at the two points, the difference between $\alpha_{3/4}$ and $\alpha_{1/4}$ is then equal to the difference between the azimuthal angles of the two points. The Equation (6.71) is then simplified as follows.

$$C_{d,tor} \approx C_{L,circ} c/2 \quad (6.73)$$

The two simplified Equation of (6.72) and (6.73) are identical with each other.

Numerical comparison

The above preliminary comparisons are having too many assumptions and is premature. There will be a numerical comparison as follows. For the comparison, the drag coefficient calculated from Equation (6.71) and (6.70) are plotted in Figure 6.18 and noted as *New* and *Pirrung*. In addition, a modification to Pirrung's method by neglecting the contribution

of $\dot{\alpha}$ in Equation (6.70) is also plotted together for comparison, and is noted as *Pirrung Mod*.

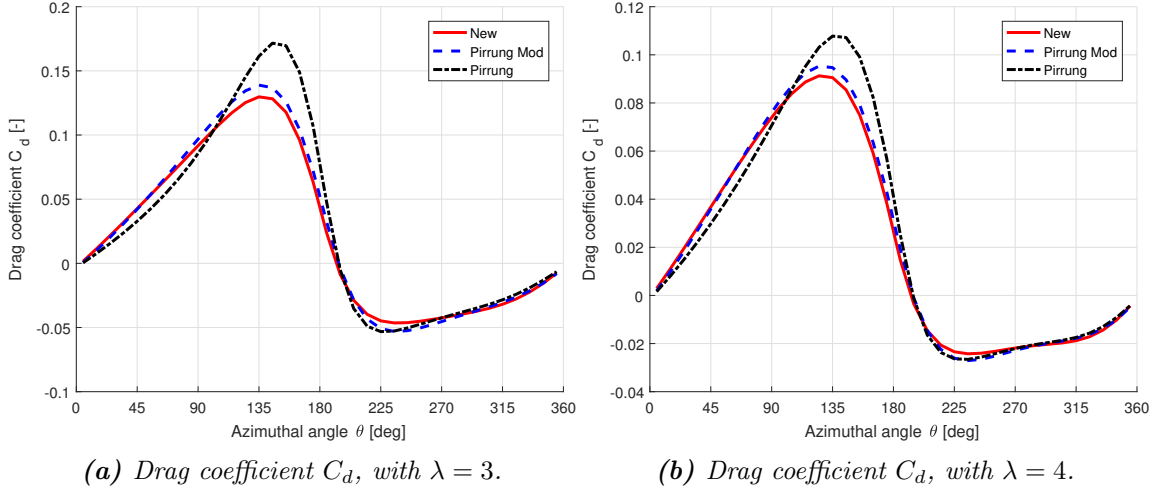


Figure 6.18: Comparison of the unsteady drag coefficient of the attached flow from Pirrung's extended model and Risø dynamic stall model, with $\sigma = 0.1$, $B = 2$.

It can visualise from the figure that the results from *new* modified model is having good agreements with modified Pirrung's method which neglects the torsion drag due to $\dot{\alpha}$. But are having deviations with the results from Pirrung's method. As a result, it could be concluded that the *new* modified model used in this report is almost identical to the Pirrung's method and could be considered as the Pirrung's method neglecting the contribution of the variation of the angle of attack to the dynamic drag.

6.8.3 VAWT at zero wind speed

It is proved by Pirrung [39] that with the method of applying the dynamic lift perpendicular to $\alpha_{3/4}$ and introducing the torsion drag term, the VAWT will not generate net torque when there is no wind speed with the assumption of inviscid flow. The proof by Pirrung is with a special condition that the blade is mounted at the half chord point and the contribution of the torque due to lift and drag force cancel out with each other.

For the *new* method used in this report, the condition of VAWT not generating net torque at zero wind speed is also able to be proved. With the zero incoming wind condition, there is no azimuthal variation of the angle of attack, the *effective* angle of attack $\alpha_{E,1/4}$ at the quarter chord point is then equal to the geometric angle of attack $\alpha_{1/4}$ at this point. The relative wind velocity at the quarter chord point is identical with the rotational velocity which is perpendicular to the line connecting the rotational axis and the quarter chord point. The lift force is then pointing to the aerodynamic centre, and there will be no drag components perpendicular to the lift. The net aerodynamic torque is then equal to zero because the length of the force arm is zero. And it does not matter how the blade is mounted because the aforementioned conditions will always be satisfied.

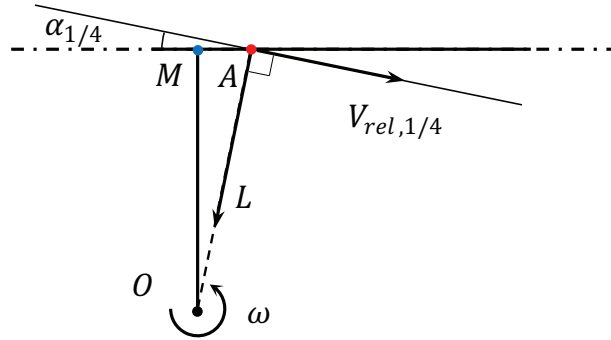


Figure 6.19: Demonstration of the direction of the lift force in the condition of zero wind speed

6.9 Conclusions of the chapter

In this section, the Risø dynamic stall model is used for the unsteady aerodynamics modellings. The model is introduced and then the inviscid part of the model is validated with panel code for the harmonic pitching motion with the coefficients obtained numerically from the step response. The coupling of the dynamic stall model with the AC model is introduced in details with detailed discussions of the direction of applying the lift force. The results calculated from the coupled dynamic AC model, with only the attached flow part of the dynamic stall model included, are compared with that from the panel code. The discoveries and main conclusions are summarised as follows.

- The ODEs in Risø dynamic stall model as well as the indicial formulation for numerical solutions are introduced. The Pirrung's simplification to the Risø dynamic stall model as well as the Pirrung's extended model are also introduced and are then derived by the author in the Appendix A.4. It is shown the extended model is similar to the Risø dynamic stall model with only minor differences.
- The inviscid step response of the NACA0015 is modelled with the panel code, and the corresponding coefficients for the airfoil are approximated numerically by minimising the RMS error. The inviscid part of the Risø dynamic stall model is validated with the harmonic pitching motion. The results indicate the model will have good agreements with the panel code when using the approximated coefficients for the NACA0015, but will have significant differences when using Jones approximation for the flat plate.
- The Risø dynamic stall model can be partially or fully implemented, and when neglecting all the unsteady effects by not including any aerodynamic state variables, the only thing left in the model is to evaluate the angle of attack at three-quarter chord point. The Risø dynamic stall model then becomes the flow curvature model as in Chapter 5. It also indicates the flow curvature effect has been implicitly implemented in the Risø dynamic stall model, there is no need for the extra modelling of the flow curvature effect when coupling the Risø dynamic stall model with the AC model. Otherwise, there will be double consideration of the flow curvature effect.

- The direction of applying the dynamic lift force is important for the implementation of the model and should be determined. With the reasoning with the bound vortex as well as comparing the results with the panel code, it can be determined the lift force should not be applied perpendicular to the effective nor geometric angle of attack at three-quarter chord point. The method of applying the lift force perpendicular to the geometric and effective angle of attack at quarter chord point are compared, and the conclusion is the latter method is having better agreements with the panel code than the former method because it is more sufficient to model the phase lag effect. It is also verified that the results are having better agreements with the panel code when using Cheng's Mod-Lin correction method than using the original Mod-Lin correction method.
- The result from the AC_4^{dyn} model, which is based on the Cheng's AC model, is having better agreements with the panel code than the AC_2^{dyn} model, which is based on the original AC model. The two models are having similar results of the normal and tangential loadings in the windward part, but for the leeward part, the AC_4^{dyn} model predicts the normal loadings and especially the tangential loading better than the AC_2^{dyn} model.
- For the validation of the induced velocities, the dynamic induced velocities are defined and validated because the steady values are not able to represent the real effects. The normal and tangential dynamic induced velocity are also validated, the former is having good agreements with panel code, but the latter is having some deviation. For the validation of the angle of attack, the effective angle of attack which is at the three-quarter chord point from the dynamic AC model is having good agreements with that from the panel code. This is because the dynamic normal induced velocity is well predicted which is more important than the dynamic tangential induced velocity for the calculation of the angle of attack. The relative wind speed is having some difference with the panel code which is due to the dynamic tangential induced velocity is not well modelled with the dynamic AC model, or the assumption of the relative wind speed remains same after downwash is not sufficient.
- The coupled dynamic AC model is worse than the previous AC models on prediction the thrust coefficient. There will be even more overestimation of the power coefficient from the dynamic AC model than the steady AC model.
- It is also demonstrated that the Mod-Lin correction method can be further improved that if the thrust coefficient is well modelled with a sufficient polynomial relationship between C_T and a . The normal and tangential loadings from the AC model will then have even better agreements with that from the panel code.
- To be noted that the advantage of AC model is the computational effort is much less than the panel code. For the U2DiVA code, it will take hours of CPU time to obtain the converged solution of a typical two bladed VAWT of a certain load case. Meanwhile for the coupled dynamic AC model, with the simplification methods introduced in Chapter 4, the computational time will be only 2 seconds. Thus, the AC model is favourable for the aeroelastic analysis as well as early stages of design and optimisation for the VAWT.

- The relationship between Pirrung's extended model and the *new* modified model used in this report has been investigated. The inviscid part of the two models are almost identical with only minor differences. The unsteady lift coefficient from the two methods will have a small phase difference. And will also be a difference for the torsion rate drag due to the variation of the angle of attack.

Double Actuator Cylinder Model

In this chapter, the double VAWT rotor layouts will be investigated. The Actuator Cylinder (AC) model is firstly modified to become the Double Actuator Cylinder (DAC) model in order to calculate the influence between the two rotors. Secondly, the performance of the DAC model on calculating the power coefficient and thrust coefficient for different tip speed ratio and solidity is validated. Thirdly, the influence between the two rotors for the cases of different rotational direction, distance between the rotors and phase difference is investigated with the result from the panel code of U2DiVA. Then, with the results from the DAC model, it is then validated that whether the influences between the two rotors have been correctly modelled. Finally, the conclusions about the DAC model and recommendations are made.

7.1 Theoretical background and derivation

In this section, there will be the theoretical background and details of the derivation of the Double Actuator Cylinder (DAC) model from the single AC model. The term of single AC model represents the AC model for the single rotor layout in order to distinguish from the DAC model for the double rotor layout which will be introduced in this section.

7.1.1 Definition of non-dimensioned coordinate systems

The dimensioned and non-dimensioned coordinate system needed for the DAC model will be firstly introduced here. For the double-rotor layout, the rotational axis of the two rotors are at the coordinate of (X_{c1}, Y_{c1}) and (X_{c2}, Y_{c2}) in the dimensioned coordinate system (X, Y) , and the radii of the two rotors are R_1 and R_2 respectively. The positive

x -axis of the coordinate system is in the free wind direction and the positive y -axis is 90° perpendicular to it. This is visualised in Figure 7.1. Even though the radius of the rotors in the same VAWT farm are usually identical, the radii of the two rotors are represented by two variables for a more general formulation. To be noted that the swept area of the two rotors will not intersect with each other for a ordinary layout in reality. As a result, the distance between the rotational axis of the two rotors is larger than the sum of the two radii of R_1 and R_2 .

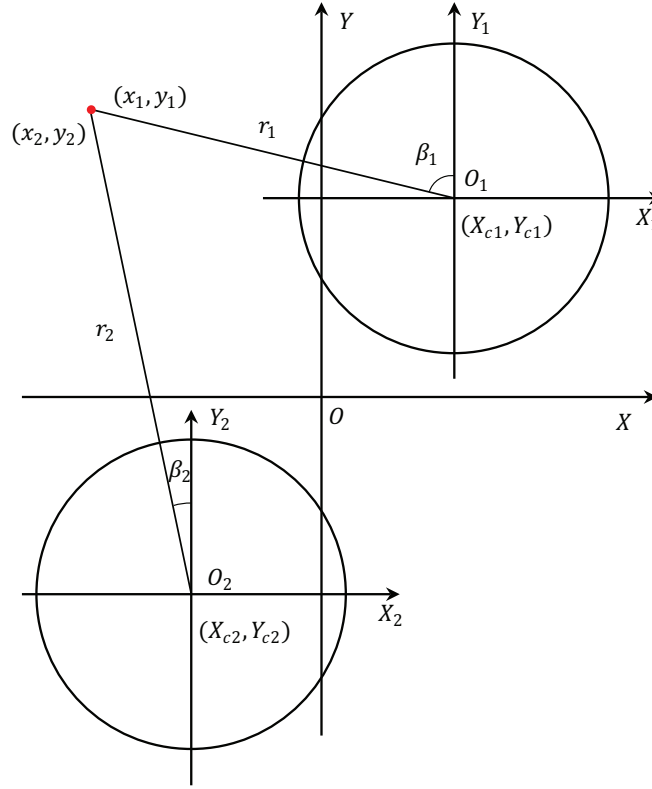


Figure 7.1: The coordinate systems for the Double Actuator Cylinder model

In order to let equations for the DAC model having similar formulation as that of the single AC model, one non-dimensioned coordinate system is introduced for every rotor in the layout. For the rotor number i , its non-dimensioned coordinate system is noted as of (x_i, y_i) with the origin located at the rotational axis of this rotor, and the positive x -axis and y -axis are in the same direction as that of the dimensioned coordinate system (X, Y) . The coordinate is non-dimensioned with the radius of the number i rotor R_i . With the above definitions, the coordinate of an arbitrary point (X, Y) in the dimensioned coordinate system could be transformed to the non-dimensioned coordinate corresponding to rotor number i with following equations.

$$x_i = (X - X_{ci})/R_i \quad (7.1)$$

$$y_i = (Y - Y_{ci})/R_i \quad (7.2)$$

In addition, the non-dimensioned coordinate (x_i, y_i) could also be transformed to the non-dimensioned polar coordinate system (r, θ) with the coordinate of (r_i, β_i) . The coordinate

systems are visualised in Figure 7.1 for demonstration. To be noted that for a double-rotor layout, an arbitrary point in the flow field will have two non-dimensioned coordinate which are corresponding to the two rotors respectively.

7.1.2 Derivation with linear solution properties

The linear solution of the DAC model will be derived in this subsection with the properties of the linear solution of the single AC model. The formulation of the linear solution of the induced velocity in x and y for the double-rotor layout with the DAC model will be obtained.

Linear part of pressure

According to Madsen [32], the induced velocity could be written to be the sum of the linear part and the non-linear part. And the linear part of the induced velocity is calculated from the linear part of the pressure as in Equation (7.3) and (7.4). The linear part of the pressure is due to the contribution of the volume forces and is derived from the Poisson type equation with the formulation in (7.5). To be noted that the notation of f represents the linear part which is to be consistent with the notation in [32] and [8].

$$w_x(f) = -p_f + \int_{-\infty}^x f_x dx' \quad (7.3)$$

$$w_y(f) = - \int_{-\infty}^x \frac{\partial p_f}{\partial y} dx' + \int_{-\infty}^x f_y dx' \quad (7.4)$$

$$p_f = \frac{1}{2\pi} \iint \frac{f_x(x-\xi) + f_y(y-\eta)}{(x-\xi)^2 + (y-\eta)^2} d\xi d\eta \quad (7.5)$$

In the equation above, the variable of x and y are the non-dimensioned coordinate of the location to be evaluated, the variable of f_x and f_y are the volume forces in x - and y -directions, and the variable of ξ and η are dummy variables of the non-dimensioned coordinate in x - and y -direction of where the volume forces are located. The value of p_f is calculated from integrating throughout the whole flow field for the non-zero volume forces. For the single rotor layout, the volume forces are located at the swept area of the blades which is assumed to be an infinitely thin annulus and corresponds to the Actuator Cylinder in the AC model. For the double rotor layout, the non-zero volume forces are then located at the swept area of the two rotors which will then corresponds to the two infinitely thin annulus and corresponds to two Actuator Cylinders in the DAC model.

For the double rotor layout, if directly using Equation (7.5) to calculate the pressure and then use the Equation (7.3) and (7.4) to calculate the induced velocities, the derivation will be very complicated and also for the formulation of induced velocities. In order to use the formulation of the linear part of the induced velocity in the single AC model, the Equation (7.5) is written as the sum of the contribution due to the volume forces on the two Actuator Cylinders as follows due to the linear charme forces.

$$p_f = p_{f,1} + p_{f,2} \quad (7.6)$$

And the explicit equation of the contribution to the pressure due to each AC is then as follows.

$$p_{f,h} = \frac{1}{2\pi} \iint \frac{f_{x,h}(x_h - \xi_i) + f_{y,h}(y_h - \eta_i)}{(x_h - \xi_h)^2 + (y_h - \eta_i)^2} d\xi_h d\eta_h \quad (7.7)$$

In the above equation, the subscript of h represents the variables are corresponding to the rotor number h . And the non-dimensioned coordinate system of (x_h, y_h) has been defined in subsection 7.1.1. It could be indicated that the contribution to the linear part of the pressure due to the volume forces on each Actuator Cylinder is then in the same form as the formulation for the single AC model. Because for the contribution of each rotor, with the corresponding non-dimensioned coordinate system, the Actuator Cylinder is located on the annulus with the radius of 1.

Linear part of induced velocity

With the formulation of the linear part of the induced velocities given in Equation (7.3) and (7.4), subtracting the linear pressure p_f with the sum of two parts as Equation (7.6), the induced velocity in x - and y -directions could be then calculated as follows with the contribution due to the two rotors.

$$w_x(f) = \sum_{h=1}^2 w_{x,h}(f) \quad (7.8)$$

$$w_y(f) = \sum_{h=1}^2 w_{y,h}(f) \quad (7.9)$$

with

$$w_{x,h}(f) = -p_{f,h} + \int_{-\infty}^{x,h} f_{x,h} dx' \quad (7.10)$$

$$w_{y,h}(f) = - \int_{-\infty}^{x,h} \frac{\partial p_{f,h}}{\partial y, h} dx' + \int_{-\infty}^{x,h} f_{y,h} dx' \quad (7.11)$$

Because the formulation of each contribution is identical to that of the single AC model with the definition of the non-dimensioned coordinate system. The two parts of the contribution to the induced velocity could then be calculated with same equations as that for the single AC model. When using the original AC model that the induced velocities are only dependent on the normal loadings.

$$w_{x,h}(x_h, y_h) = -\frac{1}{2\pi} \int_0^{2\pi} Q_{n,h}(\phi) \frac{-(x_h + \sin \phi) \sin \phi + (y_h - \cos \phi) \cos \phi}{(x_h + \sin \phi)^2 + (y_h - \cos \phi)^2} d\phi \\ - Q_{n,h}(\cos^{-1} y_h)^* + Q_{n,h}(-\cos^{-1} y_h)^{**} \quad (7.12)$$

$$w_{y,h}(x_h, y_h) = -\frac{1}{2\pi} \int_0^{2\pi} Q_{n,h}(\phi) \frac{-(x_h + \sin \phi) \cos \phi - (y_h - \cos \phi) \sin \phi}{(x_h + \sin \phi)^2 + (y_h - \cos \phi)^2} d\phi \quad (7.13)$$

As a result, the DAC model is derived which could be considered as using two single AC model to calculate the contribution due to the loadings on the two rotors respectively and then sum together. To be noted that the two extra terms of (*) and (**) should be included when the location to be evaluated is inside and in the direct wake of the rotor h respectively when calculating the contribution due to this rotor.

7.1.3 Multiple Actuator Cylinder model

The DAC model derived above could be further extended to multiple AC model for the application of the layout with an arbitrary number of rotors N_r in the flow field. The derivation will be very similar to the above for the double-rotor layout. For the layout with N_r rotors, in order to calculate the induced velocity of an arbitrary point in the flow field, there will be N_r contributions due to each rotor and will need N_r different non-dimensional coordinate systems. The analysis in this chapter is focused on the double-rotor layout and the layout with multiple rotors is beyond the scope of this report.

7.2 Implementation of the DAC model

In this section, the details about the implementation of the DAC model in the computer code such as MATLAB will be discussed. Firstly, there will be the discretization method and the explicit form of the induced velocities as well as influence coefficients for the DAC model based on the original AC model. Secondly, there will be the formulation for the DAC model based on the Cheng's modified AC model. Thirdly, there will be matrix formulation of the induced velocities. And finally, there will be the summarise of four different DAC models. In this section, it is assumed that none of the two rotors is partially or fully in the direct wake of the other rotor for simplicity.

7.2.1 Four different types of the DAC models

For the single AC model that does not consider the unsteady aerodynamics, there are four different models of AC1 to AC4 which are defined in section 5.4. There will then be four different DAC models which were inherited from the corresponding single AC models are summarised into the table below.

Table 7.1: Four different Double Actuator Cylinder Models.

Name	Inherited	Dependence of Loading	Evaluation point
DAC1	AC1	Q_n	1/4 c
DAC2	AC2	Q_n, Q_t	3/4 c
DAC3	AC3	Q_n	1/4 c
DAC4	AC4	Q_n, Q_t	3/4 c

The DAC2 and DAC4 model could model the flow curvature effect since they are inherited from the AC2 and AC4 model respectively, while the DAC1 and DAC3 model are not able to model the effect since they are inherited from the AC1 and AC3 model. Thus, only the DAC2 and DAC4 models are taken into account in the following.

7.2.2 DAC model based on original AC model

Firstly, the explicit form of the induced velocities on the control points for the DAC model based on the original AC model is derived.

Discretization

For each rotor, the discretization of the Actuator Cylinder could be done in the same method as that of the single AC model with Equation (3.6). The formulation of the locations of the control points in the non-dimensioned coordinate system corresponding to itself will also be identical to that of the single AC model with Equation (3.9) and (3.10).

Induced velocity

For the DAC model that based on the original AC model, the induced velocities will be dependent only on the normal loadings. And for simplicity, the control points are assumed to be moved just outside of the AC for both windward and leeward in the following of this section. With this assumptions, the explicit form of the induced velocities on the control points in x and y could then be obtained according to Equation (7.12) and (7.13) and is as follows.

$$w_{x,k,j} = \sum_{h=1}^2 \left(-\frac{1}{2\pi} \sum_{i=1}^N Q_{n,h,i} I_{1,k,h,j,i} \right) - (Q_{n,k,N+1-j})^* + (Q_{n,k,j})^* \quad (7.14)$$

$$w_{y,k,j} = \sum_{h=1}^2 \left(-\frac{1}{2\pi} \sum_{i=1}^N Q_{n,h,i} I_{2,k,h,j,i} \right) \quad (7.15)$$

The notion of the subscript should be firstly explained to avoid confusions. The subscript of j and k represent the control point to be evaluated is the number j control point on the AC number k . And the subscript of h and i represents the loading that inducing velocity is at the control point i of AC number h .

Integral part of induced velocity

The influence coefficients are important for the integral part of the induced velocity and the explicit form should be obtained. With the notation of the subscripts defined above, the

influence coefficient $I_{1,k,h,j,i}$ then represents that the influence coefficient I_1 of the loading at the control point i of AC number h inducing on the control point j of AC number k . The explicit form of the influence coefficient of $I_{1,k,h,j,i}$ and $I_{2,k,h,j,i}$ could be obtained from Equation (3.17) and (3.18) as follows.

$$I_{1,k,h,j,i} = \int_{\theta_i-1/2\Delta\theta}^{\theta_i+1/2\Delta\theta} \frac{-(x_{k,h,j} + \sin \phi) \sin \phi + (y_{k,h,j} - \cos \phi) \cos \phi}{(x_{k,h,j} + \sin \phi)^2 + (y_{k,h,j} - \cos \phi)^2} d\phi \quad (7.16)$$

$$I_{2,k,h,j,i} = \int_{\theta_i-1/2\Delta\theta}^{\theta_i+1/2\Delta\theta} \frac{-(x_{k,h,j} + \sin \phi) \cos \phi - (y_{k,h,j} - \cos \phi) \sin \phi}{(x_{k,h,j} + \sin \phi)^2 + (y_{k,h,j} - \cos \phi)^2} d\phi \quad (7.17)$$

The variable of $x_{k,h,j}$ and $y_{k,h,j}$ are the coordinate of the control point j on rotor number k in the non-dimensional coordinate of rotor number h which could be calculated with Equation (7.1) and (7.2).

With the influence coefficients obtained, the integral part of the induced velocities could then be calculated with Equation (7.14) and (7.15) with the (*) term neglected. It could be concluded from the two equations that the contribution to the induced velocities due to the loadings on all the control points of both the two rotors are calculated and then summed together.

Additional terms of the induced velocity

The two additional terms which are marked by (*) in Equation (7.14) of the induced velocity in x -direction should be included when the control point j on rotor k is in on the leeward of the AC. This is due to the assumption that the control points for both windward and leeward parts are moved just outside of the AC. The two terms here correspond to the (*) and (**) terms in Equation (7.12). The explicit form of the extra terms in the Equation (7.14) for other methods of moving the control points could be obtained by referring to subsection 3.3.4.

With the assumption that neither of the two rotors is partially or fully in the direct wake of the other, the integration path will then only pass one Actuator Cylinder instead of two. The additional terms in Equation (7.14) is then outside of the bracket because the location could not be in the direct wake of two rotors. Similar to the single AC model, when the control point j is on the leeward part of the AC number k with the condition of $j > N/2$, the integration path will then pass the control point $N + 1 - j$ in the windward part and the control point j in the leeward part. The loadings at the two points are then corresponding to the two (*) terms in Equation (7.14).

7.2.3 DAC model based on Cheng's AC model

The DAC model could also be developed from Cheng's single AC model that the induced velocities are dependent on the both the normal and tangential loadings. The equation of

the induced velocities at an arbitrary point in x - and y -direction could be obtained from Equation (3.101) and (3.102) and as follows.

$$\begin{aligned}
 w_{x,h}(x_h, y_h) = & -\frac{1}{2\pi} \int_0^{2\pi} Q_{n,h}(\phi) \frac{-(x_h + \sin \phi) \sin \phi + (y_h - \cos \phi) \cos \phi}{(x_h + \sin \phi)^2 + (y_h - \cos \phi)^2} d\phi \\
 & - \frac{1}{2\pi} \int_0^{2\pi} Q_{t,h}(\phi) \frac{-(x_h + \sin \phi) \cos \phi - (y_h - \cos \phi) \sin \phi}{(x_h + \sin \phi)^2 + (y_h - \cos \phi)^2} d\phi \\
 & + \left(-Q_{n,h}(\cos^{-1} y_h) - (Q_{t,h}(\cos^{-1} y_h) \frac{y_h}{\sqrt{1-y_h^2}}) \right)^* \\
 & + \left(Q_{n,h}(-\cos^{-1} y_h) - (Q_{t,h}(-\cos^{-1} y_h) \frac{y_h}{\sqrt{1-y_h^2}}) \right)^{**} \quad (7.18)
 \end{aligned}$$

$$\begin{aligned}
 w_{y,h}(x_h, y_h) = & -\frac{1}{2\pi} \int_0^{2\pi} Q_{n,h}(\phi) \frac{-(x_h + \sin \phi) \cos \phi - (y_h - \cos \phi) \sin \phi}{(x_h + \sin \phi)^2 + (y_h - \cos \phi)^2} d\phi \\
 & + \frac{1}{2\pi} \int_0^{2\pi} Q_{t,h}(\phi) \frac{-(x_h + \sin \phi) \sin \phi + (y_h - \cos \phi) \cos \phi}{(x_h + \sin \phi)^2 + (y_h - \cos \phi)^2} d\phi \quad (7.19)
 \end{aligned}$$

With the assumptions that all the control points are moved just outside of the AC, and neither of the rotors is in the direct wake of the other, the equation of the induced velocities on the control points could be obtained similarly to Equation (3.105) and (3.106) and as follows.

$$\begin{aligned}
 w_{x,k,j} = & \sum_{h=1}^2 \left(-\frac{1}{2\pi} \sum_{i=1}^N Q_{n,h,i} I_{1,k,h,j,i} - \frac{1}{2\pi} \sum_{i=1}^N Q_{t,h,i} I_{2,k,h,j,i} \right) - (Q_{n,k,N+1-j})^* + (Q_{n,k,j})^* \\
 & - (Q_{t,k,N+1-j})^* \frac{y_{k,k,j}}{\sqrt{1-y_{k,k,j}^2}} - (Q_{t,k,j})^* \frac{y_{k,k,j}}{\sqrt{1-y_{k,k,j}^2}} \quad (7.20)
 \end{aligned}$$

$$w_{y,k,j} = \sum_{h=1}^2 \left(-\frac{1}{2\pi} \sum_{i=1}^N Q_{n,h,i} I_{2,k,h,j,i} + \frac{1}{2\pi} \sum_{i=1}^N Q_{t,h,i} I_{1,k,h,j,i} \right) \quad (7.21)$$

7.2.4 Matrix formulations

Similar to the single AC model, the calculation of the induced velocities with the DAC model could also be written in the matrix form.

Original DAC model

Similar to the matrix formulation of the original AC model as in Equation (3.71), the matrix formulation of the DAC model based on the original AC model is as follows.

$$\begin{bmatrix} w_{x,1} \\ w_{x,2} \end{bmatrix} = \begin{bmatrix} A_{x,1,1} & A_{x,1,2} \\ A_{x,2,1} & A_{x,2,2} \end{bmatrix} \begin{bmatrix} Q_{n,1} \\ Q_{n,2} \end{bmatrix} \quad (7.22)$$

In the above equation, $w_{x,1}$ and $w_{x,2}$ are two column vectors of the induced velocity in x -direction for the control points on the two ACs respectively. $Q_{n,1}$ and $Q_{n,2}$ are also two column vectors of the normal loadings on the control points of the two ACs, and are assembled into one column vector for calculation. The matrix of $A_{x,k,h}$ is the influence coefficient matrix for the loading on AC number h inducing on the control points of AC number k . Similar to Equation (3.71), the influence coefficient $A_{x,k,h}$ is the sum of the direct influence coefficient $D_{x,k,h}$ and the wake coefficient matrix $W_{x,k,h}$ as follows.

$$A_{x,k,h} = D_{x,k,h} + W_{x,k,h} \quad (7.23)$$

With each of the AC is discretized into N sections, the direct influence coefficient matrix for the loading on AC number h inducing on the control points of AC number k will then contains $N \times N$ elements and could be obtained according to Equation (7.14).

$$D_{x,k,h} = -\frac{1}{2\pi} \begin{bmatrix} I_{1,k,h,1,1} & I_{1,k,h,1,2} & \cdots & I_{1,k,h,1,N} \\ I_{1,k,h,2,1} & I_{1,k,h,2,2} & \cdots & I_{1,k,h,2,N} \\ \vdots & \vdots & \ddots & \vdots \\ I_{1,k,h,N,1} & I_{1,k,h,N,2} & \cdots & I_{1,k,h,N,N} \end{bmatrix} \quad (7.24)$$

The matrix could also be assembled element by element with the influence coefficients of $I_{1,k,h,j,i}$ with the similar method as Equation (3.74).

$$D_{x,k,h}(j,i) = -\frac{1}{2\pi} I_{1,k,h,j,i} \quad (7.25)$$

With the assumption that the neither of the rotor is in the direct wake of another, the wake influence coefficient will have none-zero elements only when $k = h$. And with the assumption that the control points are moved just outside of the AC, the matrix could then assembled according to Equation (7.14).

$$W_{x,k,k}(j, N+1-j) = -1 \quad , j > N/2 \quad (7.26)$$

$$W_{x,k,k}(j, j) = 1 \quad , j > N/2 \quad (7.27)$$

The calculation of the induced velocity in y -direction could also be done with matrix operation which is similar to that for the x -direction.

$$\begin{bmatrix} w_{y,1} \\ w_{y,2} \end{bmatrix} = \begin{bmatrix} A_{y,1,1} & A_{y,1,2} \\ A_{y,2,1} & A_{y,2,2} \end{bmatrix} \begin{bmatrix} Q_{n,1} \\ Q_{n,2} \end{bmatrix} \quad (7.28)$$

The column vector of $w_{y,k}$ and $Q_{t,k}$ are corresponding to the induced velocity in y -direction and tangential loading for the AC number k respectively. The influence coefficient matrix of $A_{y,k,h}$ is for the loadings on AC number h inducing on control points of AC number k . It could be assembled according to Equation (7.15) as follows.

$$A_{y,k,h}(j,i) = -\frac{1}{2\pi} I_{2,k,h,j,i} \quad (7.29)$$

Cheng's modified DAC model

For the DAC model that derived from Cheng's single AC model, the calculation of the induced velocities in x - and y -directions could also be done with matrix operation. The matrix formulation could be obtained according to Equation (7.20) in the similar form as Equation (3.107). There are two possible methods which will have the same results, the first method is as follows.

$$\begin{bmatrix} w_{x,1} \\ w_{x,2} \end{bmatrix} = \begin{bmatrix} A_{x,1,1} & A_{x,1,2} \\ A_{x,2,1} & A_{x,2,2} \end{bmatrix} \begin{bmatrix} Q_{n,1} \\ Q_{t,1} \\ Q_{n,2} \\ Q_{t,2} \end{bmatrix} \quad (7.30)$$

In the equation above, the influence coefficient matrix $A_{x,k,h}$ is the sum of direct influence coefficient matrix $D_{x,k,h}$ and the wake coefficient matrix $W_{x,k,h}$.

$$A_{x,k,h} = D_{x,k,h} + W_{x,k,h} \quad (7.31)$$

With the AC discretized into N sections, the matrices here will be the size of $N \times 2N$ which are consists of the two parts which corresponding to the influence due to normal loadings and tangential loadings respectively.

$$\begin{bmatrix} A_{x,n,k,h} & A_{x,t,k,h} \end{bmatrix} = \begin{bmatrix} D_{x,n,k,h} & D_{x,t,k,h} \end{bmatrix} + \begin{bmatrix} W_{x,n,k,h} & W_{x,t,k,h} \end{bmatrix} \quad (7.32)$$

The induced velocity in y -direction could also be calculated with matrix operation and the formulation could be obtained similar to Equation (3.114)

$$\begin{bmatrix} w_{y,1} \\ w_{y,2} \end{bmatrix} = \begin{bmatrix} A_{y,1,1} & A_{y,1,2} \\ A_{y,2,1} & A_{y,2,2} \end{bmatrix} \begin{bmatrix} Q_{n,1} \\ Q_{t,1} \\ Q_{n,2} \\ Q_{t,2} \end{bmatrix} \quad (7.33)$$

The influence coefficient matrix $A_{y,k,h}$ is consisted of two parts which are corresponding to the contribution due to normal and tangential loading respectively.

$$A_{y,k,h} = \begin{bmatrix} A_{y,n,k,h} & A_{y,t,k,h} \end{bmatrix} \quad (7.34)$$

The influence coefficient matrix of $D_{x,n,k,h}$ and $A_{y,n,k,h}$ could be assembled with identical method as in Equation (7.25) and (7.29) respectively which are for the formulation of the original DAC model. And the following relationship could be obtained according to Equation (7.20) and (7.21).

$$A_{y,t,k,h} = -D_{x,n,k,h} \quad (7.35)$$

$$D_{x,t,k,h} = A_{y,n,k,h} \quad (7.36)$$

And now, only the wake coefficient matrix is needed to be obtained. With the assumption that neither of the two rotors is in the direct wake of the other and the assumption of all the control points are moved just outside of the AC, the wake terms could then be obtained according to Equation (7.20).

$$\mathbf{W}_{x,n,k,k}(j, N+1-j) = -1, j > N/2 \quad (7.37)$$

$$\mathbf{W}_{x,n,k,k}(j, j) = 1, j > N/2 \quad (7.38)$$

$$\mathbf{W}_{x,t,k,k}(j, N+1-j) = -\frac{y_{k,k,j}}{\sqrt{1-y_{k,k,j}^2}}, j > N/2 \quad (7.39)$$

$$\mathbf{W}_{x,t,k,k}(j, j) = -\frac{y_{k,k,j}}{\sqrt{1-y_{k,k,j}^2}}, j > N/2 \quad (7.40)$$

The second method is similar to the method above and with some differences. The induced velocity in x -direction in Equation (7.30) is then written the form as follows.

$$\begin{bmatrix} w_{x,1} \\ w_{x,2} \end{bmatrix} = \begin{bmatrix} \mathbf{A}_{x,n} & \mathbf{A}_{x,t} \end{bmatrix} \begin{bmatrix} Q_{n,1} \\ Q_{n,2} \\ Q_{t,1} \\ Q_{t,2} \end{bmatrix} \quad (7.41)$$

The two matrices of $\mathbf{A}_{x,n}$ and $\mathbf{A}_{x,t}$ are both with the size of $2N \times N$, and are as follows. The matrices of $\mathbf{A}_{x,n,k,h}$ and $\mathbf{A}_{x,t,k,h}$ are both with the size of $N \times N$ and could be also be assembled element by element and are identical to that for the first method.

$$[\mathbf{A}_{x,n}] = \begin{bmatrix} \mathbf{A}_{x,n,1,1} & \mathbf{A}_{x,n,1,2} \\ \mathbf{A}_{x,n,2,1} & \mathbf{A}_{x,n,2,2} \end{bmatrix} \quad (7.42)$$

$$[\mathbf{A}_{x,t}] = \begin{bmatrix} \mathbf{A}_{x,t,1,1} & \mathbf{A}_{x,t,1,2} \\ \mathbf{A}_{x,t,2,1} & \mathbf{A}_{x,t,2,2} \end{bmatrix} \quad (7.43)$$

Similarly, the induced velocity in y -direction in Equation (7.33) is written in the following form.

$$\begin{bmatrix} w_{y,1} \\ w_{y,2} \end{bmatrix} = \begin{bmatrix} \mathbf{A}_{y,n} & \mathbf{A}_{y,t} \end{bmatrix} \begin{bmatrix} Q_{n,1} \\ Q_{n,2} \\ Q_{t,1} \\ Q_{t,2} \end{bmatrix} \quad (7.44)$$

The matrices of $\mathbf{A}_{y,n}$ and $\mathbf{A}_{y,t}$ are also with the size of $2N \times N$, and are as follows. The matrices of $\mathbf{A}_{y,n,k,h}$ and $\mathbf{A}_{y,t,k,h}$ are with the size of $N \times N$.

$$[\mathbf{A}_{y,n}] = \begin{bmatrix} \mathbf{A}_{y,n,1,1} & \mathbf{A}_{y,n,1,2} \\ \mathbf{A}_{y,n,2,1} & \mathbf{A}_{y,n,2,2} \end{bmatrix} \quad (7.45)$$

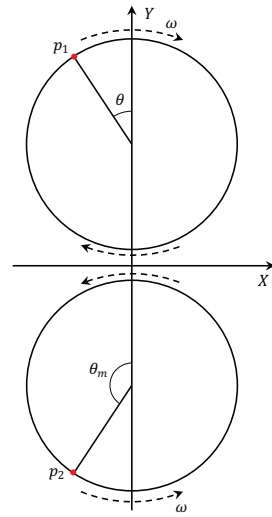
$$[\mathbf{A}_{y,t}] = \begin{bmatrix} \mathbf{A}_{y,t,1,1} & \mathbf{A}_{y,t,1,2} \\ \mathbf{A}_{y,t,2,1} & \mathbf{A}_{y,t,2,2} \end{bmatrix} \quad (7.46)$$

7.3 Layouts of the two rotors

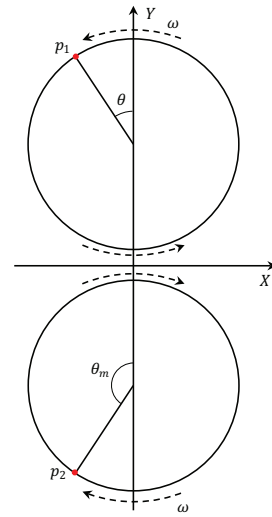
For the rotational directions of the two-rotor layout, there are four different combinations that each rotor could be either counter-clockwise rotation or clockwise rotating. The four

different combinations could be visualised in Figure 7.2. The implementation of different cases of rotational direction layout for the two rotors will be firstly introduced and then validated with the mirror effect. The implementation will also be validated for the case that the two rotors are infinitely far from each other. And finally, the performance of the DAC models on evaluating the power coefficient and thrust coefficient for different load cases is evaluated.

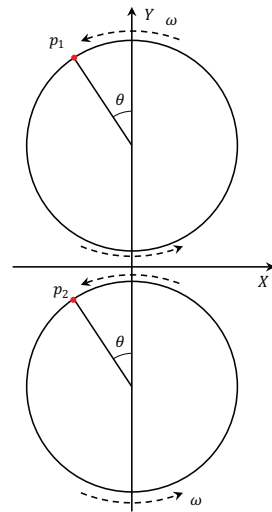
For the investigation in this section, the two rotors are identical and operating with same tip speed ratio with uniform incoming wind and the yaw angle is also set to be zero. For simplicity, with the non-dimensioned distance between the two rotors to be d , the rotational axis of the two rotors are placed on the y -axis with the non-dimensioned y coordinate to be $1 + d/2$ and $-1 - d/2$ respectively. The corresponding two rotors are named *north* and *south* rotor respectively according to the location of the rotational axis.



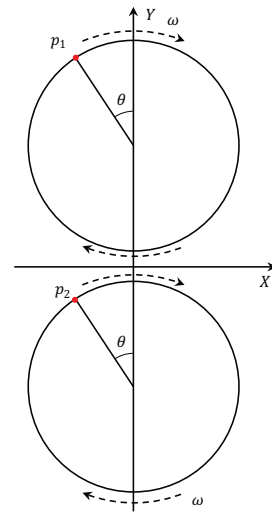
(a) Counter-Up layout.



(b) Counter-Down layout.



(c) Counter-clockwise Co-Rotating layout.



(d) Clockwise Co-Rotating layout.

Figure 7.2: The four different rotational direction layouts of a double-VAWT layout.

7.3.1 Different cases of rotational direction layouts

When the two rotors are with different rotational directions, the layout is named *Counter-Rotation*. And when the two rotors are with rotating in the same direction, the layout is named *Co-Rotation*.

There are two cases for the *Counter-Rotating* layout which are corresponding to Figure 7.2(a) and (b), and the two cases are named *Counter-Up* and *Counter-Down* respectively. The term of *Up* and *Down* are corresponding to the relationship of the direction of rotational velocity between the two rotors and the direction of incoming wind. For the *Counter-Up* layout, the direction of the rotational velocities at coordinate of $(0, d/2)$ and $(0, -d/2)$ are opposite with that of the free wind velocity. And for the *Counter-Down* layout, the rotational velocity between the two rotors are in the same direction as the free wind velocity. For the two cases of *Co-Rotating* layout that the two rotors are both counter-clockwise rotating or both clockwise rotating, they could be summarised into a single case. According to subsection 3.3.2 that for a single rotor layout, the clockwise rotating case could be transformed to the counter-clockwise rotating case with the mirror effect. Similarly, the case that the two rotors are clockwise *Co-Rotating* could also be transformed to the counter-clockwise *Co-Rotating*. As a result, the two cases could then be summarised into a single case of *Co-Rotating*. This will be validated later in this section with numerical results.

Thus, with the four combinations of rotational directions of the two rotors, there will be three different case which are *Counter-Up*, *Counter-Down* and *Co-Rotating* layouts.

7.3.2 Validation with mirror effect

The mirror effect that introduced in Chapter 3 is a very important phenomenon for the double-rotor layout. It could also be used for the validation of the implementation of the DAC model. The mirror effect will be firstly determined and then validated for the cases of *Counter-Rotating* and *Co-Rotating* respectively.

Validation of the *Counter-Rotating* layout

For the *Counter-Rotating* layout with zero yaw angle, the properties at the azimuthal angle of θ on the counter-clockwise rotating rotor will be the mirrored properties of the azimuthal angle of θ_m on the clockwise rotating rotor. It could then be concluded that the properties of the two rotors could then be represented by the of the rotors. The properties of the counter-clockwise rotating rotor is then used in order to be consistent with the plots for the single rotor layout. The counter-clockwise rotating rotor is the south rotor for the *Counter-Up* layout and is the north rotor for the *Counter-Down* layout.

The mirror effect could be considered as the properties of the north and south rotors are symmetry with respect to the x -axis. The induced velocities in x -direction of the

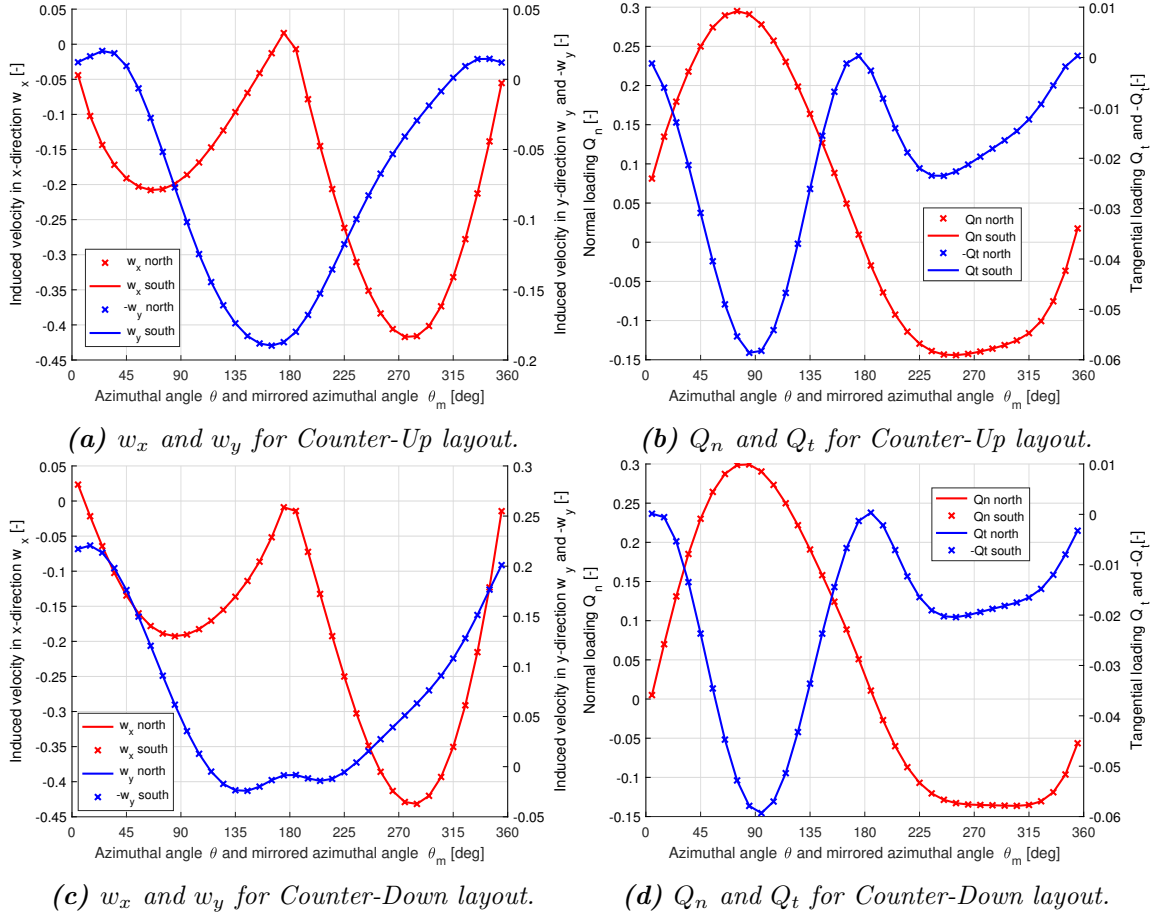


Figure 7.3: Validation of the mirror effect for the Counter-Up and Counter-Down layout from the DAC2 model with induced velocities and loadings, with $\lambda = 4$, $\sigma = 0.07$, $B = 2$, $d = 0.1$.

two mirrored locations of two rotors of the *Counter-Rotating* layout are identical, and it is also for the normal loadings. But the induced velocities in y -direction of the two mirrored locations are additive inverses which means they are in different directions with same magnitude and are in the same coordinate system as in Figure 7.2, it is also for the tangential loadings. The relative wind speed could be calculated directly with the induced velocities and are identical for the two mirrored locations. The angle of attack of the two mirrored locations will be identical because of the definition of the angle of attack for the counter-clockwise is as Figure 3.4, and for the clockwise rotation is as Figure 3.8.

The induced velocity in x - and y -directions as well as the normal and tangential loadings are used for the validation. The angle of attack and relative wind speed could be calculated directly from the induced velocities and are thus not validated separately. It could also be argued that with the normal and tangential loadings validated, the angle of attack and relative wind speed will then be validated.

The validation will be done for the *Counter-Up* and *Counter-Down* layout with the DAC2 and DAC4 model which represent the DAC model from the original single AC model and

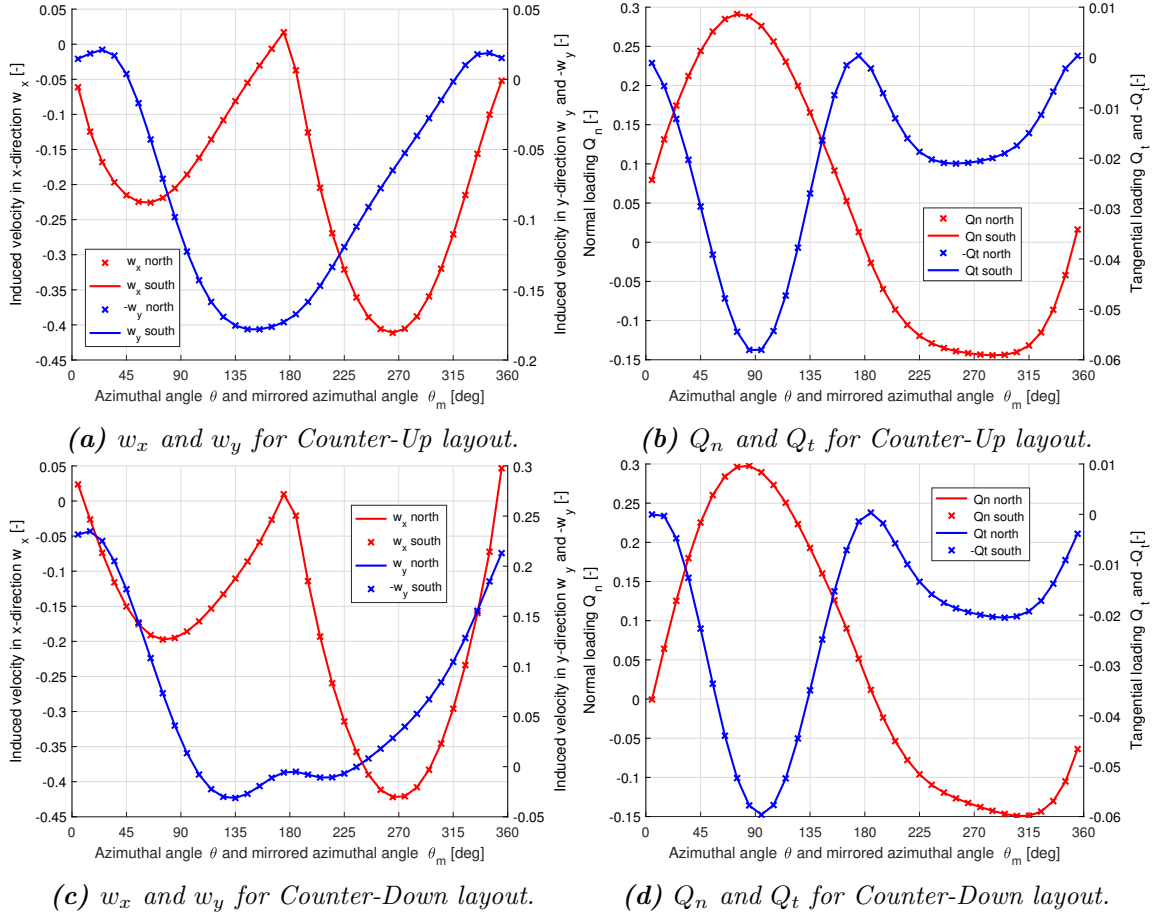


Figure 7.4: Validation of the mirror effect for the Counter-Up and Counter-Down layout from the DAC4 model with induced velocities and loadings, with $\lambda = 4$, $\sigma = 0.07$, $B = 2$, $d = 0.1$.

from the Cheng's modified single AC model respectively. The results for the two models are plotted in Figure 7.3 and 7.4.

It could be visualised from Figure 7.3 and 7.4 that the converged solution of the induced velocity in x -direction as well as the normal loading for the mirrored points are identical. And the converged solution of induced velocity in y -direction as well as the tangential loading of the mirrored points are additive inverses. It could then be concluded that the mirror effect of the properties of the two *Counter-Rotating* layouts are then verified. It could also be validated that the DAC2 and DAC4 model are correctly implemented for the *Counter-Rotating* layout in the MATLAB code.

Validation of the *Co-Rotating* layout

As introduced previously in this section, the two identical clockwise *Co-Rotating* rotor could be represented by two counter-clockwise *Co-Rotating* rotor according to the mirror effect. The properties on the north and south rotor of the clockwise *Co-Rotating* layout

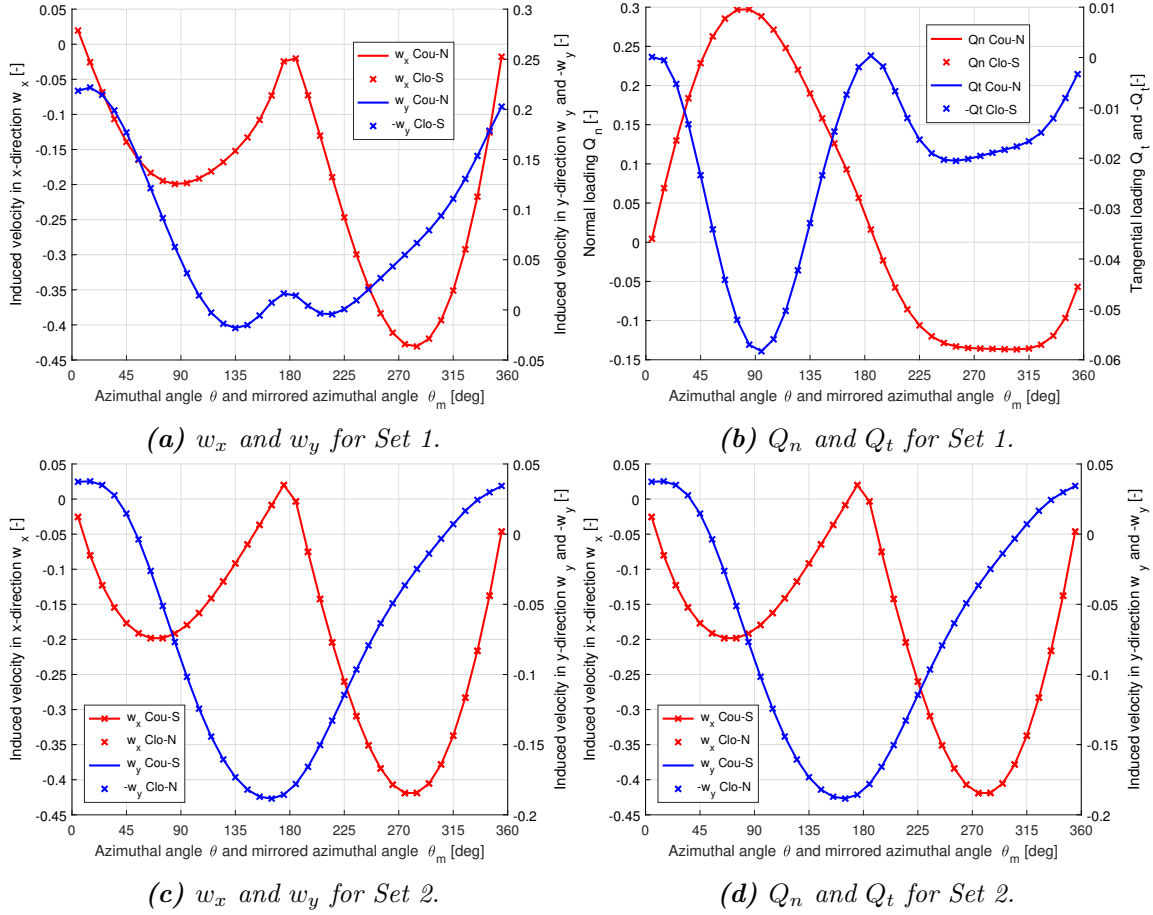


Figure 7.5: Validation of the mirror effect for the *Co-Rotating* layout from the *DAC2* model with induced velocities and loadings, with $\lambda = 4$, $\sigma = 0.07$, $B = 2$, $d = 0.1$.

will be the mirrored properties of the south and rotor of the counter-clockwise *Co-Rotating* layout. With the mirror effect, the induced velocity in x -direction, angle of attack, relative wind speed and normal loadings are identical for the two mirrored points. And the induced velocity in y -direction as well as tangential loadings will be additive inverses for the two mirrored points. The conclusion is consistent with the *Counter-Rotating* layouts. However, the mirror effect is applied to the north and south rotors in the same layout for cases the *Counter-Rotating*, but is applied to the two corresponding rotors in different layout for the cases of *Co-Rotating*.

The details of the validation is consistent with the validation for the *Counter-Rotating* layouts. The induced velocities in x - and y -directions as well as normal and tangential for the mirrored points are validated, and the properties at the azimuthal angle of θ for the counter-clockwise rotating rotor is compared with the azimuthal angle of θ_m for the corresponding mirrored clockwise rotating rotor. There will be two sets of validation for the *Co-Rotating* layouts with mirror effects and are as follows.

- Set 1: The north rotor of the counter-clockwise *Co-Rotating* layout and the south

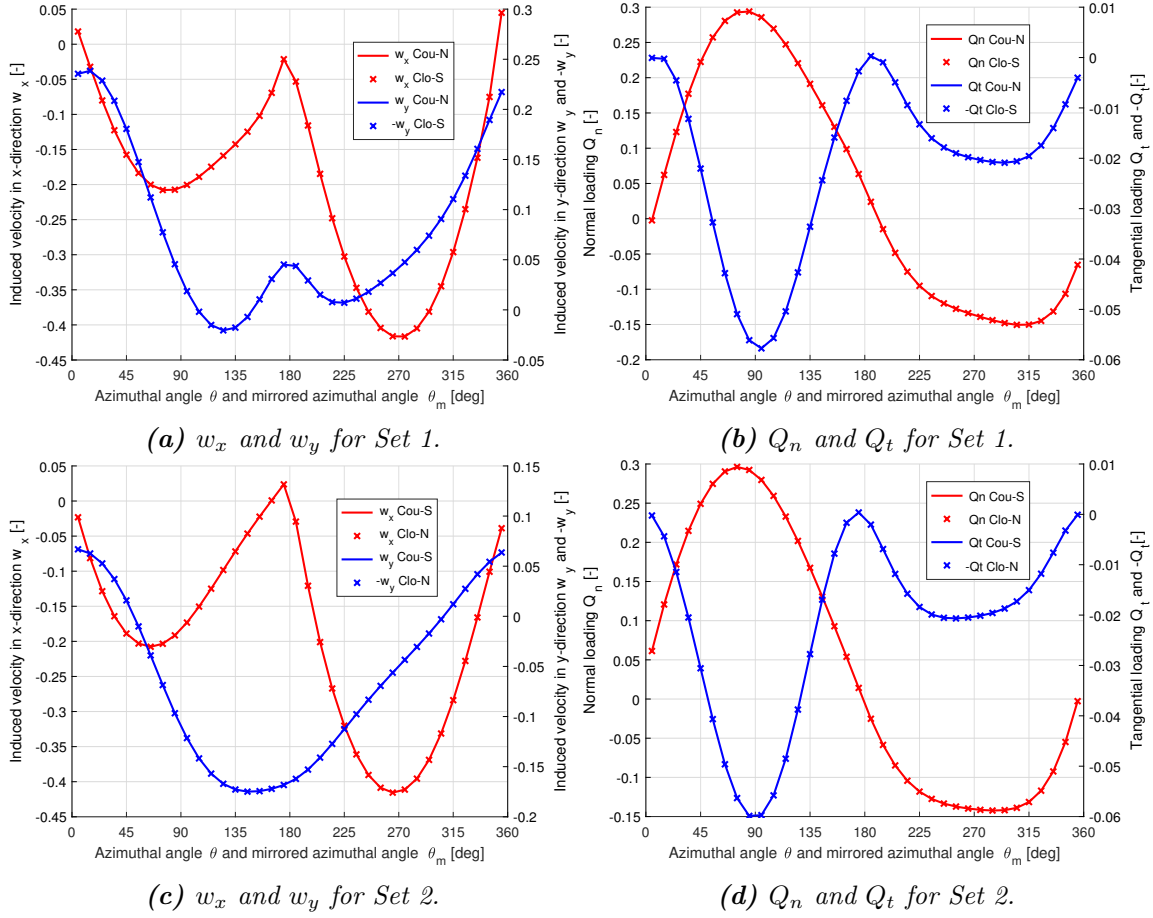


Figure 7.6: Validation of the mirror effect for the *Co-Rotating* layout from the *DAC4* model with induced velocities and loadings, with $\lambda = 4$, $\sigma = 0.07$, $B = 2$, $d = 0.1$.

rotor of the clockwise *Co-Rotating* layout.

- Set 2: The south rotor of the counter-clockwise *Co-Rotating* layout and the north rotor of the clockwise *Co-Rotating* layout.

The validation for the two sets should also be done with the *DAC2* and *DAC4* models and the results are plotted in Figure 7.5 and 7.6.

It could be visualised from the Figure 7.5 and 7.6 that converged solution of w_x and Q_n are identical for the mirrored locations, while the converged solution of w_y as well as Q_t are additive inverses for the mirrored locations for both the *DAC2* and *DAC4* model. It could then be concluded that the mirror effect between the two *Co-Rotating* layouts is then validated which also validates the clockwise and counter-clockwise *Co-Rotating* layouts could be represented by each other and then summarised into a single case. The *DAC2* and *DAC4* models are also validated to be correctly implemented in the MATLAB code for the *Co-Rotating* layouts.

7.3.3 Validation with infinite distance between rotors

When the distance between the two rotors are much larger comparing to the radius of them, the influence between the two rotors are then small enough to be neglected. This will then be identical to have only one of the rotors in the whole flow field. As a result, this will be another method to validate the DAC model with the condition of very large distance and compare with the result from the single AC model.

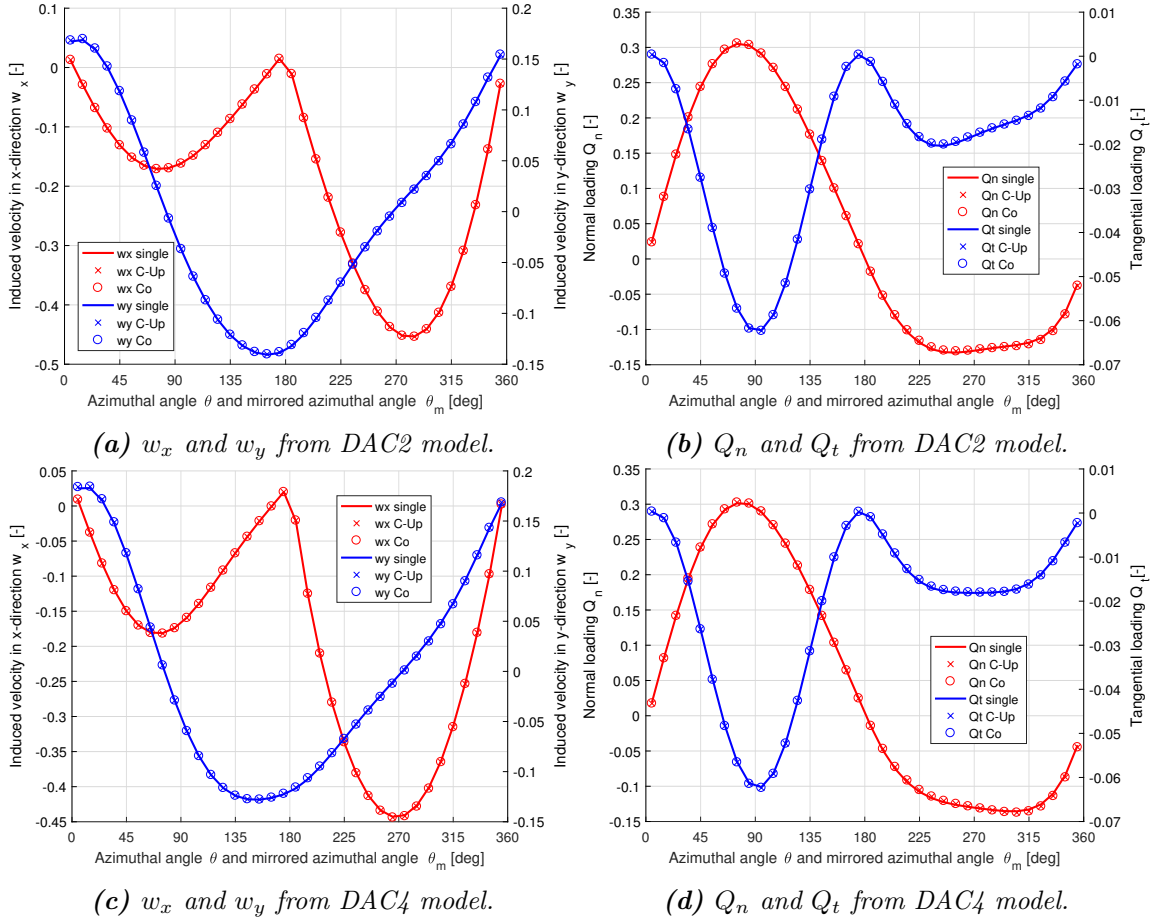


Figure 7.7: Validation when the distance between the two rotors is infinitely large with the induced velocities and loadings from the DAC2 and DAC4 model, with $\lambda = 4$, $\sigma = 0.07$, $B = 2$.

It has been validated with the mirror effect in subsection 7.3.2 that the properties of two rotors could be represented for the *Counter-Rotating* layouts, and the two *Co-Rotating* layouts could be represented by each other. And for simplicity, only the case of *Counter-Up* is validated for the *Counter-Rotating* layouts. The south rotor of the *Counter-Up* and counter-clockwise *Co-Rotating* layouts are compared with the corresponding counter-clockwise rotating single rotor, to be noted that the aforementioned rotors are all counter-clockwise rotating. The three cases are noted as *C-Up*, *Co* and *single* in the figures for abbreviation.

For the validation, the distance between the two rotors is set to be 1,000 times of the radius of the two rotors which should be large enough for the influence between the two rotors to be eliminated. The induced velocities in x - and y -directions as well as normal and tangential loadings are used for the validation. The validation should be done for both DAC2 and DAC4 model and the corresponding single AC model will then be AC2 and AC4 respectively, and the results are plotted in Figure 7.7.

It could be visualised from the figures that the converged solution of induced velocities as well as the loadings for the three cases are coincided with each other. It verifies that the influence between the two rotors are eliminated when the distance between the two rotors are very large. As a result, the DAC2 and DAC4 models are again validated to be correctly implemented.

7.3.4 Power and thrust coefficients

The implementation of the DAC models has been validated for different rotational direction layouts previously in this section, the performance of the DAC models on calculating the power coefficient and thrust coefficient for different tip speed ratio and solidity will be evaluated. The evaluation will be done for all four DAC models for the three rotational direction layouts, which are *Counter-Up*, *Counter-Down* and *Co-Rotating* layout. The results will then be compared with that from the panel code of U2DiVA for evaluation. The result from the DAC1 and DAC3 model will be plotted together, while the result from the DAC2 and DAC4 model will be plotted together. To be noted that for the *Co-Rotating* layout, the power and thrust coefficient are the mean value from the two rotors for comparison which represents the mean performance of the two rotors.

Counter-Up layout

For the double-rotor layout of *Counter-Up*, the results of power and thrust coefficient from the four DAC models are calculated and plotted together with the results from the panel code in Figure 7.8.

It could be visualised from the Figure 7.8 that the thrust coefficient from the DAC1 and DAC3 model are almost identical with each other, while the result from the DAC2 and DAC4 model are close to each other. The thrust coefficient from the DAC models are having good agreements with that from the panel code for the cases that the rotors are not heavily loaded with the condition of $C_T < 1$. This corresponds to the low tip speed ratio λ and solidity σ . For the high loading case with the condition of $C_T > 1$, the DAC models will underestimate the thrust coefficient and the underestimation will increase with the increase with the tip speed ratio λ and solidity σ . It could also be visualised that the DAC1 and DAC3 are having better agreements with the panel code because there is less underestimation. It could also be visualised that the power coefficient from the DAC models are generally overestimated compare with that from the panel code. The power coefficient from DAC3 and DAC4 models are having less overestimation that the DAC1 and

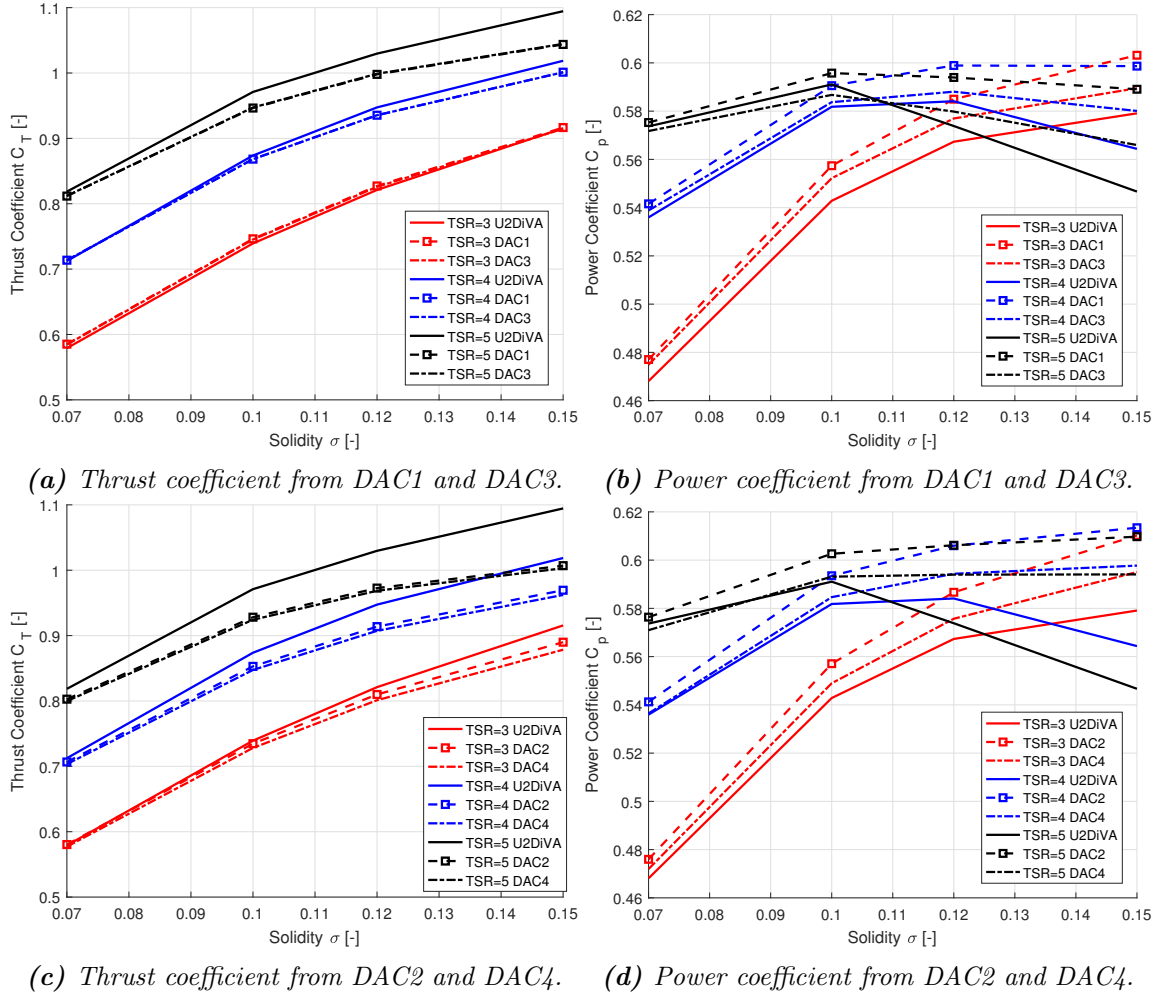


Figure 7.8: Thrust and power coefficient for different tip speed ratio and solidity with the Counter-Up layout from four DAC models, with $B = 2$, $d = 0.2$.

DAC2 models when comparing with the result from the panel code. The overestimation increase with the increasing of the tip speed ratio λ and solidity σ .

The general trend of the thrust coefficient with the increase of solidity could be well modelled with all four DAC models. The trend of power coefficient that firstly increase and then decrease for the condition of $\lambda = 5$ could not be well modelled with the DAC2 and DAC4 models. However, the DAC1 and DAC3 models are sufficient to model the trend. The relative relationship of the thrust coefficients for a certain solidity but different tip speed ratio could be well modelled with all the four DAC models. And the relative relationship of the power coefficient for a certain solidity with different tip speed ratio could be well modelled with the DAC1 and DAC3 model, but the DAC2 and DAC4 model could not model the relative relationship when $\sigma > 0.1$. As a result, the DAC1 and DAC3 model are having better agreements compared to the results from the DAC2 and DAC4 model with that from the panel code. And the DAC1 is slightly better than DAC3 model because it is better in predicting the power coefficient.

Counter-Down layout

The thrust coefficient and power coefficient for the *Counter-Down* layout is also calculated from the four DAC models and are compared with that from the panel code in Figure 7.9.

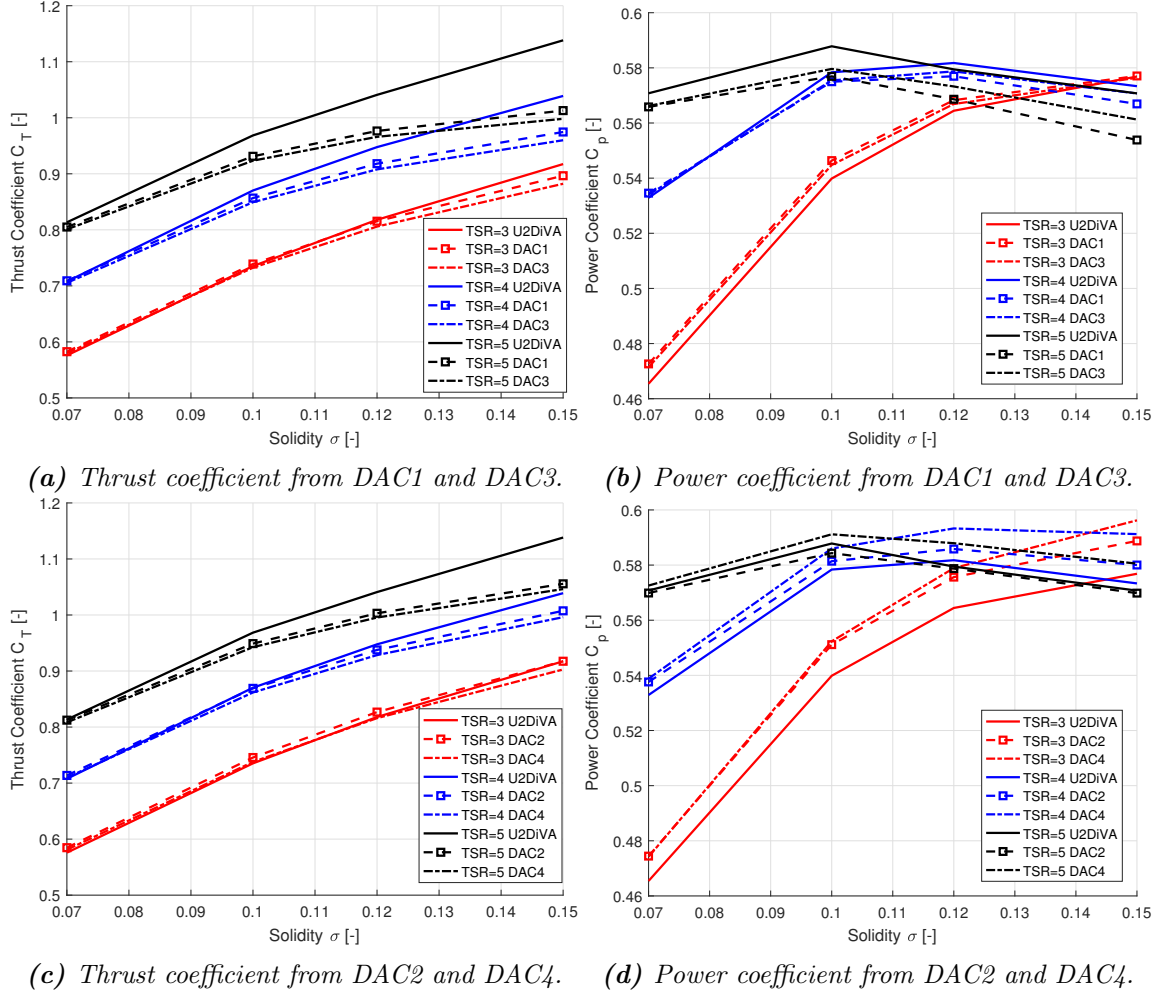


Figure 7.9: Thrust and power coefficient for different tip speed ratio and solidity with the *Counter-Down* layout from four DAC models, with $B = 2$, $d = 0.2$.

It could be visualised from the figure that the thrust coefficient from DAC1 and DAC3 model are close to each other, the thrust coefficient from DAC2 and DAC4 model are also close to each other. The results are having good agreements with the panel code when the rotors are not heavily loaded with the condition of $C_T < 1$ and will underestimate compare to the panel code when the rotor is heavily loaded. As a result, the underestimation will increase with the increase of tip speed ratio and solidity. The trend of the thrust coefficient with the increase of the solidity could be well modelled with all the four DAC models. And the relative relationship of the thrust coefficient for a certain solidity but different tip speed ratio could also be modelled with the four DAC models.

The power coefficient from the DAC1 and DAC3 models will be overestimated for the condition of $\lambda = 3$ and will be generally underestimated for the condition of $\lambda = 4$ and

$\lambda = 5$ compare to the result from the panel code. The DAC2 model overestimates for the condition of $\lambda = 3$ and 4, the results are slightly underestimated for the condition of $\lambda = 5$. The DAC4 model overestimate for all the three tip speed ratios. The relative relationship of the power coefficient for a certain solidity with different tip speed ratio could be correctly modelled with the all the four DAC models which will have the same relationship as the results from the panel code.

Co-Rotating layout

For the double-rotor layout of *Co-Rotating*, the average value of thrust coefficient and power coefficient of the two rotors are calculated from the four DAC models and plotted together with that from the panel code in Figure 7.10.

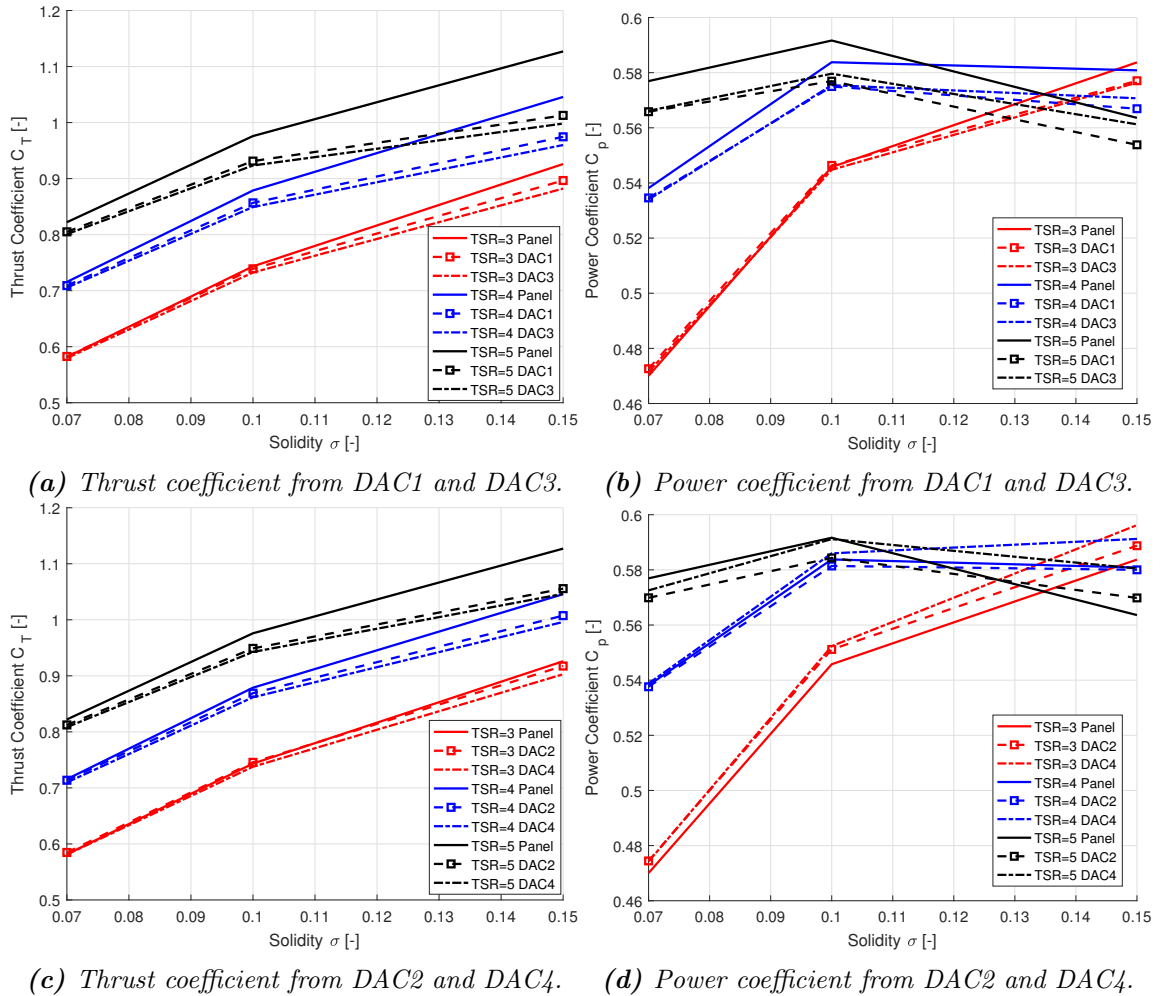


Figure 7.10: Thrust and power coefficient for different tip speed ratio and solidity with the Co-Rotating layout from four DAC models, with $B = 2$, $d = 0.2$.

It could be visualised from the figure that the thrust coefficient from the DAC1 and DAC3 model are close to each other and also for the thrust coefficient from the DAC2 and DAC4

model. The thrust coefficient from DAC1 and DAC2 model are slightly higher than that from the DAC3 and DAC4 model respectively. And the average thrust coefficient of the two rotor is also underestimated by the DAC models when the rotor is heavily loaded with high tip speed ratio and solidity.

The power coefficient from the DAC1 and DAC2 models are slightly higher than that from the DAC3 and DAC4 model respectively. The power coefficients from the DAC1 and DAC3 model are underestimated for the condition of $\lambda = 4$ and $\lambda = 5$ are having good agreements with panel code when $\lambda = 3$. The power coefficients from the DAC2 and DAC4 model are having relatively good agreements with that from the panel code. It could also be concluded that the relative relationship of the thrust coefficient and power coefficient for a certain solidity but different tip speed ratios could be well modelled with all the four DAC models.

7.4 Influence between rotors for different layouts

For the double-rotor layout, there will be influence between the two rotors because the bound and shed vortices of one rotor will induced velocity on the other rotor and the wake of it, and vice versa. The influence between the two rotors will decrease with the increasing of the distance between the two rotors and will be infinitesimal and could be neglected when the distance is much larger than the radius of the rotors. To be noted that the zero yaw angle condition is assumed that neither of the rotors will be in the wake of another.

In order to investigate the influence between the two rotors for different rotational direction layouts, the results of the case that two rotors are placed relatively close together is compared with the case that the two rotors are placed infinitely far from each other which could be presented by the corresponding single rotor layout according to subsection 7.3.3.

7.4.1 investigation of the influence with panel code

Firstly, the influence between the two rotors for different rotational direction layouts is investigated with the result calculated from the panel code of U2DiVA. The results for the double-rotor layouts are compared with the single rotor layout which represents the two rotors are placed infinitely far away as explained before.

For the *Counter-Rotating* layouts, the properties of the two rotors in the layout could be represented by either of the rotors according to the mirror effect as in subsection 7.3.2. In order to be consistent with previous validations, the one that counter-clockwise rotating is chosen which is the south rotor for the *Counter-Up* layout and is the north rotor of the *Counter-Down* layout. For the *Co-Rotating* layout, either of the counter-clockwise *Co-Rotating* rotor could be used for validation, and the south rotor is chosen.

The normal and tangential loadings as well as the angle of attack are investigated. In

addition, the distributed local thrust coefficient $C_{T,l}$ as well as the distributed local power coefficient $C_{P,l}$ are also used for the investigation, the definition of the two variables are as follows.

Local thrust coefficient

The local thrust coefficient $C_{T,l}$ is defined as the integrand in Equation (3.51) of the thrust coefficient, and the explicit form is as follows.

$$C_{T,l}(\theta) = Q_n(\theta) \sin \theta - Q_t(\theta) \cos \theta \quad (7.47)$$

According to the form of Equation (7.47), the local thrust coefficient $C_{T,l}$ could be considered as the non-dimensioned loading in the opposite direction of the incoming wind which is the direction of the thrust force. This equation is able to be used for both the results from the AC model and that from the panel code.

Local power coefficient

For the AC model, the local power coefficient $C_{P,l}$ is defined to be the integrand in Equation (3.149) of the power coefficient, the explicit form of $C_{P,l}$ is then as follows.

$$C_{p,l}(\theta) = -\lambda Q_t(\theta) \quad (7.48)$$

For the results from the panel code, by substituting Equation (A.12) in to Equation (A.13), the power coefficient is then as follows.

$$C_p = \int_0^{2\pi} \frac{B\omega M_b(\theta) d\theta}{2\pi R \rho V_\infty^3} \quad (7.49)$$

The local thrust coefficient $C_{p,l}$ is the integrand in Equation (7.49).

Difference between two methods

It has been mentioned in subsection 3.4.2 that if using Equation (3.149) to calculate the power coefficient for the panel code, there will be deviation from the real value. Similarly, when using Equation (7.48) for panel code, the results will also deviate from that calculated from Equation (7.49). This difference of the local power coefficient is investigated with the results of two single rotor layouts here.

It could be visualised from Figure 7.11, the magnitude of the local thrust coefficient from the two methods will have slightly difference and there is no visible phase difference of the two curves. According to Equation (7.48) when the rotor is counter-clockwise rotating, the

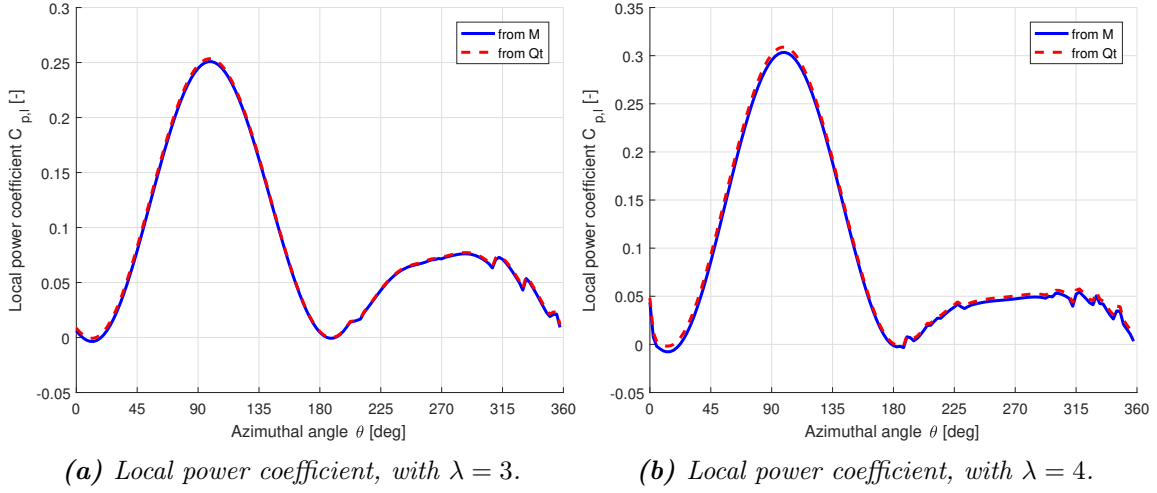


Figure 7.11: Comparison of the local power coefficient calculated from two methods, with $\sigma = 0.1$, $B = 2$.

local power coefficient is linear proportional to the negative value of the tangential loading Q_t . As a result, when investigating the influence between two rotors on the local power coefficient, it is then analysed with the distributed by the tangential loading Q_t , thus the local thrust coefficient calculated from Equation (7.49) will not be plotted in the following for simplicity.

With the definitions above, the physical meaning of the two variables of local thrust and power coefficient are the normalised azimuthal distribution of the contribution to the thrust coefficient and power coefficient.

Counter-Rotating layout

Firstly, the *Counter-Rotating* layouts of *Counter-Up* and *Counter-Down* are calculated with the panel code, and the properties of the two counter-clockwise rotating rotors are compared with that of the corresponding counter-clockwise rotating single rotor layout in Figure 7.12.

It could be visualised from the figure that there is a lead in phase of the properties for the *Counter-Up* layout, and a lag in phase of the properties for the *Counter-Down* layout when comparing against that of the single rotor. The shift of phase could be observed for the properties of normal loadings Q_n , tangential loadings Q_t , the angle of attack of α_{qc} , local thrust coefficient $C_{T,l}$ and also the local power coefficient $C_{p,l}$.

It could also be visualised that when comparing the *Counter-Rotating* layouts with the single rotor layout, there is an transfer of the aforementioned properties between the windward and leeward part of the rotor. The maximum amplitude of the properties decrease in the windward part and increase in the leeward part. The maximum amplitude of angle of attack is in the windward part as in Figure 7.12(c). Thus, for the *Counter-Up* and *Counter-*

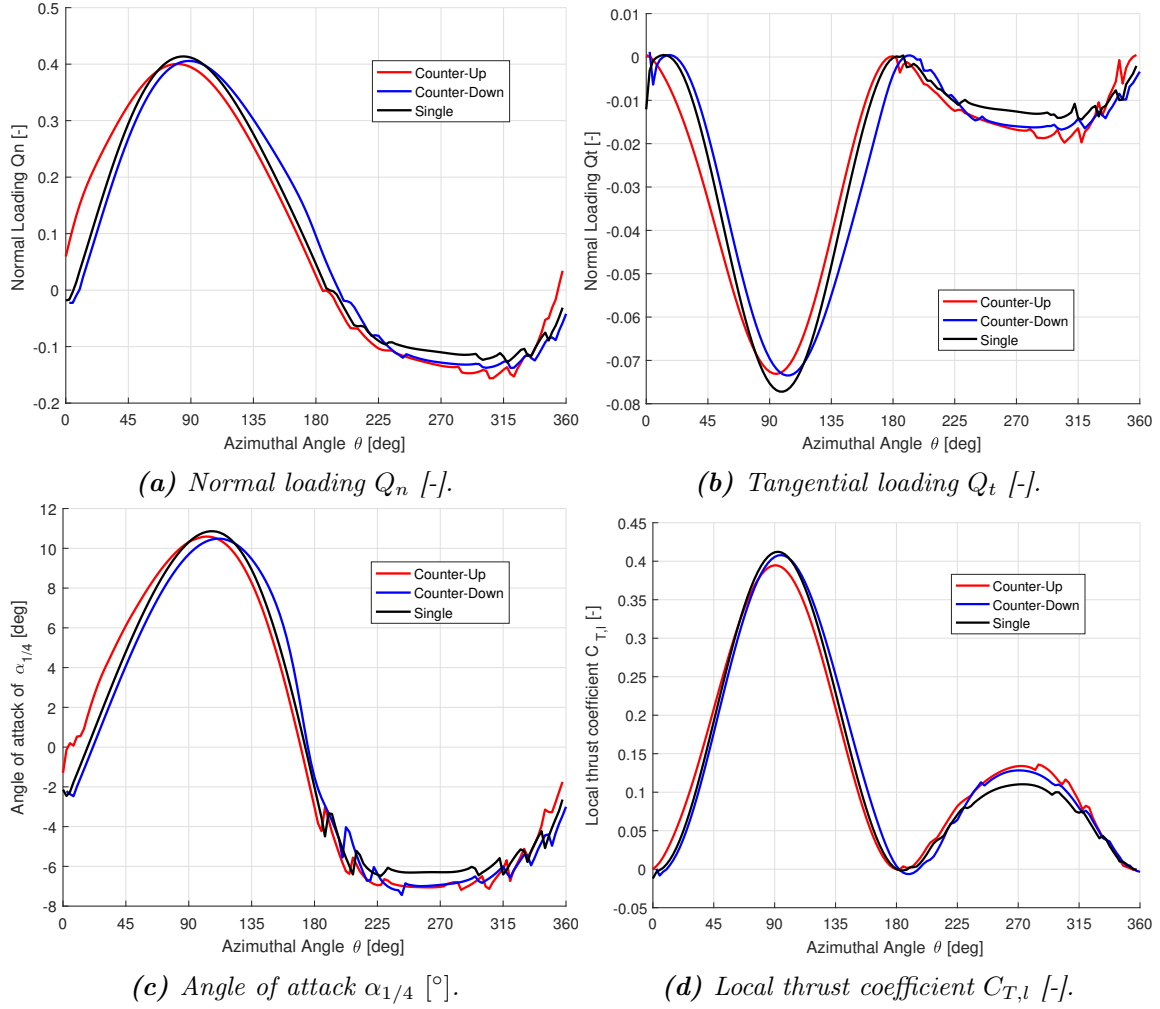


Figure 7.12: Comparison of the variables for the Counter-Up layout and Counter-Down layout against the single rotor layout from the panel code, with $\lambda = 4$, $\sigma = 0.1$, $B = 2$, $d = 0.1$.

Down layout, the maximum amplitude of angle of attack decrease compared to the single rotor case. As a result, there will be less dynamic stall effects and the performance of the rotor should improve.

For the normal and tangential loadings are re-distributed between the windward and the leeward part for the two *Counter-Rotating* layouts. For the normal loadings Q_n , the curve is approaching the centrosymmetric of sine function. And for the tangential loading Q_t , the curve is approaching the *W* shape. There is also transfer of the local thrust $C_{T,l}$ and power coefficient $C_{p,l}$ to be more evenly distributed between the windward and leeward part. As a result, the contribution to the thrust force and the aerodynamic power from the windward and the leeward part of the rotor is more evenly distributed. In consequence, there will be less contribution to thrust force and aerodynamic power due to the windward part and more due to the leeward part.

To be noted that there is only insignificant decrease of the local thrust coefficient for the

windward part of the *Counter-Down* layout, the decrease is much smaller than that of the *Counter-Up* layout. This could be due to the direction of the phase shift of the normal and tangential loadings are different for the *Counter-Up* and *Counter-Down* layout.

Co-Rotating layout

Secondly, the case that the two rotors are counter-clockwise *Co-Rotating* is investigated. The properties of the north and south rotor does not have the mirror effect which means they could not be represented by each other. The properties of the two rotors are then calculated and then compared with that of the corresponding single rotor layout in Figure 7.13.

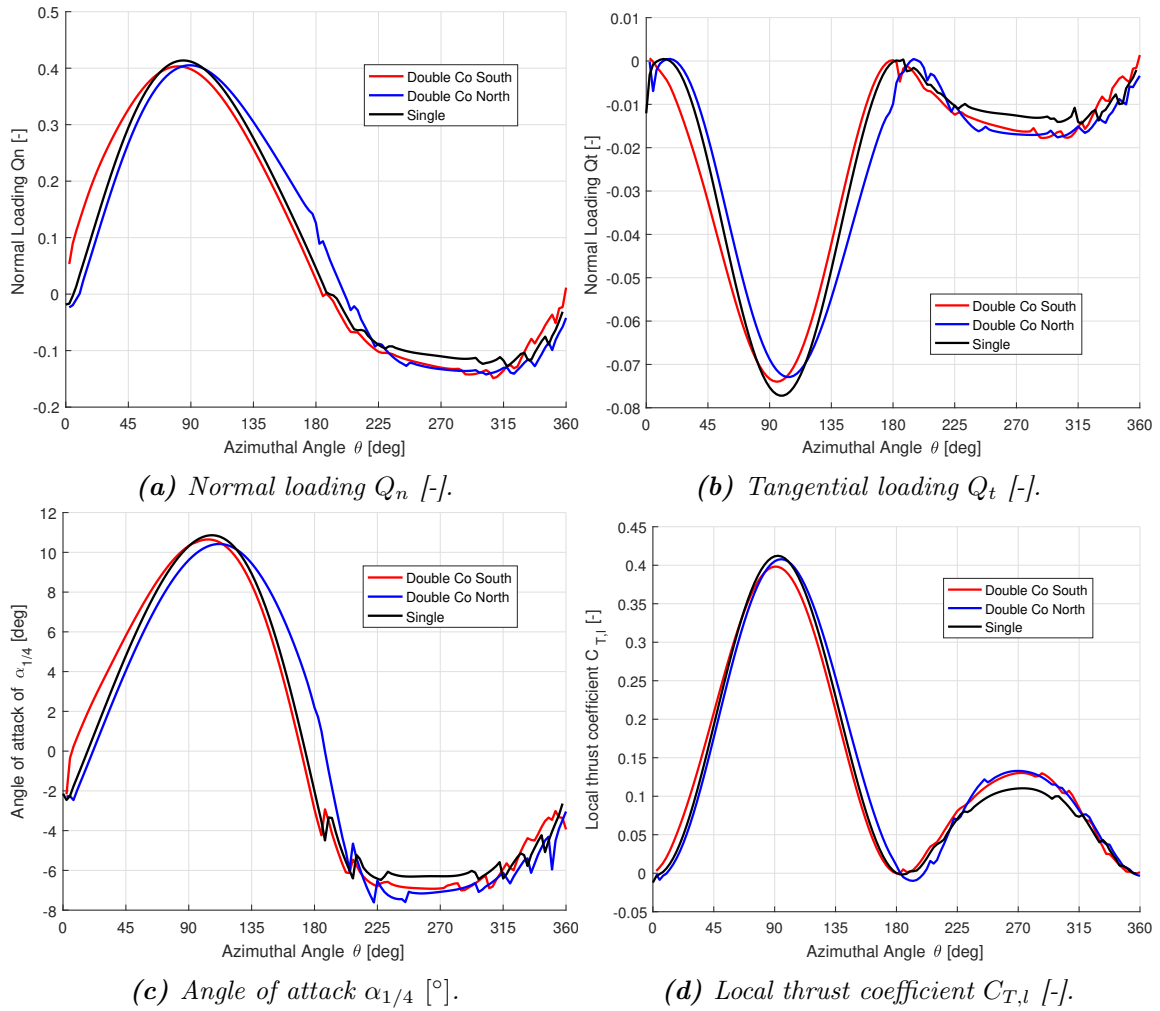


Figure 7.13: Comparison of the variables for the *Co-Rotating* layout against the single rotor layout from the panel code, with $\lambda = 4$, $\sigma = 0.1$, $B = 2$, $d = 0.1$.

It could be visualised from the figure that there is a lead in phase of the properties for the south rotor of the counter-clockwise *Co-Rotating* layout, and a lag in phase for the north rotor when comparing with that of the single rotor. The shift of phase for the two

rotors could be observed for the properties of normal loadings Q_n , tangential loadings Q_t , the angle of attack of $\alpha_{1/4}$, local thrust coefficient $C_{T,l}$ and also the local power coefficient $C_{p,l}$. The phase shift of the north and south rotors of the counter-clockwise *Co-Rotating* layout are similar to that of the *Counter-Up* and *Counter-Down* layout respectively.

From the figure, it could also be visualised that there is also transfer of the aforementioned properties between the windward and the leeward part of the rotor. The normal and tangential loadings are more evenly distributed between the windward and the leeward part. And the contribution to the aerodynamic thrust and aerodynamic power due to the windward and leeward part of the rotor is more even as well. There is less contribution due to the windward part and more contribution due to the leeward part. However, for the local thrust coefficient in the windward part of the north rotor, there is only insignificant increase compare to that of the south rotor. This is similar to the *Counter-Down* layout and the reason could also be the same which is due to the different direction of phase shift. The maximum amplitude of the angle of attack of the two rotors in one revolution decrease which result less dynamic stall effects compare to the single rotor layout and could enhance the performance of the rotors.

7.4.2 Influence between rotors from DAC models

The influence between the two rotors for different rotational direction layouts have been investigated with the panel code in subsection 7.4.1. In this subsection, it will be validated whether the influence between the two rotors for different rotational direction layouts could be correctly modelled with the DAC models. For the validation, the normal and tangential loadings, angle of attack as well as local thrust and power coefficient for the three rotational direction layouts will from the DAC models will be compared with that from the corresponding AC models. The DAC2 and DAC4 models, which are able to model the flow curvature effect, and the corresponding single AC models are AC2 and AC4 will be used for the validation. In order to be consistent with the investigation with the panel code in subsection 7.4.1, the counter-clockwise rotating rotors are used for the validation. For the two *Counter-Rotating* layouts, the rotor is the south rotor of the *Counter-Up* layout and is the north rotor of the *Counter-Down* layout. For the *Co-Rotating* layout, the two rotors are set to be counter-clockwise rotating and both of them are used for validation.

According to the results from the panel code in subsection 7.4.1, the influences between the two rotors could be summarised into the phase shift of the properties and the transfer of the properties between the windward and the leeward part of the rotor. The aforementioned two influences should then be used to evaluate whether the DAC models are sufficient to model the influences between the two rotors. The phase shift could be directly visualised and determined from the figures. However, it could not be directly determined whether the transfer of the properties has been well modelled with the DAC models. According to the results from the panel code, due to the transfer of the properties, the maximum amplitude of the properties will decrease and increase for the windward and leeward part of the rotor respectively. As a result, by comparing the changes of the maximum amplitudes of the properties for different layouts, it could be determined whether the transfer has been well modelled. To be noted that the evaluation should be done for the windward and leeward

part of the rotor respectively.

Counter-Rotating from DAC2 model

Firstly, the *Counter-Rotating* layouts are calculated with the DAC2 model and the results are compared against that from the corresponding single AC2 model in Figure 7.14.

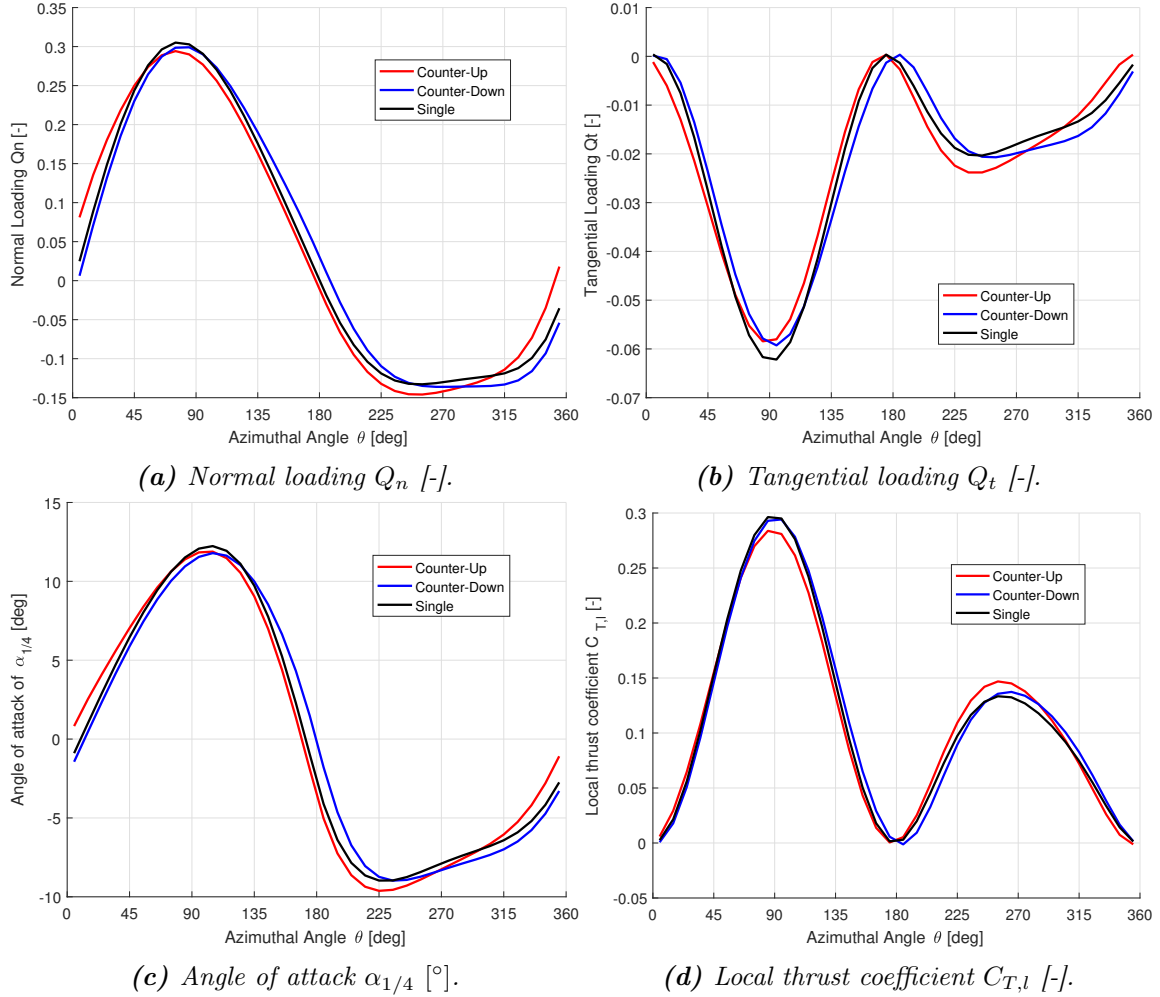


Figure 7.14: Comparison of the variables for the Counter-Up layout and Counter-Down layout against the single rotor layout from DAC2 model, with $\lambda = 4$, $\sigma = 0.1$, $B = 2$, $d = 0.1$.

It could be visualised from the figure that the properties of the *Counter-Up* layout and *Counter-Down* layout from the DAC2 model are having lead and lag in phase respectively when compared to the single rotor layout calculated from the AC2 model. The conclusion is identical with that obtained from the panel code which means the DAC2 model is sufficient to model the shift of the phase for the two *Counter-Rotating* layouts. It could also be visualised from the Figure 7.14 that there is also transfer of the properties to be more evenly distributed between the windward and the leeward part. The transfer of the

properties modelled by the DAC2 model should be evaluated in details by comparing the changes of maximum amplitudes of the properties for the *Counter-Up* and *Counter-Down* layout with respect to that for the single rotor layout.

In the windward part, the maximum amplitudes of the properties will decrease compared to the single rotor layout. The relationship of the maximum amplitudes from the two *Counter-Rotating* layouts from the DAC2 model will be compared with that from the panel code as follows.

- For the normal and tangential loadings from the DAC2 model, the maximum amplitudes for the *Counter-Down* layout is slightly higher than that for the *Counter-Up* layout.
- For the angle of attack from the DAC2 model, the maximum amplitude for the *Counter-Down* layout is slightly lower than that for the *Counter-Up* layout.
- For the local thrust coefficient, the maximum amplitude for the *Counter-Down* layout is much higher than that for the *Counter-Up* layout, with the former to be only slightly lower than that for the single rotor layout. The decrement for the former is then much less than the latter.

With the result from the panel code in Figure 7.12, the aforementioned three points could also be concluded. As a result, the DAC2 model could well modelled the transfer of the properties in the windward part of the rotor for the *Counter-Rotating* layouts.

In the leeward part, the maximum amplitudes of the properties will increase, and the relationship of the maximum amplitudes from the DAC2 model will also be compared with that from the panel code.

- For the normal and tangential loadings from the DAC2 model, the maximum amplitudes for the *Counter-Up* layout is larger than that for the *Counter-Down* layout with the latter to be only slightly lower than that for the single rotor layout. The increment for the latter is then much less than the former. In addition, the general trend of the curves of the normal and tangential loadings from the DAC2 model for the two different layouts are different. The curves of the normal and tangential loadings from the panel code for the *Counter-Down* and *Counter-Up* layouts are close to each other, with the maximum amplitudes of the former to be slightly larger than the latter. As a result, the relative relationship of the maximum amplitudes of the normal and tangential loadings are correctly modelled with the DAC2 model, but the increment of the amplitudes of the normal and tangential loadings for the *Counter-Down* layout in the leeward part is significantly underestimated.
- For the angle of attack from the DAC2 model, the maximum amplitudes for the *Counter-Up* layout is much larger than that for the *Counter-Down* layout with the former to be almost identical with the single rotor layout. The increment of the latter is almost zero while the increment of the former is visible. However, according to the results from the panel code, the curve of angle of attack for the two layouts

are very close to each other. The increment of the maximum amplitude of angle of attack from the panel code are then very close to each other. As a result, the DAC2 model significantly underestimated the increment of the maximum amplitude for the *Counter-Down* layout in the leeward part.

- For the local thrust coefficient from the DAC2 model, similar to the normal and tangential loadings, the relative relationship is correctly modelled with the DAC2 model, but the increment of the amplitudes of the angle of attack for the *Counter-Down* layout in the leeward part is significantly underestimated.

For the *Counter-Rotating* layouts, the DAC2 model could well model the transfer of the properties in the windward part. But the DAC2 model will underestimate the increment of the amplitudes of the properties in the leeward part for the *Counter-Down*, which means the model is not sufficient enough to model the transfer of the properties in the leeward part of the rotor.

***Co-Rotating* from DAC2 model**

Secondly, the *Co-Rotating* layouts are also calculated with the DAC2 model and the results are compared against that from the corresponding AC2 model in Figure 7.15.

It could be visualised from the figure that the properties of the south and the north rotor of the counter-clockwise *Co-Rotating* layout are having lead and lag in phase respectively when compared to the single rotor layout calculated from the AC2 model. The conclusion is identical with that obtained from the panel code which means the DAC2 model is sufficient to model the shift of the phase for the two rotors of the *Co-Rotating* layout. From Figure 7.15, it could also be visualised that for both the north and south rotors, there is transfer of the properties between the windward and the leeward part of the rotor. The details of the transfer of the properties from the DAC2 model should be evaluated by comparing the changes of maximum amplitudes of the properties for the north and south rotors with the single rotor layout.

In the windward part, similar to the *Counter-Rotating* layouts, the maximum amplitudes of the properties for the two rotors of the *Co-Rotating* layout will also decrease. The maximum amplitudes for the two rotors from the DAC2 model as well as the panel code will be compared as follows.

- For the normal loading from the DAC2 model, the maximum amplitude for the north and south rotors are almost identical. For the tangential loading from the DAC2 model, the maximum amplitude for the north rotor is smaller than that for the south rotor.
- For the angle of attack from the DAC2 model, the maximum amplitude for the north rotor is smaller than that for the north rotor. The decrement for the former is then more than the latter.

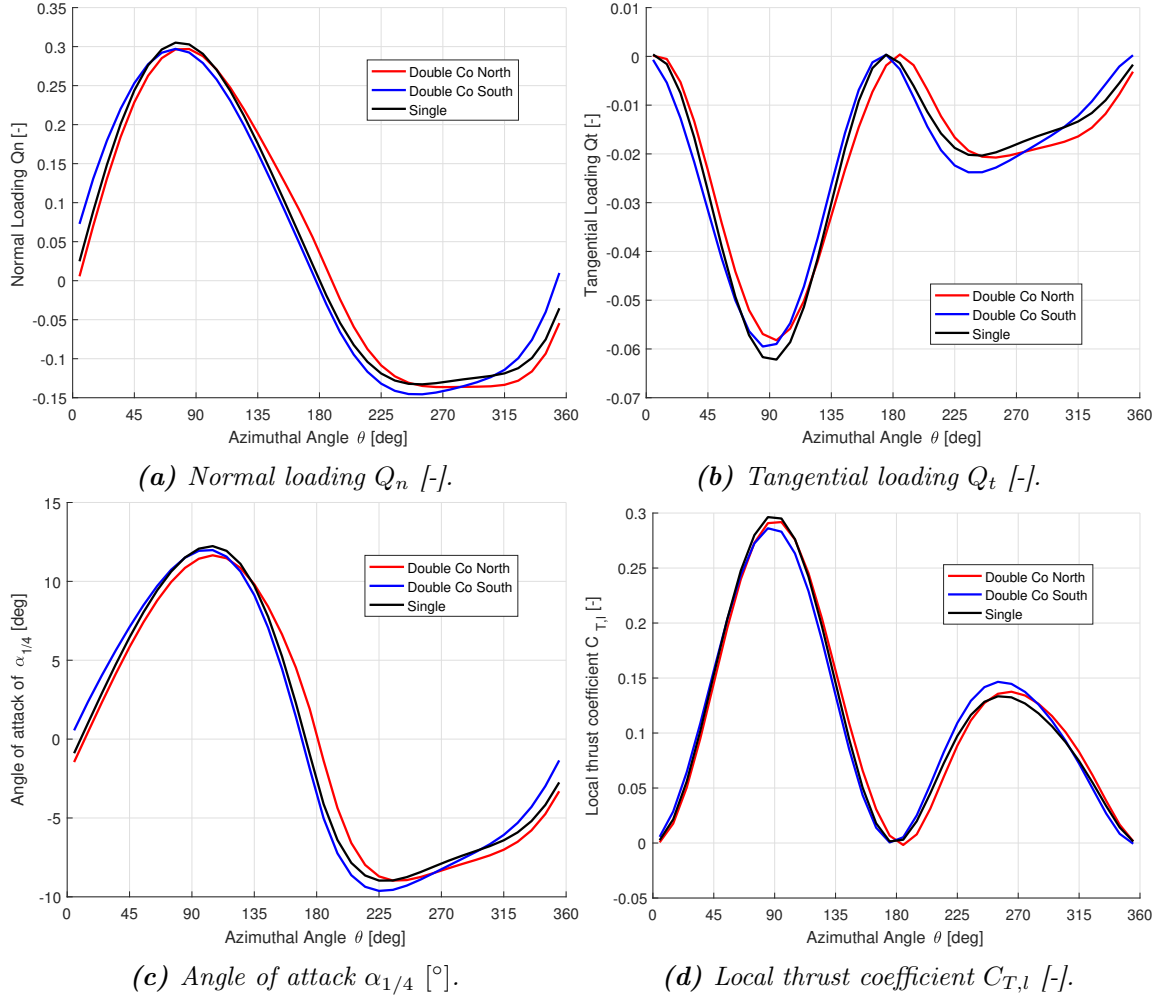


Figure 7.15: Comparison of the variables for the Co-Rotating layout against the single rotor layout from DAC2 model, with $\lambda = 4$, $\sigma = 0.1$, $B = 2$, $d = 0.1$.

- For the local thrust coefficient, the maximum amplitude for the north rotor is larger than that for the south rotor.

For the three points above, the same conclusion could be obtained from the result from the panel code in Figure 7.13. As a result, the DAC2 model is sufficient to model the transfer of the properties in the windward part of the rotor for both of the rotors of the Co-Rotating layout.

In the leeward part, the maximum amplitudes of the properties for the Co-Rotating layout will increase which is similar to the Counter-Rotating layout. The maximum amplitudes from the DAC2 model as well as panel code for the two rotors of the Co-Rotating layout will be compared as follows.

- For the normal and tangential loadings from DAC2 model for the north and the south rotor of the Co-Rotating layout, the results are very similar to that for the Counter-

Down and *Counter-Up* layout respectively. However, the results from the panel code indicate that the maximum amplitudes for the two rotors are almost identical with each other. The conclusion could then be obtained that the relative relationship of the maximum amplitudes of the normal and tangential loadings could not be well modelled with the DAC2 model. The reason is the increment of the amplitudes of the normal and tangential loadings for the south rotor of the *Co-Rotating* layout in the leeward part is significantly underestimated.

- For the angle of attack from the DAC2 model, the results for the north and south rotor of the *Co-Rotating* layout are very similar to that for the *Counter-Down* and *Counter-Up* layout respectively. The maximum amplitudes for the north rotor is much smaller than that of the south rotor, with the former to be almost identical with the single rotor layout. However, the results from the panel code show that the maximum amplitude for the north rotor is even larger than that of the south rotor. As a result, the DAC2 model could not model the relative relationship of the maximum amplitude of the angle of attack for the north and the south rotor. The reason is due to the increment of the amplitude of the angle of attack is significantly underestimated for north rotor in the leeward part.
- For the local thrust coefficient from the DAC2 model, the maximum amplitude for the north rotor is smaller than that for the south rotor. However, with the result from the panel code, the maximum amplitudes are almost identical for the two rotors. As a result, the DAC2 model could not model the relative relationship of the local thrust coefficient for the two rotors of the *Co-Rotating* layout because the increment of the north rotor is significantly underestimated.

It could then be concluded that for the *Co-Rotating* layout, the DAC2 model could well model the transfer of the properties in the windward part but will significantly underestimate the increment of the amplitudes of the properties in the leeward part of the south north rotor of the counter-clockwise *Co-Rotating* layout. The DAC2 model is then insufficient to model the transfer of the properties in the leeward part of the *Co-Rotating* layout.

***Counter-Rotating* from DAC4 model**

Thirdly, the *Counter-Rotating* layouts are calculated with the DAC4 model and the results are compared with that from the corresponding single AC model of AC4 in Figure 7.16.

It could be visualised from the figure that the phase shift of the *Counter-Up* and *Counter-Down* layouts could be well modelled with the DAC4 model.

In order to validate whether the DAC4 model is sufficient to model the transfer of the values of the variables between the windward and leeward part of the rotor, the results from the DAC4 model are firstly compared with the DAC2 model for simplicity, instead of directly compare with that from the panel code.

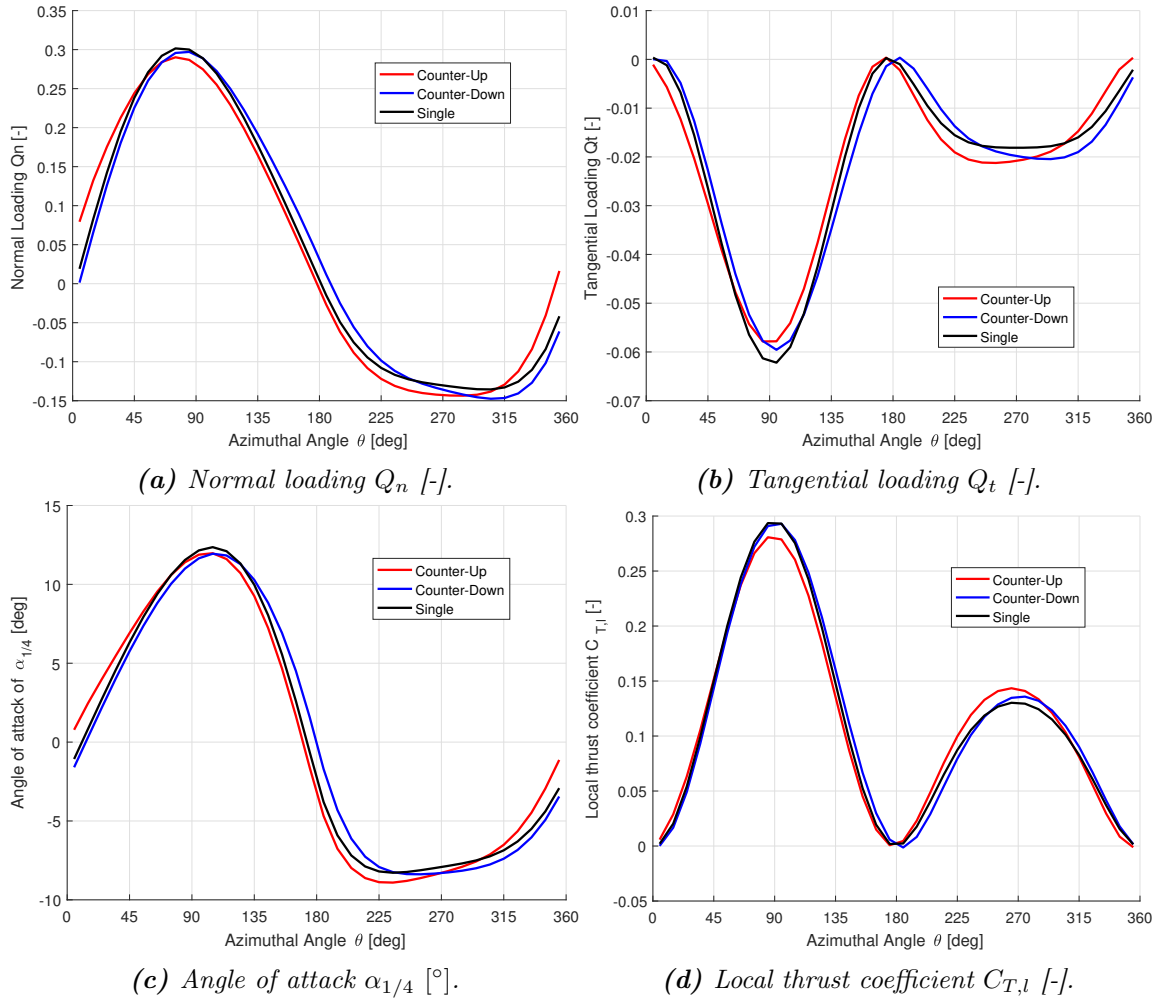


Figure 7.16: Comparison of the variables for the Counter-Up layout and Counter-Down layout against the single rotor layout from DAC4 model, with $\lambda = 4$, $\sigma = 0.1$, $B = 2$, $d = 0.1$.

For the windward part of the rotor, by comparing the Figure 7.14 and 7.16, it could be visualised that the values of the variables from the two DAC models are almost identical with each other. The reason is that the DAC4 and DAC2 models are derived from the AC4 and AC2 models respectively. According to Figure 3.23, the results of loadings and angle of attack calculated from the AC4 and AC2 model are almost identical in the windward part and the difference is mainly in the leeward part. Since the DAC2 model is sufficient to model the transfer for the windward part for the *Counter-Rotating* layouts, the DAC4 model is then also sufficient to model it.

For the leeward part of the rotor, also by comparing the Figure 7.14 and 7.16, it could be visualised that the values of the variables from the two DAC models are different from each other. The results from the DAC4 model are evaluated as follows.

- For the normal and tangential loadings from the DAC4 model, the maximum amplitudes for the *Counter-Down* layout are much closer to that for the *Counter-Up* layout

compare to that from the DAC2 model. The increment of the maximum amplitude for the *Counter-Down* layout is then close to that for the *Counter-Up* layout instead of being almost zero-valued as from the DAC2 model. The results from the DAC4 model are then having better agreements than the DAC2 model with the panel code. However, the shape of the curves for the *Counter-Rotating* layouts from the DAC4 model are having more difference than that from the panel code.

- For the angle of attack, the maximum amplitude for the *Counter-Down* layout is still much smaller than that for the *Counter-Up* layout, and is almost identical to that for the single rotor layout. The increment of the maximum amplitude for the *Counter-Down* layout is then still significantly underestimated when comparing with the panel code.
- For the local thrust coefficient from the DAC4 model, the difference between the maximum amplitudes for the two layouts is smaller than that from the DAC2 model. The result from the DAC4 model is then having better agreement with the panel code.

In conclusion, for the two *Counter-Rotating* layouts, the DAC4 model could well model the transfer for the windward part, and could model the transfer of the normal loading, tangential loading and local thrust coefficient better than the DAC2 model. However, the increment of the maximum amplitude of the angle of attack in the leeward part due to the transfer is still underestimated.

***Co-Rotating* from DAC4 model**

Finally, the *Co-Rotating* layout is calculated with the DAC4 model and the results are compared with that from the corresponding single AC model of AC4 in Figure 7.16.

It could be visualised from Figure 7.17 that the phase shift of the north and south rotor for *Co-Rotating* layout could be well modelled with the DAC4 model.

For the validation of the DAC4 model on modelling the transfer of the value of the variables for the *Co-Rotating* layout, the results from the DAC4 model is firstly compared with that from the DAC2 model for simplicity. This is similar to evaluating the DAC4 model for the transfer of the variables for the *Counter-Rotating* layout as explained before.

For the windward part, by comparing the variables in Figure 7.17 and 7.15, it could be visualised that the results from the DAC4 model is almost identical with that from the DAC2 model. As a result, the DAC4 model could well model the transfer of the value of the variables for the windward part of the two rotors of the *Co-Rotating* layout.

For the leeward part, also by comparing the variables in Figure 7.17 and 7.15, it could be visualised the results from the two DAC models are different. The results from the DAC4 model are evaluated as follows.

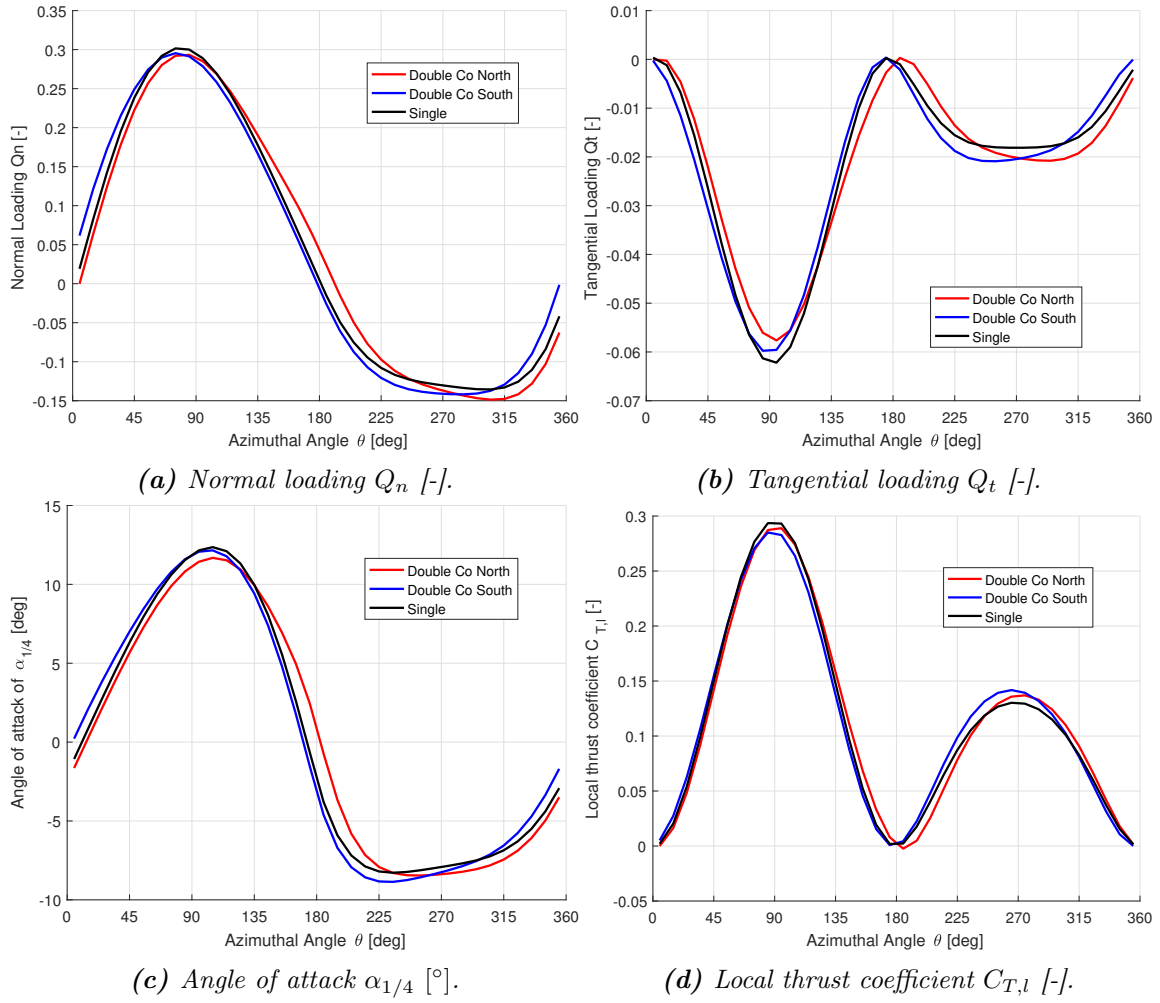


Figure 7.17: Comparison of the variables for the Co-Rotating layout against the single rotor layout from DAC4 model, with $\lambda = 4$, $\sigma = 0.1$, $B = 2$, $d = 0.1$.

- For the normal and tangential loading from the DAC4 model, the maximum amplitudes for the north rotor is close to that for the south rotor, instead of being almost equal to that for the single rotor layout as that from the DAC2 model. The results from the DAC4 model are then having better agreements with the panel code. However, similar to the DAC4 model for the *Counter-Rotating* layouts, the shapes of the curves for the two rotors of the *Co-Rotating* layout are also having more difference than that from the panel code.
- For the angle of attack, the maximum amplitude for the north rotor layout from the DAC4 model is slightly larger than that for the single rotor layout. However, there is still some underestimation compare to that from the panel code.
- For the local thrust coefficient from the DAC4 model, difference between the maximum amplitudes for the two rotors are smaller than that from the DAC2 model. The angle of attack from the DAC4 model is then having better agreements with that from the panel code.

In conclusion, for the two rotors of the *Co-Rotating* layout, the DAC4 model could well model the transfer for the windward part, and model the transfer for the leeward part better than the DAC2 model. However, the shape of the curves of the normal and tangential loadings in the leeward part are not well modelled, and the transfer of the value of angle of attack for the north rotor is underestimated for the leeward part.

7.5 Variation of the influence with distance

With the two rotors placed in the flow field, there will then be influence between the two rotors. The influence between the two rotors will decrease when the distance between the rotors increase, and could be neglected when the distance is large enough. It has been validated in subsection 7.3.3 that the DAC models are able to correctly model the condition of the distance between the two rotors is very large. It has also been validated in section 7.4 that the DAC models are also able to model the influence between the two rotors when the two rotors are placed close to each other. In this section, the performance of the DAC models on modelling the relationship of the influence between the two rotors and the distance will be validated with the results from the panel code.

For the validation, the two rotors are identical and are operating with same tip speed ratio. Only the distance between the two rotors is the independent variable and other variables are identical for different cases, and the zero yaw angle condition is also applied for simplicity. The thrust coefficient and power coefficient for different distances between the two rotors are calculated from the DAC models as well as the panel code. To be noted, the thrust coefficient from the DAC models and the panel code will not be identical with each other for both single- and double-rotor layout. In order to determine the change of influence between the two rotors with the distance, the normalised thrust and power coefficients, which are defined the values for the double rotor layout divided by the corresponding single rotor layout, are then calculated and compared. The load cases are identical with that in section 7.3, with $\lambda = 4$, $\sigma = 0.07$ and $\theta_p = 0$.

7.5.1 *Counter-Rotating* layout

The two *Counter-Rotating* layouts, which are the *Counter-Up* and *Counter-Down* layouts will be firstly investigated.

Counter-Up layout

The performance of the DAC models to calculate the relationship of the thrust and power coefficient with the distance between the two rotors for the *Counter-Up* layout will be validated in this subsection. To be noted that due to the mirror effect, the value of the thrust coefficient as well as power coefficient for the two rotors in *Counter-Up* layout are

identical. The results from the DAC models are plotted together with that from the panel code in Figure 7.18.

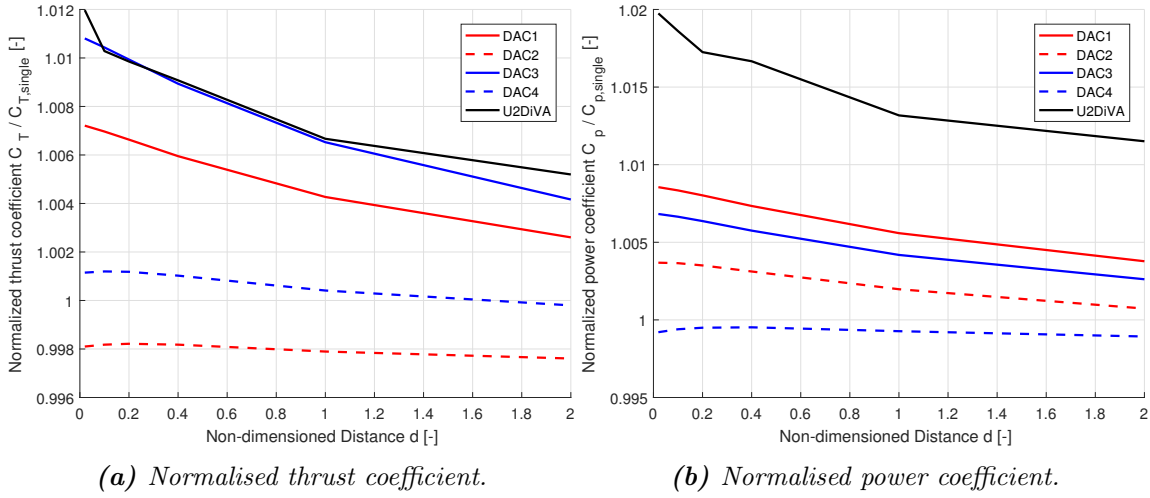


Figure 7.18: Influence of the distance on the thrust coefficient and power coefficient for the Counter-Up layout, with $\lambda = 4$, $\sigma = 0.07$, $B = 2$.

Firstly, it could be visualised that the thrust coefficient and power coefficient will decrease with the increasing of the distance between the two rotors for the *Counter-Up* layout. The general trend of decreasing of the variables could be modelled with the DAC models.

Secondly, the thrust coefficient and power coefficient when the non-dimensioned distance between the two rotors is $d = 0.02$, which represents the two rotors are very close to each other, will be evaluated. The results from the panel code show the relative increment of the thrust and power coefficient to be 1.2% and 2.0% respectively with respect the single rotor layout. For the thrust coefficient, the DAC3 model is generally having good agreement with panel code, but the other models, especially the DAC2 and DAC4 model will underestimate the thrust coefficient. For the power coefficient, all the models will significantly underestimates the power coefficient, the result from the DAC4 model is even smaller than the result for the single rotor layout.

Thirdly, the change of the thrust and power coefficient with the distance is evaluated by comparing the decrements of the normalised thrust and power coefficient when the non-dimensioned distance d between the two rotors increase from 0.02 to 2.0. The results from the DAC models as well as the panel code are listed in Table 7.2.

Table 7.2: Decrements of normalised thrust and power coefficient with distance d increase from 0.02 to 2.0 for the Counter-Up layout.

	DAC1	DAC2	DAC3	DAC4	Panel
$C_T / C_{T,single} [\%]$	0.4606	0.0494	0.6640	0.1351	0.6777
$C_p / C_{T,single} [\%]$	0.4772	0.2955	0.4205	0.0277	0.8236

According to the table, the decrement of the thrust coefficient is well modelled with the DAC3 model and is slightly underestimated by the DAC1 model. However, the DAC2 and

DAC4 models will significantly underestimate the decrements. For the power coefficient, the decrement calculated from the DAC1, DAC2 and DAC3 model are about half of that from the panel code, and the DAC4 model will significantly underestimate the decrement.

Counter-Down layout

The DAC models are also validated for the *Counter-Down* layout with the relationship of the thrust and power coefficient with the distance between the two rotors. The results from the DAC models as well as the panel code are plotted in Figure 7.19.

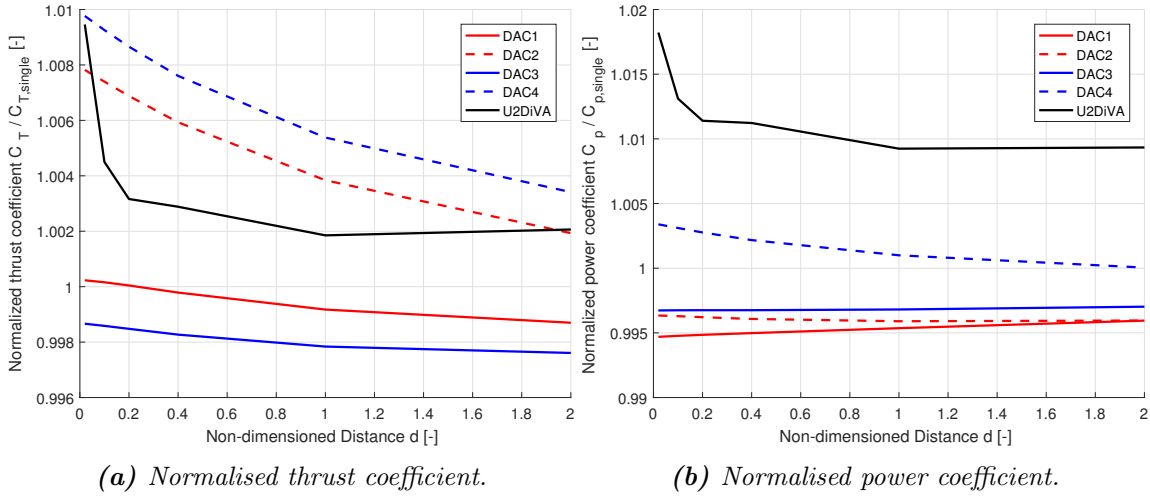


Figure 7.19: Influence of the distance on the thrust coefficient and power coefficient for the Counter-Down layout, with $\lambda = 4$, $\sigma = 0.07$, $B = 2$.

Firstly, it could be visualised that the thrust coefficient and power coefficient from the panel code will decrease very fast with the increment of the distance when $d < 0.2$ and then reach almost constant value when $d > 1.0$. The sudden decrement of the values of the variables with the distance could not be modelled by the DAC models. For the DAC1 and DAC3 model, the values of the power coefficient increase with the increasing of the distance instead of decrease as that from the panel code.

Secondly, the thrust and the power coefficient when the two rotors are very close together with the condition of $d = 0.02$ is investigated. The results from the panel code indicates the relative increment of the thrust and power coefficient are 0.95% and 1.82% respectively. For the thrust coefficients, the DAC2 and DAC4 model are having relative good agreements with the panel code, with the result of relative increments of 0.78% and 0.98% respectively. The results from the DAC1 and DAC3 model are 0.02% and -0.13% which are not sufficient. For the power coefficient, only the DAC4 model is having higher value compared to the single rotor layout, but with the relative increment to be only 0.34%.

Thirdly, the change of the thrust and power coefficient with the distance is also evaluated by comparing the decrements of the normalised aforementioned coefficient when the non-dimensional distance d increase from 0.02 to 2.0. The results are listed in Table 7.3.

Table 7.3: Decrements of normalised thrust and power coefficient with distance d increase from 0.02 to 2.0 for the Counter-Down layout.

	DAC1	DAC2	DAC3	DAC4	Panel
$C_T/C_{T,single}[\%]$	0.1531	0.5888	0.1054	0.6356	0.7396
$C_p/C_{p,single}[\%]$	-0.1251	0.0387	-0.0290	0.3345	0.8883

According to the table, the decrement of the thrust coefficient is generally well modelled with the DAC4 and DAC2 model. The result from the DAC1 and DAC3 model will significantly underestimate the decrements. For the power coefficient, the DAC4 model will underestimate the decrement. The results from the DAC2 and DAC3 models are not having much decrement, and the power coefficient from the DAC1 and DAC3 model increase instead of decrease with the increasing of the distance d .

7.5.2 Co-Rotating layout

For the *Co-Rotating* layout, the variables of the two rotors could not be directly related because the mirror effect could not be applied to the two rotors in the layout. The results of the normalised thrust and power coefficient for the north and south rotors are calculated from the DAC models as well as the panel code and are compared in Figure 7.20.

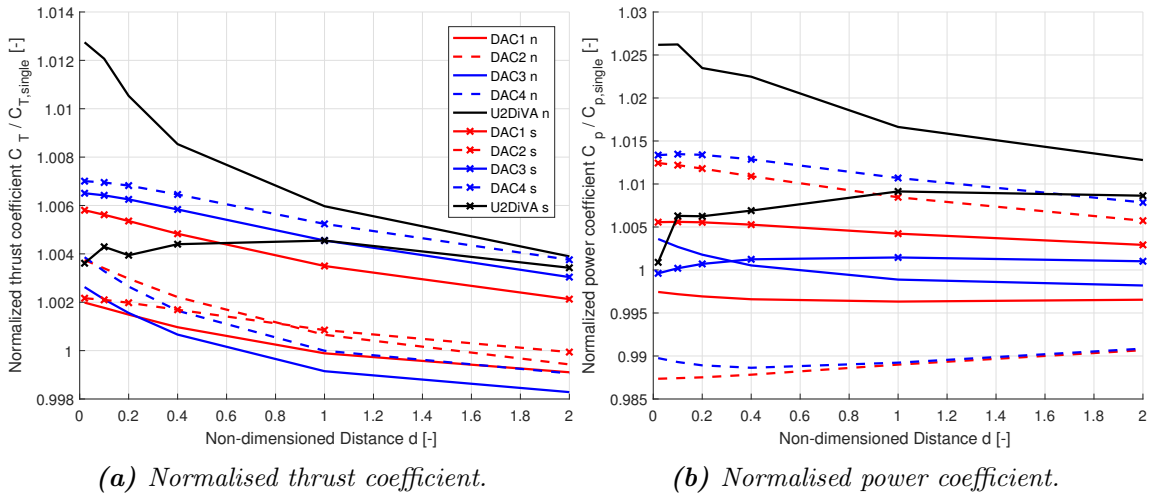


Figure 7.20: Influence of the distance on the thrust coefficient and power coefficient for the Co-Rotating layout, with $\lambda = 4$, $\sigma = 0.07$, $B = 2$.

Firstly, it could be visualised from the panel code that the thrust and power coefficient for the north rotor is higher than that for the south rotor. However, the values of the variables from the DAC models for the south rotor is higher than the north rotor.

Secondly, for the thrust coefficient from the panel code for the north rotor, the value is decreasing with the distance, the trend could be correctly modelled with the DAC models. For the thrust coefficient from the panel code for the south rotor, the value is firstly increasing and then decreasing with the distance, the trend could not be modelled with

the DAC models. For the power coefficient from the panel code, the values for the north and south rotor are increasing and decreasing with the distance respectively. This trend could only be correctly modelled with the DAC3 model.

For further validation, the mean value of the thrust coefficient and power coefficient for the two rotors are calculated and compared in Figure 7.21.

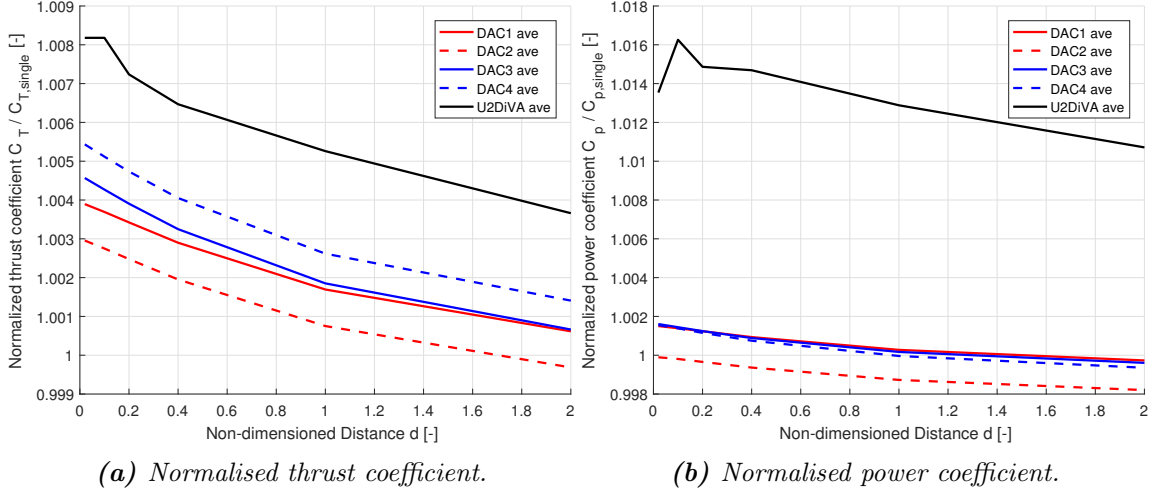


Figure 7.21: Influence of the distance on the mean value of the thrust coefficient and power coefficient for the two rotors of the Co-Rotating layout, with $\lambda = 4$, $\sigma = 0.07$, $B = 2$.

Firstly, it could be visualised that for the average thrust coefficient and power coefficient from the panel code, the values of the variables are decreasing with the distance which could be modelled by the DAC models.

Secondly, the thrust and the power coefficient when the non-dimensional distance between the two rotors is $d = 0.02$ is investigated. For the result from the panel code, there is 0.82% increment compare to the single rotor layout. The result from the DAC models will underestimate the increment, the values are 0.39%, 0.30%, 0.46% and 0.54% for the DAC1 to DAC4 models respectively. For the power coefficient, the result from the panel code show 1.35% of increment compare to the single rotor layout. However, the result from the DAC models significantly underestimate the increment, with the maximum value to be less than 0.18%.

Thirdly, the change of the thrust and power coefficient with the non-dimensional distance d increase from 0.02 to 2.0 is also calculated. The results are listed in Table 7.4.

Table 7.4: Decrements of averaged value of normalised thrust and power coefficient with distance d increase from 0.02 to 2.0 for the two rotors of Co-Rotating layout.

	DAC1	DAC2	DAC3	DAC4	Panel
$C_T / C_{T, \text{single}} [\%]$	0.3278	0.3271	0.3905	0.4026	0.4519
$C_p / C_{p, \text{single}} [\%]$	0.1772	0.1691	0.2001	0.2200	0.2825

According to the table, the decrement of the thrust coefficient is generally well modelled

with the DAC3 and DAC4 model with slightly underestimation. The result from the DAC1 and DAC2 model are having more underestimation but not very significant. For the power coefficient, the decrement with distance is underestimated with the DAC models compare to the panel code.

7.5.3 Predicting relative relationship of thrust and power coefficient

In addition, with the results calculated previously in this section, it is also able to validate whether the DAC models are sufficient to model the relative relationship of the thrust and power coefficient for different rotational direction lay outs for a certain tip speed ratio and solidity. By combining the results from Figure 7.18 to 7.21 for different layouts, the mean thrust and power coefficients of the two rotors are plotted in Figure B.8 and B.9 in the Appendix. The results from the panel code of U2DiVA is compared with that from DAC1 and DAC3 together and then compared with DAC2 and DAC4.

From the figures, it could be visualised that according to the results from the panel code, the thrust and power coefficient for the *Counter-Up* setup is higher than that for the *Counter-Down* setup. And the results for the *Co-Rotating* is generally between the two *Counter-Rotating* layouts mentioned above. This general relationship is correctly predicted by the DAC1 and DAC3 model for both thrust and power coefficient. The DAC2 and DAC4 model are not able to correctly predict the relationship of the thrust coefficient for different layouts. The thrust coefficient for the *Counter-Down* layout is higher than that for the *Counter-Up* layout instead. The DAC2 model is able to correctly model the relationship of the power coefficient for different layouts, but the relationship is not correctly predicted by the DAC4 model.

7.6 Influence due to phase difference

For the double-rotor layouts calculated with the panel code in the previous sections, the phase difference of the two rotors is set to be zero. This means that for the *Co-Rotating* layout, the azimuthal locations of the blades in one rotor are identical to the corresponding blades in the other rotor. For the *Counter-Rotating* layout, the azimuthal locations of the blades in one rotor are identical to the mirrored azimuthal locations of the corresponding blade in the other rotor. This means the mirror effect between the corresponding blades in the two rotors is satisfied all the time. However, if the phase difference between the two rotors is not zero, the condition will deviate from the condition with zero phase difference. The mirror effect is not able to be satisfied anymore.

The influence due to the phase difference is not able to be modelled with the DAC model because this model is a quasi-steady model which is explained in section 6.4. The influence due to the phase difference will then be an error the DAC model is used. This influence is investigated in this section with the panel code of U2DiVA and it should be indicated whether the influence is significant or is small enough to be neglected.

The layout of the two-bladed double rotors for the investigation is identical to the previous sections that the two rotors are identical with each other and with no yaw angle. For the investigation, the phase difference is varying from -90° to 90° with the spacing of 10° . The investigation is done for all the three different layouts of *Counter-Up*, *Counter-Down* and *Co-Rotating*. The converged solutions of the thrust coefficient and power coefficient of each rotor, which is calculated from the mean value of the two blades in the rotor, are calculated and used to demonstrate the influence due to phase difference.

7.6.1 *Counter-Up* layout

Firstly, for the *Counter-Up* layout, the thrust coefficient and power coefficient of the two rotors as well as the mean value are calculated from the panel code. The results are plotted in Figure 7.22 as follows.

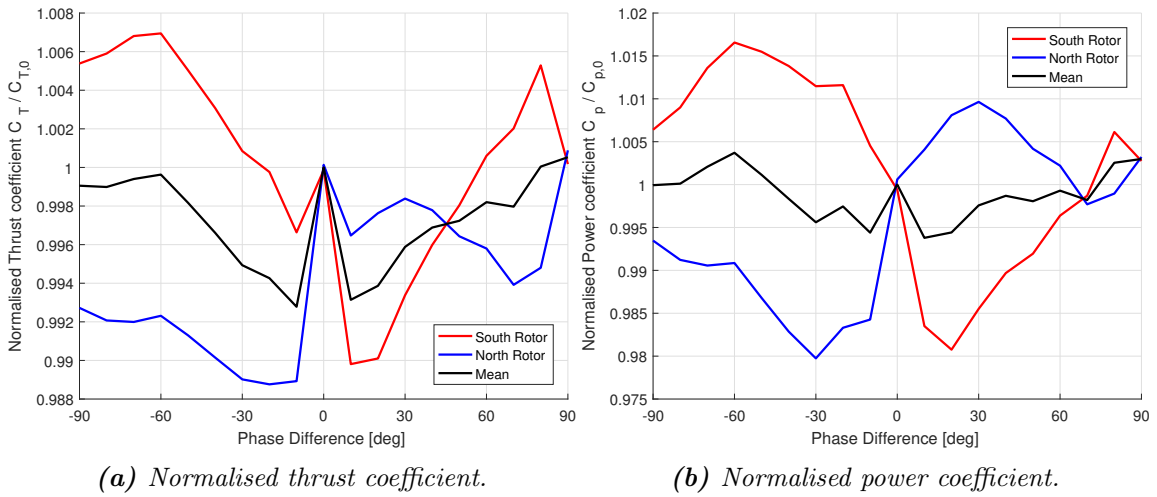


Figure 7.22: Influence of the phase difference on the thrust coefficient and power coefficient for the *Counter-Up* layout, with $\lambda = 4$, $\sigma = 0.1$, $B = 2$, $d = 0.1$.

From the figures, it could be visualised the thrust coefficient and power coefficient of the two rotors are having difference with each other which is due to the phase difference. However, the mean values of the thrust and power coefficients of the two rotors vary little with the variation of the phase difference. It could also be visualised that when the phase difference is zero, the thrust and power coefficient of the two rotors are identical with each other. This is because the condition for the mirror effect is satisfied. When using the case of having zero phase difference to represent all cases, the maximum relative error of the thrust coefficient and power coefficient are 0.73% and 0.48% respectively, which are very small values. As a result, using the zero-phase difference case to represent the performance of the two rotors with the *Counter-Up* layout is sufficient.

7.6.2 Counter-Down layout

Secondly, for the *Counter-Down* layout, the thrust and power coefficient of the two rotors as well as the mean value are calculated from the panel code. The results are plotted in Figure 7.23.

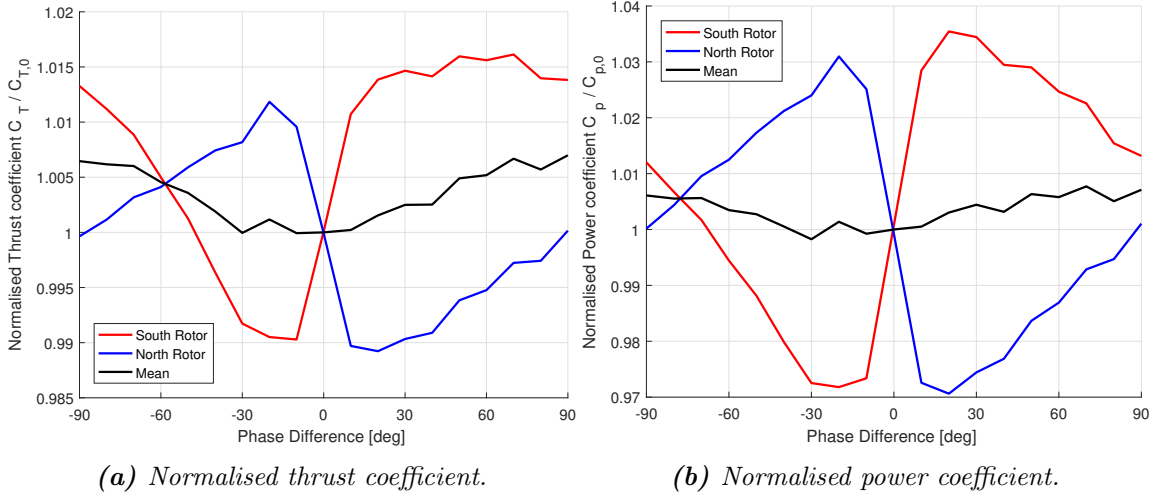


Figure 7.23: Influence of the phase difference on the thrust coefficient and power coefficient for the *Counter-Down* layout, with $\lambda = 4$, $\sigma = 0.1$, $B = 2$, $d = 0.1$.

From the figures, it could be visualised that similar to the *Counter-Up* layout, the mean value of the thrust and power coefficient for the two rotors also vary little with the phase difference. Thus the total performance of the two rotors will not change much with the phase difference. The maximum relative difference of the thrust and power coefficients comparing with the case of zero phase difference are 0.70% and 0.77% respectively which are small values. Thus, the performance of the two rotors with *Counter-Down* layout could also be replaced with the zero-different phase case.

7.6.3 Co-Rotating layout

Thirdly, the thrust and power coefficient for the *Co-Rotating* layout is also calculated from the panel code. The results for the two rotors and their mean values are plotted in Figures 7.24.

It could be visualised from the figures that the thrust coefficient and the power coefficient of the two rotors are not same for the zero-phase-difference condition because there is no mirror effect for the two rotors in the *Co-Rotating* layout. The mean value of the power coefficient and thrust coefficient does not change much with the phase difference. And the maximum relative difference of the thrust and power coefficient comparing with the case of zero phase difference are 0.66% and 0.67% respectively, which are small values. As a result, the performance of the two rotors with *Co-Rotating* layout could also be replaced with the zero-different phase case.

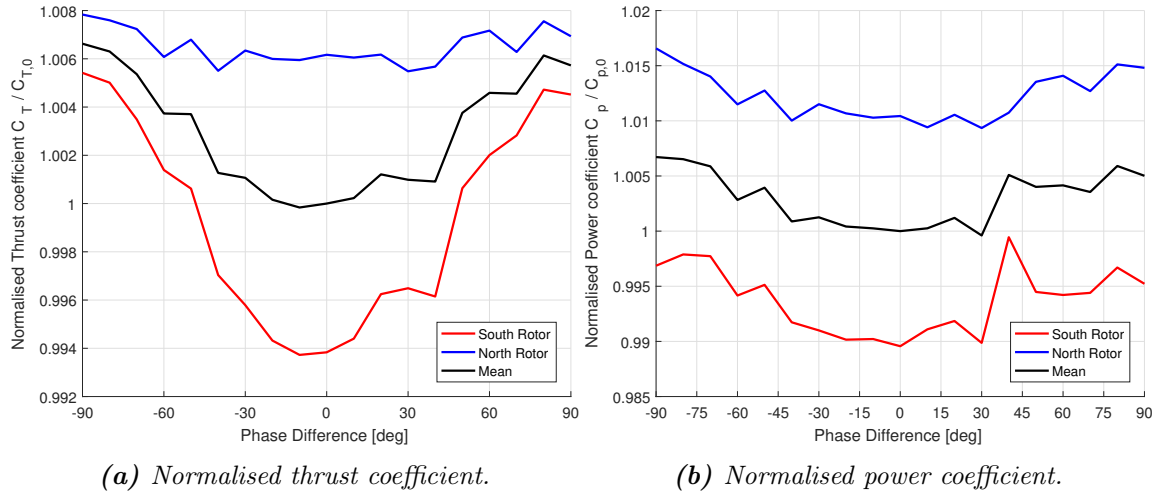


Figure 7.24: Influence of the phase difference on the thrust coefficient and power coefficient for the Counter-Down layout, with $\lambda = 4$, $\sigma = 0.1$, $B = 2$, $d = 0.1$.

7.7 Conclusion

In this chapter, the Double Actuator Cylinder (DAC) model is derived, and implementation of the DAC models from the original AC model as well as Cheng's AC model in both explicit formulation and matrix formulation. The implementation is validated and the performance of the DAC models are investigated. The new findings and the main conclusions are listed as follows.

- With appropriate non-dimensioned coordinate system as well as the linear characteristic of the linear solution of the AC model, the linear solution of the DAC model is derived in the form of the summation of the single AC model.
- For the two identical rotors with zero yaw angle, there are three different rotational direction layouts which are *Counter-Up*, *Counter-Down* and *Co-Rotating*. With the mirror effect, for the two *Counter-Rotating* layouts, the value of the variables of one rotor is identical to the mirrored point. Thus, the properties of the two rotors can be represented either one of them. For the *Co-Rotating* layout, the two rotors counter-clockwise or clockwise Co-rotating can be summarised into a single case due to the mirror effect. The mirror effect then can be used as a tool to validate whether the DAC models are correctly implemented.
- There is another method to validate the DAC model which is to calculate the case that the two rotors are placed with a very large distance between each other. The influence between the two rotors could then be neglected and the results should be identical with the corresponding single rotor layout calculated from the single AC model.
- The power coefficient and thrust coefficient from the DAC models that based on the original AC model is higher than the DAC models based on Cheng's AC model.

- The general trend of the power coefficient as well as thrust coefficient for a certain tip speed ratio with increasing of solidity can be modelled with the DAC models for different rotational direction layouts. However, for the *Counter-Up* layout, the DAC2 and DAC4 model are not able to model the general trend of power coefficient when $\lambda = 5$.
- The relative relationship of the thrust coefficient as well as power coefficient for a certain solidity but different tip speed ratio is also able to be modelled by the DAC models. However, the relative relationship of the power coefficient for the *Counter-Up* layout is not able to be modelled with the DAC2 and DAC4 model when $\sigma > 0.1$.
- The influence between the two rotors is investigated with the panel code by comparing the results for different rotational direction layouts with the condition that the two rotors are placed far apart which is represented by the single rotor layout. The first influence is the value of the variables will have a lead or lag in the phase compared to the single rotor layout. It is then validated that the DAC2 and DAC4 model are sufficient to correctly model the lead or lag of phase for different rotational direction layouts.
- The second influence between the two rotors is the transfer of the value of the variables between the windward and leeward part of the rotor. It is validated that the influence in the windward part can be well modelled by both DAC2 and DAC4 model. For the leeward part, the DAC2 model is insufficient to model the increments of the maximum amplitudes of the variables for *Counter-Down* layout or for the north rotor of the counter-clockwise *Co-Rotating* layout. The DAC4 model is not sufficient to model the transfer of the angle of attack for the aforementioned two layouts. In addition, the shape of the curves of the normal and tangential loadings for different rotational direction layouts are not well modelled with the DAC models.
- The variation of the influence between the two rotors, which is represented by the thrust and power coefficient, with the increase of the distance is also investigated. For the two *Counter-Rotating* layouts, neither of the two DAC models are sufficient to correctly model for both the layouts. For the *Co-Rotating* layout, the relative relationship of the thrust coefficient as well as power coefficient for the two rotors are not able to be modelled with the two DAC models, thus the mean value of the two rotors are then validated. The trend of the mean thrust and power coefficients can be modelled the DAC models, but the relative value compared to the single rotor layout is generally underestimated which means the influence between the two rotors is underestimated.
- For the influence due to phase difference, it is concluded that the mean value of the thrust and power coefficient of the two rotors does not change much with the phase difference. The difference of the relative values of thrust and power coefficient with respect to the zero phase difference case is within 0.8%. Thus, the method of using the case of zero phase difference to represent the performance of the two rotors is sufficient.

Final Remarks

8.1 Conclusions

In this work the influence between the two Vertical Axis Wind Turbines (VAWTs) placed close together for different rotational direction setups is investigated with the newly developed Double Actuator Cylinder (DAC) model as well as the panel code of U2DiVA. It is shown that there will be a slight increase of the power coefficient as well as the thrust coefficient when the two rotors are placed together. Much supportive work has also been carried out during this project in order to achieve the main research aim. These works can be summarised to be the details of the implementation of the AC model, derivation of some relevant analytical solutions, modelling the flow curvature effect and including the unsteady aerodynamics by coupling the modified Risø dynamic stall model with the AC model. Meanwhile, some interesting discoveries related to the AC model have been obtained. With the supportive work, the coupled dynamic AC model is obtained and validated against the panel code to be a sufficient tool for predicting the azimuthal variation of the distributed loadings, induced velocities, angle of attack and relative wind speed, despite it is shown further improvements could be made. Only with a sufficient single AC model could the DAC model, which is derived from the single AC model, also be sufficient. The detailed conclusions for this work have already been listed in the last section of each chapter. Thus, only the most critical results will be briefly summarised here.

- The details of the AC model, are investigated including the discretization method, Mod-Lin correction, iteration procedure, implementation in the MATLAB code and validate against HAWC2 code. Some interesting aspects such as Cheng's modified AC model[8], the matrix formulation of equations, *mirror effect* for different rotational directions, the explicit form of the wake terms, continuity of velocity and the influence due to the mounting point has been investigated. The performance of the original AC model is validated against the panel code which shows significant deviations of the

normal and tangential loadings. By comparing the lift and drag coefficient with the panel code, the reason of the deviation is that the flow curvature effect and unsteady aerodynamics are not included in the current AC model.

- The analytical solutions of the influence coefficients are derived with which the computational effort of the AC model is further decreased and the properties of the influence coefficients are obtained, which show more physical meanings. The convergence problem encountered when using numerical integration to calculate the influence coefficients is also investigated accordingly. The analytical solution of the induced velocity of w_x^n on the control point in x -direction due to arbitrary normal loadings is also derived which is in very simple form and clearly reveals the physical meaning of the AC model.
- The flow curvature effect has been investigated with the Migliore's conformal mapping method, and the resulting virtual airfoil is evaluated with the panel code. It is then shown the virtual camber due to the flow curvature effect could be modelled with the local angle of attack at three-quarter chord point. This method is implemented in the AC model and with the lift applied at the quarter chord point perpendicular to the local angle of attack at this point. The modified AC model is validated against the panel code which shows the flow curvature effect has been well modelled. However, the loadings are still having deviations because the phase lag due to the unsteady aerodynamics is not modelled.
- The Risø dynamic stall model is used to model the unsteady effect, and it is revealed that the flow curvature effect is implicitly included in the model. Thus it is not necessary to model the flow curvature effect separately. The method of applying the lift perpendicular to the *effective* angle of attack at the quarter chord point models the lag effect better than applying perpendicular to the geometric angle of attack at the quarter chord point. The normal and tangential loadings from the coupled dynamic AC model are shown to have good agreements with the panel code if Cheng's modified Mod-Lin correction method is applied. It is also shown that there is the possibility of further improve the Mod-Lin correction method for better agreements with the panel code.
- The DAC model is developed according to Ning's formulation [36]. There will be four different possible DAC models depending on whether including Cheng's modification as well as the flow curvature modelling, with the latter being the steady part of the modified Risø model. The implementation of the DAC model is validated with the mirror effect for different rotational direction setups. It is also validated the influence between the two rotors will diminish when the distance between the two rotors is infinitely large.
- It is validated that for different rotational direction setups, the thrust and power coefficient from the DAC model are not having good agreements with the panel code as that of the single AC model. The influence between the two rotors for different setups is investigated with the panel code by comparing the distributed loadings, the angle of attack and local thrust coefficient for the case of two rotors placed close together with the case of two rotors placed infinitely far from each other which could be represented by the single rotor setup. It is concluded that the aforementioned variables will have phase lead-lag effect as well as transfer of the values between the

windward and leeward part of the rotor. With the results from the DAC model compared with the single AC model, it is concluded that DAC model predicts the phase lead-lag correctly but the transfer of the values are not well modelled for some cases. It is also validated that the variation of the thrust and power coefficient with the distance between the two rotors is underestimate and the steep increase of the power and thrust coefficient when the two rotors are placed very close together is not able to be modelled with the DAC model. The influence due to the phase difference cannot be modelled with the DAC model but it is investigated with the panel code that the influence is small. The current DAC model is then not fully sufficient to model the double rotor setup with only some of the influences between the two rotors are correctly modelled.

8.2 Recommendations

Throughout the work in this thesis, multiple issues have been encountered which needs further investigations. This section will present some ideas of the recommendations for future research.

- In this report, it is shown the results of induced velocities are dependent on whether evaluating just outside or inside of the AC. The discontinuity is due to the tangential loadings and is in the tangential direction with respect to the AC. However, it has not been determined in this thesis whether the control point in the windward and leeward part of the AC should be moved inside or outside of the AC. Even though the influence due to this discontinuity of velocity is small because it does not affect the angle of attack much, it is still favourable to have detailed investigations to determine the location of evaluating the control points.
- The analytical solution of the influence coefficient I_2 is favourable to be derived, with which the analytical solution of w_y^n on the control points in y -direction due to normal loading will then be obtained. Further more, the components of the induced velocities on the control points due to tangential loadings are then also able to be derived. With the aforementioned analytical solutions, the induced velocities on the control points of the AC for an arbitrary form of normal and tangential loadings will be directly calculated.
- The Cheng's modified Mod-Lin correction method is shown to have improved compared to the original Mod-Lin correction method but is still not sufficient enough. It has been shown that there is the possibility to further improve the Mod-Lin correction method to let the results from the coupled dynamic AC model to have even better agreements with the panel code. The possible method of obtaining the corresponding polynomial function could be regression analysis.
- Currently, only the linear part of the AC model is implemented, and the Mod-Lin correction method is applied to let the results approach the full AC model. By implementing the full AC model and then couple with the dynamic stall model, it will be possible to have better agreements with the panel code than the current

coupled dynamic AC model. Moreover, for the DAC model derived from the full AC model, it is also possible to have better agreements with the panel code.

- In this report, the coupled dynamic AC model, with only the inviscid part of the Risø dynamic stall model, is validated against the panel code. This is due to the current panel code is not able to model the flow separation. The full Risø dynamic stall model with trailing edge separation as well as the Pirrung's extended model coupled with the AC model is favourable to be validated against a more high-fidelity method such as CFD code.
- A sufficient modified Mod-Lin correction method for the DAC model is favourable to be introduced. In this report, the unsteady effects are neglected in the DAC model, only the *steady* part of the Risø dynamic stall model is included, which is equivalent to modelling the flow curvature effect. This is because the current Mod-Lin method is not sufficient for the DAC model since the thrust coefficient is not well modelled. If the unsteady effects in the Risø model are included, the thrust coefficients from the coupled dynamic AC Model will have even worse agreements with panel code. If a sufficient Mod-Lin correction method is obtained and the dynamic effects could then be included. There is the potential of letting the corresponding coupled dynamic DAC model have better agreements with the panel code.
- For the condition that one rotor is in the direct wake of the other rotor if the currently Mod-Lin correction method is used, a single correction factor, which is calculated from the thrust coefficient of the whole rotor, will be applied to the whole rotor and could be considered as an averaged value. However, the thrust will be lower for the part in the direct wake of the other rotor than the part outside the direct wake. Further development of a piecewise function of the Mod-Lin correction is a possible method.

APPENDIX A

Derivation of equations

A.1 Derivation of the thrust coefficient and power coefficient

The explicit form of the thrust coefficient and power coefficient in Equation (3.51) and (3.149) in Chapter 3 will be derived here.

A.1.1 Derivation of the thrust coefficient

When one of the blade is located at the azimuths angle of θ , the aerodynamic force in the free wind direction, which is the force in x -direction, for this blade could be obtained with the normal and tangential forces which are defined to be with respect to the airfoil.

Counter-clockwise rotation

Firstly, when the rotor is counter-clockwise rotating, the relationship could be obtained with Figure 3.4 and as follows. To be noted that the term of *force* here actually represents forces per unit length which will be newton per meter in the metric system.

$$F_x(\theta) = F_n(\theta) \sin(\theta - \theta_p) - F_t(\theta) \cos(\theta - \theta_p) \quad (\text{A.1})$$

The total aerodynamic force in the free wind direction for all B blades, which is the sum of the forces when the blades are located at the corresponding azimuthal angles, is the thrust force of the rotor. The average value of the thrust force for one revolution could be calculated as follows.

$$T_{ave} = \frac{1}{2\pi} B \int_0^{2\pi} F_x(\theta) d\theta \quad (\text{A.2})$$

The thrust coefficient is the non-dimensioned value of the aforementioned average value of the thrust force and is as follows.

$$C_T = \frac{T_{ave}}{\frac{1}{2}\rho V_\infty^2 2R} \quad (A.3)$$

Substitute the Equation (A.2) and (A.1) into Equation (A.3), the thrust coefficient C_T could then be expressed as:

$$C_T = \frac{B}{2\pi\rho V_\infty^2 R} \int_0^{2\pi} \left(F_n(\theta) \sin(\theta - \theta_p) - F_t(\theta) \cos(\theta - \theta_p) \right) d\theta \quad (A.4)$$

With the *Addition and Subtraction Formulas*, the Equation (A.4) could be then written as follows.

$$C_T = \frac{B}{2\pi\rho V_\infty^2 R} \int_0^{2\pi} \left[(F_n(\theta) \cos \theta_p - F_t(\theta) \sin \theta_p) \sin \theta - (F_n(\theta) \cos \theta_p + F_t(\theta) \sin \theta_p) \right] d\theta \quad (A.5)$$

And with the Equation (3.32) and (3.33) for the normal and tangential loadings, the thrust coefficient C_T could be derived to be as follows which is in the same form as in Equation (3.51).

$$C_T = \int_0^{2\pi} \left(Q_n(\theta) \sin \theta + Q_t(\theta) \cos \theta \right) d\theta \quad (A.6)$$

Clockwise rotation

For the condition that the rotor is clockwise rotating, the relationship of the aerodynamic force in x -direction with the normal and tangential blade aerodynamic forces could be obtained according to Figure 3.8b as follows.

$$F_x(\theta) = F_n(\theta) \sin(\theta + \theta_p) + F_t(\theta) \cos(\theta + \theta_p) \quad (A.7)$$

The difference with Equation (A.1) is because of the definition of the tangential blade force F_t and pitch angle θ_p are different from that for the counter-clockwise rotating setup. The thrust coefficient C_T for the clockwise rotating condition is then as below:

$$C_T = \frac{B}{2\pi\rho V_\infty^2 R} \int_0^{2\pi} \left[(F_n(\theta) \cos \theta_p - F_t(\theta) \sin \theta_p) \sin \theta + (F_n(\theta) \cos \theta_p + F_t(\theta) \sin \theta_p) \right] d\theta \quad (A.8)$$

With the Equation (3.32) and (3.98) for the normal and tangential loading for the clockwise rotating case, the equation could then be simplified. And the explicit form of the equation is identical to the counter-clockwise rotating case as in Equation (3.51).

A.1.2 Derivation of the power coefficient

The aerodynamic power could be calculated with the fundamental physical equation of power which is the product of the torque M and the angular velocity ω .

$$P = \omega M \quad (A.9)$$

When a blade is at the azimuthal angle of θ , the instantaneous aerodynamic power of this blade is then as follow. The subscript of b represent the power is for one blade.

$$P_b(\theta) = \omega M_b(\theta) \quad (\text{A.10})$$

The torque is the product of the force and the force arm, which could also be calculated with the product of the tangential force with respect to the rotor $F_{t,r}(\theta)$ and the distance between the rotational axis and the aerodynamic centre which is the radius of the rotor R . The explicit equation is as follows which is valid for both counter-clockwise and clockwise rotating condition.

$$M_b(\theta) = F_{t,r}(\theta)R = (F_t(\theta) \cos \theta_p + F_n(\theta) \sin \theta_p)R \quad (\text{A.11})$$

The total aerodynamic power for all the blades are then the sum of the instantaneous aerodynamic power for each blade at their corresponding azimuthal locations. The average value of the total aerodynamic power for the rotor in one revolution is then as follows.

$$P_{ave} = \frac{1}{2\pi} \int_0^{2\pi} B\omega M_b(\theta) d\theta \quad (\text{A.12})$$

The power coefficient is the non-dimensioned averaged aerodynamic power for the rotor and is as follows.

$$C_p = \frac{P_{ave}}{\frac{1}{2}\rho V_\infty^3 2R} \quad (\text{A.13})$$

Subtracting Equation (A.11) and (A.12) into Equation (A.13), the power coefficient C_p is then as follows.

$$C_p = \frac{\omega R \int_0^{2\pi} B(F_t(\theta) \cos \theta_p + F_n(\theta) \sin \theta_p) d\theta}{V_\infty 2\pi R \rho V_\infty^2} \quad (\text{A.14})$$

With the definition of the tip speed ratio in Equation (3.39) as well as Equation (3.33) and (3.98) for the tangential loading for counter-clockwise and clockwise rotating rotor respectively, the power coefficient C_p could then be simplified to be:

$$C_p = \begin{cases} -\lambda \int_0^{2\pi} Q_t(\theta) d\theta & , \text{Counter-clockwise} \\ \lambda \int_0^{2\pi} Q_t(\theta) d\theta & , \text{Clockwise} \end{cases} \quad (\text{A.15})$$

A.2 Transform from Cartesian to polar coordinate

For the simplified method to calculate the influence coefficient in Equation (4.1) and (4.8), the non-dimensioned coordinate (x, y) of the point to be evaluated should be transformed to the non-dimensioned polar coordinate (r, θ) . The definition of the two coordinate system are as in Figure 3.1. To be noted that the polar coordinate system defined for the Actuator Cylinder model is a *generalised* polar coordinate system because the polar axis is coincided with the y -axis instead of the x -axis. The transformation from the polar coordinate system to the Cartesian coordinate system could be easily done with Equation (3.3) and (3.4). However, the backward transformation is a little bit more complicated and could be done in two steps in practical as follows.

The first step is to transform the Cartesian coordinate system (x, y) to a new non-dimensioned coordinate system (x_2, y_2) that the x -axis will coincide with the polar axis.

$$x_2 = y \quad (\text{A.16})$$

$$y_2 = -x \quad (\text{A.17})$$

The second step is to transform the Cartesian coordinate (x_2, y_2) to the polar coordinate system (r, θ) . The radius r could be calculated with the non-dimensioned distance from the point to the origin.

$$r = \sqrt{x_2^2 + y_2^2} \quad (\text{A.18})$$

The azimuthal angle θ could not be directly calculated with the arctangent function, because the range is $(-\pi/2, \pi/2)$ which does not cover all the condition of the azimuthal angles. There are two methods to calculate the azimuthal angle θ .

With *atan2* function

the first method is to calculate with the *atan2* function which is the arctangent function with two arguments. This function has been implemented in a couple of computer codes such as MATLAB, which could be used directly.

$$\theta_0 = \text{atan2}(y_2, x_2) \quad (\text{A.19})$$

The resulting angle is positive for the condition of $y_2 > 0$ and is negative for the condition of $y_2 < 0$, and the output is in the range of $(-\pi, \pi]$ by definition. The azimuthal angle θ for the AC model is in the range of $(0, 2\pi]$ which means when the output is less than zero, the value should be added by 2π .

$$\theta = \begin{cases} \theta_1 & , \text{if } \theta_1 \geq 0 \\ \theta_1 + 2\pi & , \text{if } \theta_1 < 0 \end{cases} \quad (\text{A.20})$$

There are different methods to achieve the *atan2* function, and one possible method is to use the following piecewise equation.

$$\text{atan2}(y, x) = \begin{cases} \tan^{-1}(y/x) & , \text{if } x > 0 \\ \tan^{-1}(y/x) + \pi & , \text{if } x < 0 \text{ and } y \geq 0 \\ \tan^{-1}(y/x) - \pi & , \text{if } x < 0 \text{ and } y < 0 \\ +\pi/2 & , \text{if } x = 0 \text{ and } y > 0 \\ -\pi/2 & , \text{if } x = 0 \text{ and } y < 0 \\ \text{undefined} & , \text{if } x = 0 \text{ and } y = 0 \end{cases} \quad (\text{A.21})$$

With argument function for complex number

The second method is to use the principal value of the argument function for the complex number. Firstly, the complex number z_2 is defined to have the real part of x_2 and imagine

part of y_2 . And the principle value of the argument could be calculated with the $Arg(z)$ function.

$$z_2 = x_2 + y_2 i \quad (\text{A.22})$$

$$\theta_1 = Arg(z_2) \quad (\text{A.23})$$

The principle value of the argument is in the range of $(-\pi, \pi]$, as a result, the azimuthal angle should then be calculated with Equation (A.20).

A.3 Calculate analytical solution with Cauchy principal value

The derivation of the Equation (4.7) which is the analytical solution of the influence coefficient I_1 for the condition of $\beta \in [\theta_i - \frac{1}{2}\Delta, \theta_i + \frac{1}{2}\Delta]$ will be derived with the Cauchy principal value of integration as follows.

$$I_{1,i}(r, \beta) = PV \int_{\theta_i - \beta - \frac{1}{2}\Delta\theta}^{\theta_i - \beta + \frac{1}{2}\Delta\theta} f_1(r, \varphi) d\varphi \quad (\text{A.24})$$

Let $\delta, \epsilon > 0$ and $\delta, \epsilon \rightarrow 0$, and with the notation of $\delta, \epsilon \rightarrow 0^+$, the Cauchy principal value is then as follows. To be noted that the condition of $r \neq 1$ is assumed.

$$I_{1,i}(r, \beta) = \lim_{\delta, \epsilon \rightarrow 0^+} \left(\int_{\epsilon}^{\theta_i - \beta + \frac{1}{2}\Delta\theta} f_1(r, \varphi) d\varphi + \int_{\theta_i - \beta - \frac{1}{2}\Delta\theta}^{-\delta} f_1(r, \varphi) d\varphi \right) \quad (\text{A.25})$$

As a result, it is important to calculate $\lim_{\epsilon \rightarrow 0^+} I_{in}(\epsilon)$ and $\lim_{\delta \rightarrow 0^+} I_{in}(-\delta)$.

$$\lim_{\epsilon \rightarrow 0^+} I_{in}(\epsilon) = - \lim_{\epsilon \rightarrow 0^+} \left[\tan^{-1} \left(\frac{r-1}{r+1} \cot \frac{\epsilon}{2} \right) - \frac{\epsilon}{2} + C_1 \right] \quad (\text{A.26})$$

$$\lim_{\delta \rightarrow 0^+} I_{in}(-\delta) = \lim_{\delta \rightarrow 0^+} \left[\tan^{-1} \left(\frac{r-1}{r+1} \cot \frac{\delta}{2} \right) - \frac{\delta}{2} + C_1 \right] \quad (\text{A.27})$$

With the assumption of $r \neq 1$, there are two conditions of the value of r which are $r > 1$ and $r < 1$. The two conditions corresponds to the point to be evaluated is inside and outside of the Actuator Cylinder respectively.

When the location is outside of the AC with $r > 1$,

$$\lim_{\epsilon \rightarrow 0^+} \left(\frac{r-1}{r+1} \cot \frac{\epsilon}{2} \right) = +\infty \quad (\text{A.28})$$

Substituting Equation (A.28) into Equation (A.26),

$$\lim_{\epsilon \rightarrow 0^+} I_{in}(\epsilon) = - \tan^{-1}(+\infty) + 0^+ + C_1 = -\frac{\pi}{2} + C_1 \quad (\text{A.29})$$

Similarly, the Equation (A.27) could also simplified.

$$\lim_{\delta \rightarrow 0^+} I_{in}(-\delta) = \tan^{-1}(+\infty) + 0^+ + C_1 = \frac{\pi}{2} + C_1 \quad (\text{A.30})$$

And finally, subtract Equation (A.29) and (A.30) into Equation (A.25), the influence coefficient $I_{1,i}(r, \beta)$ is as follows.

$$I_{1,i}(r, \beta) = I_{1in}(r, \theta_i - \beta + \frac{1}{2}\Delta\theta) - I_{1in}(r, \theta_i - \beta - \frac{1}{2}\Delta\theta) + \pi, r > 1 \quad (\text{A.31})$$

When the location is inside the AC with the condition of $r < 1$,

$$\lim_{\epsilon \rightarrow 0^+} \left(\frac{r-1}{r+1} \cot \frac{\epsilon}{2} \right) = -\infty \quad (\text{A.32})$$

The Equation (A.26) then becomes:

$$\lim_{\epsilon \rightarrow 0^+} I_{1in}(\epsilon) = \tan^{-1}(+\infty) + 0^+ + C_1 = \frac{\pi}{2} + C_1 \quad (\text{A.33})$$

And similarly, the Equation (A.27) could be simplified as well.

$$\lim_{\delta \rightarrow 0^+} I_{1in}(-\delta) = \tan^{-1}(-\infty) + 0^+ + C_1 = -\frac{\pi}{2} + C_1 \quad (\text{A.34})$$

As a result, the influence coefficient $I_{1,i}(r, \beta)$ is then as follows.

$$I_{1,i}(r, \beta) = I_{1in}(r, \theta_i - \beta + \frac{1}{2}\Delta\theta) - I_{1in}(r, \theta_i - \beta - \frac{1}{2}\Delta\theta) - \pi, r < 1 \quad (\text{A.35})$$

A.4 Derivation of Pirrung's simplification

The simplified form of the indicial formulations of the aerodynamic state variables as well as effective angle of attack for the inviscid part of the Risø dynamic model is given by Pirrung [39]. Detailed derivation is done by the author as follows based on the steps of the derivation for the Risø dynamic stall model by Hansen [18].

According to Hansen[18], the effective downwash at the three-quarter chord point $w_{3/4}^{eff}$ is as follows.

$$w_{3/4}^{eff} = w_{3/4}(1 - A_1 - A_2) + y_1 + y_2 \quad (\text{A.36})$$

The variables of y_1 and y_2 are two aerodynamic state variables with the definition as follows which is identical with that in the Risø dynamic stall model.

$$\dot{y}_i + b_i \frac{2U}{c} y_i = b_i A_i \frac{2U}{c} w_{3/4} \quad (\text{A.37})$$

In the equation above, the subscript of i represents the index of the aerodynamic state variables which can be 1 or 2 for the inviscid part. By substituting the downwash $w_{3/4}$ with the angle of attack at the three-quarter chord point $\alpha_{3/4}$ with the relationship of $w_{3/4} = \alpha_{3/4}U$, the Equation (A.37) is then rewritten as:

$$\dot{y}_i + b_i \frac{2U}{c} y_i = b_i A_i \frac{2U^2}{c} \alpha_{3/4} \quad (\text{A.38})$$

The Equation (A.38) is a first-order ordinary differential equation (ODE) in the form of:

$$\dot{y}_i + P_i y_i = Q_i \quad (\text{A.39})$$

with

$$P_i = b_i \frac{2U}{c} \quad (\text{A.40})$$

$$Q_i = b_i A_i \frac{2U^2}{c} \alpha_{3/4} \quad (\text{A.41})$$

The solution of the ODE at time $t = t_e$ is as below according to Hansen [18], where the variable of t_s is the initial time.

$$y_i(t_e) = \int_{t_s}^{t_e} Q_i e^{-\int_t^{t_e} P_i d\tau} dt + y_i(t_s) \quad (\text{A.42})$$

The solution at time $t = t_e - \Delta t$ is then derived to be:

$$y_i(t_e - \Delta t) = \int_{t_s}^{t_e - \Delta t} Q_i e^{-\int_t^{t_e - \Delta t} P_i d\tau} dt + y_i(t_s) \quad (\text{A.43})$$

In order to obtain the relationship of the solution at the two neighbouring time steps, the Equation (A.42) is written in the following forms.

$$y_i(t_e) = \int_{t_s}^{t_e - \Delta t} Q_i e^{-\int_t^{t_e} P_i d\tau} dt + \int_{t_e - \Delta t}^{t_e} Q_i e^{-\int_t^{t_e} P_i d\tau} dt + y_i(t_s) \quad (\text{A.44})$$

$$y_i(t_e) = e^{-\int_{t_e - \Delta t}^{t_e} P_i d\tau} \int_{t_s}^{t_e - \Delta t} Q_i e^{-\int_t^{t_e - \Delta t} P_i d\tau} dt + \int_{t_e - \Delta t}^{t_e} Q_i e^{-\int_t^{t_e} P_i d\tau} dt + y_i(t_s) \quad (\text{A.45})$$

Substitute Equation (A.43) into Equation (A.45), and with the initial condition of $y_i(t_s) = 0$, the solution at the current time step t_e is able to be represented by the solution at the previous time step $(t_e - \Delta t)$ in the following form:

$$y_i(t_e) = C_{dec,i} y_i(t_e - \Delta t) + I_{new,i} \quad (\text{A.46})$$

Where the decaying factor $C_{dec,i}$ and the increment factor $I_{new,i}$ are as follows.

$$C_{dec,i} = e^{-\int_{t_e - \Delta t}^{t_e} P_i d\tau} \quad (\text{A.47})$$

$$I_{new,i} = \int_{t_e - \Delta t}^{t_e} Q_i e^{-\int_t^{t_e} P_i d\tau} dt \quad (\text{A.48})$$

At time step j

$$P_i^j = b_i \frac{2U^j}{c} \quad (\text{A.49})$$

$$Q_i^j = b_i A_i \frac{2U^{j2}}{c} \alpha_{3/4}^j \quad (\text{A.50})$$

With the assumption of piecewise constant of P_i , and Q_i , the decaying factor and increments factor are then in the same form as Equation (6.26) and (6.27). Where the mean values are represented by the midpoint values calculated with the linear interpolation.

$$\bar{P}_i^j = \frac{1}{2}(P_i^{j-1} + P_i^j) = \frac{b_i}{c}(U_i^{j-1} + U_i^j) \quad (\text{A.51})$$

$$\bar{Q}_i^j = \frac{1}{2}(Q_i^{j-1} + Q_i^j) = \frac{b_i A_i}{c}(U^{j2} \alpha_{3/4}^j + U^{j-12} \alpha_{3/4}^{j-1}) \quad (\text{A.52})$$

With the assumption that the variation of the relative wind speed is small enough to be neglected, which means $U_i^{j-1} \approx U_i^j$, the piecewise constant values could then be simplified as follows.

$$\bar{P}_i^j \approx \frac{2b_i U_i^j}{c} = b_i / T_u^j \quad (\text{A.53})$$

$$\bar{Q}_i^j \approx \frac{b_i A_i}{c} U^{j2} (\alpha_{3/4}^j + \alpha_{3/4}^{j-1}) = \frac{1}{2} \frac{b_i}{T_u^j} A_i U^j (\alpha_{3/4}^j + \alpha_{3/4}^{j-1}) \quad (\text{A.54})$$

Finally, the time step j and $j - 1$ is transformed to the time at $t = t_e$ and $t = t_e - \Delta t$ respectively, the Equation (A.42) could then be simplified as follows.

$$y_i(t_e) = y_i(t_e - \Delta t) e^{-b_i \Delta t / T_u} + \frac{1}{2} (\alpha_{3/4}(t_e - \Delta t) + \alpha_{3/4}(t_e)) A_i U(t_e) (1 - e^{-b_i \Delta t / T_u}) \quad (\text{A.55})$$

The equation above is identical with Equation (6.39), as a result, the derivation of Pirrung's simplification the Risø dynamic stall model is then finished.

A.5 Derivation of Pirrung's extended model

The Pirrung's extended model is also derived by the author and is as follows. The derivation is also based on the steps of the derivation for the Risø dynamic stall model.

The effective downwash $w_{3/4}^{eff}$ is as follows according to Equation (5) in [18].

$$w_{3/4}^{eff} = w_{3/4} \phi(0) - \int_0^t w_{3/4}(t') \frac{d\phi}{dt'} \left(\frac{2}{c} \int_{t'}^t U(\tau) d\tau \right) dt' \quad (\text{A.56})$$

And the two time-lags terms of ϕ is represented by two first order ODEs, and is as below according to Equation (7) in [18].

$$\frac{d\phi}{dt'} \left(\frac{2}{c} \int_{t'}^t U(\tau) d\tau \right) = -\frac{2U(t')}{c} \sum_{i=1}^2 b_i A_i e^{-b_i \frac{2}{c} \int_{t'}^t U(\tau) d\tau} \quad (\text{A.57})$$

The value of $\phi(0)$ could be obtained with Equation (6.50),

$$\phi(0) = 1 - A_1 - A_2 \quad (\text{A.58})$$

By substituting Equation (A.57) and (A.58) into (A.56), the effective downwash can be written as

$$w_{3/4}^{eff} = w_{3/4} (1 - A_1 - A_2) + \sum_{i=1}^2 b_i A_i \frac{2}{c} \int_0^t w_{3/4}(t') U(t') e^{-b_i \frac{2}{c} \int_{t'}^t U(\tau) d\tau} dt' \quad (\text{A.59})$$

With the definition of the aerodynamic state variables of y_1 and y_2 in [18], the Equation (A.59) can be re-written as

$$w_{3/4}^{eff} = w_{3/4}(1 - A_1 - A_2) + y_1 + y_2 \quad (\text{A.60})$$

Let the effective angle of attack be written in the following form

$$\alpha_E = \alpha_{3/4} - \frac{g_1}{U} - \frac{g_2}{U} \quad (\text{A.61})$$

The effect downwash is then

$$w_{3/4}^{eff} = w_{3/4} - g_1 - g_2 \quad (\text{A.62})$$

To be noted that the Equation A.61 is identical with Equation (6.40), but with the state variables of y_1 and y_2 noted as g_1 and g_2 . The reason is to let the definition of the state variable of y_i in this derivation to be identical with Equation (9) in [18] for the Risø dynamic stall model.

And by comparing the Equation (A.62) with Equation (A.60), the state variables of g_1 and g_2 are then defined as follows

$$g_i = y_i + A_i w_{3/4} \quad (\text{A.63})$$

Differentiate Equation (A.63) with respect to time t

$$\dot{g}_i = \dot{y}_i + A_i \dot{w}_{3/4} \quad (\text{A.64})$$

And then, substitute Equation (A.38) into (A.64)

$$\dot{g}_i = -b_i \frac{2U}{c} y_i + b_i A_i \frac{2U}{c} w_{3/4} + A_i \dot{w}_{3/4} \quad (\text{A.65})$$

The equation can be re-written in the following form

$$\dot{g}_i = -b_i \frac{2U}{c} (y_i + A_i w_{3/4} - A_i w_{3/4}) + b_i A_i \frac{2U}{c} w_{3/4} + A_i \dot{w}_{3/4} = -b_i \frac{2U}{c} g_i + A_i \dot{w}_{3/4} \quad (\text{A.66})$$

The Equation (A.66) is then also a first-order ordinary differential equation (ODE) in the form of:

$$\dot{g}_i + P_i g_i = Q_i \quad (\text{A.67})$$

with

$$P_i = b_i \frac{2U}{c} \quad (\text{A.68})$$

$$Q_i = A_i \dot{w}_{3/4} \quad (\text{A.69})$$

The relationship of the state variable of g_i in the current time step and the previous time step is in the identical form as that in section A.4,

$$g_i(t_e) = C_{dec,i} g_i(t_e - \Delta t) + I_{new,i} \quad (\text{A.70})$$

The decaying factor $C_{dec,i}$ and the increment factor $I_{new,i}$ are also with the same formulation as in Equation (A.47) and (A.48). At time step j

$$P_i^j = b_i \frac{2U^j}{c} \quad (\text{A.71})$$

$$Q_i^j = A_i \dot{w}_{3/4}^j \quad (\text{A.72})$$

With the assumption of piecewise constant of P_i , and Q_i , the value of the variables at the midpoint between time step $j-1$ and j are used.

$$\bar{P}_i^j = \frac{1}{2}(P_i^{j-1} + P_i^j) = \frac{b_i}{c}(U_i^{j-1} + U_i^j) \quad (\text{A.73})$$

$$\bar{Q}_i^j = Q_i^{j-\frac{1}{2}} \approx A_i \frac{w_{3/4}^j - w_{3/4}^{j-1}}{\Delta t} \quad (\text{A.74})$$

And with the assumption that the variation of the speed U is small enough to be neglected with $U^{j-1} \approx U^j$, the value of \bar{P}_i^j is then

$$\bar{P}_i^j \approx \frac{2b_i U_i^j}{c} = \frac{b_i}{T_u^j} \quad (\text{A.75})$$

Letting the time step j represents time $t = t_e$ and time step $j-1$ represents time $t = t_e - \Delta t$. The Equation (A.70) is then re-written as

$$g_i(t_e) = g_i(t_e - \Delta t)e^{b_i \Delta t / T_u} + (w_{3/4}(t) - w_{3/4}(t - \Delta t)) \frac{A_i T_u}{b_i \Delta t} (1 - e^{b_i \Delta t / T_u}) \quad (\text{A.76})$$

By multiplying the last term with the scaling factor of f_{scale} , the Equation (A.76) is then in the same form as Equation (6.41). As a result, the derivation of the Pirrung's extended method is finished.

APPENDIX B

Results from steady AC models

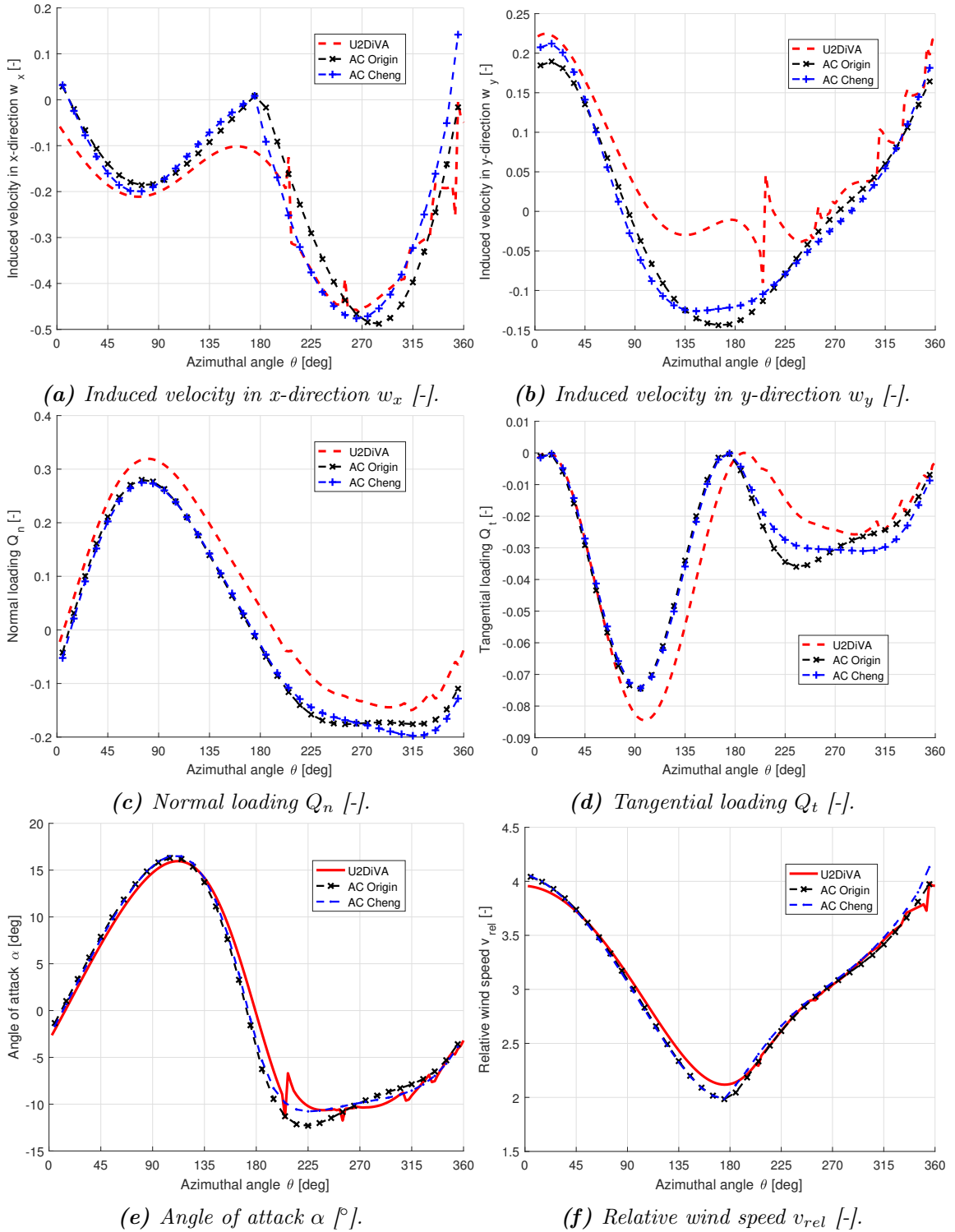


Figure B.1: Validate the AC1 and AC3 model against panel code, with $\lambda = 3$, $\sigma = 0.1$, $B = 2$.

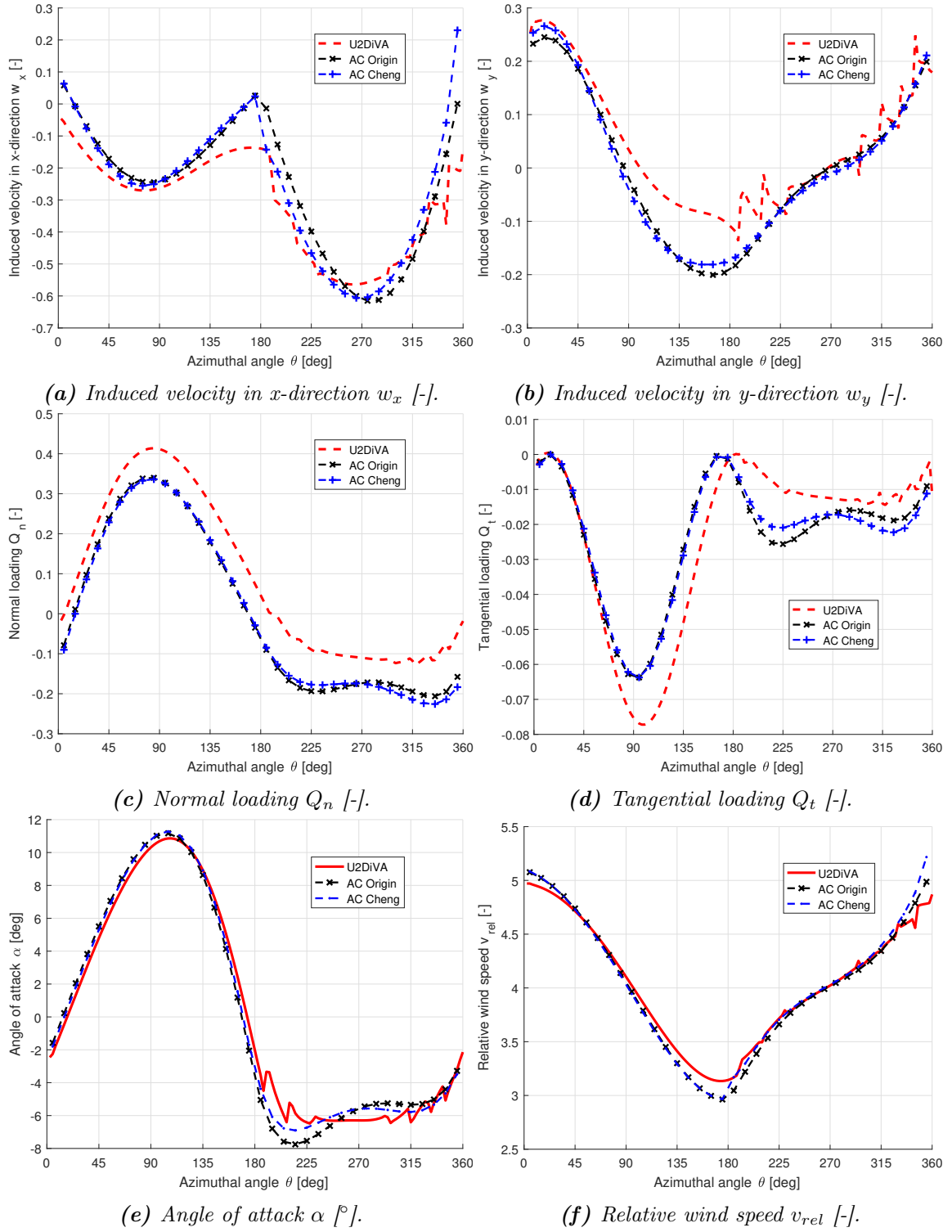


Figure B.2: Validate the AC1 and AC3 model against panel code, with $\lambda = 4$, $\sigma = 0.1$, $B = 2$.

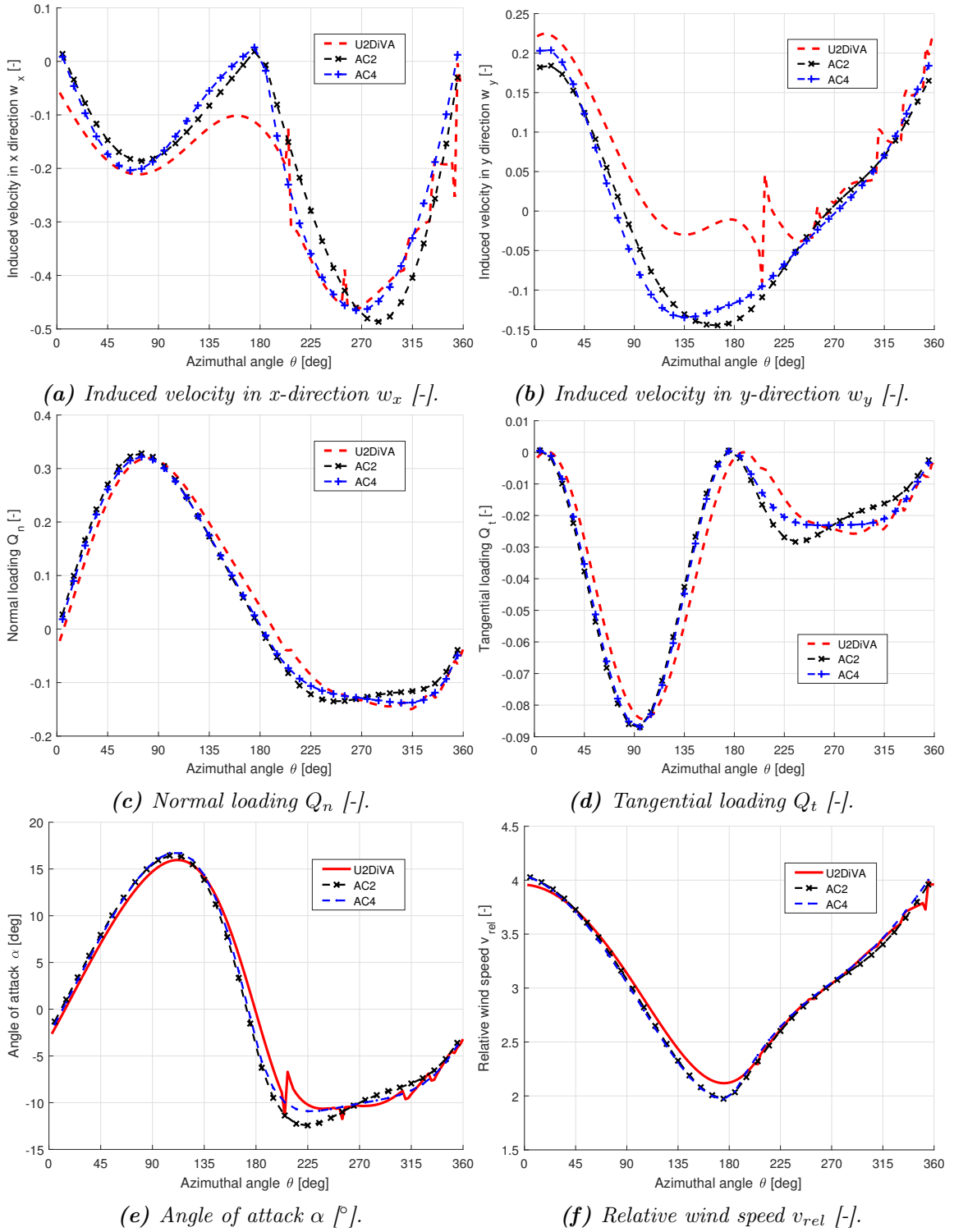


Figure B.3: Validate the AC2 and AC4 model against panel code, with $\lambda = 3$, $\sigma = 0.1$, $B = 2$.

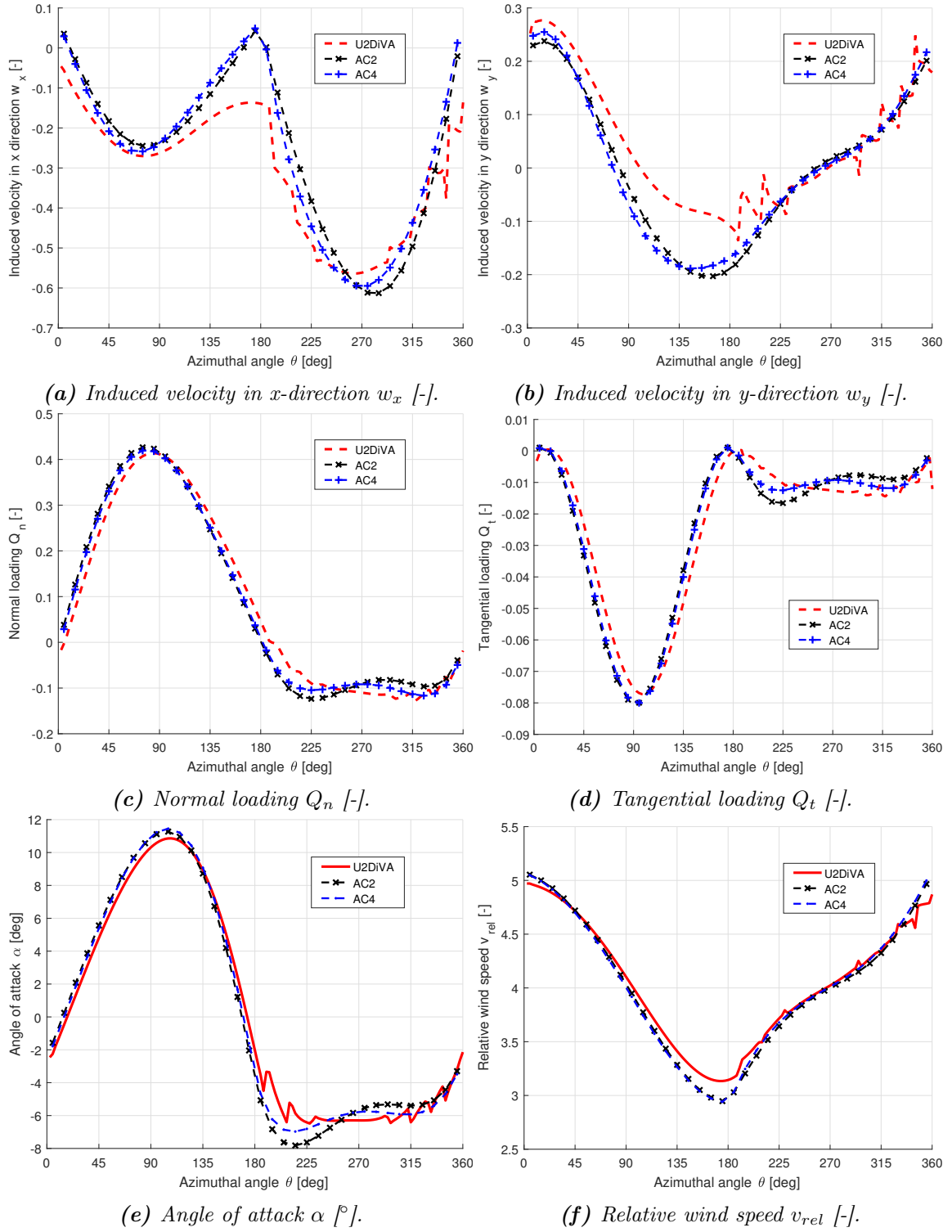


Figure B.4: Validate the AC2 and AC4 model against panel code, with $\lambda = 4$, $\sigma = 0.1$, $B = 2$.

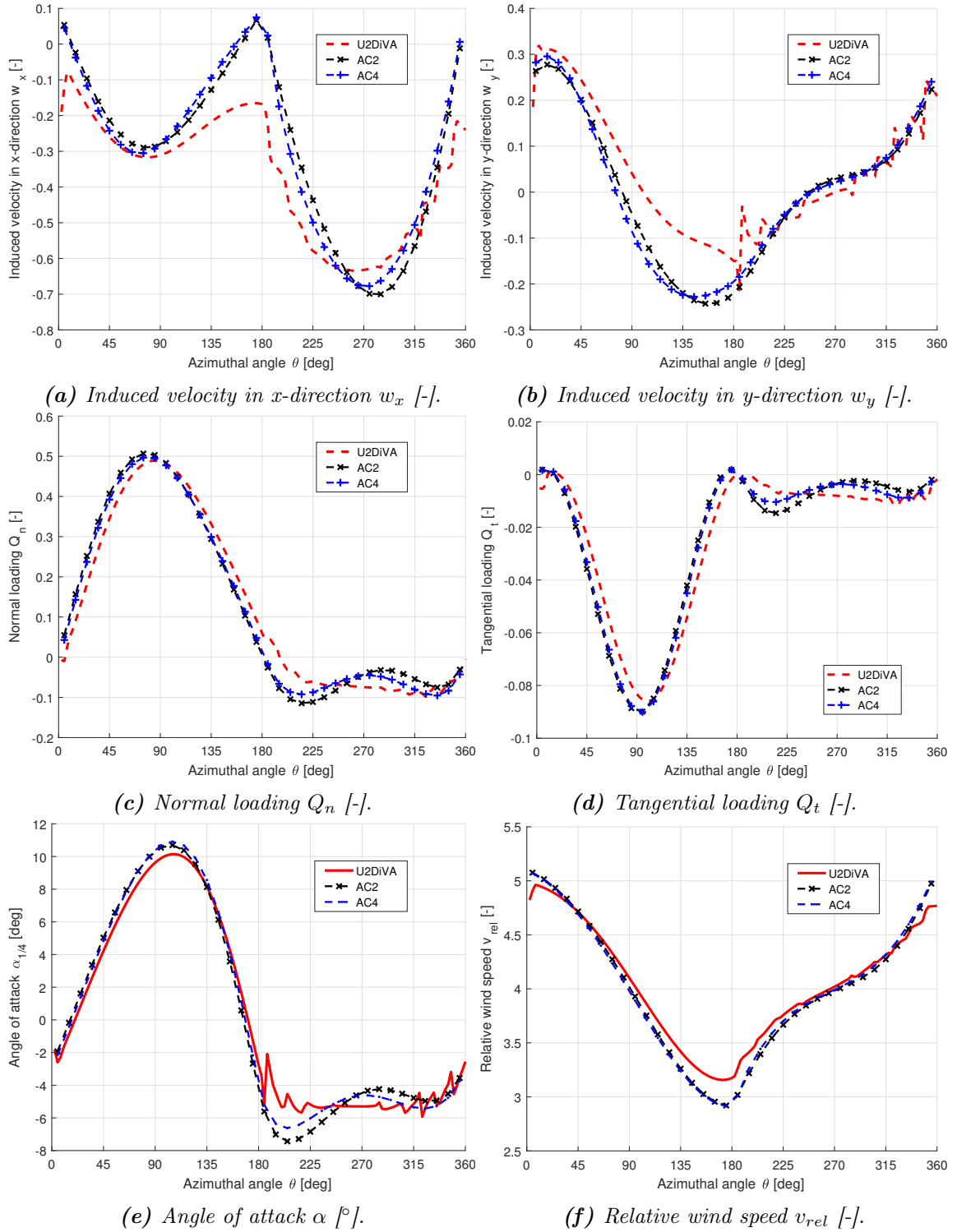


Figure B.5: Validate the AC2 and AC4 model against panel code, with $\lambda = 4$, $\sigma = 0.12$, $B = 2$.

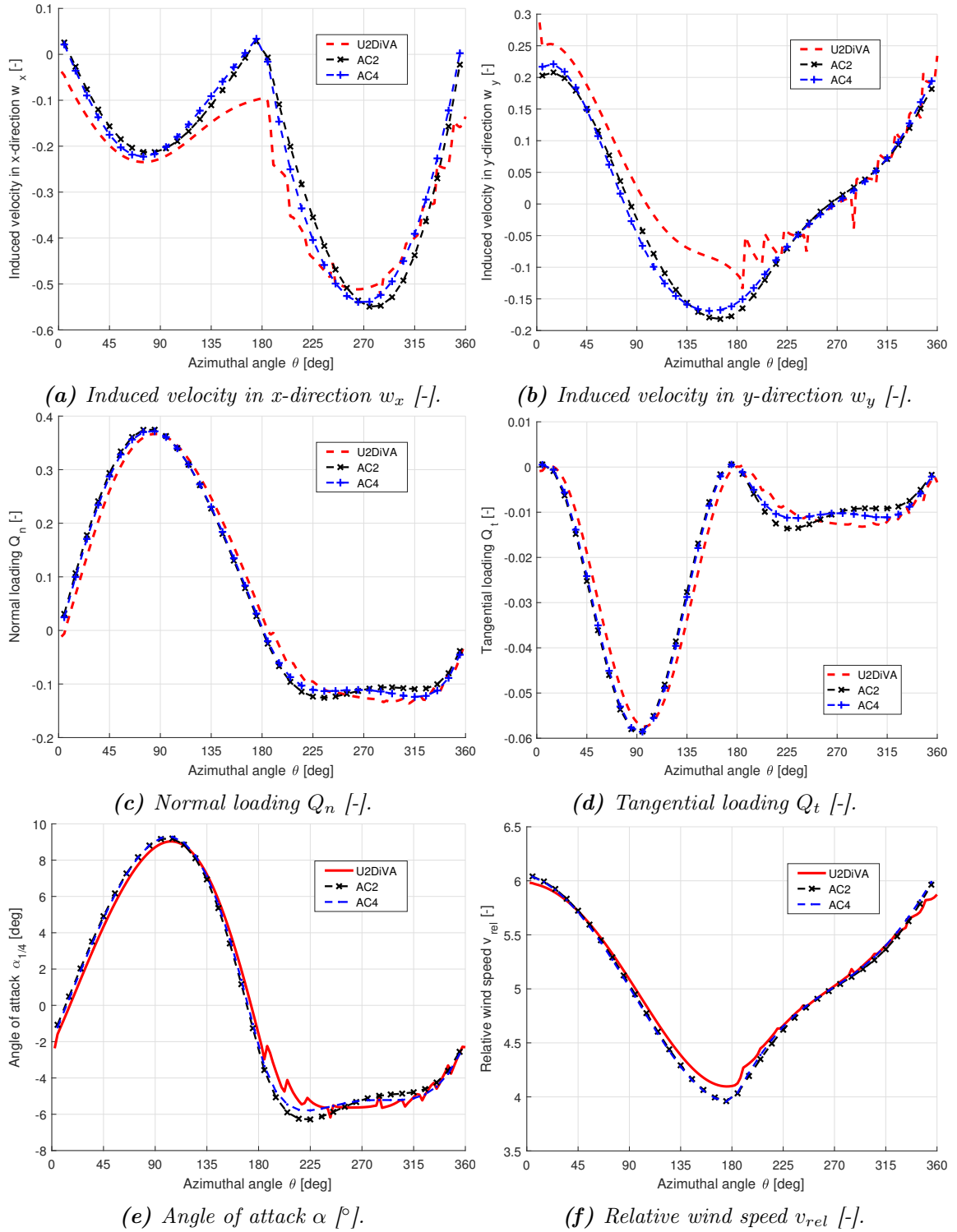
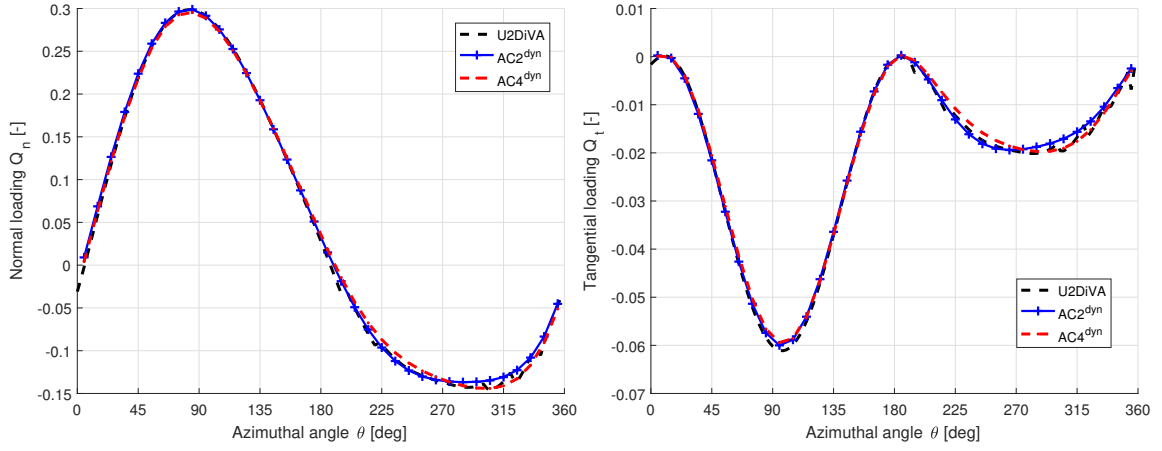
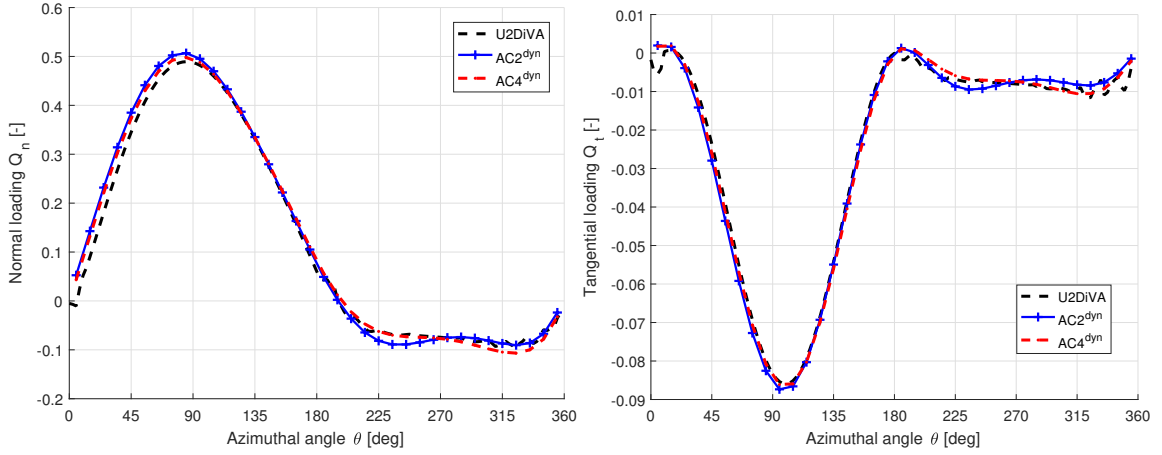


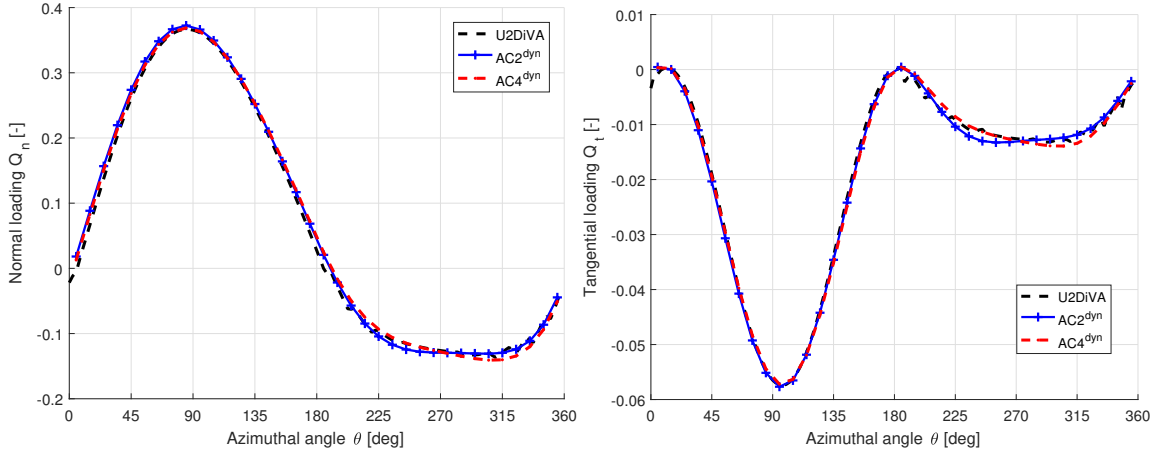
Figure B.6: Validate the AC2 and AC4 model against panel code, with $\lambda = 5$, $\sigma = 0.07$, $B = 2$.



(a) Normal Loading Q_n , with $\lambda = 4$, $\sigma = 0.07$. (b) Tangential Loading Q_t , with $\lambda = 4$, $\sigma = 0.07$.



(c) Normal Loading Q_n , with $\lambda = 4$, $\sigma = 0.12$. (d) Tangential Loading Q_t , with $\lambda = 4$, $\sigma = 0.12$.



(e) Normal Loading Q_n , with $\lambda = 5$, $\sigma = 0.07$. (f) Tangential Loading Q_t , with $\lambda = 5$, $\sigma = 0.07$.

Figure B.7: Validation of the normal and tangential loadings from the AC_2^{dyn} and AC_4^{dyn} model against the panel code, with $B = 2$.

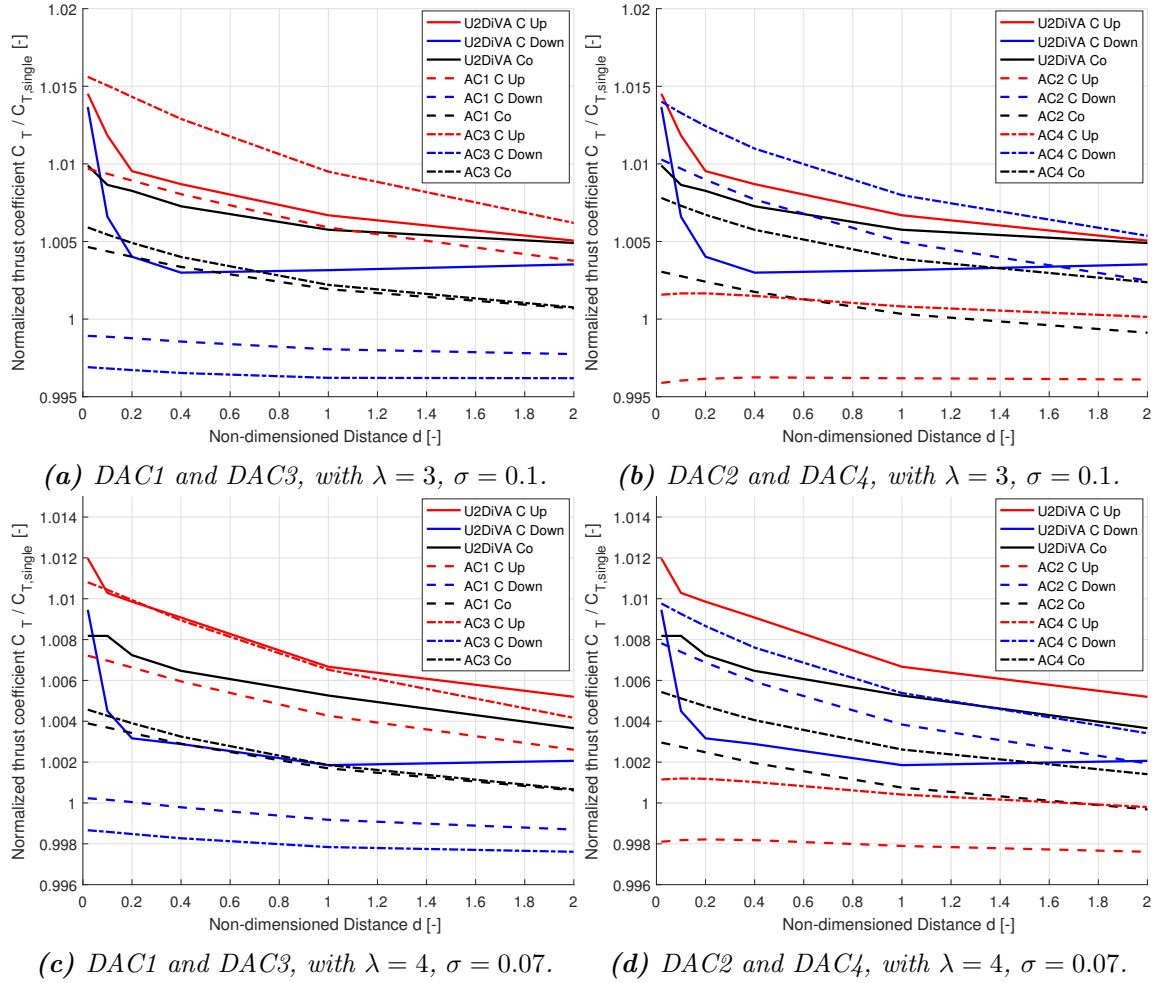


Figure B.8: Validation of the DAC models on predicting the relationship of the thrust coefficient for different rotational direction layouts.

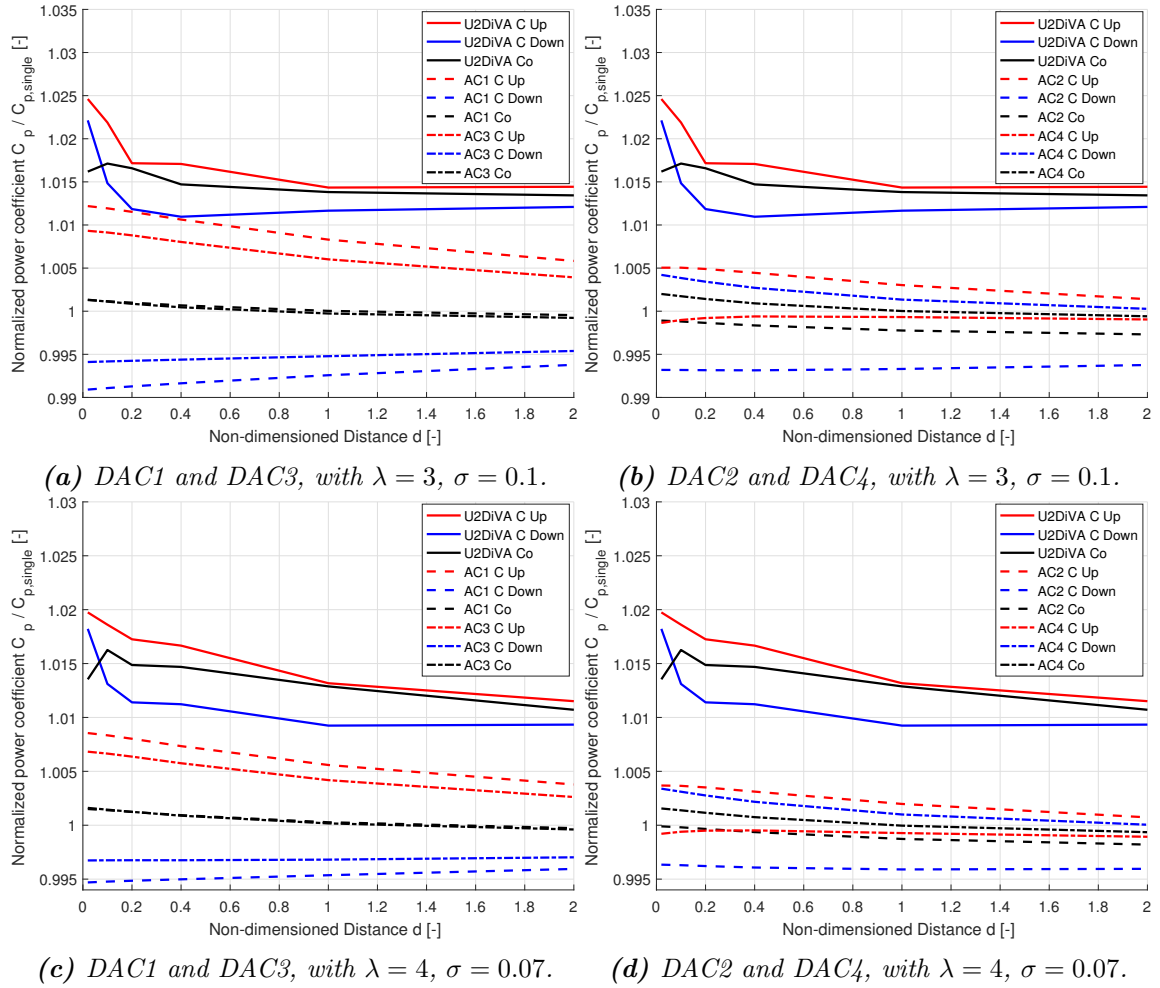


Figure B.9: Validation of the DAC models on predicting the relationship of the power coefficient for different rotational direction layouts.

Bibliography

- [1] H. Akimoto, K. Tanaka, and K. Uzawa. Floating axis wind turbines for offshore power generation-a conceptual study. *Environmental Research Letters*, 6(4):044017, 2011.
- [2] T. Beddoes. A synthesis of unsteady aerodynamic effects including stall hysteresis. *Vertica*, 1(2):113–123, 1976.
- [3] D. E. Berg. Improved double-multiple streamtube model for the darrieus-type vertical-axis wind turbine. Technical report, Sandia National Labs., Albuquerque, NM (USA), 1983.
- [4] L. Bergami, M. Gaunaa, and J. Heinz. Indicial lift response function: an empirical relation for finite-thickness airfoils, and effects on aeroelastic simulations. *Wind Energy*, 16(5):681–693, 2013.
- [5] R. Bielawa. Synthesized unsteady airfoil data with applications to stall flutter calculations. In *Proceedings of the 31st Annual Forum of the American Helicopter Society*, pages 13–15, 1975.
- [6] R. E. Brown and A. J. Line. Efficient high-resolution wake modeling using the vorticity transport equation. *AIAA journal*, 43(7):1434, 2005.
- [7] F. O. Carta. An analysis of the stall flutter instability of helicopter rotor blades. *Journal of the American Helicopter Society*, 12(4):1–18, 1967.
- [8] Z. Cheng, H. A. Madsen, Z. Gao, and T. Moan. Aerodynamic modeling of floating vertical axis wind turbines using the actuator cylinder flow method. *Energy Procedia*, 94:531–543, 2016.
- [9] J. O. Dabiri. Potential order-of-magnitude enhancement of wind farm power density via counter-rotating vertical-axis wind turbine arrays. *Journal of renewable and sustainable energy*, 3(4):043104, 2011.
- [10] M. Drela. Xfoil: An analysis and design system for low reynolds number airfoilsii. *University of Notre Dame*, 1989.

- [11] E. Dyachuk and A. Goude. Simulating dynamic stall effects for vertical axis wind turbines applying a double multiple streamtube model. *Energies*, 8(2):1353–1372, 2015.
- [12] C. Ferreira and F. Scheurich. Demonstrating that power and instantaneous loads are decoupled in a vertical-axis wind turbine. *Wind Energy*, 17(3):385–396, 2014.
- [13] C. S. Ferreira, H. A. Madsen, M. Barone, B. Roscher, P. Deglaire, and I. Arduin. Comparison of aerodynamic models for vertical axis wind turbines. In *Journal of Physics: Conference Series*, volume 524, page 012125. IOP Publishing, 2014.
- [14] C. S. J. Ferreira. *The near wake of the VAWT: 2D and 3D views of the VAWT aerodynamics*. PhD thesis, Delft University of Technology, 2009.
- [15] E. Ferrer Vaccarezza and R. HJ Willden. Blade-wake interactions in cross-flow turbines. *International Journal of Marine Energy*, (11):71–83, 2015.
- [16] R. E. Gormont. A mathematical model of unsteady aerodynamics and radial flow for application to helicopter rotors. Technical report, BOEING VERTOL CO PHILADELPHIA PA, 1973.
- [17] D. W. Gross and F. D. Harris. Prediction of in-flight stalled airloads from oscillating airfoil data. In *25th Annual Forum of the American Helicopter Society*, pages 14–16, 1969.
- [18] M. H. Hansen, M. Gaunaa, and H. A. Madsen. A beddoes-leishman type dynamic stall model in state-space and indicial formulations. 2004.
- [19] M. O. Hansen. *Aerodynamics of wind turbines*. Routledge, 2015.
- [20] C. Hirsch and A. C. Mandal. Flow curvature effect on vertical axis darrieus wind turbine having high chord-radius ratio. *Commission of the European Communities, (report) Eur*, pages 405–410, 1985.
- [21] M. Islam, D. S.-K. Ting, and A. Fartaj. Aerodynamic models for darrieus-type straight-bladed vertical axis wind turbines. *Renewable and Sustainable Energy Reviews*, 12(4):1087–1109, 2008.
- [22] R. T. Jones. The unsteady lift of a wing of finite aspect ratio. 1940.
- [23] J. Katz and A. Plotkin. *Low-speed aerodynamics*, volume 13. Cambridge university press, 2001.
- [24] J. W. Larsen, S. R. Nielsen, and S. Krenk. Dynamic stall model for wind turbine airfoils. *Journal of Fluids and Structures*, 23(7):959–982, 2007.
- [25] T. J. Larsen and H. Aagaard Madsen. On the way to reliable aeroelastic load simulation on vawt’s. In *European Wind Energy Conference & Exhibition 2013*, 2013.
- [26] T. J. Larsen and A. M. Hansen. How 2 hawc2, the user’s manual. *target*, 2:2, 2015.
- [27] G. J. Leishman. *Principles of helicopter aerodynamics with CD extra*. Cambridge university press, 2006.

- [28] J. Leishman and K. Nguyen. State-space representation of unsteady airfoil behavior. *AIAA journal*, 28(5):836–844, 1990.
- [29] J. G. Leishman and T. Beddoes. A semi-empirical model for dynamic stall. *Journal of the American Helicopter society*, 34(3):3–17, 1989.
- [30] J. G. Leishman and G. L. Crouse. State-space model for unsteady airfoil behavior and dynamic stall. *AIAA paper*, pages 89–1319, 1989.
- [31] H. Madsen, T. Larsen, L. Vita, and U. Paulsen. Implementation of the actuator cylinder flow model in the hawc2 code for aeroelastic simulations on vertical axis wind turbines. In *51st AIAA Aerospace Sciences Meeting including the New Horizons Forum and Aerospace Exposition*, number 51st, 2013.
- [32] H. A. Madsen. *The actuator cylinder: a flow model for vertical axis wind turbines*. PhD thesis, Aalborg University Centre, 1982.
- [33] P. Migliore, W. Wolfe, and J. Fanucci. Flow curvature effects on darrieus turbine blade aerodynamics. *Journal of Energy*, 4(2):49–55, 1980.
- [34] P. G. Migliore and W. P. Wolfe. Effects of flow curvature on the aerodynamics of darrieus wind turbines. Technical report, West Virginia University, Morgantown, West Virginia, 1980.
- [35] B. Newman. Actuator-disc theory for vertical-axis wind turbines. *Journal of Wind Engineering and Industrial Aerodynamics*, 15(1-3):347–355, 1983.
- [36] A. Ning. Actuator cylinder theory for multiple vertical axis wind turbines. *Wind Energy Science*, 1(2):327, 2016.
- [37] I. Paraschivoiu. *Wind turbine design: with emphasis on Darrieus concept*. Presses inter Polytechnique, 2002.
- [38] N. Parneix, R. Fuchs, A. Immas, F. Silvert, and P. Deglaire. Efficiency improvement of vertical-axis wind turbines with counter-rotating lay-out.
- [39] G. R. Pirrung and M. Gaunaa. Dynamic stall model modifications to improve the modeling of vertical axis wind turbines. Technical report, Danmarks Tekniske Universitet, Risø Nationallaboratoriet for Bæredygtig Energi, 2016.
- [40] F. Scheurich, T. M. Fletcher, and R. E. Brown. Simulating the aerodynamic performance and wake dynamics of a vertical-axis wind turbine. *Wind Energy*, 14(2):159–177, 2011.
- [41] J. H. Strickland. Darrieus turbine: a performance prediction model using multiple streamtubes. Technical report, Sandia Labs., Albuquerque, N. Mex.(USA), 1975.
- [42] J. H. Strickland, B. Webster, and T. Nguyen. A vortex model of the darrieus turbine: an analytical and experimental study. *Journal of Fluids Engineering*, 101(4):500–505, 1979.
- [43] R. Templin. Aerodynamic performance theory for the nrc vertical-axis wind turbine. *NASA STI/Recon Technical Report N*, 76, 1974.

- [44] T. Theodorsen and W. Mutchler. General theory of aerodynamic instability and the mechanism of flutter. 1935.
- [45] C. Tran and D. Petot. Semi-empirical model for the dynamic stall of airfoils in view of the application to the calculation of responses of a helicopter blade in forward flight. 1980.
- [46] S. Van der Horst. Airfoil design for vertical axis wind turbines including correct simulation of flow curvature. Master's thesis, Delft University of Technology, 2015.
- [47] B. G. Van der Wall and J. Leishman. On the influence of time-varying flow velocity on unsteady aerodynamics. *Journal of the American Helicopter Society*, 39(4):25–36, 1994.
- [48] H. Wagner. Über die entstehung des dynamischen auftriebes von tragflügeln. *ZAMM-Journal of Applied Mathematics and Mechanics/Zeitschrift für Angewandte Mathematik und Mechanik*, 5(1):17–35, 1925.
- [49] A. Zanon, P. Giannattasio, and C. J. Simão Ferreira. A vortex panel model for the simulation of the wake flow past a vertical axis wind turbine in dynamic stall. *Wind Energy*, 16(5):661–680, 2013.
- [50] A. Zervos. Aerodynamic evaluation of blade profiles for vertical axis wind turbines. In *European Community wind energy conference*, pages 611–616, 1988.

Technical University of Denmark

Department of Wind Energy

Frederiksborgvej 399

4000 Roskilde

Denmark

Telephone 46 77 50 85

info@vindenergi.dtu.dk

www.vindenergi.dtu.dk